From Molten Sodium to Solid-State: Design and Optimization of Sodium-Based Batteries Using Computational Models

Zur Erlangung des akademischen Grades eines

Doktors der Ingenieurwissenschaften (Dr.-Ing.)

von der KIT-Fakultät für Chemieingenieurwesen und Verfahrenstechnik des Karlsruher Instituts für Technologie (KIT)

genehmigte

Dissertation

von

Felix Gerbig, M.Sc.
aus Darmstadt

Tag der mündlichen Prüfung:	23.05.2025
Erstgutachter:	Prof. Dr.-Ing. habil. Hermann Nirschl
Zweitgutachterin:	Prof. Dr.-Ing. Ulrike Krewer

"If something doesn't work, it's probably a battery."

— John S. Newman

Acknowledgements

I would like to begin by expressing my deepest gratitude to my supervisor, Prof. Dr.-Ing. habil. Hermann Nirschl, for his invaluable guidance, unwavering support, and insightful feedback throughout the course of this research. His expertise, patience, and encouragement have been instrumental in shaping this thesis. I am truly grateful for the opportunities he provided for academic and personal growth and for his constant belief in my potential.

I also extend my sincere gratitude to Prof. Dr.-Ing. Ulrike Krewer, my co-examiner, for dedicating her time to thoroughly evaluate my thesis. Her thoughtful assessment and valuable insights have greatly enriched the quality of this work.

I am immensely thankful to my office co-workers, Susanne, Amadeus, Kirsten, and Steffen, for fostering a collaborative and supportive work environment. Their friendship, constructive discussions, and daily encouragement turned challenging moments into manageable ones. Whether it was sharing ideas, offering support, or providing a much-needed break, their camaraderie was invaluable.

Beyond the office, I am grateful to all my colleagues at the Institute of Mechanical Process Engineering and Mechanics. The fruitful scientific discussions—often venturing beyond the scope of battery research—have broadened my perspective and enriched my understanding. Their unwavering help during the ups and downs of the research process, as well as the joy shared during coffee breaks, conferences, and social events, brought balance and camaraderie to this journey.

A heartfelt thanks goes to the master's students Juan, Maximilian, Renata, Jakob, Fariba, Stefan, and Jérôme, whom I had the pleasure of supervising. Their dedication, hard work, and enthusiasm significantly contributed to the progress of this research. From experiments to simulations, their efforts and insights have been vital to advancing this project, making it a rewarding experience to work with them.

I am deeply grateful to the administrative and technical staff at the institute for their dedication and efficiency, which ensured a smooth research process. I am especially thankful to Amuthavalli, who handled my last-minute inquiries with understanding and great patience.

I would like to express my sincere gratitude to Prof. Robert Kee at the Colorado School of Mines for generously supporting my research stay in his group. His openness and expert guidance provided a unique opportunity to gain new perspectives and significantly advance my work. I

am equally thankful to the PhD students in the graduate student office for welcoming me so warmly and fostering a collegial, inspiring atmosphere. Our scientific exchanges, as well as shared experiences beyond the lab, made my stay both intellectually stimulating and personally enriching. This research stay was generously funded by the Karlsruhe House of Young Scientists (KHYS), whose support I gratefully acknowledge.

I would also like to warmly thank Yannick, Alejandro, Anshuman, and Isabella for taking the time to review my thesis. Their careful reading, thoughtful suggestions, and honest feedback helped me to refine both the structure and clarity of the manuscript. I truly appreciate their support and the many constructive discussions that emerged from their comments.

On a personal level, I owe an enormous debt of gratitude to my family for their unwavering love, support, and encouragement. Their belief in me has been a constant source of strength, inspiring me to persevere through challenges.

Finally, I want to express my deepest thanks to my partner, Sophie, for her unwavering support and understanding throughout this journey. Her emotional strength and encouragement have been my rock, especially during the most demanding times. I cannot thank her enough for taking care of so many things on my behalf, allowing me to fully dedicate myself to this work. Her patience, understanding, and love have been invaluable, and I am profoundly thankful for the sacrifices she made to help me reach this milestone.

Abstract

In the transition to a more sustainable energy future, electrochemical storage systems like batteries are vital for enabling large-scale integration of renewable energy sources. This thesis focuses on the design and optimization of sodium-based batteries, which offer a promising alternative to lithium-ion batteries for stationary energy storage and other large-scale applications. Sodium's abundance and its potential for cost-effective production position it as a key solution to challenges in renewable energy integration. The study explores two different sodium-based battery technologies—sodium-iodine (a molten sodium battery) and all-solid-state sodium-ion batteries (ASSSIB)—key representatives of the two main categories of sodium-based batteries, employing advanced microscale simulations to analyze their performance and guide design improvements.

The sodium-iodine battery, with a molten sodium anode and aqueous iodine-based catholyte, is modeled using a 3D, spatially resolved electrochemical framework, marking a significant advance over traditional 1D models by capturing complex spatial effects. Key results show that diffusion limitations, particularly in two-dimensional electrodes, constrain performance of electrodes with thicknesses beyond 1 cm with an optimal 8 M iodine catholyte concentration balancing theoretical capacity and practical performance. Switching to three-dimensional electrodes, such as glassy carbon foam, overcame these diffusion limitations, enhancing capacity utilization by increasing and more evenly distributing the surface area for electrochemical reactions and improving ion transport. Interestingly, porosity was found to be more critical than surface area, as higher porosity facilitates smoother sodium-ion transit between the cells of the foam, significantly boosting battery efficiency.

In matching the model with early experimental data, incorporating the pentaiodide species (I_5^-) was essential to aligning the model capacity predictions with experimental observations. This adjustment improved agreement with experimental polarization curves, though discrepancies—likely from iodine precipitation or higher polyiodide formation—suggest further investigation is needed.

The second part of the thesis investigates all-solid-state sodium-ion batteries (ASSIBs) using polymer-ceramic composite electrolytes, which offer significant advantages in terms of safety, cycle life, and stability. A dual-modeling approach combined microscale particle-resolved simulations and a pseudo-two-dimensional (P2D) model to assess the impact of electrode and electrolyte properties on battery performance. Microscale simulations identified ion transport

limitations, particularly in thick, low-porosity cathodes, as the main performance bottleneck, with high active material content exacerbating these limitations during charging by creating steep concentration gradients close to the separator.

To address this, a P2D model was developed to investigate optimized cathode structures showing that non-uniform porosity, with a gradient from the separator to the current collector, significantly improves ion transport and capacity utilization. By combining the Zehner-Bauer-Schlünder and Maxwell-Garnett models, the P2D simulations retained the accuracy of the fully resolved model while achieving a notable increase in computational efficiency. The P2D model, integrated in a differential evolution algorithm, optimized parameters like cathode thickness and material distribution. In contrast to a one-factor-at-a-time approach, the findings revealed discharging as the key bottleneck, with optimized designs performing better during charging across all C-rates.

Reevaluating ionic transport mechanisms in polymer-ceramic composite electrolytes, through comparison with early experimental data, challenged existing assumptions. Superionic interphases—regions with enhanced conductivity near particle surfaces—were hypothesized to explain the experimental measurements for $Na_{3.4}Zr_2Si_{2.4}P_{0.6}O_{12}$.

The thesis contributes to the growing body of research on sodium-based batteries by providing detailed insights into the electrochemical and transport processes that dictate their performance. The findings on sodium-iodine batteries emphasize the importance of 3D electrode structures in overcoming diffusion limitations, while the results on ASSSIBs highlight the need for optimized material distribution in composite electrolytes. Together, these results underscore the potential of sodium-based batteries to meet the growing demand for sustainable, scalable energy storage solutions, thereby facilitating the large-scale adoption of renewable energy technologies.

Zusammenfassung

Der Übergang zu einer nachhaltigeren Energiezukunft hängt maßgeblich von der Integration erneuerbarer Energiequellen in großem Maßstab ab. Dabei spielen elektrochemische Energiespeicher wie Batterien eine entscheidende Rolle. Die vorliegende Arbeit fokussiert sich auf die Entwicklung und Optimierung von Natrium basierten Akkumulatoren für die stationäre Energiespeicherung sowie andere großtechnische Anwendungen. Aufgrund der hohen Verfügbarkeit und geringen Kosten von Natrium stellt es eine vielversprechende Alternative zu Lithium-Ionen-Akkumulatoren da. Die Untersuchungen fokussieren sich auf je ein neuartiges Konzept für die zwei wichtigsten Kategorien für Natriumbatterien, nämlich der Natrium-Iod-Batterie (Flüssigmetallbatterien) sowie der Natriumfestkörperbatterie (ASSSIB) in der Kategorie der Natrium-Ionen-Batterien. Schwerpunkt der Arbeit sind Simulationen im Mikromaßstab, um die Leistungsfähigkeit der beiden Natriumbatterien zu analysieren und Verbesserungen im Batteriezelldesign aufzuzeigen.

Zunächst kommt für die Modellierung der Natrium-Iod-Batterie mit einer flüssigen Natriumanode und einem wässrigen Katholyten auf Iodbasis ein räumlich aufgelöstes elektrochemisches Modell zum Einsatz. Dies stellt eine Weiterentwicklung gegenüber herkömmlichen 1D-Modellen dar, um komplexe räumliche Effekte zu erfassen. Die wichtigsten Ergebnisse legen dar, dass Diffusionslimitierungen, insbesondere bei zweidimensionalen Elektroden, die Leistungsfähigkeit von Kathoden mit einer Dicke von mehr als einem Zentimeter einschränken, während sich eine Iod-Katholyt-Konzentration von $8\,\mathrm{mol\,L^{-1}}$ als optimal erweist.

Die Weiterentwicklung der Elektrodenstruktur hin zu dreidimensionalen Elektroden, wie beispielsweise Glaskohlenstoffschaum, führt zu einer Überwindung der zuvor genannten Diffusionslimiterung. Dies steigert die Ausnutzung der Kapazität, ausgelöst durch eine Vergrößerung und gleichmäßigere Verteilung der Oberfläche für elektrochemische Reaktionen sowie eine Verbesserung des Ionentransports. Hierbei hat die Porosität einen entscheidenderen Einfluss auf die Leistungsfähigkeit der Batterie als die Größe der Elektrodenoberfläche: Eine höhere Porosität ermöglicht einen reibungsloseren Natrium-Ionen-Transport zwischen den Zellen des Glaskohlenstoffschaums und steigert hierdurch die Leistungsfähigkeit des Batteriesystems. Durch eine Erweiterung des elektrochemischen Modells um Pentaiodid-Ionen (I_5^-) gelingt eine Übereinstimmung der Kapazitätsvorhersage der Simulation mit ersten experimentellen Ergebnissen. Die Anpassungen verbesserten die Übereinstimmung mit der experimentellen Polarisationskurve.

Verbleibende Diskrepanzen lassen Iodausfällungen oder die Bildung höherer PolyIodide vermuten und bedürfen weiteren experimentellen Untersuchungen.

Im zweiten Teil der Arbeit liegt der Fokus auf numerischen Untersuchungen von Natriumfestkörperbatterien unter Verwendung von polymerkeramischen Kompsitelektrolyten. Diese bieten gegenüber Flüssigelektrolyten erhebliche Vorteile in Bezug auf Sicherheit, Zykluslebensdauer und Stabilität. Ein dualer Modellierungsansatz kombiniert mikroskalige, partikelaufgelöste Simulationen mit einem pseudo-zweidimensionalen (P2D-)Modell, um die Auswirkungen der Elektroden- und Elektrolyteigenschaften auf die Batterieleistung zu bewerten. Mikrostruktursimulationen sagen Einschränkungen beim Ionentransport, insbesondere Kathoden mit hoher Dicke bei geringer Porosität, als entscheidenden Faktor für die Leistungsfähigkeit des Batteriesystems voraus. Ein hoher Aktivmaterialgehalt führt zu hohen Konzentrationsgradienten in der Nähe des Separators und beeinträchtigt insbesondere den Ladevorgang. Ein in dieser Arbeit entwickeltes P2D-Modell, ermöglicht die Ermittlung optimierter Kathodenstrukturen um diese Einschränkungen zu überwinden. Es zeigte sich, dass eine Porositätsverteilung mit einem Gradienten vom Separator zum Stromkollektor den Ionentransport und folglich die Kapazitätsausnutzung deutlich verbessert. Die kombinierte Nutzung des Zehner-Bauer-Schlünder- und des Maxwell-Garnett-Modells erhält die Genauigkeit des vollständig aufgelösten Modells und verkürzt gleichzeitig die Rechenzeit deutlich. Dies ermöglichte die Einbindung des P2D-Modells in ein Optimierungsverfahren basierend auf einem evolutionären Algorithmus zur globalen Optimierung von Parametern wie der Kathodendicke und der räumlichen Partikelverteilung. Im Gegensatz zu einem Ansatz, bei dem jeweils nur ein Faktor verändert wird, zeigten die Ergebnisse für alle C-raten, dass der Entladevorgang den Engpass darstellt.

Der Vergleich von Simulationsergebnissen dieser Arbeit zu Ionentransportmechanismen in polymerkeramischen Kompositelektrolyten mit frühen experimentellen Daten deutet auf die Existenz superionischer Zwischenphasen—Bereiche mit erhöhter Leitfähigkeit in der Nähe von Partikeloberflächen—an. Diese erklären für $Na_{3.4}Zr_2Si_{2.4}P_{0.6}O_{12}$ die gemessenen effektiven Leitfähigkeiten.

Die Dissertation liefert detaillierte Einblicke in die leistungsbestimmenden elektrochemischen und Transportprozesse von zwei der vielversprechendsten Batterietypen in den beiden wichtigsten Natriumbatteriekategorien. Die Resultate zu Natrium-Iod-Batterien verdeutlichen die Relevanz von dreidimensionalen Elektrodenstrukturen zur Überwindung von Diffusionslimitierungen, während die Resultate zu Natriumfestkörperbatterien die Notwendigkeit einer optimierten Materialverteilung in Kompositelektrolyten hervorheben. Die Ergebnisse unterstreichen das Potenzial von natriumbasierten Batterietechnologien, den wachsenden Bedarf nach nachhaltigen, skalierbaren Energiespeicherlösungen zu befriedigen.

Contents

Symbols

a_s	surface area per unit volume, $m^2\,m^{-3}$	48
a_s	specific interfacial surface area, $m^2\,m^{-3}$	93
A_{cc}	current collector plate area, m^2	95
A_c	total contact area of the domain, m^2	98
A_f	contact area between two particles, m^2	98
c_{el}	electrolyte sodium ion concentration, $mol\,m^{-3}$	73
c_s	active material sodium ion concentration, $mol\,m^{-3}$	73
C	C-rate, h^{-1}	29
C_f	shape factor	97
d	space dimension	97
D_{el}	electrolyte sodium ion diffusion coefficient, $m^2\,s^{-1}$	73
D_k^{el}	catholyte diffusion coefficient of species k, $m^2\,s^{-1}$	22
D_s	active material sodium diffusion coefficient, $m^2\,s^{-1}$	73
$E^\ominus$	standard potential, V	5
F	Faraday constant, $C\,mol^{-1}$	22
i_{BV}	Butler-Volmer current density, $A\,m^{-2}$	90
i_0	exchange current density, $A\,m^{-2}$	23
i_{cell}	total cell current density, $A\,m^{-2}$	29
$\boldsymbol{i}_{el}$	electrolyte current density, $A\,m^{-2}$	25
$\boldsymbol{i}_{ed}$	electrode current density, $A\,m^{-2}$	24
$\boldsymbol{i}_s$	active material current density, $A\,m^{-2}$	93
j_{BV}	Butler-Volmer flux density, $mol\,m^{-2}\,s^{-1}$	93
$\boldsymbol{J}$	surface flux density, $mol\,m^{-2}\,s^{-1}$	22
k	Butler-Volmer reaction constant, $m^{2.5}\,mol^{-0.5}\,s^{-1}$	75
k_c	reduced core ionic conductivity in the ZBS model	98
k_f	reaction rate constant, $m^3\,s^{-1}\,mol^{-1}$	24
k_{f,I_5^-}	reaction rate constant, $m^3\,s^{-1}\,mol^{-1}$	65
k_P	ratio of ionic conductivities of dispersed and continuous phase in the ZBS model	98
$K_{I_3^-}$	equilibrium constant of the triiodide recombination reaction, $m^3\,mol^{-1}$	23
$K_{I_5^-}$	equilibrium constant of the pentaiodide recombination reaction, $m^3\,mol^{-1}$	65
K_{NaTFSI}	ionic conductivity prefactor for the PEO-NaTFSI system, $м^{-1}$	74

L_{pos}	length of the positive half cell, m	111
L_{sep}	length of the separator, m	111
$\boldsymbol{n}$	surface unit normal vector pointing outside the computational domain	76
N_{P}	number of particles	98
r_k	molar production rate, $\text{mol m}^{-3}\,\text{s}^{-1}$	22
R	universal gas constant, $\text{J mol}^{-1}\,\text{K}^{-1}$	22
R_{AM}	active material particle radius, m	107
s_i	signed stoichiometric coefficient	74
t_+^0	transference number of sodium ions in the electrolyte	73
T	temperature, K	22
U_{eq}	equilibrium potential, V	75
q	physical quantity	97
X_k	electrolyte concentration of species k, mol m^{-3}	22
z_k	catholyte charge	22
b_{Brug}	Bruggeman exponent	100
γ	flattening coefficient	97
γ_k	damping factor	33
ϵ	porosity	48
ε_{s}	active material porosity	101
κ	electrolyte ionic conductivity, S m^{-1}	26
κ_{d}	electrolyte diffusional conductivity, S m^{-1}	74
κ_{fil}	active filler ionic conductivity, S m^{-1}	98
κ_{pol}	polymer ionic conductivity, S m^{-1}	98
ν	number of moles of ions into which a mole of electrolyte dissociates	74
ν_i	moles of ion i produced when a mole of its salt dissociates	74
ρ_{ed}	charge density, C m^{-3}	24
σ_{ed}	electrode conductivity, S m^{-1}	24
σ	active material conductivity, S m^{-1}	73
τ	electrode tortuosity	100
Φ_{el}	electrolyte potential, V	22
Φ_{ed}	electrode potential, V	24
Φ_{s}	active material potential, V	73
φ_{AM}	active material content	105
φ_{fil}	active filler volume fraction	109
φ_{pol}	polymer volume fraction	108
$\varphi_{\text{el,fil}}$	electrolyte active filler volume fraction	85
$\varphi_{\text{el,pol}}$	electrolyte polymer volume fraction	97
χ	mole fraction, м м^{-1}	79

1 Introduction

In the last century, the global economy has heavily relied on fossil fuels for energy. However, concerns over the finite nature of fossil fuel reserves and their significant environmental impact—particularly the contribution to global warming through the greenhouse effect caused by carbon dioxide emissions—have intensified the search for alternative energy sources.

According to the 2023 International Energy Outlook by U.S. Energy Information Administration, global energy demand is predicted to rise significantly, reaching 854.7 quadrillion British thermal units from the current 637.8 [1]. The recent surge in atmospheric CO_2 concentrations to 416 ppm underscores the urgent need to enhance efforts to keep global warming below 2 °C above pre-industrial levels. Consequently, 50 % of the projected rise in energy consumption is anticipated to rely on alternative energy sources.

1.1 The role of energy storage in renewable energy integration

Since the 1990s, significant advancements have been made in substituting traditional energy sources with renewable ones, such as solar, wind, and geothermal energy. However, the inherent intermittency and instability of solar and wind energy pose significant challenges which can be addressed with reliable energy storage solutions for both stationary and mobile applications. The existing electrical grid systems worldwide are not equipped to handle large-scale integration of intermittent energy sources without risking serious disruptions. It is generally accepted that more than 20 % penetration from intermittent renewables can greatly destabilize grid systems [2].

Large-scale energy storage technologies play a crucial role in addressing these challenges by smoothing out fluctuations in energy supply, thereby facilitating the efficient integration of renewables into the power grid.

Energy storage technologies can be broadly classified into five categories, as described by Zhao et al. [3]:

Mechanical Storage includes technologies like pumped hydro storage (PHS), compressed air energy storage (CAES), and flywheels. PHS systems are suitable for bulk energy

applications due to their long discharge times, while flywheels offer high energy efficiency and rapid response times, making them ideal for frequency regulation.

Electrochemical Storage is category that encompasses various battery technologies, including lithium-ion (LIB), sodium-ion, sulfur, and flow batteries.

Chemical Storage Involves hydrogen energy storage systems (HydESS), which offer the advantage of dual-use as both an energy carrier and a raw material in industries like chemicals and steel. However, high capital costs and low efficiency of electrolyzers and fuel cells are significant drawbacks.

Thermal Storage stores energy in the form of heat, offering potential for integration with thermal power plants and industrial processes.

Electrical Storage includes supercapacitors, known for their near-unlimited cycle stability, high power density, and fast charging/discharging capabilities. Despite these advantages, their low energy density limits their application to short-duration storage needs.

Among the various energy storage technologies, electrochemical energy storage, such as battery systems, stands out due to its environmental benefits, high energy density, and scalability. Beyond batteries, other forms of energy storage, such as CAES and PHS, have been developed or are under development for large scale storage. PHS, in particular, remains the most widespread technology with over 90 % market share [1]. However, both CAES and PHS are constrained by specific geographic requirements, which severely limit their broader application.

Scaling up from portable power sources to transportation-scale and grid-scale applications necessitates careful consideration of several factors in the design of electrochemical storage systems. These factors include the cost and abundance of materials, the environmental and eco-efficiency of cell chemistries, as well as life cycle and safety analyses [4]. While some existing rechargeable battery technologies can meet many of these sustainability requirements, intrinsic limitations in energy storage capacity or technological hurdles continue to impede their deployment on a large scale [2].

An added advantage of most renewable energy sources is their modular nature, which supports distributed power generation. Such decentralization minimizes the economic and ecological effects related to power transmission from centralized power plants. Furthermore, the distributed characteristic of renewable energy systems offers a socio-economic advantage by potentially fostering economic expansion in underdeveloped areas. Therefore, it is sensible to develop energy storage technologies that can deliver power economically at various scales, from small to medium and large-scale storage solutions.

In addition to cost considerations, other factors such as consumer trust, safety, and the reliability of new systems will be decisive for the success of stationary battery technologies. The risk-averse

nature of the utility industry poses a significant market entry barrier for emerging technologies. Therefore, it is pragmatic to initially promote battery technologies as medium-sized energy storage solutions, which can later be scaled up to large-scale applications. This strategy may encounter less resistance than attempting to introduce large-scale energy storage technologies from the outset.

In addition, battery storage is not only vital for the integration of renewable energy but also offers solutions for conventional power generation challenges. Traditional power systems require a near-instantaneous balance between supply and demand, which often necessitates the use of peaking power plants that remain idle for extended periods. This inefficiency leads to higher electricity costs.

The decreasing cost of solar and wind energy, coupled with rising electricity prices from fossil fuels and increasing costs of CO_2 certificates, has further enhanced the economic viability of electrical energy storage.

1.2 Challenges and opportunities for battery technologies

For renewable to dominate the primary energy mix by mid-century, grid-compatible electricity storage technologies must meet key requirements, including high capacity, rapid charge/discharge rates, operating temperature, high energy density, long cycle life, stable operation, reliability, cost-effectiveness, and scalability. No single technology can meet all these criteria, leading to a wide variety of storage options, each suited to different applications depending on factors like cost, performance, and scalability. As a result, researchers are continually exploring new battery technologies with unique properties tailored to specific needs.

Lithium-ion batteries (LIBs) have become the dominant technology due to their high energy density and long lifespan, making them the preferred choice for portable electronics and electric vehicles [5]. However, the high cost of LIBs, along with the limited availability and geopolitical concentration of lithium resources, poses significant challenges. Additionally, the environmental impact of lithium mining and processing is a growing concern [6, 7].

Sodium-based batteries have emerged as a promising alternative, particularly for applications where energy density is less critical, such as stationary energy storage and large mobile applications like ships, trains, and trucks.

Figure 1.1 presents the relative abundances of selected elements within the Earth's crust. Elements such as lithium, cobalt, and nickel, which are critical for the most advanced lithium-ion battery (LIB) technologies, are relatively scarce. In stark contrast, sodium is found in much higher

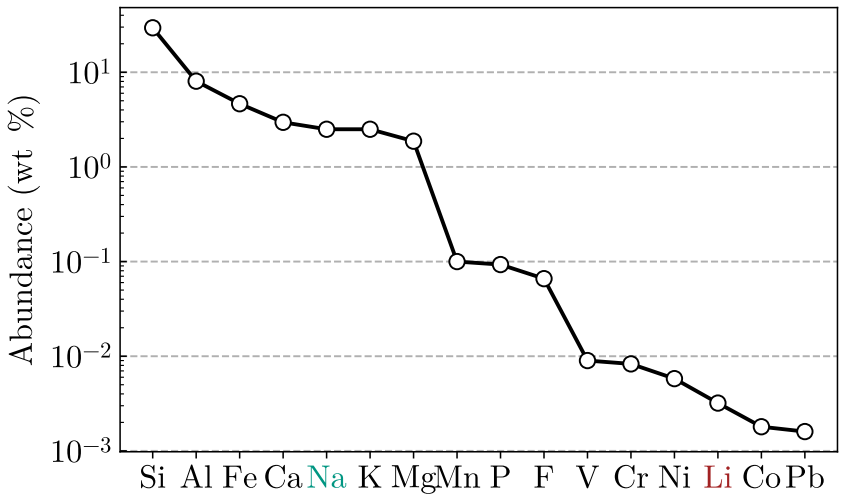

Figure 1.1: Abundances of chemical elements in the Earth's crust. The data is derived from Yaroshevsky [8]. Lines are for eye guidance only.

concentrations, constituting approximately 2.5 wt% of the Earth's crust. Additionally, vast sodium resources are present in the oceans, further facilitating the extracting of this element.

The plentiful availability of sodium offers several significant advantages. Chief among these is the reduction of geopolitical risks associated with supply chains, which is a growing concern for materials like lithium and cobalt. Moreover, the abundant and widely distributed nature of sodium resources promises to stabilize sodium prices, potentially providing a more cost-effective alternative to lithium for future battery technologies.

Table 1.1: Comparison of Na and Li properties. Data is taken from [9–12]

	Na	Li
Molar mass ($g\,mol^{-1}$)	23.00	6.94
Ionic radii (Å)	1.02	0.76
Stokes radius in water (Å)	1.84	2.38
$E^{\ominus}$ vs. SHE (V)	−2.71	−3.04
Melting point (°C)	97.9	180.5
Theoretical capacity ($mA\,h\,cm^{-3}\,m$)	1131	2062
Density at 20 °C ($kg\,L^{-1}$)	0.97	0.53

Sodium-based batteries, along with other novel battery technologies, are often categorized under terms such as post-lithium-ion batteries or post-lithium batteries in literature [13, 14]. However, it's important to note the distinction between these categories, as they refer to different technological trajectories. The term *post-lithium-ion batteries* encompasses not only sodium-ion batteries

but also novel lithium-based technologies, including lithium-sulfur [15], lithium-air [16], and lithium-metal batteries [17]. These advancements aim to push the boundaries of performance, particularly in terms of energy density and cost-effectiveness.

In contrast, the *post-lithium* category refers specifically to battery technologies that are entirely lithium-free. These technologies are being explored to reduce dependence on lithium.

While the post-lithium technologies aim to eventually replace LIBs, the post-lithium-ion technologies are more about evolving the existing lithium-based framework to overcome current limitations. Even with these advancements, battery performance—especially energy density—cannot be increased indefinitely due to fundamental theoretical constraints. For instance, the standard electrode potential of lithium ($E^{\ominus}_{\mathrm{Li/Li^+}} = 3.04\,\mathrm{V}$) is the most negative in the galvanic series, making it unlikely that a radically superior battery system will be discovered in the near future. Nevertheless, after lithium, sodium stands as the second lightest and smallest alkali metal, rendering it a suitable substitute for lithium due to its plentiful supply and standard potential ($E^{\ominus}$). Table 1.1 presents a comparison of $Na^+$and Li^+ properties.

Given these constraints, a total replacement of lithium-based batteries by lithium-free alternatives is improbable. Instead, a more plausible scenario is the partial substitution of LIBs in specific applications where their current dominance is due more to their market readiness than to an ideal fit for the application. Sodium-based batteries, along with other "post-lithium" technologies, could serve as more appropriate alternatives in such contexts.

Another justification for the post-lithium-ion category is the desire to develop battery chemistries that remain closely aligned with LIBs, allowing for a smoother transition in both research and manufacturing [7, 18]. The extensive focus on LIBs has led to a significant accumulation of expertise and established methodologies. Moreover, the recent surge in electric vehicle (EV) production, driven by policies such as the planned bans on internal combustion engines in the European Union and the United Kingdom, has greatly expanded global LIB manufacturing capacity [19].

Batteries categorized as post-lithium-ion can take advantage of this existing infrastructure, potentially accelerating their path to market readiness [20]. This is crucial, given the urgent need to develop new battery technologies that can meet global challenges like climate change and energy security. Therefore, while post-lithium refers to a future beyond lithium, post-lithium-ion represents a strategic evolution within the lithium framework, enhancing the prospects for timely and scalable innovations in energy storage.

1.3 Structure and objectives of the thesis

The overarching aim of this thesis is to position sodium-based batteries as a promising candidate for post-lithium battery technologies. This goal is pursued through two primary objectives: (1) gaining deeper insights into the battery system's functionality and (2) predicting how design variations impact overall performance.

A central component of this work involves the development of robust physical models that accurately represent the real-world behavior of sodium batteries. Since many internal processes are difficult to observe experimentally, these models are essential for capturing the underlying electrochemical and transport phenomena. Building on these physical models, simulations are then conducted to explore the system's behavior in detail, assess how different design choices influence key performance metrics, and guide design improvements.

This thesis leverages microscale simulations, which operate at time and length scales that bridge the gap between material-level characteristics and the overall performance of the battery. It is essential to acknowledge that the phrase 'microscale simulations' is interpreted variously across the literature, contingent on the classification system different researchers use. A detailed explanation of the simulation methodologies used in this study is provided in section 2.3.

The work is structured into two main parts, each focusing on a novel battery concept representing one of the two primary categories of sodium-based batteries:

- Chapter 3 investigates sodium-iodine batteries, representing the category of liquid sodium batteries, with a focus on their design, performance, and potential improvements.
- Chapter 4 examines all-solid-state sodium-ion batteries (ASSSIB), highlighting their development, key challenges, and potential applications.

Before delving into these specific battery systems, chapter 2 lays the groundwork by providing the theoretical background and reviewing the current state-of-the-art in sodium-based battery technology. This chapter revisits the most relevant types of sodium batteries, summarizes the progress of research on electrode materials and electrolytes, provides a general overview on battery modeling and simulation, and identifies gaps in the literature, thereby underscoring the significance of the present work.

2 Theoretical Foundation

A battery is galvanic cell and comprised of three main constituents: the positive electrode (cathode), the negative electrode (anode) and the electrolyte between them. In rechargeable batteries, electrical energy is reversible converted to electrochemical energy and vice versa. A battery *cell*, as the smallest unit in a battery, is defined by its cell voltage and nominal charge capacity, whose multiplication gives the cell's energy capacity. Battery cells can subsequently be assembled into batteries and battery packs. Arranging them in series enhances the voltage, while connecting them in parallel boosts the charge capacity. This section delves into sodium batteries and battery modeling strategies, with a detailed examination of the fundamentals of battery technologies provided in [21–23].

2.1 Types of sodium batteries

The history of research and development in sodium and sodium-ion batteries has been extensively reviewed by Delmas [24]. Rather than reiterating the chronological progression of sodium in battery technology, this section aims to provide a concise overview of the state-of-the-art and future perspectives of sodium-based battery technologies. This overview is intended to lay a solid foundation for understanding the research undertaken in this study.

Sodium batteries can be broadly categorized into two main types: **liquid sodium batteries** (or molten sodium cells) and (mostly) solid-state sodium batteries, which are more commonly referred to as **sodium-ion batteries** (SIBs) [25]. Each category encompasses distinct technologies with varying operational principles, advantages, and challenges, all of which contribute to the diverse landscape of sodium-based energy storage solutions.

2.1.1 Molten sodium batteries

Molten sodium batteries operate with liquid sodium metal anodes, maintained above the melting temperature of sodium (T_s = 98 °C). Liquid sodium metal as an anode material offers several remarkable electrochemical advantages, including high energy density and a low standard potential—only 0.3 V more positive than lithium—leading to high cell potentials. Additionally,

liquid sodium demonstrates excellent rate capability and resists dendrite formation (tree-like structures that form during the solidification of metals), a key challenge in the development of sodium metal anodes [26]. These advantageous characteristics have spurred research into several battery cell concepts based on molten sodium anodes, the most notable of which are described below.

Sodium-sulfur Batteries Developed in the 1980s, sodium-sulfur (NAS) batteries should not be confused with room-temperature sodium-sulfur batteries [27], which share more similarities with lithium-sulfur battery systems [28]. NAS batteries operate at temperatures around 300 °C due to the high melting points of polysulfides [29, 30]. The cell design features a molten sodium anode and a molten sulfur cathode, separated by a solid electrolyte made of β″-alumina which acts as a fast sodium-ion conductor. The theoretical cell voltage for this system is approximately 2 V, making NAS batteries a viable option for high-temperature energy storage applications. To date, this remains the sole commercially available molten sodium battery system, predominantly found in the Japanese market, with pilot plants planned in other regions [31].

ZEBRA The ZEBRA (Zeolite Battery Research Africa) battery evolved from the NAS battery concept, featuring a molten sodium anode paired with a solid nickel chloride cathode, and a liquid electrolyte composed of sodium chloroaluminate [32]. This system operates at temperatures between 270–350 °C, with the β″-alumina solid electrolyte serving to separate the molten sodium anode from the cathode material [33]. The ZEBRA battery delivers a nominal cell voltage of 2.58 V, making it an attractive candidate for high-temperature energy storage, particularly in industrial and grid-scale applications.

Liquid metal battery Liquid metal batteries (LMB) represent a distinct class of molten sodium batteries, characterized by their three-layer structure of immiscible liquids [34]. The layers typically consist of a molten metal anode, a molten salt electrolyte, and a molten metal or semi-metal cathode. While LMBs operate at around 350 °C, challenges such as reducing the operating temperature and addressing relatively high self-discharge rates remain critical areas of ongoing research and development.

Fully molten metal halide batteries Fully molten metal halide batteries are a relatively new addition to the landscape of molten sodium batteries. These systems feature a completely liquid cathode, where the net charge reaction involves sodium halides such as chlorides, bromides, or iodides [35]. A notable advancement in this area was reported by Small et al. [36], who developed a cathode containing a 50:50 mixture of NaI and $AlCl_3$, which enabled operation at temperatures as low as 120–180 °C. Further theoretical studies by Zhu et al. explored an

aqueous electrolyte operating at 120 °C, utilizing copper-iodide and iodide-triiodide chemistries [37, 38]. These concepts were experimentally validated by Holzapfel et al., who demonstrated a proof-of-principle study using a highly concentrated aqueous bromine/bromide and iodine/iodide solution [39].

2.1.2 Sodium-ion batteries

The intercalation chemistry of sodium is similar to that of lithium, particularly in terms of cathode materials, allowing for the use of analogous compounds in both systems [40]. However, key differences arise from the larger ionic radius of Na^+ ions (1.02 Å) compared to Li^+ ions (0.76 Å), affecting phase stability, transport properties, and interphase formation [41]. This difference contributes to slower sodium diffusion rates than those of lithium in traditional lithium intercalation materials. Despite these challenges, the larger size of sodium cations results in a 20 % reduction in total binding energy due to weaker solvation shells and a decreased charge-to-radius ratio [42]. Eshetu et al. [43] provide a comprehensive summary of the differences between Na^+ and Li^+ in relation to insertion materials.

Furthermore, SIBs have the advantage of using aluminum for the anode current collector, while LIBs rely on copper. This distinction is economically important, as copper is not only more costly but is also designated as a critical material by the U.S. Department of Energy [44] and a strategic material by the European Comission [45].

Key cathode materials for SIBs include:

Sodium Layered Oxide Cathode Materials Layered oxides, which are the most prominent class of active materials in LIBs [46], have led to extensive research on analogous compounds in SIBs, particularly $NaMO_2$, where M represents a transition metal. Despite the structural similarity, the larger ionic radius of Na^+ compared to Li^+ results in significant differences in crystal structures. This structural diversity, however, offers a great degree of customization, enabling the tuning of properties to meet specific requirements. While promising energy densities have been achieved with these materials, challenges remain in ensuring cycling stability and mitigating volume changes during operation [47].

Phosphate-Based Electrode Materials This category includes various subfamilies, with sodium transition metal phosphates ($(PO_4^{-3})_3$) being particularly notable. Among these, $Na_3V_2(PO_4)_3$ (NVP) and its derivatives have garnered significant attention [48–50]. NVP exhibits an energy density of 117.6 mA h g^{-1} at 3.4 V and is renowned for its high sodium diffusion coefficients [51, 52]. To address its low electrical conductivity, carbon coating has been employed as an effective strategy [53].

Prussian Blue Electrode Materials Prussian blue analogues (PBA) are coordination polymers composed of metal hexacyanometallates, typically formulated as $Na_xT[M(CN)_6] \cdot zH_2O$, where M is usually a transition metal, and T represents nitrogen-coordinated transition metal ions [54]. While PBAs offer the advantage of using low-cost, abundant, and non-toxic elements, the stable synthesis of these materials remains a significant challenge.

Another key distinction between LIBs and SIBs lies in the choice of the negative electrode. While graphite is commonly used as the anode material in LIBs due to its ability to intercalate Li^+ ions, it is generally ineffective for Na^+ intercalation. Instead, hard carbon is employed as the preferred anode material for SIBs [55]. For a more detailed discussion on hard carbon as an anode material, readers are directed to existing literature, as insertion anodes are not the primary focus of this work [56].

2.2 Electrolytes for sodium-ion batteries

The electrolyte, although often overshadowed by the focus on anode and cathode materials, is a critical component in the design and operation of a battery cell. Its significance extends beyond merely serving as an ionic conductor between the electrodes; the electrolyte plays a pivotal role in determining the overall performance, safety, and longevity of the battery system. Issues such as bloating, leakage, flammability, and even the potential for explosive failure are closely tied to the properties and behavior of the electrolyte. Selecting the ideal electrolyte is a complex task due to the need to satisfy a range of often conflicting requirements. These include chemical inertness, a wide electrochemical stability window, high ionic conductivity paired with negligible electronic conductivity (to enable efficient ion transport while minimizing self-discharge), as well as being nontoxic, sustainable, low-cost, and capable of forming a tunable interphase [43].

In the context of sodium-ion batteries (SIBs), liquid electrolytes are commonly categorized into three primary types: non-aqueous, aqueous, and ionic liquid electrolytes [58]. Among these, non-aqueous liquid electrolytes are the most prominent and are structurally similar to those used in traditional lithium-ion batteries (LIBs). These electrolytes typically consist of sodium salts dissolved in aprotic solvents, which provide a wide electrochemical stability window and compatibility with high-energy electrodes. Comprehensive reviews of these electrolyte systems are available in the literature [11].

However, the use of liquid electrolytes is not without its challenges. Issues such as electrolyte leakage, bloating, and the formation of highly reactive interfaces can compromise the safety and reliability of the battery. These concerns have spurred significant interest in the development of solid or quasi-solid electrolytes as alternatives to traditional liquid systems [43].

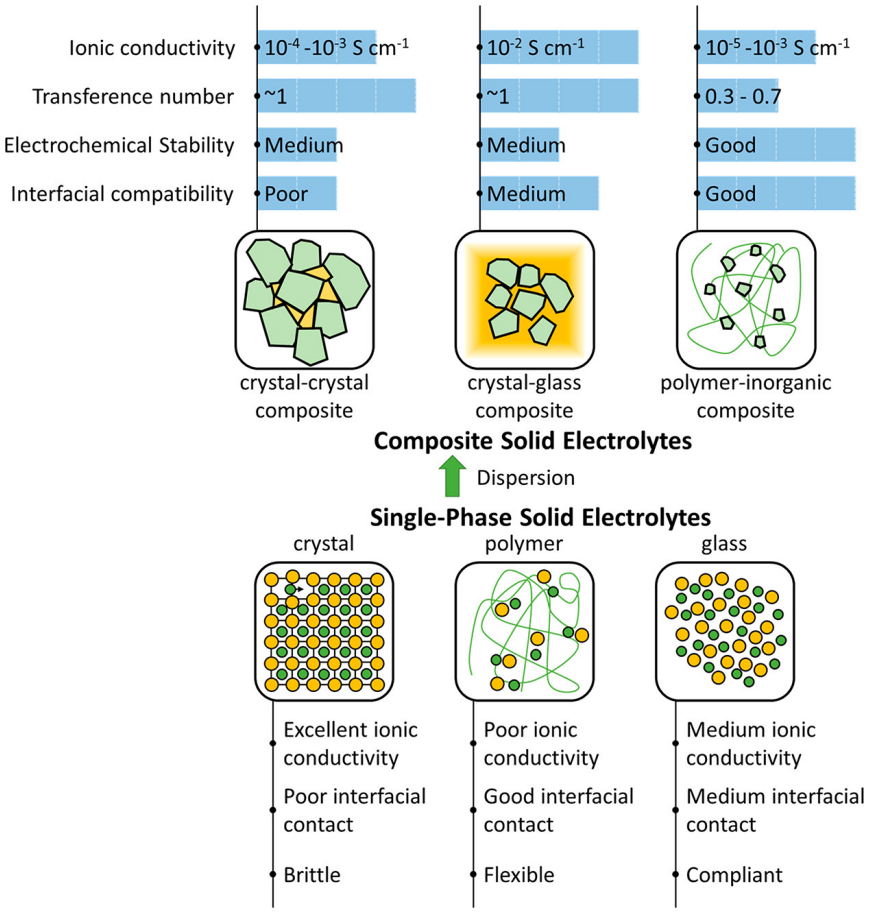

Figure 2.1: Classification of solid composite electrolytes and corresponding physicochemical characteristics. Reprinted with permission from Zou, Z. et al.: Mobile Ions in Composite Solids. *Chemical reviews*, **2020**, 120(9), 4169–4221. DOI: `10.1021/acs.chemrev.9b00760`. Copyright 2020 American Chemical Society

Solid electrolytes (SEs) offer several advantages over their liquid counterparts. They eliminate the risk of leakage and volatilization, and their inherent mechanical stability opens up new possibilities for the use of sodium metal anodes. Currently, SIBs do not employ sodium metal anodes due to challenges such as dendrite formation, high reactivity, and the instability of the passivation layer in most organic liquid electrolytes at room temperature [59]. The propagation of dendrites and the high reactivity of sodium with liquid electrolytes have been major drawbacks, preventing the widespread adoption of sodium metal anodes [60].

As the research community seeks to overcome these limitations, there is a growing shift towards the development of all-solid-state sodium-ion batteries (ASSSIBs) [61]. These next-generation SIBs promise enhanced safety and performance by replacing the liquid electrolyte with a solid-state counterpart, thereby mitigating many of the issues associated with liquid systems. The transition to solid electrolytes represents a significant step forward in the evolution of sodium-ion battery technology, bringing us closer to realizing the full potential of SIBs in a wide range of applications.

Figure 2.1 provides a summary of SEs and their composites, which will be explored in the upcoming sections.

2.2.1 Single-phase solid electrolytes

Single phase solid electrolytes (SEs) can be broadly subdivided into three main categories, each with distinct characteristics and challenges: solid polymer electrolytes (SPEs), inorganic crystalline solid electrolytes (I(C)SE), and inorganic glass and glass-ceramic solid electrolytes.

Solid Polymer Electrolytes Solid polymer electrolytes (SPEs) are a class of materials primarily composed of polymers, with poly(ethylene oxide) (PEO) being the most extensively studied. These polymers are typically combined with sodium salts to enhance ionic conductivity. SPEs offer several advantages, including good ionic conductivity above their glass transition temperature, high flexibility, and excellent interfacial contact with electrodes. However, they suffer from certain limitations, such as low mechanical stability and poor ionic conductivity at room temperature [62]. Although SPEs are generally compatible with sodium metal anodes, they are unable to withstand dendrite growth, which poses a significant challenge for long-term battery performance [63].

Gel Polymer Electrolytes Gel polymer electrolytes (GPEs) are hybrid systems that combine the properties of SPEs with those of liquid electrolytes. They are considered a transitional technology toward fully solid-state electrolytes and are not the primary focus of this work [43].

Inorganic Crystalline Solid Electrolytes These SEs are a class of inorganic materials characterized by long-range structural order, which enables fast ionic conduction. Sodium-ion transport within these materials occurs through two primary mechanisms: bulk migration via a defect-hopping mechanism and transport along grain boundaries. Inorganic crystalline solid electrolytes typically exhibit the highest ionic conductivity and transference numbers among SEs for SIBs, coupled with significant mechanical strength, making them particularly attractive for next-generation batteries [64]. Within ICSEs, there are various subcategories such as Na-β''-alumina, NaSICON, and sulfides:

Sodium Beta Alumina This category includes various sodium polyaluminates, with Na-β''-alumina being the most notable due to its high ionic conductivity and relative stability against highly reactive sodium metal anodes. Discovered as the first class of sodium fast-ion conductors, Na-β''-alumina remains a potent material for SIBs. However, challenges such as high

interfacial resistance—resulting from a potential barrier in the ion transport from the electrode to the electrolyte [65]—at room temperature and elevated costs continue to limit its widespread application [66].

NaSICON Na Super Ion CONductor (NaSICON) refers to a family of materials with the general formula $Na_{1+x}Zr_2Si_xP_{3-x}O_{12}$ ($0 \leq x \leq 3$), where Zr and Si can be partially substituted with other elements. This flexibility allows for fine-tuning of the material's properties through various doping and manufacturing strategies. NaSICON-type electrolytes have demonstrated dendrite-free sodium plating and stripping [67], making them promising candidates for use in SIBs. Nonetheless, overcoming poor physical contact between sodium and NASICON remains a challenge, with uni-axial pressing and heat treatments being explored as potential solutions [63].

Sulfides Sulfide-based solid electrolytes are another important category of SEs for SIBs. Recent advances have enabled room-temperature synthesis of these materials, although high-temperature sintering is often required to achieve optimal properties [68]. One of the primary challenges associated with sulfide SEs is the formation of reactive interfaces with sodium metal anodes, which can lead to the growth of a continuously and linearly expanding interphase, ultimately degrading battery performance [66, 69]. Additionally, their instability in air and reactivity with moisture pose significant concerns for their practical application [63].

Inorganic Glass and Glass-Ceramic Solid Electrolytes These electrolytes are closely related to their crystalline counterparts but offer several advantages, such as reduced grain boundary resistance due to their amorphous nature and the absence of high sintering temperatures during manufacturing. Although glass-ceramic sulfides have been extensively studied for LIBs, research on their sodium analogues is still in its early stages. To date, the ionic conductivity of these materials falls short of that achieved by inorganic crystalline solid electrolytes. Nevertheless, ongoing research in this area suggests that glass and glass-ceramic solid electrolytes hold significant potential for future advancements in ASSSIB technology [70].

2.2.2 Composite electrolytes

Solid polymer electrolytes (SPEs) and inorganic solid electrolytes (ISEs) each offer unique advantages, but neither fully meets the stringent requirements for practical sodium-ion batteries (SIBs). These requirements include thermal and mechanical stability, high transference number and ionic conductivity, low interfacial resistance, and electrochemical stability, which are limited by the inherent properties of SPEs and ISEs. To address these challenges, composite solid electrolytes (CSEs) have emerged as a promising solution. By combining two different solid

electrolytes, CSEs can complement and enhance the often conflicting properties of their individual components.

It is important to note that CSEs refer specifically to mixtures where the chemical bonds of the constituent materials remain intact, distinguishing them from doped or homogenized materials. Given the vast number of available solid electrolytes, the potential combinations for creating CSEs are nearly limitless. Nevertheless, Zou et al. simplify the classification of CSEs into three primary categories: crystal-crystal composites, crystal-glass composites, and polymer-inorganic composites [57]. Each of these combinations typically involves a host phase integrated with highly conductive inclusions, also known as the *dispersion phase*. These inclusion particles are usually rigid and exhibit high conductivity, while the surrounding material, or *continuous phase*, may or may not contribute significantly to the overall ionic conductivity. The continuous phase often provides mechanical flexibility and enhances interfacial contact between the electrolyte and the electrodes [71].

Interestingly, some studies suggest that the ionic transport mechanisms in certain CSEs differ fundamentally from those of the individual solid electrolytes they are composed of [57, 72]. However, the detailed conduction mechanics at the nanoscale remain poorly understood and are the subject of ongoing research [71, 73–75].

In addition to macroscale composition, nanostructural modifications of the dispersion phase, such as the introduction of nanowires or nanochannels, have been shown to positively impact the overall performance of the electrolyte [76–79]. Sophisticated nanofabrication methods, such as 3D printing and chemical etching, are essential, thereby prompting concerns regarding their economical viability for battery production. Nevertheless, as nanoscale processes are not the primary focus of this work, they will not be discussed in detail.

Among the various types of CSEs, *Composite Polymer Electrolytes* (CPEs), which combine polymers with inorganic fillers, appear to be the most promising. For instance, mixing polymer electrolytes with inorganic oxides like Al_2O_3 or SiO_2 has been shown to enhance ionic conductivity [80]. These additives, termed *inert fillers*, typically do not have intrinsic conductivity themselves. Instead, the increase in ionic conductivity is often proportional to the filler surface area, indicating that ion transport is related to the polymer-filler interface.

One proposed mechanism for this enhancement is the modification of defect thermodynamics near the polymer-crystal interface. The interface becomes a favorable pathway for ion conduction compared to single-phase solid electrolytes. The introduction of secondary phases disrupts the thermodynamic equilibrium of defects in the crystals, leading to alterations in the conduction pathway. The discontinuities at the interface cause deviations from local electroneutrality and the formation of a narrow, charged zone with modified concentrations of charge-carrying defects [72].

In some materials, the interface between the polymer and filler can form a new phase known as the *interphase*, which acts as a fast-ion conducting channel within the sub-micrometer range. The nature and role of this superionic interphase are still being actively researched, with few reports available in the literature due to the challenges of characterizing nanoscale structures. Rather than differentiating between fillers that enhance transport at the interface and those that form interphases, Xu et al. argue that the observed differences in conduction mechanisms are related to the radial extent of the fast-ion conducting zone around the filler particles [73, 74].

Another perspective suggests that fillers induce structural changes in the polymer host, creating a more favorable environment for ion conduction. For example, PEO-based solid electrolytes typically form highly conductive amorphous phases above 60 °C. The addition of inorganic fillers can stabilize these amorphous phases at room temperature, significantly improving ionic conductivity [75, 81].

When the inorganic particles actively contribute to ion transport, they are referred to as *active fillers*. However, there is still some uncertainty regarding whether combined ion transport through the polymer and active filler actually occurs, given the interfacial resistances and distinct transport mechanisms involved. In crystalline phases, ion transport is typically mediated by ion hopping, while in polymers, ion transport often occurs via a vehicular mechanism, where ions travel within a solvation shell, similar to ion diffusion in liquid electrolytes. A more in-depth discussion of this topic can be found in Zou et al. [57].

Despite these complexities, experimental evidence suggests that the use of active fillers does indeed enhance the overall ionic conductivity of CSEs. This implies that a combination of transport modes might be at play. Although the specific pathway for ion transport remains a contentious subject among scientists [59], it is evident that rapid diffusion rates across the interface are essential for enhancing the functionality of composite solid electrolytes in the future.

2.3 Modeling approaches for batteries

Simulating electrochemical systems, including batteries, requires the development of mathematical models, which may be either physics-based or empirical. These models are essential for understanding and predicting the behavior of batteries under various conditions.

Battery models are typically categorized into two main types: physics-based models, also known as white-box models, and empirical models, often referred to as black-box models, such as artificial neural network models and equivalent circuit models [82]. Additionally, there are grey-box models that incorporate elements from both categories.

Empirical models are generally favored for their quicker computation times, ease of formulation, and simpler parameterization. However, physics-based models offer a deeper understanding of

the fundamental mechanics governing electrochemical systems, enabling predictions beyond the experimentally validated data. These models are particularly valuable for extrapolating system behavior under untested conditions and exploring new design configurations.

Physics-based models can be further classified based on the length and time scales they address, following the framework established by Shi et al. [83] (fig. 2.2).

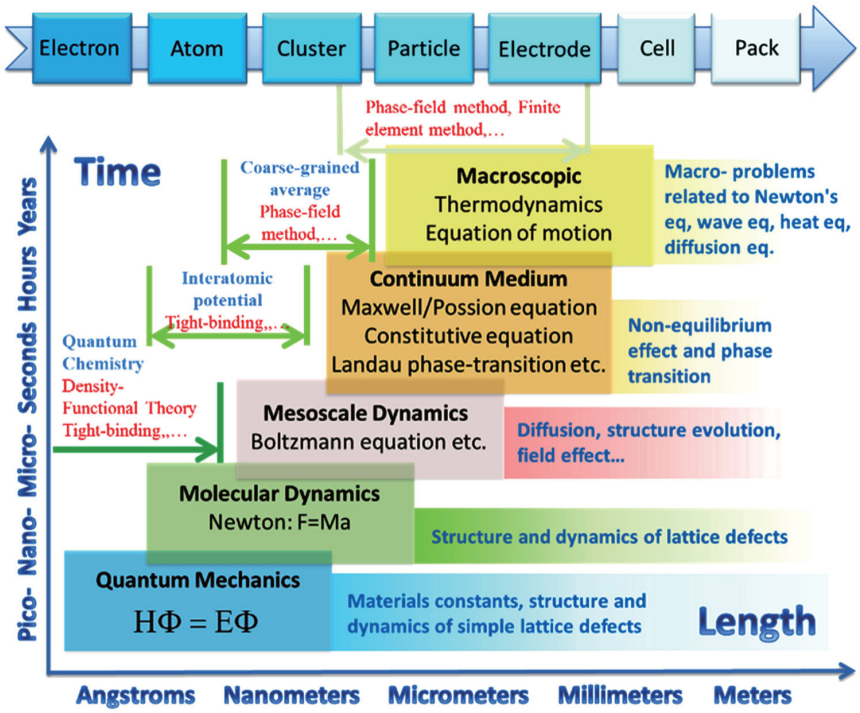

Figure 2.2: Overview on simulation methods for batteries along with their length and time scales and application. Reprinted with permission from Shi, S. et al.: Multi-scale computation methods: Their applications in lithium-ion battery research and development. *Chinese Physics B*, **2016**, 25(1), 018212. DOI: 10.1088/1674-1056/25/1/018212

The computational scales in battery modeling range from the atomic scale, where individual atoms and molecules are considered, to the scale of entire battery stacks. Due to the distinct physical processes occurring at these various scales, different computational approaches are required. Insights obtained at smaller scales can be systematically mapped to simulations at larger scales, enabling a comprehensive multiscale modeling approach.

In the literature, the term "microscale" is sometimes used ambiguously. In this work, *microscale* refers specifically to models operating at the micrometer scale, such as those describing diffusion processes. In contrast, models that describe molecular processes are referred to as *nanoscale* models.

Several nanoscale computational methods are employed to calculate the properties of electrode and electrolyte materials:

Quantum Mechanics and First-Principles Calculations have emerged as a powerful tool for the development of new electrode materials and provide accurate first-principles data, focusing on the fundamental electrochemical properties of materials [84, 85]. They allow for the prediction and interpretation of material characteristics and behaviors, the understanding of charge/discharge mechanisms at the atomic scale, and the formulation of rational design strategies for electrode materials [86].

Molecular Dynamics (MD) simulations are used to predict the movement of atoms in different systems over time, based on models of the physical interactions between atoms [87, 88]. This method is particularly useful for studying dynamic processes such as diffusion.

Density Functional Theory (DFT) has significantly contributed to the understanding of electrochemical reaction mechanisms and the virtual screening of promising energy storage materials [89]. DFT allows for the calculation of electronic properties and provides insights into the thermodynamic and kinetic aspects of material behavior.

Kinetic Monte Carlo (kMC) simulations have proven to be effective in describing physicochemical processes at the atomistic scale over extended time periods [90]. This method is often used to simulate processes such as diffusion and nucleation, where stochastic events play a critical role.

Phase-Field Modeling (PFM) is a computational approach that bridges the gap between the nano- and microscale, describing the microstructural evolution of materials based on thermodynamic principles [91]. PFM is particularly useful for modeling phenomena such as grain growth, phase transitions, and microstructure development in electrode materials.

While nanoscale models are highly powerful in capturing the intricate details of atomic and molecular processes, their computational and modeling demands limit their applicability to small scales. To explore battery dynamics at the cell level, alternative modeling approaches are required.

Continuum modeling of electrochemical systems, which forms the basis of cell-level simulations, traces its origins to the pioneering work on porous electrodes by Newman and Tobias [92]. In this context, the term *continuum* signifies that local material properties are considered uniform within defined control volumes, enabling the simplification of complex systems into more manageable mathematical representations. The foundational principles of continuum modeling are extensively covered in standard battery textbooks [23, 93]. The specific models and their extensions used in this work will be presented in detail where relevant.

Several derivatives of continuum models have been developed, each offering a trade-off between accuracy and computational efficiency. These models can be broadly categorized as follows:

Microstructure models These models resolve the battery down to the particle scale, accurately representing the microstructure of the electrode [94]. This approach is particularly valuable for studying the effects of electrode geometry on overall cell performance. Early applications

of microstructure models in lithium-ion batteries (LIBs) were demonstrated by Goldin et al. [95] and Less et al. [96]. A critical aspect of these models is the careful incorporation of electrode geometry into the virtual cell, which can be achieved through the reconstruction of image data—a process that is often challenging due to the complexity and resolution required. Alternatively, computer-generated electrode structures can be employed.

Homogenized models These models abstract the detailed microstructure by treating the electrode as a continuum, wherein the three-dimensional structure of pores, particles, and other features is averaged. This simplification necessitates modifications to the governing equations to account for the effects of the underlying microstructure while reducing computational demands [97].

Doyle-Fuller-Newman (DFN) model Also known as the pseudo-two-dimensional (P2D) model, the DFN model reduces the complexity of the three-dimensional homogenized model by assuming spherical particles in the electrode and a planar geometry in the electrolyte [98]. This model is termed "pseudo-two-dimensional" because it considers both radial diffusion within the spherical particles (a second dimension) and the one-dimensional variation in the electrolyte along the cell's thickness. As a result, the DFN model captures the essential two-dimensional dynamics of the system, offering a balance between accuracy and computational efficiency, making it widely used in battery simulations [99].

Single Particle Model (SPM) The single particle model simplifies the system further by focusing on a single representative particle within the electrode, decoupling the spatial variable within the particle from the macroscopic spatial variable [100]. This decoupling leads to a model that only considers one dimension, significantly reducing computational effort. The SPM is particularly useful in scenarios where minimal computational resources are available, such as in microcontroller applications [101].

Each of these modeling approaches has its own strengths and limitations, and the choice of model depends on the specific research question and computational resources available. In this work, appropriate models are selected and extended as necessary to address the research objectives.

3 Sodium Iodine Batteries

The sodium iodine battery, a member of the fully molten metal halide battery family, represents a significant advancement in molten sodium battery technology, as briefly described in section 2.1.1. This battery technology is the latest evolution in molten sodium systems, distinguished by its ability to operate at the sodium melting temperature, a noteworthy reduction from the higher operating temperatures traditionally associated with such batteries.

The key innovation in sodium iodine batteries lies in the utilization of a concentrated aqueous iodine/iodide solution, which enables the system to maintain promising energy densities at these lower temperatures. This reduction in operating temperature offers several critical advantages. First, it minimizes thermal losses, thereby improving overall energy efficiency and allowing for the design of smaller, more compact battery units. Second, the lower temperature expands the range of suitable materials that can be employed for components such as compartments, seals, and separators, which are often limited by the high temperatures in conventional molten sodium batteries.

This work builds upon the foundational research conducted on aqueous sodium iodine batteries, such as the studies by Zhu and Kee [38] and Holzapfel et al. [39]. By conducting first-of-its-kind microstructure simulation studies (see section 2.3), this research deepens the understanding of the electrochemical processes and sheds light on cell design influences within sodium iodine batteries and explore their potential for practical application. These simulations provide insights that bridge the theoretical framework established in the previous chapters with the practical results and findings presented in this chapter.

3.1 Working principle of sodium iodine batteries

Figure 3.1 illustrates the working principle of the sodium iodine battery. The chemical reaction directions are shown for the discharging process. The all-liquid battery system features a pure sodium anode and an aqueous catholyte solution. The catholyte not only facilitates species and charge movement—similar to intercalation batteries—but it also serves as active material since it contains the species involved in the redox reaction. During discharging, elemental sodium

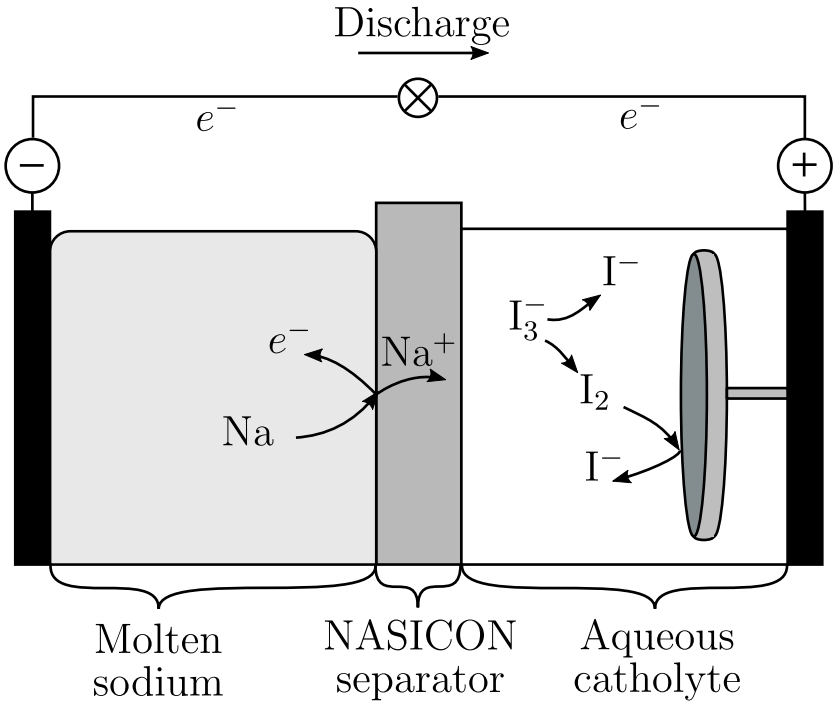

Figure 3.1: Working principle of a NaI battery with a two-dimensional electrode

oxidizes to sodium ions while iodine is reduced to iodide. The net reaction is of the sodium iodine battery with a standard potential of 3.2495 V is [102, 103]:

$$2\,Na^+ + 2\,I^- \rightleftharpoons I_2 + 2\,Na \tag{3.1}$$

At discharge, sodium ions form in the molten sodium anode at the anode-separator interface. The half-cell reaction for the negative electrode states

$$Na^+ + e^- \rightleftharpoons Na \tag{3.2}$$

at standard potential -2.714 V against hydrogen electrode. Afterwards, Na^+ travel through the separator, and enter the cathode domain. A dense separator is essential to prevent the contact between the anolyte and catholyte, thereby avoiding harmful reactions between molten sodium and water. Given the moderate operating temperatures and the neutral pH of the solution, NaSICON-type materials are suitable for this purpose. NaSICON (Na Super Ionic CONductor) is a ceramic material that acts as both a separator and a pure sodium-ion conductor, effectively dividing the cathode and anode half-cells.

NaSICON-type ceramics are particularly advantageous due to their high sodium-ion conductivity at relatively low temperatures, coupled with negligible interfacial resistance when in contact with liquid sodium [104, 105]. They also exhibit excellent stability against both molten sodium [36] and concentrated aqueous halide solutions [39], making them a compelling alternative

to the more commonly used Na-β″-alumina electrolytes. Although separating highly reactive molten sodium and an aqueous solution using a brittle separator like NaSICON may appear risky, experimental studies have reported a self-limiting effect in the event of fissures [39]. When NaSICON is supported mechanically, any breaches in the separator lead to the formation of solid products that can effectively seal the fissures, thereby mitigating the risk of catastrophic failure. This self-limiting behavior enhances the safety of the system, even under conditions where the separator's integrity is compromised.

The cathode domain comprises I_2, I^-, I_3^-, and Na^+ dissolved in water. Iodide forms at the electrolyte-cathode electrode interface from iodine and electrons delivered by the external current ($E^\ominus = 0.5355\,\mathrm{V}$) [102, 106].

$$2\,I^- \rightleftharpoons I_2 + 2\,e^- \tag{3.3}$$

Iodine itself has a low solubility in water but can homogeneously recombine to triiodide with iodide. I^-/I_3^- is an interesting redox couple due to its high solubility in aqueous solutions, low molecular weight, and high faradaic efficiency. In this context, I_3^- acts as a reservoir for I_2, which is important because iodine itself is barely soluble in water but can recombine with iodide to polyiodides thereby preventing precipitation of potentially harmful solid iodine. During the discharge, iodine is reproduced from the equilibrium reaction between iodine, iodide, and triiodide [107]. Simultaneously, the discharge process consumes elemental sodium at the anode-separator interface causing the amount of sodium in the anode compartment to decrease. However, it is worth noting that the volume of the anode is significantly lower than that of the cathode due to the high volumetric energy density of sodium metal.

3.2 Physical model

This section details the thermodynamics of a liquid sodium-iodine secondary battery, forming the foundation for the electrochemical model used in this study. The model builds upon the one-dimensional framework previously established by Zhu and Kee [38], while the fundamental thermodynamic principles are drawn from reputable sources [106, 108, 109].

Here, we introduce the essential equations and boundary conditions critical for understanding the implementation of the model. Additionally, this section presents novel extensions to the model, advancing it from a one-dimensional to a three-dimensional spatially resolved simulation, allowing for a more detailed and accurate analysis.

At its core, the model is based on the principles of charge and species conservation across all computational domains. The negative half-cell consists entirely of molten sodium, a component whose high conductivity ensures that it has minimal impact on the overall cell voltage and battery performance. This negligible influence is accounted for through specific boundary conditions

applied to the model. Consequently, the current model focuses primarily on the cathode half-cell, with the anode half-cell being excluded from the detailed analysis due to its relatively insignificant effect on the performance metrics under investigation.

3.2.1 Species transport

The species transport equation is derived from the principle of mass conservation, which accounts for both fluxes and molar production rates (r_k) within the system. This relationship is mathematically expressed as:

$$\frac{\partial X_k}{\partial t} = -\nabla \cdot \boldsymbol{J}_k + r_k \tag{3.4}$$

In this equation, the electrolyte concentration of species k (X_k), the surface flux density ($\boldsymbol{J}$) and the molar production rate (r_k) are introduced as key variables.

The fluxes are composed of both a diffusion component and a migration component, as described by the Nernst-Planck equation. Specifically, the diffusion component accounts for the movement of species due to concentration gradients, while the migration component considers the movement due to electric field effects. These components are modeled under the assumptions of dilute solution theory, resulting in the following formulation:

$$\boldsymbol{J}_k = -D_k^{\mathrm{el}} \nabla X_k - \frac{z_k F}{RT} D_k^{\mathrm{el}} X_k \nabla \Phi_{\mathrm{el}} \tag{3.5}$$

The equation incorporates catholyte diffusion coefficient of species k (D_k^{el}), catholyte charge (z_k), Faraday constant (F), universal gas constant (R), temperature (T) and electrolyte potential (Φ_{el}). The first term represents the diffusion due to concentration gradients, while the second term accounts for the migration of charged species in response to the electric field within the electrolyte.

Although the catholyte solution under study is highly concentrated, its complex multi-component nature makes it very challenging to precisely formulate its transport mechanisms and phenomena mathematically. While there is a well-established theory for concentrated binary electrolytes, theoretical approaches for multicomponent solutions are usually specific to the system and require significant experimental validation, which tends to be semi-empirical. In existing research, the Na^+, I^-, I_3^-, I_2 solution has been examined at low to moderate concentrations under ambient conditions. Nevertheless, the battery's operating conditions necessitate high temperatures and very high concentrations, leading to complications due to the solution's high vapor pressure, corrosiveness, and opacity. Given that this study is pioneering in researching this particular battery system, it is reasonable to approximate species transport using dilute solution theory [38, 110].

As previously mentioned, the cathode chemistry in the model hinges on a heterogeneous charge-transfer reaction coupled with a bulk recombination or decomposition reaction. According to the findings of Wroblowa and Saunders, the decomposition of triiodide proceeds through a three-step mechanism, with the adsorption step, as shown in eq. (3.6c), being the rate-determining step in the process [107]:

$$\mathrm{I_3^-} \rightleftharpoons \mathrm{I_2} + \mathrm{I^-} \tag{3.6a}$$

$$\mathrm{I_2} \rightleftharpoons 2\,\mathrm{I_{ads}} \tag{3.6b}$$

$$2\,\mathrm{e^-} + 2\,\mathrm{I_{ads}} \rightleftharpoons 2\,\mathrm{I^-} \tag{3.6c}$$

The reaction kinetics governing the heterogeneous charge-transfer reaction, particularly the iodide oxidation detailed in eq. (3.3), are described by the exchange current density (i_0). Zhu and Kee derive it from the elementary Marcus form of the adsorption step:

$$i_0 = {i_0}^\circ \frac{\left(\frac{[\mathrm{I_2}]}{[\mathrm{I_2}]^*}\right)^{\frac{\beta_a}{2}} \left(\frac{[\mathrm{I^-}]}{[\mathrm{I^-}]^*}\right)^{1-\beta_a}}{1 + \left(\frac{[\mathrm{I_2}]}{[\mathrm{I_2^*}]}\right)^{\frac{1}{2}}} \tag{3.7}$$

Here, the exchange current density factor i_0° is a fitting parameter calibrated against experimental data from Dané et al. [111]. The reference concentrations $[\mathrm{I_2}]^*$ and $[\mathrm{I^-}]^*$ are standardized at 1 M. In the absence of a comprehensive understanding of the reaction's symmetry, the symmetry factor β_a is conventionally assigned a value of 0.5 [112].

Due to the formation of triiodide within the catholyte as an intermediate stage in the reaction, the iodide oxidation and iodine reduction processes may occur in a two-step sequence with both reactions being of first order [113]. This phenomenon results in the appearance of two closely spaced voltammetric waves [114, 115]. However, the overall iodide oxidation process can still be broadly represented by eq. (3.3).

Since the charge transfer reaction—specifically the adsorption step—is the rate-determining step, it is imperative that the bulk reactions remain at equilibrium. In this context, the equilibrium of triiodide formation in the bulk phase is characterized by the equilibrium constant of the triiodide recombination reaction ($K_{\mathrm{I_3^-}}$), which is further modeled as a temperature-dependent parameter:

$$K_{\mathrm{I_3^-}} = \frac{[\mathrm{I_3^-}]}{[\mathrm{I^-}]\,[\mathrm{I_2}]} \tag{3.8}$$

At a temperature of 120 °C, this equilibrium constant has a value of:

$$K_{\mathrm{I_3^-},120\,^\circ\mathrm{C}} = 0.121\ \mathrm{mol\,m^{-3}} \tag{3.9}$$

as reported by Palmer et al. [116]. The model accounts for variations in species concentrations within the bulk phase due to this homogeneous reaction by employing source terms as expressed in eq. (3.4).

The formation of triiodide, being a product of the interaction between iodine and iodide, dictates that the source term $r_{I_3^-}$ is equal to the negative of r_{I_2} and r_{I^-}:

$$r_{I_2} = -k_f [I_2] [I^-] + \frac{k_f}{K_{I_3^-}} [I_3^-] = r \tag{3.10a}$$

$$r_{I^-} = -k_f [I_2] [I^-] + \frac{k_f}{K_{I_3^-}} [I_3^-] = r \tag{3.10b}$$

$$r_{I_3^-} = k_f [I_2] [I^-] - \frac{k_f}{K_{I_3^-}} [I_3^-] = -r \tag{3.10c}$$

In this model, equilibrium is maintained by assigning a sufficiently high value to the reaction rate constant (k_f), while ensuring numerical stability throughout the simulations. The electrolyte diffusion coefficients used in the model are the bulk diffusion coefficients of the respective species [117–119], which have been adjusted to the operating temperature by Zhu and Kee [38].

3.2.2 Charge transport

Cathode charge The model does not account for nanoscale phenomena, such as the formation of double layers near the cathode-electrolyte interface. Consequently, local charge neutrality is assumed, and the charge density (ρ_{ed}) is set to zero.

$$\frac{\partial \rho_{ed}}{\partial t} = 0 \tag{3.11}$$

This assumption leads to a current density field that is divergence-free, resulting in the following conservation equation for the charge within the cathode:

$$\nabla \cdot \boldsymbol{i}_{ed} = 0 \tag{3.12}$$

The electrode current density ($\boldsymbol{i}_{ed}$) is described by Ohm's law, which relates it to the electrode potential (Φ_{ed}) and the electrode conductivity (σ_{ed}):

$$\boldsymbol{i}_{ed} = -\sigma_{ed} \nabla \Phi_{ed} \tag{3.13}$$

To solve eq. (3.12), it is necessary to define several boundary conditions. One key boundary condition involves setting the electric potential at the cathode current collector to a fixed value $\Phi_{ed,cc}$ = fixed, ensuring continuity of the current throughout the cathode domain. Moreover,

the integral current density at the cathode current collector (denoted as cc) must be equal to the integral current density at the electrolyte-cathode interface (denoted as etc), as expressed in the following equation:

$$\int \boldsymbol{n} \cdot \boldsymbol{i}_{\mathrm{ed,cc}} \mathrm{d}A_{\mathrm{cc}} = -\int \boldsymbol{n} \cdot \boldsymbol{i}_{\mathrm{ed,etc}} \mathrm{d}A_{\mathrm{etc}} \tag{3.14}$$

To model the charge transfer process between the cathode and electrolyte domains, a Butler-Volmer equation is employed. This equation is a standard phenomenological approach used in electrochemical systems to describe electrode kinetics, particularly the net charge transfer rate, under the assumption of a dilute solution approximation [120, 121]. The Butler–Volmer current density depends on i_0 along with the local overpotential $(\Phi_{\mathrm{ed}} - \Phi_{\mathrm{el}} - U_{\mathrm{eq,I^-/I_2}})$:

$$i_{\mathrm{BV}} = i_0 \left[\exp\left(\frac{\alpha_a F}{RT} \left(\Phi_{\mathrm{ed}} - \Phi_{\mathrm{el}} - U_{\mathrm{eq,I^-/I_2}}(c_{\mathrm{s}}) \right) \right) - \exp\left(-\frac{\alpha_c F}{RT} \left(\Phi_{\mathrm{ed}} - \Phi_{\mathrm{el}} - U_{\mathrm{eq,I^-/I_2}}(c_{\mathrm{s}}) \right) \right) \right] \tag{3.15}$$

The exchange current density (i_0), which arises from the heterogeneous reaction kinetics at the electrolyte-cathode interface, is described by eq. (3.7). To maintain charge conservation between the cathode and the electrolyte, the electric potential at the cathode-electrolyte interface, $\Phi_{\mathrm{ed,cte}}$, must be appropriately chosen.

$$i_{\mathrm{BV}} = \boldsymbol{n} \cdot \boldsymbol{i}_{\mathrm{ed}} = -\boldsymbol{n} \cdot \boldsymbol{i}_{\mathrm{el}} \tag{3.16}$$

Assuming the activity coefficients are equal to 1, the Nernst equation provides the reversible electrode potential for the iodide-iodine reaction ($U_{\mathrm{eq,I^-/I_2}}$), which is dependent on the concentrations of the involved electrolyte species, expressed in molar units. The standard redox potential of iodine/iodide couple, $E^{\ominus}_{\mathrm{I^-/I_2}}$, is 0.5355 V relative to the standard hydrogen electrode (SHE). This value serves as the reference point for calculating the actual electrode potential under non-standard conditions, where the concentrations of the species differ from their standard states as defined by IUPAC.

$$U_{\mathrm{eq,I^-/I_2}} = E^{\ominus}_{\mathrm{I^-/I_2}} + \frac{RT}{2F} \ln\left(\frac{[\mathrm{I_2}]}{[\mathrm{I^-}]^2} \right) \tag{3.17}$$

The logarithmic term accounts for the deviation from standard conditions, reflecting the influence of the actual concentrations of the reactants and products on the electrode potential.

Electrolyte charge In line with the characteristics described in eq. (3.12), the electric current density field within the catholyte must satisfy the condition of local charge neutrality, resulting in a divergence-free current density:

$$\nabla \cdot \boldsymbol{i}_{\mathrm{el}} = 0 \tag{3.18}$$

This divergence-free condition ensures that there is no net accumulation of charge within the catholyte, which is essential for maintaining electrochemical equilibrium. The electrolyte current density ($\boldsymbol{i}_{\mathrm{el}}$), which can also be interpreted as charge flux in the electrolyte, is determined by the

concentrations and gradients of the charge-carrying species, which include both migration and diffusion components as outlined in eq. (3.4).

$$\boldsymbol{i}_{\mathrm{el}} = -\kappa \nabla \Phi_{\mathrm{el}} - \sum_k z_k F D_k^{\mathrm{el}} \nabla X_k \tag{3.19}$$

Here, the electrolyte ionic conductivity (κ) is a critical parameter in determining how efficiently ions are transported through the electrolyte. It takes the form:

$$\kappa = \sum_k \frac{{z_k}^2 F^2}{RT} D_k^{el} X_k \tag{3.20}$$

For the anode, the half-cell potential is evaluated by considering the sodium standard potential along with the sodium ion concentrations at the electrolyte-separator interface. The Nernst equation for the anode potential is:

$$U_{\mathrm{eq,Na/Na^+}} = E^{\ominus}_{\mathrm{Na/Na^+}} + \frac{RT}{F} \ln\left([\mathrm{Na^+}]\right) \tag{3.21}$$

In this equation, the standard reduction potential for sodium $E^{\ominus}_{\mathrm{Na/Na^+}}$ is $-2.714\,\mathrm{V}$.

NaSICON is employed as the separator material due to its exceptional ionic conductivity, specifically for sodium ions. Within this framework, Ohm's law is applied under the assumption that sodium ion concentration gradients do not influence the electric potential within the NaSICON. Therefore, the current density in the NaSICON is directly proportional to the electric potential difference across the separator, which is calculated using boundary conditions rather than by discretizing the charge transport equations in a separate computational domain. The current continuity at the interfaces between the separator and the electrolyte is enforced by:

$$\boldsymbol{n} \cdot \boldsymbol{i}_{\mathrm{el}} = -\boldsymbol{n} \cdot \boldsymbol{i}_{\mathrm{sep}} \tag{3.22}$$

Finally, the potential difference across the NaSICON separator can be expressed as:

$$\Delta\Phi_{\mathrm{sep}} = -\frac{\boldsymbol{n} \cdot \boldsymbol{i}_{\mathrm{sep}}}{\sigma_{\mathrm{sep}}\, l_{\mathrm{sep}}} \tag{3.23}$$

In this context, Φ_{sep} is the ionic conductivity of the separator, l_{sep} is its thickness, and $\boldsymbol{n}$ denotes the surface unit normal vector pointing outside the related domain.

3.2.3 Boundary conditions

Mass conservation To solve eq. (3.4), it is essential to introduce boundary conditions for all electrolyte species at both the electrolyte–separator interface and the electrolyte–cathode interface.

These boundary conditions are critical for accurately modeling the behavior of species as they move through the electrolyte and interact with the separator and cathode. By specifying the appropriate boundary conditions at these interfaces, the model can capture the complex transport phenomena and electrochemical reactions occurring within the system, ensuring a comprehensive and accurate solution to the governing equations.

At the electrolyte-cathode boundary, Na^+ remains inactive in the reactions. As a result, the flux of sodium ions $\boldsymbol{n} \cdot \boldsymbol{J}_{Na^+}$ becomes zero. The exchange current fully converts into iodide and iodine via the heterogeneous reaction pathway described in eq. (3.3). Simultaneously, the homogeneous reaction in eq. (3.6b) occurs to meet the required equilibrium constant. In this context, it is practical to depict the molar generation at the electrolyte-cathode boundary, induced by the homogeneous reaction, as boundary fluxes. Generally speaking, the fluxes of a species k from both the heterogeneous and homogeneous reactions contribute to the overall flux at a given boundary:

$$\boldsymbol{n} \cdot \boldsymbol{J}_{k,\mathrm{tot}} = \boldsymbol{n} \cdot \boldsymbol{J}_{k,\mathrm{het}} + \boldsymbol{n} \cdot \boldsymbol{J}_{k,\mathrm{hom}} \tag{3.24}$$

According to convention, the surface unit normal vector $\boldsymbol{n}$ points outside the computational domain. At the electrode surface, I_2 that is produced or consumed by the charge-transfer reaction is almost balanced by the triiodide recombination reaction in the bulk. In combination with the low absolute value of I_2 concentration and the high value of $K_{I_3^-}$ the corresponding homogeneous and heterogeneous reaction surface fluxes at the cathode electrode can be approximated equal.

$$\boldsymbol{n} \cdot \boldsymbol{J}_{I_2,\mathrm{het}} \approx \boldsymbol{n} \cdot \boldsymbol{J}_{I_2,\mathrm{hom}} = \boldsymbol{n} \cdot \boldsymbol{J}_{I_3^-,\mathrm{hom}} = -\boldsymbol{n} \cdot \boldsymbol{J}_{I^-,\mathrm{hom}} \tag{3.25}$$

From this approximation, the heterogeneous reaction surface fluxes $\boldsymbol{J}_{k,\mathrm{het}}$, the homogeneous reaction surface fluxes $\boldsymbol{J}_{k,\mathrm{hom}}$, and the resulting reaction surface fluxes $\boldsymbol{J}_{k,\mathrm{tot}}$ are derived and shown in Table 3.1. In total, iodine flux at the electrolyte-cathode interface is zero and all species surface fluxes are dependent on the electrolyte current density.

Table 3.1: Boundary flux densities at the electrolyte-cathode interface for heterogeneous and homogeneous electrolyte reactions.

X_k	$\boldsymbol{n} \cdot \boldsymbol{J}_{k,\mathrm{het}}$	$\boldsymbol{n} \cdot \boldsymbol{J}_{k,\mathrm{hom}}$	$\boldsymbol{n} \cdot \boldsymbol{J}_{k,\mathrm{tot}}$
I^-	$-\boldsymbol{n} \cdot \frac{\boldsymbol{i}_{\mathrm{el}}}{zF}$	$-\boldsymbol{n} \cdot \frac{1}{2}\frac{\boldsymbol{i}_{\mathrm{el}}}{zF}$	$-\boldsymbol{n} \cdot \frac{3}{2}\frac{\boldsymbol{i}_{\mathrm{el}}}{zF}$
I_2	$\boldsymbol{n} \cdot \frac{1}{2}\frac{\boldsymbol{i}_{\mathrm{el}}}{zF}$	$-\boldsymbol{n} \cdot \frac{1}{2}\frac{\boldsymbol{i}_{\mathrm{el}}}{zF}$	0
I_3^-	0	$\boldsymbol{n} \cdot \frac{1}{2}\frac{\boldsymbol{i}_{\mathrm{el}}}{zF}$	$\boldsymbol{n} \cdot \frac{1}{2}\frac{\boldsymbol{i}_{\mathrm{el}}}{zF}$

At the electrolyte-separator interface, all species flux densities vanish except for those of sodium ions:

$$\boldsymbol{n} \cdot \nabla \left[\mathrm{Na}^+\right] = -\frac{\boldsymbol{n} \cdot \boldsymbol{i}_{\mathrm{el}}}{D^{\mathrm{el}}_{\mathrm{Na}^+} F} - \frac{F}{RT} \left[\mathrm{Na}^+\right] \boldsymbol{n} \cdot \nabla \Phi_{\mathrm{el}} \tag{3.26}$$

Charge conservation To accurately model the electrochemical behavior of the system, it is essential to define appropriate boundary conditions for the electric potentials at critical interfaces, specifically at the coupled interface between the cathode and the electrolyte domains. These boundary conditions complement the fixed potentials at the current collector and the separator, ensuring a consistent and physically meaningful solution across the entire computational domain.

The Neumann-type boundary conditions are derived from the requirement of current continuity as stated in eq. (3.16). They describe the behavior of the electric potential gradients at the interfaces and are crucial for coupling the different domains—namely, the cathode and the electrolyte. In this framework, the computational interface from the electrolyte's perspective is termed the electrolyte-cathode interface, while the corresponding interface from the cathode's perspective is referred to as the cathode-electrolyte interface.

The boundary condition for the electric potential at the cathode-electrolyte interface (denoted as "cte") is given in eq. (3.27a). This equation ensures that the current flowing out of the cathode into the electrolyte is consistent with the electrochemical reaction rates described by the Butler-Volmer equation.

$$\boldsymbol{n} \cdot \nabla \Phi_{\mathrm{ed}} \Big|_{\mathrm{cte}} = -\frac{i_{\mathrm{BV}}}{\sigma_{\mathrm{ed}}} \tag{3.27a}$$

$$\boldsymbol{n} \cdot \nabla \Phi_{\mathrm{el}} \Big|_{\mathrm{etc}} = \frac{i_{\mathrm{BV}}}{\kappa} - \frac{\sum_k z_k F D^{\mathrm{el}}_k \nabla X_k}{\kappa} \tag{3.27b}$$

Similarly, the boundary condition for the electric potential at the electrolyte-cathode interface (denoted as "etc") is expressed in eq. (3.27b). These boundary conditions ensure that the electric potential fields in both the cathode and electrolyte domains are consistent with the current densities, thereby maintaining the overall charge balance and supporting the correct operation of the electrochemical cell.

3.2.4 Simulation parameters and metrics

To ensure accurate modeling and analysis of the sodium-iodine (Na-I_2) reference cell, it is crucial to establish a set of simulation parameters that reflect the physical properties and geometric dimensions of the system. These parameters serve as the foundation for the computational model, influencing the behavior and performance of the cell during simulations. Table 3.2 provides a

summary of the key parameters used in the simulations, including material properties, geometric dimensions, and kinetic factors.

Table 3.2: Geometric parameters and physical characteristics of the Na-I_2 reference cell

Parameter	**Value [units]**
symmetry factors (α_a, α_c)	0.5
Cathode conductivity (σ_{ed})	$2.5 \times 10^6\,\mathrm{S\,m^{-1}}$
cathode compartment length (l_c)	1 cm
Separator thickness (l_{sep})	0.5 mm
Exchange current factor (i_0°) [38]	$1\,\mathrm{A\,cm^{-2}}$
NaSICON conductivity (σ_{Nas}) [122, 123]	$10\,\mathrm{mS\,cm^{-1}}$
Diffusion coefficient ($D^{el}_{Na^+}$) [38]	$6.3867 \times 10^{-9}\,\mathrm{m^2\,s^{-1}}$
Diffusion coefficient ($D^{el}_{I^-}$) [38]	$7.8625 \times 10^{-9}\,\mathrm{m^2\,s^{-1}}$
Diffusion coefficient ($D^{el}_{I_3^-}$) [38]	$5.2677 \times 10^{-9}\,\mathrm{m^2\,s^{-1}}$
Diffusion coefficient ($D^{el}_{I_2}$) [38]	$5.9989 \times 10^{-9}\,\mathrm{m^2\,s^{-1}}$

During galvanostatic charging or discharging, the battery operates under a constant current, which is directly linked to the C-rate (C)—a measure of the rate at which the battery is charged or discharged relative to its maximum capacity. In general, the C-rate is determined by the total energy capacity of the battery, which in turn depends on the maximum and minimum concentrations of sodium ions in the electrolyte, as defined by the initial concentrations and the solubility limits discussed earlier. Thus the relationship between total cell current density (i_{cell}), the sodium ion concentrations and the C-rate is given by:

$$i_{cell} = \frac{[Na^+]_{max} - [Na^+]_{min}}{F} \frac{C}{3600\,s} V_{el} \tag{3.28}$$

Another critical metric for assessing battery performance is the State of Charge (SOC), which indicates the current energy level of the battery relative to its fully charged and fully discharged states. In essence, the SOC is defined as the complement of the Depth of Discharge (DoD) and is calculated using the sodium ion concentration in the electrolyte:

$$SoC = 1 - DoD = \left(\frac{\int [Na^+](x,t) dV_{el}}{V_{el}} - [Na^+]_0 \right) \frac{1}{[Na^+]_{max} - [Na^+]_0} \tag{3.29}$$

In this equation, the initial sodium concentration $[Na^+]_0$ is typically set to the minimum level permissible by solubility limits, as detailed in table 3.3.

These metrics—applied current, C-rate, and SOC—are fundamental to understanding and predicting the behavior of the battery under various operating conditions. They provide critical insights into the battery's charge/discharge characteristics, efficiency, and overall performance.

3.2.5 Initial conditions

It is essential to establish initial values for the concentrations of the catholyte species. These initial concentrations are limited by the solubility thresholds of the respective compounds. For that purpose, it is useful to define the globally constant total elemental iodine concentration which is calculated by:

$$[\mathrm{I}]_{\mathrm{tot}} = [\mathrm{I}^-] + 2\,[\mathrm{I}_2] + 3[\mathrm{I}_3^-] \tag{3.30}$$

As previously mentioned, iodine exhibits high solubility in sodium iodide solutions due to the formation of triiodide ions. According to Goldstein [124], iodine stays in solution as long as $[\mathrm{Na}]/[\mathrm{I}]_{\mathrm{tot}} < 0.476$ at 25°C with a maximum total elemental iodine concentration of $[\mathrm{I}]_{\mathrm{tot}} = 12.2\,\mathrm{M}$). This correlation holds true for various degrees of dilution. Together with charge neutrality

$$\left[\mathrm{Na}^+\right] + [\mathrm{I}^-] + [\mathrm{I}_3^-] = 0 \tag{3.31}$$

, the total elemental iodine concentration, and the equilibrium relation initial conditions for all species are evaluated.

Table 3.3: Initial concentrations of molar species for various total elemental iodine concentrations at $T = 120°\mathrm{C}$.

$[\mathrm{I}]_{\mathrm{tot}}$ (M)	$[\mathrm{Na}^+]_0$ (M)	$[\mathrm{I}^-]_0$ (M)	$[\mathrm{I}_3^-]_0$ (M)	$[\mathrm{I}_2]$ (M)
		Discharging		
6	2.857	1.295	1.561	9.894×10^{-3}
8	3.809	1.724	2.085	9.928×10^{-3}
10	4.761	2.152	2.609	9.949×10^{-3}
11.2	5.333	2.409	2.923	9.958×10^{-3}
		Charging		
6	5.999	5.999	2.995×10^{-4}	4.099×10^{-7}
8	7.999	7.998	3.995×10^{-4}	4.101×10^{-7}
10	9.999	9.998	4.995×10^{-4}	4.102×10^{-7}
11.2	11.198	11.198	5.595×10^{-4}	4.102×10^{-7}

Table 3.3 presents the initial concentrations for selected total elemental iodine concentrations. Notably, the iodine concentrations are several orders of magnitude lower than those of the other

species and exhibit minimal variation across different total elemental iodine concentrations. For numerical stability, the initial concentrations of triiodide and iodine are set to very low values, in accordance with the aforementioned equations, rather than zero.

3.3 Solver implementation and computational solution

The equations governing the operation of a sodium-iodine battery solver were implemented using OpenFOAM®, an open-source platform in its v2206 release, which utilizes the Finite Volume method [125]. Originally designed for simulating intricate fluid flow dynamics, the software facilitates the computationally-efficient numerical solution of equations on extensive three-dimensional grids. In this study, the development of the computational solver was carried out through a custom code written within the OpenFOAM framework.

During the discharge process, the movement of sodium ions from the anode through the electrolyte, represented as Na^+, is governed by eq. (3.4). Within the simulation, both charge conservation in the cathode and ionic conservation in the electrolyte are maintained by tracking the electric and ionic potentials. In the three-dimensional model, the masses of Na^+, I^-, I_3^-, and I_2 are each represented by single scalar quantities. Similarly, another scalar is used to represent the potentials in the electrolyte and cathode phases (Φ_{el} and Φ_s).

These scalar quantities are discretized numerically using structured hex-dominant cells, with a second-order finite-volume spatial scheme and an implicit first-order temporal scheme. The equations are then solved in a segregated manner, utilizing a conjugate gradient linear solver in conjunction with a geometric-algebraic multigrid solver to precondition the matrices. Each scalar equation is implicitly solved across the entire cathode and electrolyte domains.

The process of solving uncoupled linear diffusion equations, such as eq. (3.12), is relatively straightforward and efficient, even when applied to large and complex three-dimensional mesh networks. However, the computational complexity increases significantly due to the strong non-linearity introduced by the electrochemical reactions (e.g., eqs. (3.7) and (3.15)) and ion transport mechanisms, particularly the migration terms in eq. (3.19).

In the finite volume method, it is recommended to decompose the source terms in eq. (3.10) into their positive (source) and negative (sink) components, applying distinct discretization techniques to each. Specifically, the positive component is treated implicitly, while the negative component, due to the high magnitude of k_f, is linearized using a Taylor series expansion and treated explicitly. This approach ensures diagonal dominance of the coefficient matrix, thereby preventing the violation of the Scarborough criterion and avoiding potential divergence [126].

In OpenFOAM, physical quantities and their corresponding equations are linked to the computational grid. Consequently, due to the different fundamental equations, separate computational

grids are required for both the electrolyte and the cathode. The partial differential equations are then addressed individually for each computational domain in the segregated solver approach. Figure 3.2 illustrates the iterative solution algorithm, providing a step-by-step overview of the process thoroughly described in the subsequent discussion.

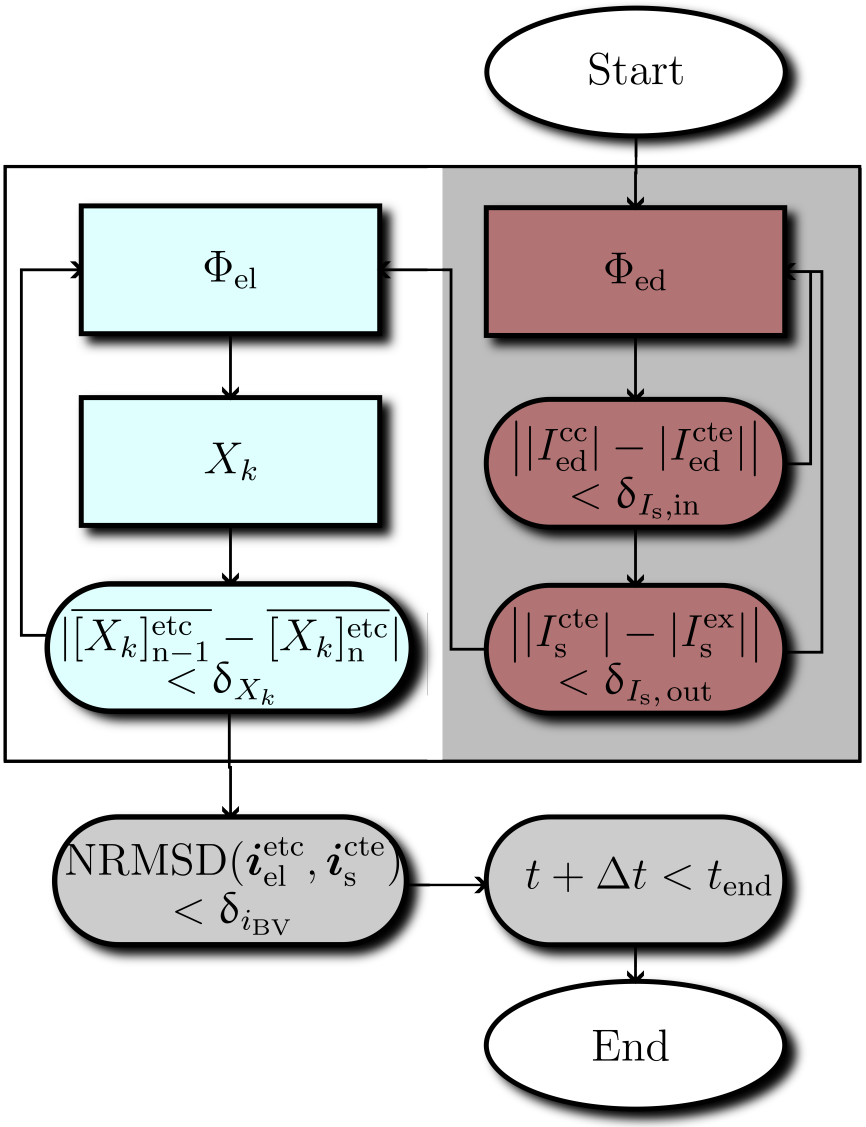

Figure 3.2: Schematic flowchart illustrating the iterative solution algorithm used in the segregated solver for the sodium iodine battery. The algorithm is designed to maintain current consistency during galvanostatic cycling. To ensure stability, under-relaxation techniques are applied. Convergence between the electrode and electrolyte currents at the coupled interfaces is evaluated using the normalized root mean square deviation (NRMSD).

Initially, the numerical solution for Φ_{s} (eq. (3.12)) is obtained. Within the cathode domain, a sufficient number of iterations are required to ensure consistency of the external current ($I_{\mathrm{s}}^{\mathrm{ex}}$), the current at the cathode–electrolyte interface ($I_{\mathrm{s}}^{\mathrm{cte}}$), and the current at the cathode current collector ($I_{\mathrm{s}}^{\mathrm{cc}}$) during galvanostatic cycling.

The need for a sufficient number of iterations arises because the boundary condition for Φ_s at the cathode-electrolyte interface (eq. (3.27a)) is implemented as a Robin-type boundary condition. This condition, which combines both a fixed value and a gradient, is essential for stabilizing the numerical solution of eq. (3.12) [127]. To achieve this, an inner iterative loop is used to update the fixed face values until the current difference between the cathode current collector and the cathode-electrolyte interface falls below a user-defined convergence threshold ($\delta_{I_s,\text{in}}$):

$$\left||I_s^{cc}| - |I_s^{cte}|\right| < \delta_{I_s,\text{in}} \tag{3.32}$$

Upon completing the inner loop, the electrode potential at the current collector (Φ_{ed}^{cc}) must be appropriately chosen to ensure current consistency with (I_s^{ex}) as detailed in section 3.2.2. To solve this problem, root-finding algorithms like the secant method, used in this study, are employed. The equation for the secant method is provided as follows:

$$x_{n+1} = x_n - \frac{f(x_n)(x_n - x_{n-1})}{f(x_n) - f(x_{n-1})} \tag{3.33}$$

Unlike the widely used Newton method, the secant method does not require the computation of derivatives, which are impractical to calculate in this context, and it offers greater robustness. The implemented equation iteratively adjusts Φ_{ed}^{cc} to converge the integral current density I_{ed}^{cc} towards the external current I_{ed}^{ex} incorporating a damping factor (γ_k).

$$\Phi_{ed,n+1}^{cc} = \Phi_{ed_n}^{cc} + \gamma_k \left(I_{ed}^{ex} - I_{ed,n}^{cc}\right) \frac{\Phi_{ed,n}^{cc} - \Phi_{ed,n-1}^{cc}}{I_{ed,n}^{cc} - I_{ed,n-1}^{cc}} \tag{3.34}$$

The γ_k is constrained to $0 < \gamma_k \leq 1$. It is incorporated to enhance the robustness, stability, and convergence behavior of the iterative process. A commonly used and straightforward approach for determining the optimal damping factor is the Armijo strategy [128]. Here, the damping factor is selected from a progression, typically following the sequence $\left\{1, \frac{1}{2}, \frac{1}{4}, \ldots, \gamma_{k,\min}\right\}$. To decide whether to accept or reject a new damping factor, monotonicity tests are conducted. If a test fails, it is repeated with $\gamma_k/2$. Should γ_k fall below $\gamma_{k,\min}$, the solver terminates with a warning. If the test is successful, the damping factor for the next iteration is updated according to

$$\gamma_{kn+1} = \min\{1,\ 2\gamma_{k,n}\}, \tag{3.35}$$

allowing the method to asymptotically approach the convergence order of the standard secant method ($(1+\sqrt{5})/2 \approx 1.618$). The described damping strategy was found to be numerically stable with $\gamma_{k,\min} = \frac{1}{32}$ and sufficiently fast for the presented numerical solver, although the implementation of more efficient strategies is possible, as discussed by Deuflhard [129].

In the solving algorithm, this strategy is employed in an outer iteration loop, where $\Phi_{\mathrm{ed}}^{\mathrm{cc}}$ is updated at each step until the outer convergence criterion ($\delta_{I_{\mathrm{s,out}}}$) is satisfied:

$$\left| |I_{\mathrm{s}}^{\mathrm{cte}}| - |I_{\mathrm{s}}^{\mathrm{ex}}| \right| < \delta_{I_{\mathrm{s,out}}} \tag{3.36}$$

Each iteration of the outer loop involves completing the inner loop to ensure the convergence of the current difference between the cathode current collector and the cathode-electrolyte interface. This process ensures overall consistency in the current distribution across the cathode.

The next step involves solving the equations for electrolyte potential and the electrolyte species. Due to the strong coupling between the species concentrations X_k, as introduced by the source terms in eq. (3.10), and the presence of Φ_{el} in the migration component of species fluxes in eq. (3.4), multiple iterations of the electrolyte equations are required. To maintain solution accuracy, the change in concentration between successive iterations must be kept minimal. Convergence of the electrolyte domain is ensured by tracking the species concentration changes at the electrolyte-cathode interface, where the concentration gradients are most pronounced:

$$|\overline{[X_k]_{\mathrm{n-1}}^{\mathrm{etc}}} - \overline{[X_k]_{\mathrm{n}}^{\mathrm{etc}}}| < \delta_{X_k} \tag{3.37}$$

Lastly, the iterative coupling between the electrolyte and cathode domains is achieved through the Butler–Volmer charge transfer mechanism. To ensure computational stability during this process, under-relaxation techniques are applied when coupling these two computational domains. Convergence is monitored by calculating the normalized root mean square deviation (NRMSD) of the currents on the coupled patches, $\boldsymbol{i}_{\mathrm{el}}^{\mathrm{etc}}$ and $\boldsymbol{i}_{\mathrm{s}}^{\mathrm{cte}}$.

$$\mathrm{NRMSD}\left(\boldsymbol{i}_{\mathrm{el}}^{\mathrm{etc}}, \boldsymbol{i}_{\mathrm{s}}^{\mathrm{cte}}\right) = \frac{\sqrt{\frac{1}{n}\sum_{i=1}^{n}\left(\boldsymbol{i}_{\mathrm{s,i}}^{\mathrm{cte}} A_{\mathrm{i}}^{\mathrm{cte}} - \boldsymbol{i}_{\mathrm{el,i}}^{\mathrm{etc}} A_{\mathrm{i}}^{\mathrm{etc}}\right)^2}}{\frac{1}{A^{\mathrm{etc}}}\sum_{i=1}^{n} \boldsymbol{i}_{\mathrm{s,i}}^{\mathrm{cte}} A_{\mathrm{i}}^{\mathrm{cte}}} \tag{3.38}$$

For convergence, the NRMSD must fall below a predefined criterion ($\delta_{i_{\mathrm{BV}}}$) to guarantee current consistency. In most simulation scenarios, convergence criteria δ_i of 1×10^{-3} were found to be sufficient to maintain accuracy of the solution.

The simulations were performed on a high-performance computing (HPC) system using 2 nodes, each with 40 Intel Xeon Gold 6230 cores operating at 2.1 GHz, and 96 GB of main memory per node. Each simulation averaged approximately 24 hours of runtime.

3.4 Two-dimensional electrodes[1]

This section presents the model-predicted effects of variations in cathode electrode design, material, and catholyte composition on battery performance. Simulations were conducted using a hex-dominant computational grid comprising approximately 1 million cells, with a cell size of 2.5×10^{-4} m in the bulk electrolyte. To capture the high-gradient regions more accurately, local grid refinement reduced the cell size to 30 µm. The time step used in the simulations varied between $\Delta t = 1$ s and $\Delta t = 10$ s depending on the C-rate, with smaller time steps employed at the beginning and end of the cycling process to account for larger potential changes.

3.4.1 Solver validation

Initially, a simulation was performed using a three-dimensional geometry equivalent to the one-dimensional model introduced by Zhu and Kee [38]. This comparison aimed to verify the spatially resolved model by aligning all parameters with those of the homogenized model. For this purpose, the cathode compartment in this model is set at 1 mm in length and contained evenly distributed carbon fibers with a specific surface area of $80\,000\,\mathrm{m^2\,m^{-3}}$ and a porosity of 0.8. Battery cycling starts from a fully charged or discharged state, assuming an even distribution of species across the cathode domain, with initial concentrations determined by the total elemental iodine concentration as outlined in section 3.2.5.

Furthermore, the current density is calculated based on the C-rate and total species concentration (eq. (3.28)). Figure 3.3 illustrates the cell voltages at two different C-rates for both the spatially resolved model and the one-dimensional model from Zhu and Kee. The dashed lines represent the cell voltages extracted from Zhu and Kee's work, while the solid lines represent the results obtained from the current model.

Overall, the discharge curves at different C-rates show good agreement between the two models. However, during the 5 C discharge, the curves diverge towards the end of the discharge process, with the current model predicting an earlier termination. For charging, the cell voltage predicted by the current model is slightly lower. Despite these differences, the rate of decrease in cell voltage as a function of the state of charge is comparable to that in the model by Zhu and Kee. The maximum relative deviation between the two models is only about 3 %, equivalent to approximately 82 mV.

[1] This section includes results and findings that were previously reported in Gerbig, F., Cernak, S., and Nirschl, H.: 3D Simulation of Cell Design Influences on Sodium–Iodine Battery Performance. *Energy Technology*, **2021**, 9(6), 2000857. DOI: 10.1002/ente.202000857

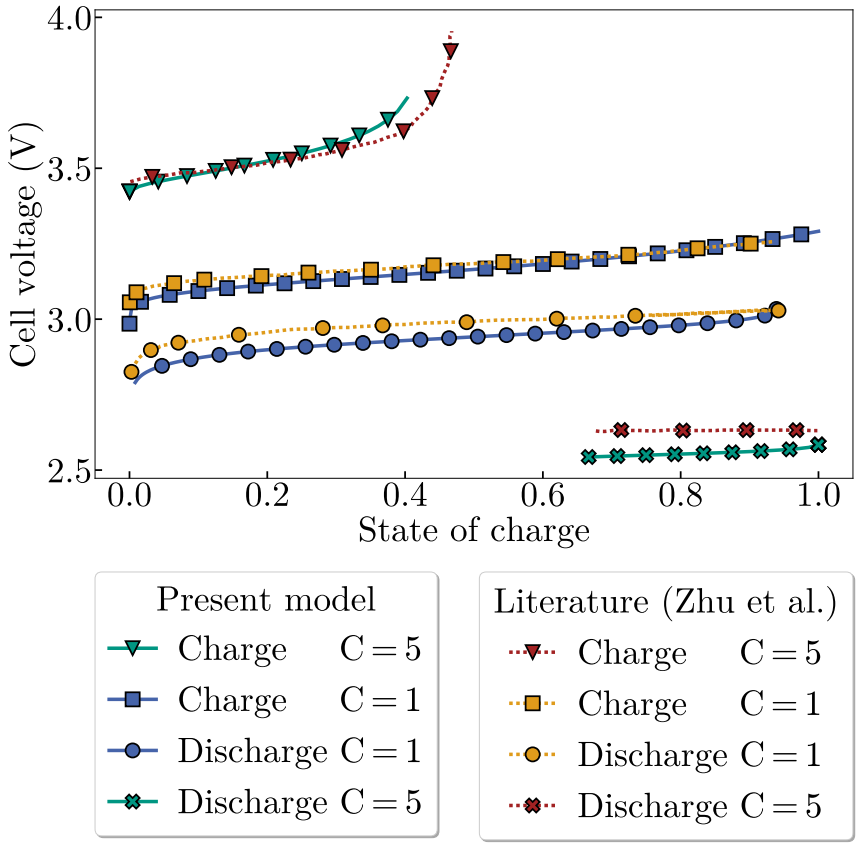

Figure 3.3: Comparison between the spatially resolved simulation model and the one-dimensional model introduced by Zhu and Kee [38]

3.4.2 Spatially resolved battery simulation setup

This study employs a spatially resolved model to investigate the impact of various factors on the performance of a sodium iodine battery, focusing on a simplified cell design. Specifically, a two-dimensional cathode electrode design is utilized for its simplicity, which is desirable for large-scale battery applications. In this configuration, the cathode structure is modeled as a solid plate positioned at the center of the cathode compartment. This arrangement minimizes the distance between the electrolyte and the cathode, thereby reducing diffusion path lengths and mitigating diffusion-related limitations.

The cathode is designed as a circular disc with a thickness of 1 mm and a radius of 2.5 cm, with blunt edges to prevent the formation of voltage peaks that typically occurs at sharp corners and edges. The material chosen for the cathode is titanium, known for its high electronic conductivity and excellent chemical resistance, making it a reliable electrode material. Finally, the cathode is connected to the current collector via a thin wire. The cathode compartment itself is modeled as a rectangular volume, with a variable distance between the separator and the cathode current collector, while maintaining a constant length of 6 cm on the other two sides.

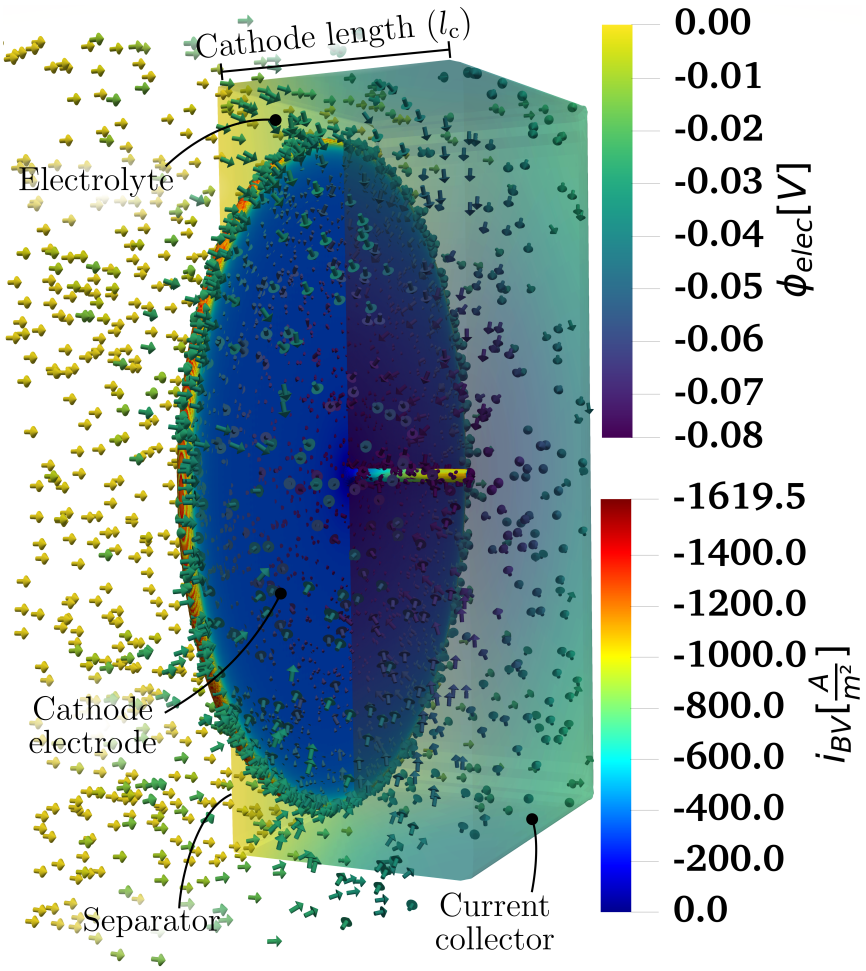

Figure 3.4: Schematic of the cathode half-cell compartment showing the separator (left) and the cathode current collector (right). The distance between the separator and the current collector is l_c = 2 cm, with a C-rate C = 0.2 and I = 8 M.

Figure 3.4 provides a three-dimensional representation of a simulated cathode half-cell. The separator is illustrated on the left, and the current collector appears on the right. The circular cathode is color coded to represent the Butler-Volmer current density i_{BV}, which is negative, indicating that the process is proceeding in the cathodic direction (discharge). In particular, red areas on the electrode signify regions of high Butler-Volmer current density, corresponding to high reaction rates. Notably, these areas are most pronounced at the edges of the electrode and near the connection point between the electrode and the current collector. For clarity, the electrolyte region is partially clipped in the figure. Within this region, the colors represent the electric potential, while arrows indicate the direction of ionic current flow.

3.4.3 Impact of cathode compartment length on battery performance

The performance characteristics of the sodium-iodine (Na-I) battery are profoundly affected by the length of the cathode compartment, particularly in terms of energy capacity and external current density. In this study, a series of simulations were conducted, all of which commenced from equilibrium conditions to ensure consistency. The external current density i_{cell} was systematically varied according to the C-rate, with values set at 106.4 mA cm^{-2} for 1 C, 53.2 mA cm^{-2} for 0.5 C, 26.5 mA cm^{-2} for 0.2 C, and 13.2 mA cm^{-2} for 0.1 C.

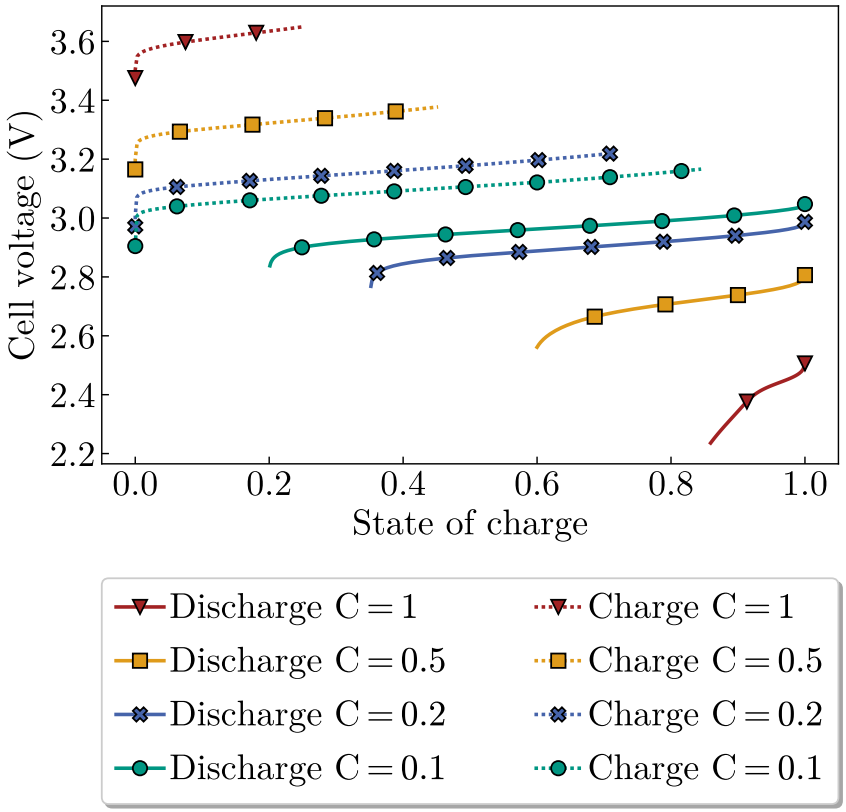

Figure 3.5: Dependence of cell voltage oon the state of charge (SOC) for various C-rates, with a **cathode compartment length of 1 cm**. Charging cycles are indicated by dashed lines, while discharging cycles are shown with solid lines. The data for different C-rates, spanning from 0.1–1 C, are distinguished by distinct colors and markers.

Figure 3.5 presents the cell voltages as a function of the state of charge (SOC) for a cathode compartment length of 1 cm under various C-rates. The relationship between cell voltage and SOC exhibits a logarithmic dependence, which stems from the Nernst equation governing the equilibrium potential, leading to a voltage plateau as SOC increases. The cell voltage is strongly dependent on the C-rate (see eqs. (3.7) and (3.19), with higher current densities inducing greater electric potential gradients and, consequently, larger electrostatic potential differences within the cathode ($\Delta\Phi_s$) and separator ($\Delta\Phi_{sep}$).

As the C-rate increases, the demand for migration flux—driven by the need to maintain the required species flux—becomes more pronounced due to the relatively slow diffusion process. This, in turn, necessitates an increase in the electrostatic potential differences within the electrolyte ($\Delta\Phi_{el}$). Consequently, a higher external current leads to an elevated Butler-Volmer current density at the interface between the cathode and electrolyte, which drives the observed overpotentials.

The comparison of cell voltages between different C-rates, ranging from 0.1–1 C, demonstrates a substantial variance of up to 0.5 V during both charging and discharging phases. This variance is particularly notable at higher C-rates, where the SOC achievable during discharging decreases significantly. For example, at a C-rate of 0.1 C, the SOC remains relatively high, approximately 0.85, but drops drastically to around 0.2 at 1 C. This decline is primarily due to the accelerated consumption of triiodide at the cathode surface, a direct consequence of the Butler-Volmer reaction, which increases with the C-rate. The discharge process ultimately ceases when triiodide is entirely depleted at the cathode surface, a diffusion-limited condition that occurs more rapidly at higher C-rates.

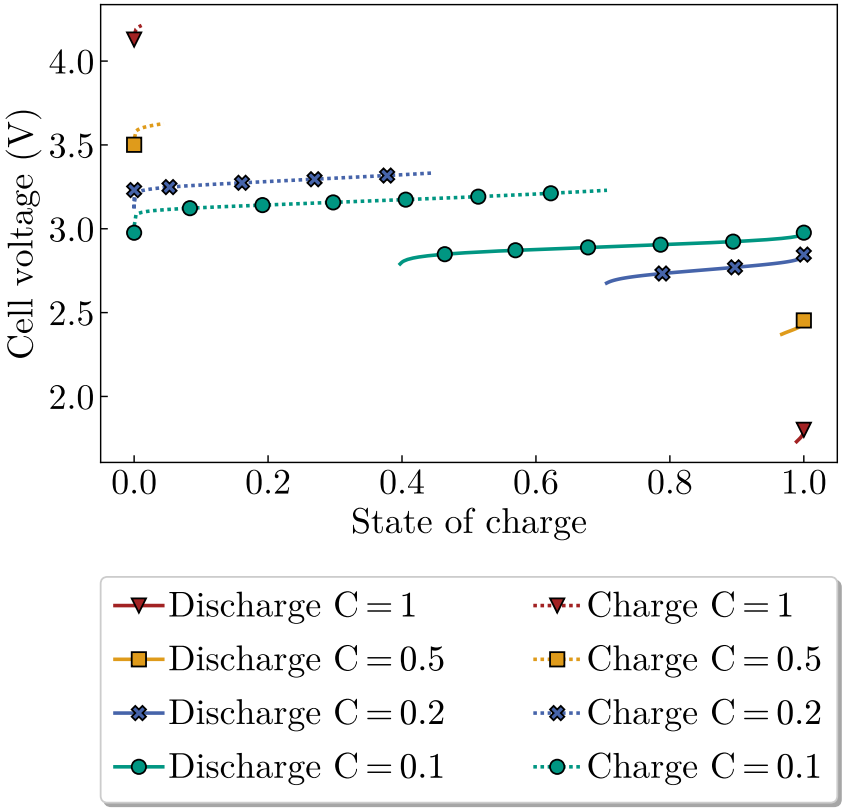

Figure 3.6: Dependence of cell voltage oon the state of charge (SOC) for various C-rates, with a **cathode compartment length of 2 cm**. Charging cycles are indicated by dashed lines, while discharging cycles are shown with solid lines. The data for different C-rates, spanning from 0.1–1 C, are distinguished by distinct colors and markers.

In the charging process, a similar trend is observed: the SOC decreases as the C-rate increases. However, the termination of charging occurs later than that of discharging across all C-rates. The

formation of triiodide from iodine and iodide during charging leads to a gradual reduction in the elemental iodine-to-sodium ratio. As this ratio decreases, the charging process eventually halts to prevent the precipitation of iodine, which would otherwise occur if the charging continued. At higher charge rates, the diffusion of triiodide towards the NaSICON membrane is insufficient to maintain the necessary concentrations, resulting in a $[Na^+]/[I]$ ratio falling below 0.46 and subsequent NaI precipitation, which forces the charging process to stop.

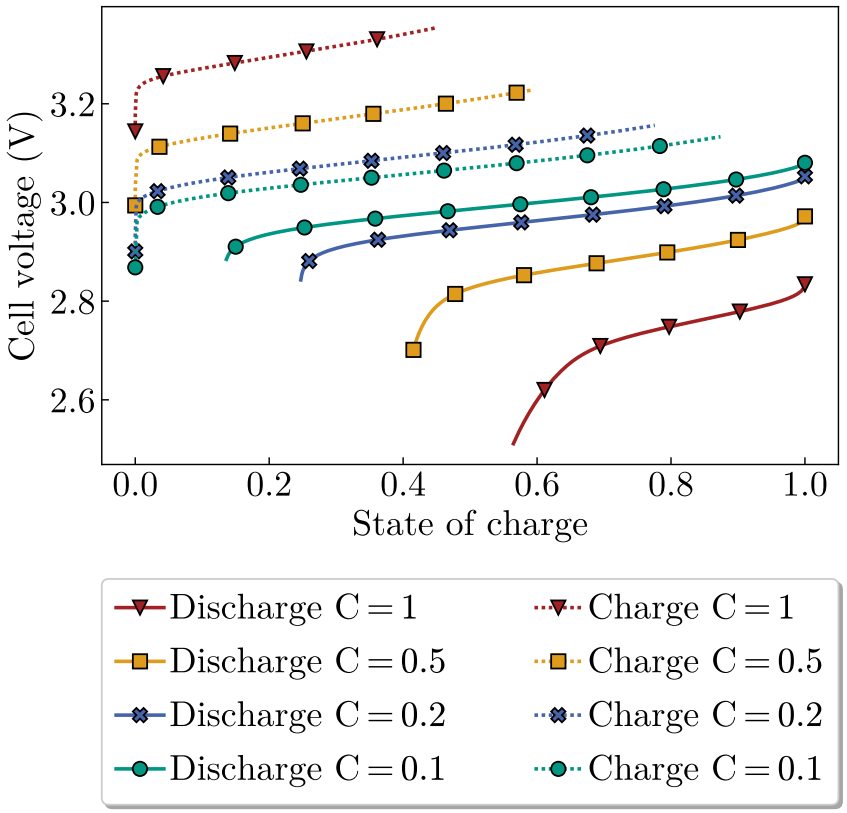

Figure 3.7: Dependence of cell voltage oon the state of charge (SOC) for various C-rates, with a **cathode compartment length of 0.5 cm**. Charging cycles are indicated by dashed lines, while discharging cycles are shown with solid lines. The data for different C-rates, spanning from 0.1–1 C, are distinguished by distinct colors and markers.

The influence of cathode compartment length on these processes is further elucidated in fig. 3.6, which presents the charge and discharge behaviors for a cathode compartment length of 2 cm. With this increased length, the external current densities are approximately doubled relative to the 1 cm case, reaching 218.9 mA cm^{-2} for 1 C and proportionally lower values for other C-rates. The trends observed in the voltage behavior are consistent with those seen in the 1 cm case, though the absolute values of cell potential differ. For instance, at the lowest C-rate of 0.1 C, the cell voltages are nearly identical between the 1 cm and 2 cm cases. However, as the C-rate increases, the voltage differences become more pronounced, with deviations of up to 0.5 V at 1 C. At these higher C-rates, the charging process is truncated shortly after initiation due to iodine precipitation. During discharging, an SOC of about 0.7 is achievable at 1 C, but the process stops when triiodide

is exhausted at the cathode surface, particularly for higher C-rates like 0.5 C and 1 C. Here, the slower transport of sodium ions from NaSICON towards the cathode current collector results in NaI precipitation, marking the end of the discharge cycle when sodium ion concentrations reach saturation.

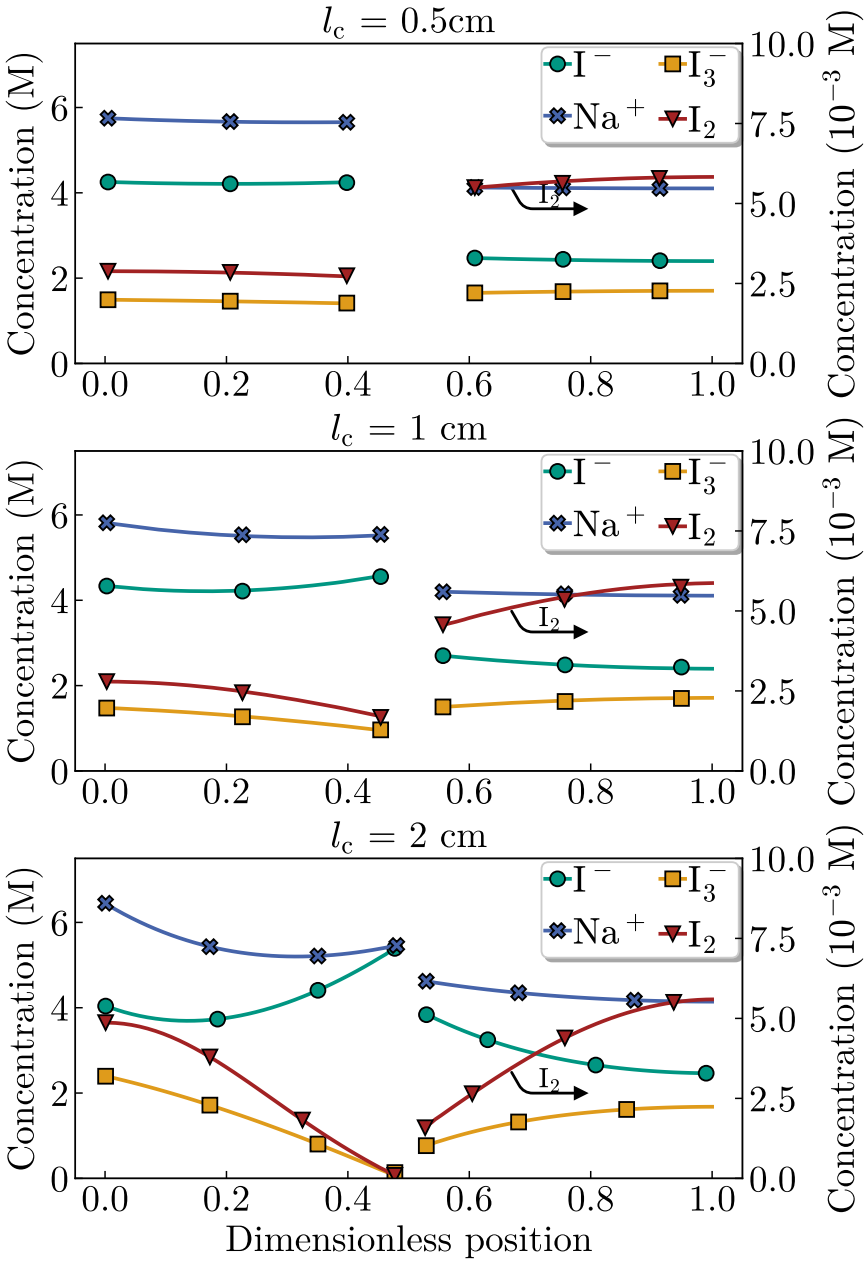

Figure 3.8: Concentration profiles of electrolyte species iodide (I^-), sodium-ion (Na^+), triiodide (I_3^-), and iodine (I_2) along the dimensionless position (x/l_c) across the cathode half-cell, extending from the separator (left) to the cathode current collector (right). The profiles illustrate the distribution of species after discharging the battery for one hour with 0.2 C, highlighting the variations in concentration along the length of the cathode

The analysis of a 0.5 cm cathode compartment length, as illustrated in fig. 3.7, further clarifies the impact of cathode compartment length on the battery's performance. In this case, the variations

in cell voltage are less pronounced than those observed for longer cathode compartment lengths of 1 cm and 2 cm. This is primarily due to the lower external current density associated with the shorter cathode, which moderates the electrochemical processes. As a result, the charging process concludes later, with the SOC approaching the theoretical maximum at 0.1 C. At this C-rate, the cell can achieve nearly half of its maximum SOC even at 1 C. The discharge process at lower C-rates (0.1 C and 0.2 C) is extensive, with minimal voltage increase, indicating efficient energy utilization. However, at higher C-rates (0.5 C and 1 C), the achievable SOC is significantly reduced, and the associated voltage drop is more pronounced, reflecting the increased deviation from the equilibrium potential.

The concentration profiles of various species within the electrolyte, as shown in fig. 3.8, provide further insights into the internal processes occurring within the half-cell as the cathode compartment length varies. These profiles highlight the impact of cathode compartment length on the spatial distribution of species, which in turn affects global performance parameters such as cell voltage. The concentration gradients of four key species are depicted as functions of the dimensionless cathode compartment length (x/l_c) during a 0.2 C discharge after one hour. Notably, the concentrations of iodine, which are significantly lower, are plotted on the right axis to enhance visibility of their changes. In general, the concentration gradients increase as the cathode compartment length extends, a direct consequence of the rising external current. This increase in current necessitates greater sodium flux at the NaSICON separator and enhanced species fluxes at the cathode electrode, driven by the Butler-Volmer reaction.

In particular, sodium ions enter the cathode through the separator, causing greater deviations from initial concentrations in the region between the separator and cathode electrode (left side) compared to the area between the cathode electrode and cathode current collector (right side). The Butler-Volmer reaction is more pronounced on the left side of the cathode. For a cathode compartment length of 2 cm in the battery, the discharge process terminates due to diffusion limitations. Triiodide and iodine are depleted on the left side, restricting the reaction to the right side only. Consequently, discharge ceases when triiodide and iodine are entirely exhausted on the cathode surface, as no charge-carrying species are available to sustain the charge transfer reaction described by eq. (3.3).

Figure 3.9 provides an overview of battery performance for different cathode compartment lengths under a constant external current of 501.7 A m^{-2}. The stored energy correlates with the amount of substances, leading to variations in C-rates. Notably, cell voltages during charging are relatively consistent across different cathode compartment lengths, although the 2 cm case shows earlier termination. In contrast, the discharge behavior of the 2 cm cathode compartment length differs markedly from that of shorter cathode compartment lengths, with a significantly reduced achievable SOC and lower cell voltage.

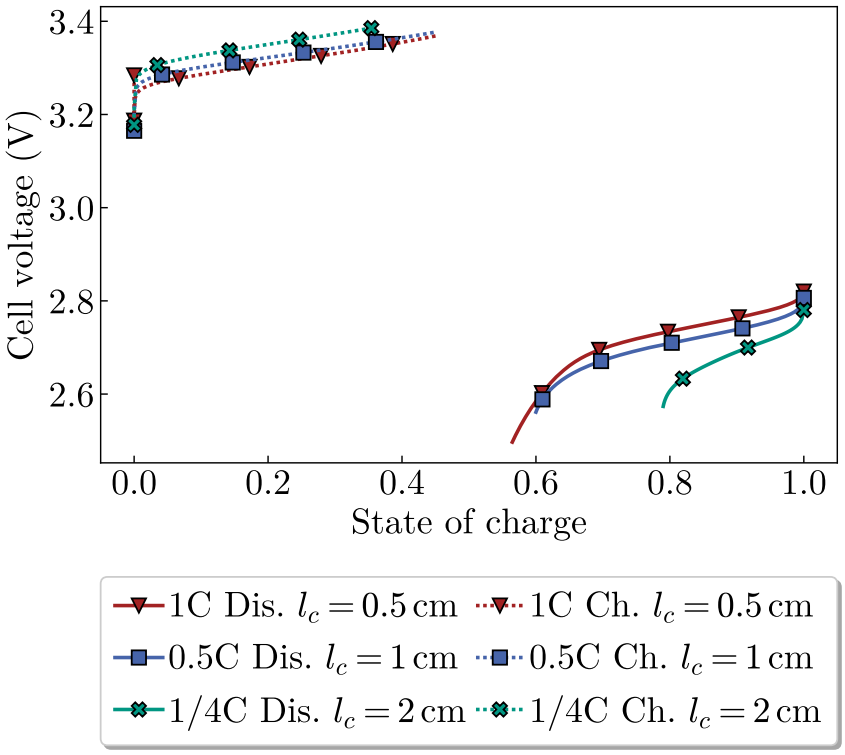

Figure 3.9: Cell voltage as a function of SOC for different cathode compartment lengths with **constant external current**

3.4.4 Influence of conductivity

Titanium is employed as the cathode material in the reference simulation due to its favorable characteristics, including chemical stability in the presence of an aqueous iodine solution. However, the choice of cathode material can significantly influence the overall performance of the battery, primarily through variations in electrical conductivity. This subsection delves into the impact of different electronic conductivities of cathode materials on battery performance.

Figure 3.10 illustrates the effects of varying the electronic conductivity of the cathode material on the cell voltage across the state of charge (SOC). The study compares the performance of several materials with differing conductivities: Titanium, with an electrical conductivity of $2.5 \times 10^6\,\mathrm{S\,m^{-1}}$, is used as the baseline. In addition, materials such as stainless steel and glassy carbon, which have conductivities of $1.5 \times 10^6\,\mathrm{S\,m^{-1}}$ and $2 \times 10^4\,\mathrm{S\,m^{-1}}$ respectively, are also considered. These materials are commonly used in secondary battery applications due to their respective conductivity properties and chemical resistance [131, 132]. Additionally, a hypothetical material with an intermediate conductivity of $1.5 \times 10^5\,\mathrm{S\,m^{-1}}$ is included in the study to generalize the influence of conductivity on cell performance. For consistency, other battery parameters, such as the cathode compartment length of 1 cm and a C-rate of 0.2, are kept constant throughout the simulations.

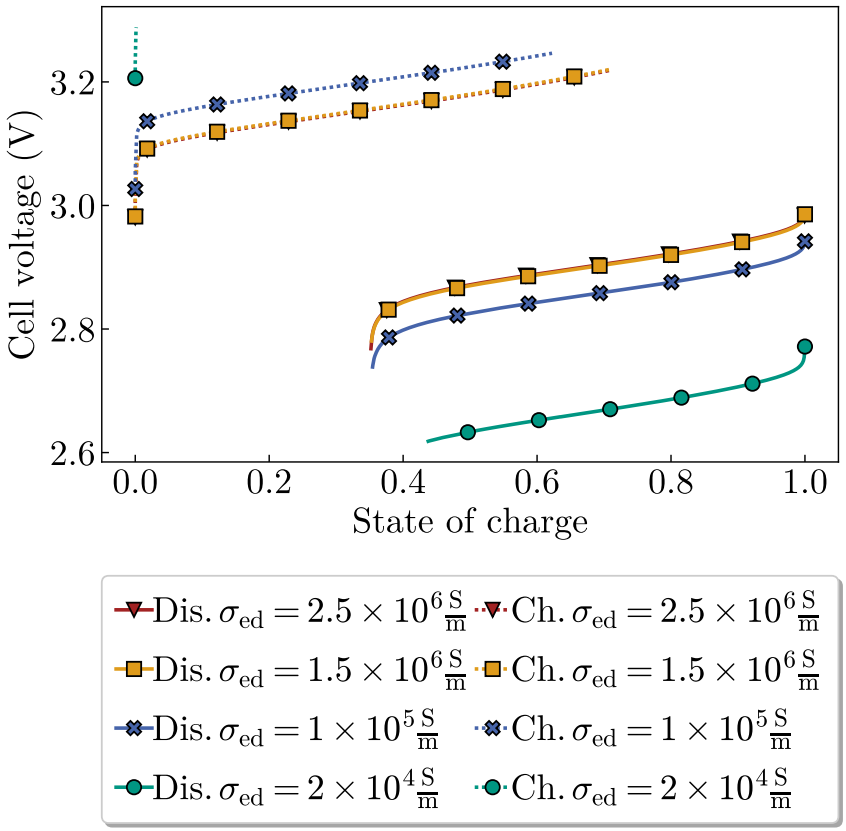

Figure 3.10: Cell voltage as a function of SOC for varying electrical conductivities of the cathode electrode, with a cathode compartment length l_c = 1 cm and a C-rate of 0.2. Dashed lines indicate charging, while solid lines represent discharging.

The results demonstrate that cell voltage decreases with reducing conductivity during discharge, with a more pronounced voltage drop observed at lower conductivities. This outcome is attributable to the increased electric potential gradients required to sustain the same current through materials with lower conductivity, which, in turn, leads to an increased potential difference, denoted as $\Delta\Phi_s$. The simulation results reveal that cell voltages for materials with conductivities of $2.5 \times 10^6\,\mathrm{S\,m^{-1}}$ and $1.5 \times 10^6\,\mathrm{S\,m^{-1}}$ are nearly indistinguishable, indicating that the potential gradients in these highly conductive materials are minimal. As a result, the discharge curves for these materials overlap significantly. The maximum achievable SOC for these high-conductivity materials, as well as the material with an intermediate conductivity of $1.5 \times 10^5\,\mathrm{S\,m^{-1}}$, stabilizes at approximately 0.35.

The charging behavior shows similar trends to those observed during discharging. The cell voltages for titanium and stainless steel, with conductivities of $2.5 \times 10^6\,\mathrm{S\,m^{-1}}$ and $1.5 \times 10^6\,\mathrm{S\,m^{-1}}$, respectively, align closely, with the charging curves almost coinciding. For all materials tested, charging is eventually terminated when the ratio of sodium ions to iodine ($[Na^+]/[I]$) falls below 0.46, leading to the precipitation of iodine. Notably, the charging process terminates earlier for cathodes with lower electrical conductivities. This earlier termination is caused by increased local

variations in electric potential, which in turn amplify the Butler-Volmer current density variations. Such variations result in uneven iodine consumption and can lead to localized precipitation of iodine when solubility limits are exceeded.

For the material with the lowest conductivity, the charging process is especially problematic: Due to the limited surface area available for the Butler-Volmer reaction, particularly near the connection between the cathode electrode structure and the cathode current collector, the reaction is driven predominantly towards this small region. Inevitably, this localization of the reaction causes significant gradients and rapid iodide consumption, leading to an almost immediate termination of the charging process. Consequently, the lowest conductivity material exhibits the poorest performance, with a severe reduction in both discharge and charge capacities.

3.4.5 Effect of initial concentrations

Figure 3.11 illustrates the impact of varying initial species concentrations on the cell voltage within the specified battery setup. In this study, the cathode compartment length is maintained at 1 cm and the simulations are conducted at a C-rate of 0.2 C. The dashed lines in the figure correspond to the charging process, while the solid lines depict the discharging process. Each line is distinguished by different colors and markers, representing various total elemental iodine concentrations.

During discharging, the cell voltage demonstrates a clear trend of decreasing as the total elemental iodine concentration increases. This behavior is attributable to the higher current densities associated with elevated total elemental iodine concentrations, which in turn induce greater electric potential differences across the cathode, electrolyte, and separator regions, as well as increased overpotentials. In particular, simulations with total elemental iodine concentrations of 6 M and 8 M show termination of the discharging process at a state of charge (SOC) of approximately 0.35. This early termination is due to the depletion of triiodide at the cathode electrode, which limits the continuation of the discharge process. On the other hand, simulations with higher initial concentrations, such as 10 M and 11.2 M, stop even earlier. This earlier termination occurs because the increased sodium-ion concentration near the separator exceeds the solubility limits of sodium iodide, leading to its precipitation and thus halting the discharge process.

In contrast to discharging, the charging process exhibits lower cell voltage, particularly at the beginning of the cycle. This is primarily due to the higher total concentration of charge-carrying species, which—according to the Nernst-Einstein relation (eq. (3.20)—increases the ionic conductivity of the electrolyte. The resulting decrease in internal potential gradients leads to a lower overall cell voltage during early charging. Despite these lower potential differences, the charging process must be carefully managed to avoid iodine precipitation. Simulation results show that at higher initial iodine concentrations—especially at [I] = 11.2 M—precipitation occurs

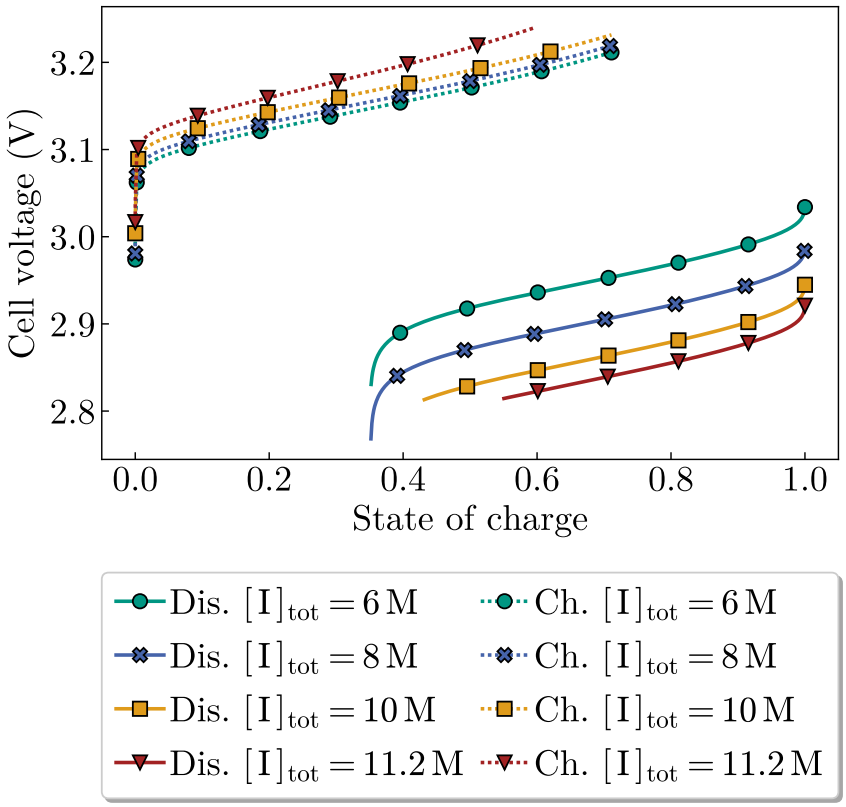

Figure 3.11: Cell voltage as a function of SOC for various initial species concentrations with a cathode compartment length l_c = 1 cm and C = 0.2. Dashed lines indicate charging, while solid lines indicate discharging

earlier, which necessitates early termination of the charging process to prevent undesired side reactions.

3.5 Three dimensional electrodes[2]

Extensive numerical studies in section 3.4 have identified transport limitations as the primary constraint on overall battery performance [130]. To address these limitations, it is crucial to develop an enhanced cathode electrode structure that maximizes the surface area available for surface reactions while maintaining high porosity. Such a design is essential to achieve the desired energy capacity and resource efficiency of the battery system. Consequently, three-dimensional electrodes have been widely adopted in electrochemical processes to mitigate the transport limitations inherent in traditional two-dimensional electrodes [134].

[2] This section includes results and findings that were previously reported in Gerbig, F., Holzapfel, M., and Nirschl, H.: Simulating the Impact of Glassy Carbon Foam Electrodes on the Performance of Sodium Iodine Batteries. *Journal of The Electrochemical Society*, **2023**, 170(4), 040517. DOI: 10.1149/1945-7111/accab7

Various types of three-dimensional electrodes, including packed-bed electrodes, porous electrodes, active fluidized-bed electrodes, and moving-bed electrodes, have been implemented [135]. Among these, porous structures such as cloths, felts, or foams are particularly well-suited for sodium-iodine batteries. These materials offer simplicity and cost-effectiveness, making them ideal for stationary energy storage applications. Open-pore foams, in particular, present a promising option for cathode geometry [136] and have already been explored in the context of lead flow batteries [137].

Metal foams are extensively documented in the literature and have applications in catalysis and heat transfer [138, 139]. In addition, solid foams are employed in the aviation industry to create high-strength materials. Typically, foams are produced by combining a liquid material with a blowing agent, which solidifies upon cooling. As a result, dry foams are mathematically described by minimal surface structures, with the Kelvin cell being the most recognized model. This 14-sided tetrakaidecahedron, composed of six quadrilateral and eight hexagonal faces, is widely used for the idealized representation of foams [140].

Although Weaire and Phelan proposed a structure with a slightly smaller surface area [141], the difference is minimal, amounting to less than 0.3 %. Moreover, the Weaire-Phelan structure is more complex, comprising six 14-sided polyhedra and two 12-sided polyhedra with irregular faces (see fig. 3.12a). The computational effort required to generate and simulate virtual Weaire-Phelan foams, as well as to implement appropriate cyclic boundary conditions, is significant. Studies on the mechanical properties and heat transfer characteristics of foams have demonstrated negligible differences between the Kelvin cell and Weaire-Phelan models [142, 143]. Therefore, this work primarily focuses on Kelvin's conjecture.

The Kelvin cell (see fig. 3.12b) is space-filling, and the foam unit cell can be conceptualized by subtracting a sphere from the Kelvin cell [144]. Since the size of the Kelvin cell directly influences the size of the parent bubble in the foam, the porosity and pore size are determined by the ratio between the Kelvin cell size and the sphere diameter. Thus, this method allows for the creation of foams of any desired length and thickness by appropriately arranging the resulting foam unit cells.

A wide range of materials is viable for constructing open-pore foam structures, including polymers, carbon-based materials, and various metals. However, many conventional battery electrode materials lack chemical stability when exposed to the aggressive iodine-rich environments typical of sodium-iodine batteries. In contrast, glassy carbon exhibits exceptional long-term stability in such catholyte solutions [39]. Consequently, reticulated vitreous carbon (RVC) foams, commonly referred to as glassy carbon foams, emerge as highly suitable candidates for these batteries.

Reticulated vitreous carbon foams are typically produced through the carbonization of resin-coated, open-cell polyurethane foams at temperatures ranging from 700–1100 °C. The process of foam formation involves capillary drainage and rapid wall thinning, which ultimately results in open-pore structures resembling Kelvin cells. The pioneering work of Tentorio and Casolo-Ginelli introduced a reticulated, three-dimensional electrode by metallizing polyurethane foams via

an electrochemical process [145]. A subsequent review in 2009 highlighted the potential of reticulated vitreous carbon as an innovative carbon material for battery applications [146].

One of the key advantages of RVC foams is their exceptionally high void volume, which can reach up to 97 %, enabling electrochemically active species to permeate the structure and thus achieving high volumetric energy densities. Moreover, the rigid and robust nature of RVC enables it to withstand the battery operating temperatures around 100 °C. Additionally, RVC foams are cost-effective, readily available, and can potentially be derived from sustainable sources. They also exhibit chemical inertness against a wide array of substances, including halides, making them particularly versatile for various applications. Further supporting their versatility, kinetic studies by Mastragostino and Gramellini demonstrated the effectiveness of vitreous carbon electrodes when paired with the bromine/bromide redox couple in aqueous solutions [147]. Despite their lower conductivity compared to metals, RVC foams are the focus of this section due to their aforementioned advantages.

This section aims to introduce the concept of three-dimensional electrodes and to propose an enhanced cathode architecture specifically tailored for sodium-iodine batteries. Addressing a notable gap in the existing literature, the current study seeks to identify an optimized cell design through spatially resolved electrochemical simulations of glassy carbon foam electrodes. The insights gained from this research are anticipated to contribute significantly to the development of advanced aqueous iodine cathodes with superior reversible efficiency and power density.

3.5.1 Mathematical modeling of foam electrode structures

Reticulated vitreous carbon foams, known for their high volumetric porosity and chemical inertness, are utilized as cathode structures in batteries. To fully understand their impact on battery performance, it is crucial to quantitatively characterize these foam properties. The key characteristics of the foam structures include porosity (ϵ) and surface area per unit volume (a_s). The mathematical modeling of a Kelvin foam structure is accomplished by subtracting a sphere from Kelvin's conjecture. Porosity, defined as the ratio of the empty volume fraction to the total volume, ranges between 0 and 1:

$$\epsilon = \frac{V_{\text{empty}}}{V} \tag{3.39}$$

Since the Kelvin unit cell is both packable and symmetric in every direction [148], it is sufficient to analyze a single unit cell. Figure 3.12 presents the Kelvin cell as well as the Weaire-Phelan unit cell and the foam unit cell utilized in this study, which will be further developed in this section.

In the process of mathematical modeling, the volume of the Kelvin unit cell, also referred to as truncated octahedron in its uncurved variant, is considered equivalent to the total volume

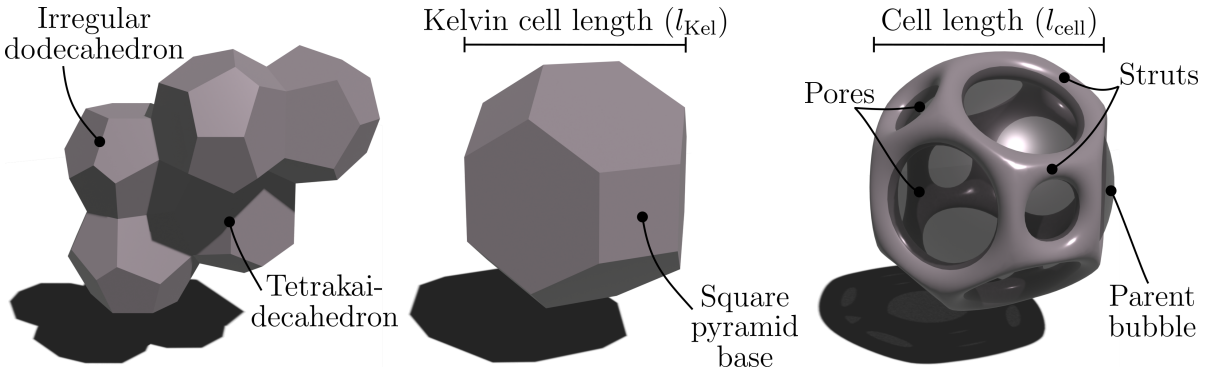

(a) Weaire-Phelan unit cell **(b)** Kelvin unit cell **(c)** Smoothed open-pored foam unit cell

Figure 3.12: Comparison of the Weaire-Phelan unit cell **(a)**, the Kelvin unit cell **(b)**, and the foam unit cell used in this work **(c)**.

($V = V_{Kel}$). The volume of the Kelvin cell is then calculated by subtracting the volumes of six square pyramids, each with a height h, from the volume of a regular octahedron [149]:

$$V_{Kel} = V_{octahedron} - 6V_{square\ pyramid} = 8\sqrt{2}\left(\frac{l_{pyramid}}{3}\right)^3 \tag{3.40}$$

A regular octahedron, classified as a Platonic solid, comprises eight identically sized equilateral triangles and is formed by joining two square-based pyramids with equilateral sides. The void space of the Kelvin foam structure calculates from the spherical parent bubble $V_{bub,Kel}$ by subtracting the volumes of 14 sphere caps V_{cap} which protrude the truncated octahedron sides:

$$V_{empty} = V_{bub,Kel} - 8V_{cap,hexagon} - 6V_{cap,square} \tag{3.41}$$

The spherical cap volumes depend on the parent bubble diameter l_{bub}:

$$V_{cap} = \frac{\pi h^2}{3}\left(\frac{3}{2}l_{bub}\right) \tag{3.42}$$

The specific surface area a_s describes the total surface area per bulk volume which, in the case of a Kelvin foam structure, takes the form:

$$a_{s,foam,Kel} = \frac{S_{foam,Kel}}{V_{Kel}} \tag{3.43}$$

The total surface area is obtained by subtracting the curved areas of the 14 spherical caps from the parent bubble surface

$$S_{foam,Kel} = S_{bub,Kel} - 8S_{cap,hexagon} - 6S_{cap,square} \tag{3.44}$$

with $\{S_{\text{cap,hexagon}}, S_{\text{cap,square}}\} \in \mathbb{R}_{\geq 0}$. The curved area of a spherical cap is calculated by [150]:

$$S_{\text{cap}} = \pi l_{\text{bub}} h \tag{3.45}$$

3.5.2 Comparison between simple and three-dimensional foam cathode design[3]

The forthcoming sections, sections 3.5.2 and 3.5.3, present the model-predicted impacts of three-dimensional glassy carbon foam cathode electrodes on battery performance. Glassy carbon, known for its inertness and high electrical conductivity, is a prevalent material for battery electrodes and serves as the current-collecting foam material in the investigations detailed herein [131].

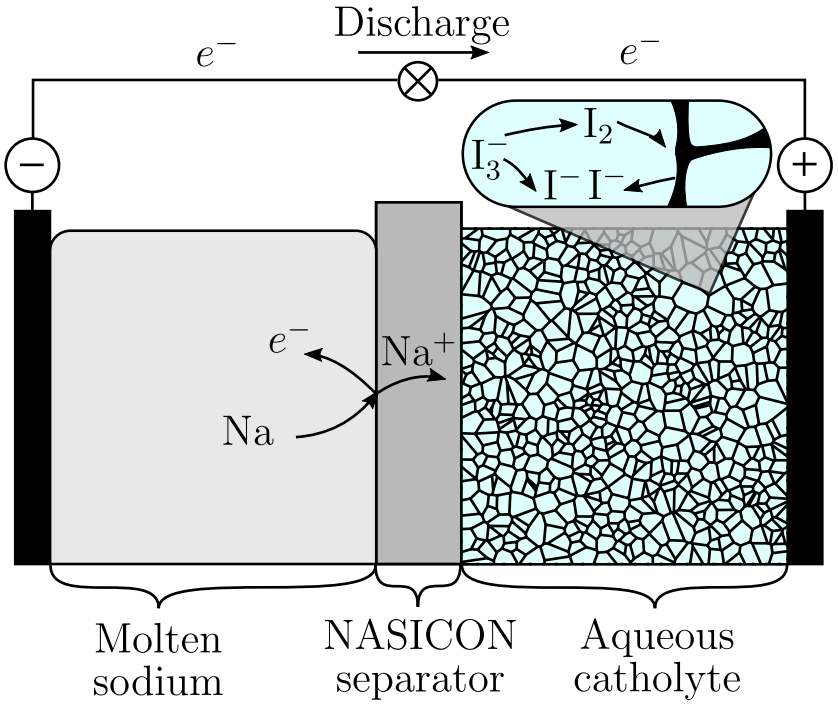

Figure 3.13: Working principle of a NaI battery with a three-dimensional glassy carbon foam electrode.

The simulations were performed on a hex-dominant computational grid comprising approximately two million cells, with a nominal cell size of 2.5×10^{-4} m in the bulk electrolyte. To enhance accuracy in regions with steep gradients, local grid refinement was applied, reducing the cell size to 30 µm. The time step used in the simulations varied between $\Delta t = 1$ s and $\Delta t = 10$ s, depending on the C-rate. This time step was kept significantly smaller at the beginning and end

[3] This section includes results and findings that were previously reported in Gerbig, F., Cernak, S., and Nirschl, H.: Towards a Novel Sodium-Iodine Battery with an Aqueous Catholyte: Numerical Investigations of Complex Cathode Structures. *ECS Transactions*, **2021**, 104(1), 123–130. DOI: 10.1149/10401.0123ecst

of the charge-discharge cycles to adequately capture the more pronounced changes in potential during these phases.

Section 3.4 explored a two-dimensional cathode design for sodium-iodine batteries, utilizing a vertically oriented, round-shaped titanium disc. While this design provided a basic approach to evaluating battery performance, it was limited by the constrained surface area available within the cathode compartment, which impacted the effective utilization of active species.

To address this limitation, this section introduces a preliminary study employing a Kelvin cell design to model a reticulated vitreous foam structure. Figure 3.13 depicts the working principle of a NaI battery utilizing this type of electrode structure. The approach is intended to demonstrate the potential of foam structures in overcoming the surface area constraints of two-dimensional designs. Incorporating a foam structure allows for an evaluation of its general capability to enhance battery performance by providing a more extensive and evenly distributed surface area.

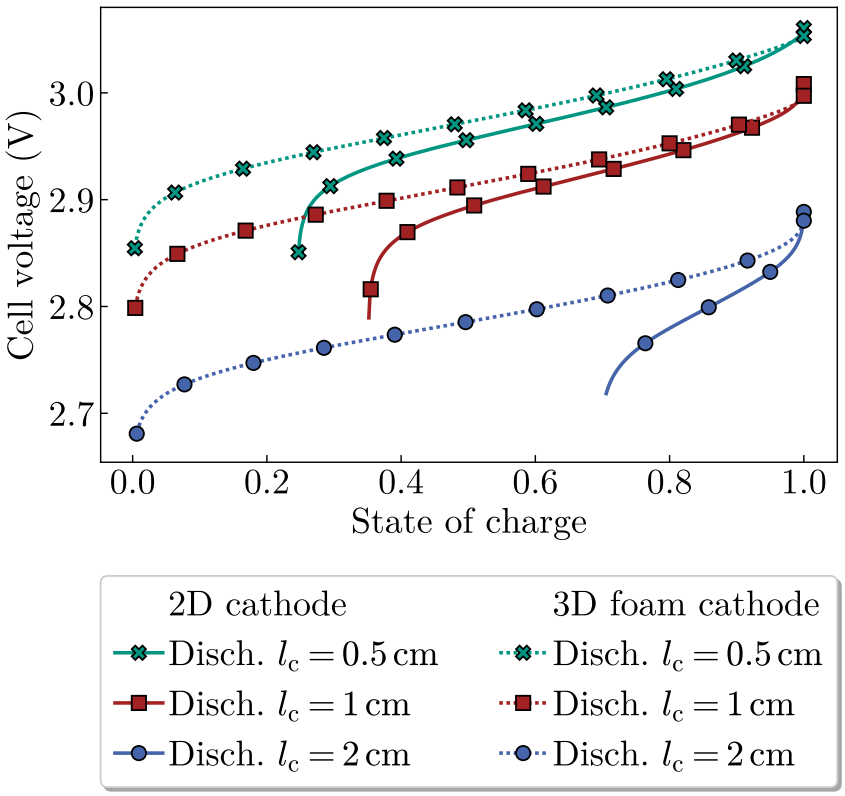

Figure 3.14: Comparison of cell voltage curves between a two-dimensional cathode design versus a foam structure constructed from Kelvin unit cells, each with a length of 1 mm. The curves depict the performance during a the C/5 discharge, with initial electrolyte concentrations corresponding to [I] = 8.3 M in the fully discharged state.

Figure 3.14 presents a comparative analysis of discharge curves for two distinct cell designs, each evaluated at various cathode compartment lengths l_c under a C-rate of 1/5. The discharge process initiates from a fully charged state and is halted as soon as the concentration of sodium iodide (NaI)

or iodine (I_2) in the electrolyte surpasses the solubility limit. The initial species concentrations at full charge are determined based on iodine solubility relations as detailed in [124, 130].

As the cathode compartment length increases, the duration of discharging decreases for the two-dimensional cell design, leading to earlier termination of the discharge process. In contrast, the discharge simulations for the cell design incorporating a glassy carbon foam structure, based on Kelvin's conjecture, approach nearly complete discharge states, reaching a state of charge (SoC) close to zero. Notably, within this foam-based design, variations in cathode compartment length do not significantly affect the attainable SoC, although they do influence the cell voltage.

When maintaining a constant C-rate, the external current density scales proportionally with the volume of the electrolyte. Consequently, cells with thicker cathode compartments exhibit increased ohmic resistance and higher overpotentials. This results in a reduction in cell voltage for such designs.

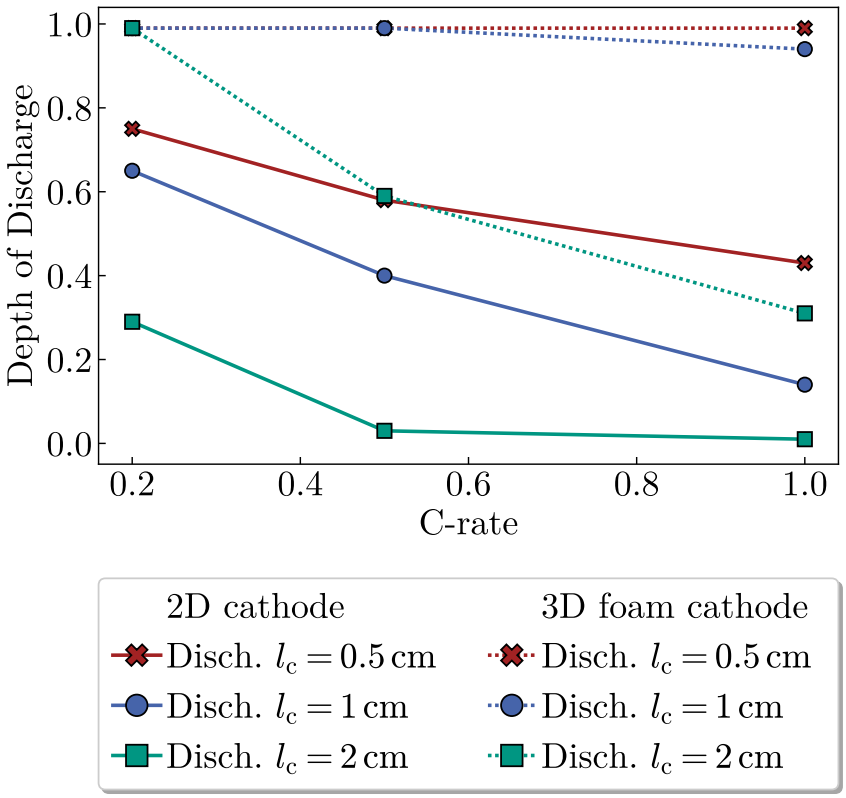

Figure 3.15: Comparison of cell performance between a two-dimensional cathode design versus a foam structure constructed from Kelvin unit cells, each with a length of 1 mm. The figure illustrates the depth of discharge achieved for various cathode compartment lengths (l_c) and C-rates. The initial electrolyte concentrations correspond to [I] = 8.3 M in the fully discharged state.

Figure 3.15 illustrates the achievable depth of discharge (DoD) during the discharge process across various C-rates and cathode compartment lengths. This analysis compares the performance between the conventional two-dimensional cathode design and the foamy cathode design.

The results reveal that the two-dimensional cathode design leads to insufficient DoD in the majority of the simulation scenarios. Specifically, only at low C-rates, such as 0.2 C, and with a cathode compartment length of 0.5 cm, does the DoD exceed 0.5. In stark contrast, the implementation of the foamy cathode design significantly enhances the DoD, achieving values close to 1 for cathode compartment lengths of 0.5 cm and 1 cm in the whole 0–1 C range.

For the battery with a cathode compartment length of 2 cm, the simulations demonstrate a high utilizable capacity at a C-rate of 0.2 C. However, this capacity diminishes as the C-rate increases, indicating a notable decrease in performance under higher discharge rates.

3.5.3 Quality assessment and characterization of virtually produced foam electrode structures

After establishing that three-dimensional electrodes can significantly enhance battery performance in preliminary simulations, the subsequent section delves deeper into the specific effects of varying these foam structures. By systematically altering the virtual foam architecture, we aim to assess its influence on key performance metrics of sodium iodine batteries. The primary goal of this investigation is to identify the optimal cathode electrode configuration that maximizes the efficiency, capacity, and overall performance of the battery system, providing critical insights for the development of next-generation energy storage solutions.

To optimize the performance of sodium iodine batteries, it is crucial to first understand the influence of directly controllable variables on key structural parameters, specifically the specific surface area (A_{sp}) and porosity.

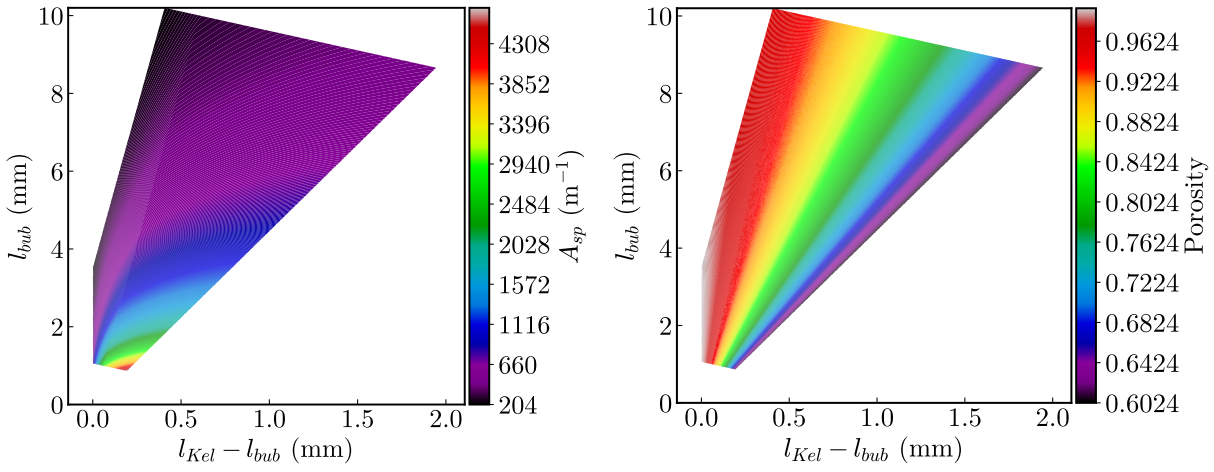

(a) Specific surface area

(b) Porosity

Figure 3.16: Specific surface area **(a)** and porosity **(b)** of open-pored foam structures based on Kelvin's conjecture

Figure 3.16 visually represent the relationship between these parameters and the parent bubble size (l_{bub}), as well as the difference between the Kelvin cell length and the parent bubble size ($l_{\mathrm{Kel}} - l_{\mathrm{bub}}$). In this context, this difference can be interpreted as the shell thickness of the foam bubbles.

These values are derived from the geometric equations governing Kelvin's conjecture, as discussed in section 3.5.1. It should be emphasized that the shell thickness is limited within a specific range to ensure the foam structure remains mechanically stable (lower bound) while still producing open pores (upper bound). In battery applications, it is generally accepted that both a high specific surface area and high porosity are advantageous. Specifically, high porosity indicates that the cathode electrode structure occupies less space, thereby allowing a larger volume for the electrolyte, which in turn enhances the energy density of the battery. Meanwhile, a high specific surface area reduces overpotentials and lowers specific molar production rates at the electrode surface, potentially preventing early battery cycling termination due to the local depletion or precipitation of molar species.

Both porosity and specific surface area are widely recognized as critical parameters in the literature, particularly in homogenized battery models where they account for the battery's microstructure and morphology [152, 153]. Figure 3.16b demonstrates that increasing the parent bubble size while maintaining a constant shell thickness (moving up along the y-axis) results in higher porosity, but at the expense of a lower specific surface area (fig. 3.16a). Conversely, increasing the shell thickness (progressing along the x-axis) enhances the specific surface area while reducing porosity. Consequently, it is impossible to maximize both properties simultaneously; improving one will inevitably lead to a decrease in the other.

The relevance of the simulation results for real batteries is validated by first comparing the virtual foams with experimentally produced glassy carbon foams, created by co-authors [133]. In fig. 3.17, a µCT scan reconstruction reveals the structure of an open-pored glassy carbon foam.

The glassy carbon foam synthesis was based on a commercially available polyurethane-based filter foam with a pore density of 10 ppi. The process involved repeated impregnation of the foam with a phenol-formaldehyde resin (molar ratio 1:2.5) followed by drying. The impregnated foam was then heated under argon, with the temperature gradually increased at $5\,\mathrm{K\,min^{-1}}$ up to 300 °C, then at $10\,\mathrm{K\,min^{-1}}$ to 600 °C, and finally at $20\,\mathrm{K\,min^{-1}}$ to 1350 °C. This temperature was maintained for 5 h before allowing the foam to cool naturally to room temperature.

The resulting glassy carbon foam structure featured large parent bubbles, each subdivided into about nine smaller, similarly sized pores. The pore size measured approximately 2.5 mm, with parent bubbles around 4 mm in size. This comparison confirms that the virtual foam model in this work accurately reflects the physical characteristics observed in real foams, thus supporting its use in predicting battery performance for practical applications.

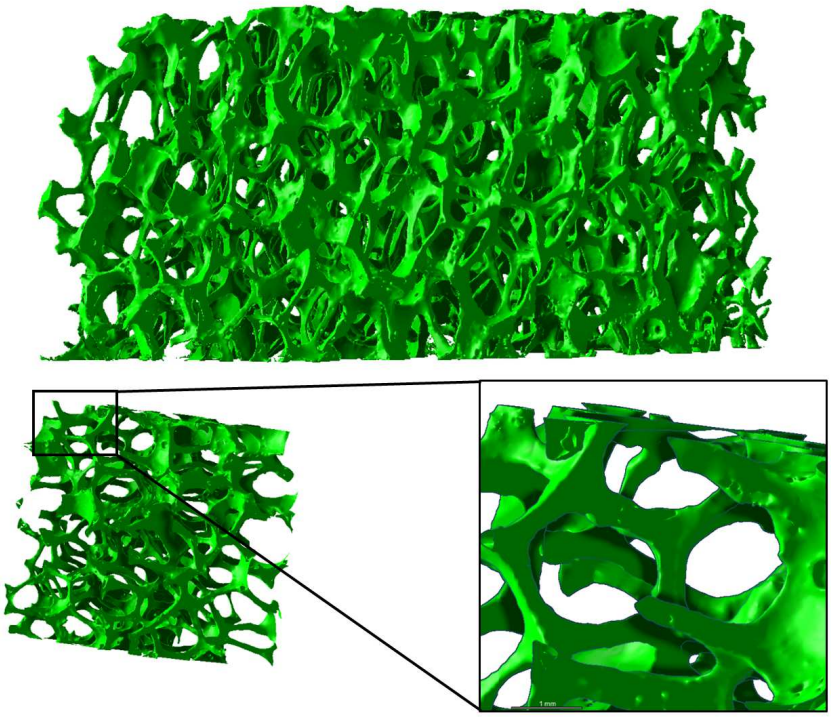

Figure 3.17: µCT imaging of a glassy carbon foam [133]

The basic structure of the experimentally produced foam aligns well with the foam unit cell derived from Kelvin's conjecture. However, µCT scans reveal some discrepancies: the struts in the real foam are noticeably thicker than those in the Kelvin cell-based virtual foam structures. In addition, the edges of the real foam, especially around the pores, are less sharp compared to the virtual Kelvin foam cells. This difference is largely due to the solidification process of the material, which thickens the foam junctures in the experimentally manufactured foam.

To create a more realistic unit cell that better represents these characteristics, further refinement is necessary. The Blender® software package provides algorithms specifically designed to manipulate and smooth virtual shapes, which were applied to the Kelvin cell foam structures [154]. A wireframe structure was generated from the original mathematical unit cell, utilizing subdivision surface modeling methods based on the Catmull-Clark algorithm [155]. This approach was applied to soften sharp corners, enhance the thickness of struts, and strengthen the connections within the foam architecture.

Figure 3.18 presents a comparison between a foam based on the original Kelvin unit cells and one based on the smoothed unit cells. A qualitative assessment reveals that the smoothed cells more accurately capture the key features of the glassy carbon foams. By applying these smoothing algorithms, the virtual foam structure is significantly enhanced, bringing it closer to a realistic representation of glassy carbon foam. Consequently, the following studies are based on this refined and smoothed virtual cell design.

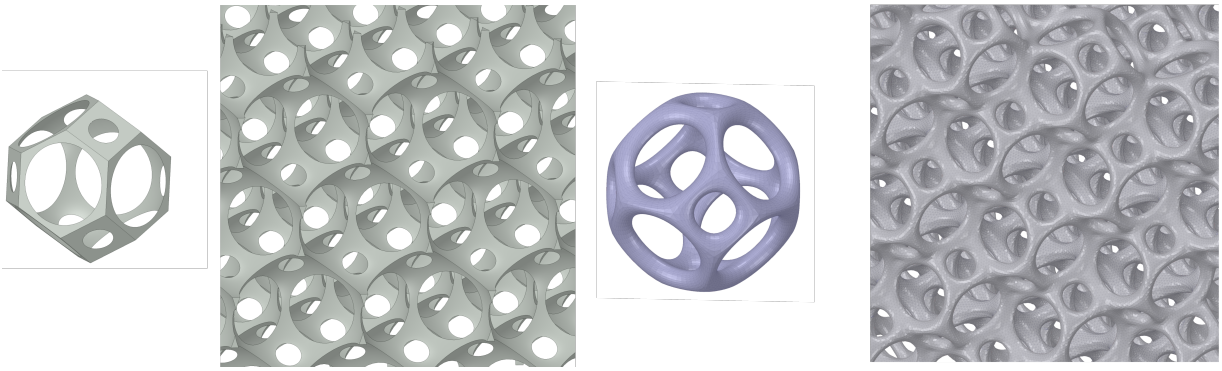

(a) vrtual foam: Kelvin cells **(b)** virtual foam: smoothed cells

Figure 3.18: Comparison between foam structures based on the Kelvin cell **(a)** and foam structures with additional manipulation and smoothing **(b)**.

Using the previously described method, twelve distinct smoothed virtual foam structures were generated by varying the thickness of the strut and cell size, with the cathode compartment length consistently fixed at 2 cm.

Table 3.4: Characteristics of smoothed virtual foam structures based on Kelvin's conjecture

d_{strut} (mm)	l_{cell} (mm)	ϵ (%)	A_{sp} (m^{-1})
0.1	10	97.4	150.6
0.05	5	97.4	375.1
0.02	2	97.4	743.4
0.01	1	97.4	1479.5
1.0	10	86.1	297.7
0.5	5	86.1	744.7
0.2	2	86.1	1479.4
0.1	1	86.1	2990.1
2	10	64.6	397.5
1	5	64.6	993.9
0.4	2	64.6	1969.6
0.2	1	64.6	3982.9

Table 3.4 provides a detailed overview of the porosity and specific surface area for each of these virtual foam structures. The data reveals two key trends:

First, porosity is directly influenced by the diameter of the strut, which decreases as the diameter of the strut increases. The structure with the thinnest strut in this study achieves the highest porosity at 97.4 %, while the structure with the thickest strut exhibits a porosity approximately

40 % lower. These two cases represent the extremes of porosity achievable using this method, with sensible strut thicknesses and pore sizes.

Second, the specific surface area exhibits an inverse relationship to porosity, increasing with both strut diameter and the number of cells. The foam structure with a 1 mm cell size and the largest strut diameter demonstrates a specific surface area approximately 26 times greater than that of the structure with the lowest surface area. These findings underscore the impact of structural variations on the key parameters of porosity and specific surface area.

3.5.4 Performance analysis of NaI batteries featuring smoothed virtual foam electrodes

Foam electrode discharging characteristics

Building on the structural analysis of the smoothed virtual foams, this section delves into the discharge behavior of sodium-iodine batteries equipped with three-dimensional Kelvin-cell-based foam electrodes. By systematically varying foam properties such as porosity and cell size, the analysis aims to elucidate how these factors influence key performance metrics, including volumetric capacity and depth of discharge (DoD). This investigation is crucial for optimizing the electrode architecture to maximize battery efficiency and longevity.

Figure 3.19 illustrates the termination states for a galvanostatic C/4 discharge process across the twelve foam structures detailed in table 3.4. The solid lines indicate volumetric capacity, plotted on the primary y-axis, while the dashed lines represent the corresponding depth of discharge (DoD) on the secondary y-axis. Different markers and line colors differentiate the porosity levels of the associated foam structures.

The foam structure with the highest porosity, nearly reaching a fully discharged state, consistently achieves DoDs greater than 0.9 across all cell sizes. In contrast, the foam with 86.1 % porosity reaches near-complete discharge for foam cell sizes of 1 mm and 2 mm, yet falls short by about 0.1 in DoD compared to the more porous foam for larger cell sizes. The densest foam, with 64.6 % porosity, achieves an acceptable DoD greater than 0.9 for the smallest cell size but experiences a decline to around 0.8 for the largest simulated foam cell size of 10 mm.

The observed drop in volumetric capacity from the most porous to the densest foam is more pronounced than the drop in DoD. This is because denser foams carry less electrolyte, resulting in a lower theoretical maximum capacity. Consequently, the usable volumetric capacity for the most porous foam structure is approximately $100\,\mathrm{A\,h\,L^{-1}}$, while it more than halves for the densest foam structure, which still achieves a DoD of 0.6 for a cell size of 10 mm. The performance of the foam structure with 86.1 % porosity lies between these extremes. For comparison, the

theoretical capacity of a cathode without a glassy carbon foam and filled solely with electrolyte is $117\,\mathrm{A\,h\,L^{-1}}$.

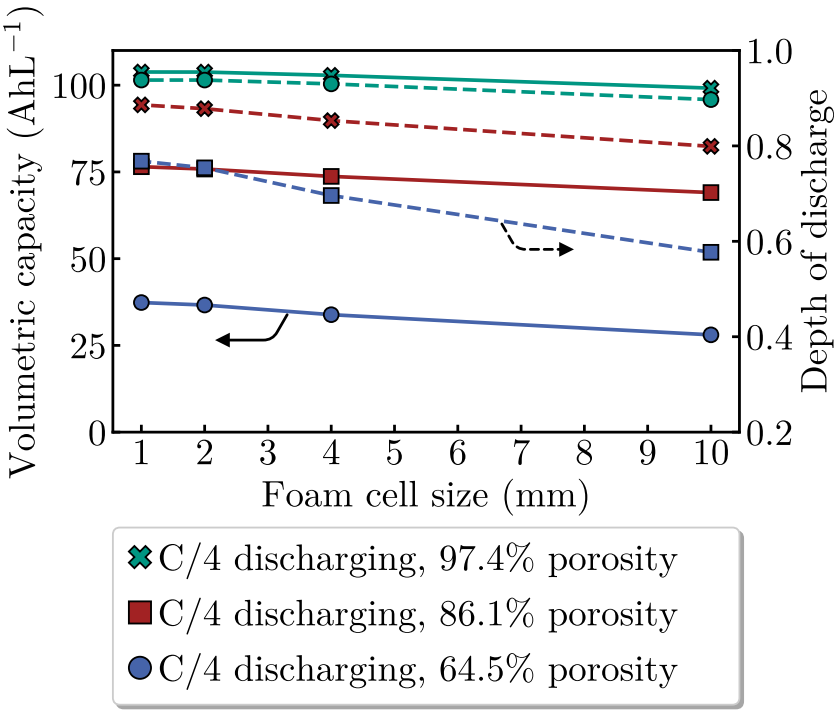

Figure 3.19: The solid lines illustrate the utilizable volumetric capacity of a sodium-iodine battery using glassy carbon foam structures as current collectors, while the dashed lines indicate the corresponding depth of discharge as a function of foam cell size. Under **C/4 discharge** conditions, green lines represent a foam porosity of 97.4 %, red lines correspond to a porosity of 86.1 %, and blue lines denote a porosity of 64.6 %.

The same discharging process for a C-rate of 0.5 is laid out in fig. 3.20. The discharge process at a C-rate of 0.5, as shown in fig. 3.20, reveals generally lower achievable DoDs across all foam structures, ranging from 0.73 to 0.64 for the most porous foam structure, and from 0.4 to 0.2 for the densest foam structure.

Figure 3.21a presents the electrolyte species concentrations averaged along the axis between the separator and cathode current collector during a C/2 discharge process for a foam cell size of 10 mm. Notably, the iodine concentration is three orders of magnitude smaller than other species concentrations, necessitating its representation on the secondary y-axis. It is evident that the iodine concentration near the cathode current collector decreases with increasing foam porosity—down to 1×10^{-3} M for the most porous foam compared to 5×10^{-3} M.

The foam structure with 97.4 % porosity, possessing the smallest surface area, exhibits the highest electric potential drop within the glassy carbon foam. This can be attributed to the thinner struts in highly porous foams, which require greater electric potential gradients to drive the same electric current across the cathode cell. Consequently, the Butler-Volmer reaction primarily

occurs near the cathode current collector, where iodine is consumed. More critically, the sodium ion concentration near the NaSICON separator locally exceeds 11.3 M, leading to sodium iodide precipitation, which poses a significant risk of irreversible damage to the separator. Notably, the axis-averaged sodium ion concentration in fig. 3.21a is lower, underscoring the ability of spatially resolved simulations to predict local exceedances of solubility limits.

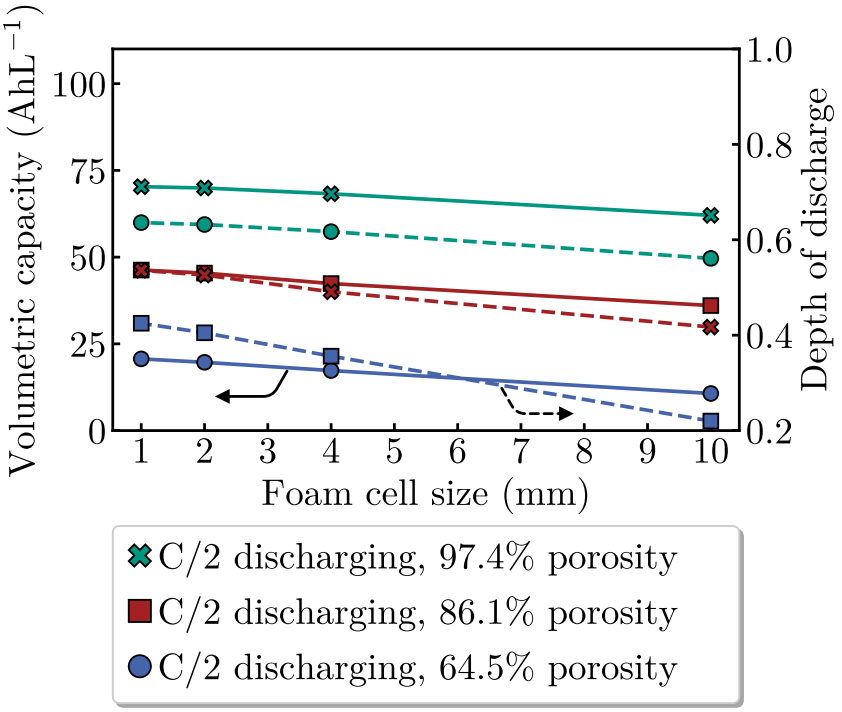

Figure 3.20: The solid lines illustrate the utilizable volumetric capacity of a sodium-iodine battery using glassy carbon foam structures as current collectors, while the dashed lines indicate the corresponding depth of discharge as a function of foam cell size. Under **C/2 discharge** conditions, green lines represent a foam porosity of 97.4 %, red lines correspond to a porosity of 86.1 %, and blue lines denote a porosity of 64.6 %.

Overall, the DoD tends to decrease with increasing cell size and decreasing porosity. Smaller cell sizes are advantageous due to the higher specific surface area of the glassy carbon foam, which enhances the Butler-Volmer surface reaction. However, increasing surface area by reducing porosity negatively impacts achievable DoD. The smaller pores in denser foams, despite a constant cell size, impede sodium ions from traveling through the cathode compartment toward the cathode current collector. This results in a higher concentration of sodium ions near the separator, which exceeds the solubility limit of sodium iodide and leads to premature termination of the discharge process.

The performance of denser foams deteriorates further when considering their porosity and comparing the capacities of different structures, as shown in figs. 3.19 and 3.20. Denser foams occupy more space with glassy carbon, thereby reducing their theoretical capacity compared to thinner foams from the outset.

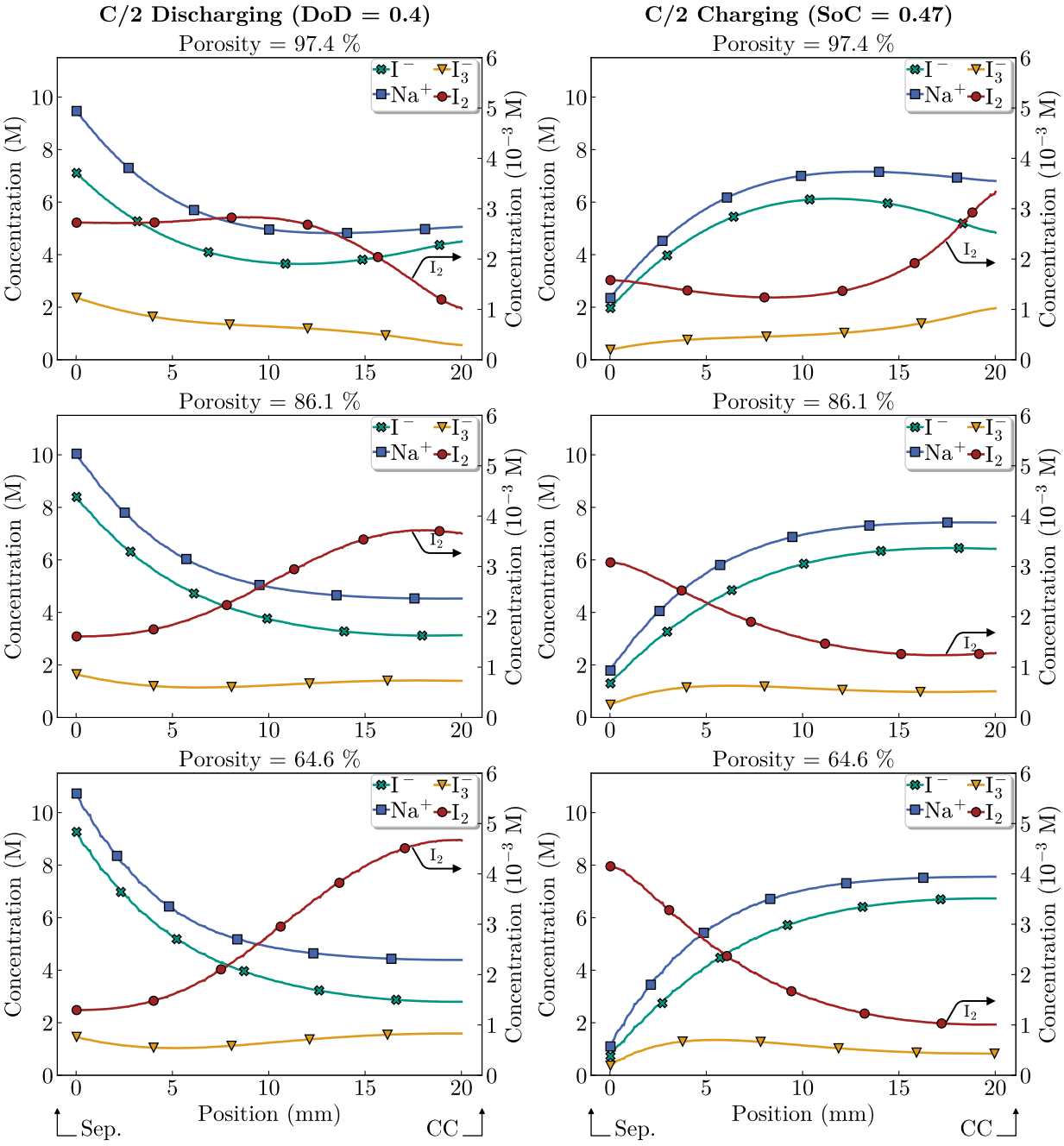

(a) Concentrations of electrolyte species simulated during an initial **C/2 discharge** for a 2 mm cell. The concentrations of the catholyte species are averaged across the region between the separator and the cathode current collector (CC).

(b) Concentrations of electrolyte species simulated during an initial **C/2 charge** for a 2 mm cell. The concentrations of the catholyte species are averaged across the region between the separator and the cathode current collector (CC).

Figure 3.21: Simulated concentrations of electrolyte species for a 2 mm cell size during different operational phases.

Foam electrode charging characteristics

Following the discharge analysis, this section focuses on the charging behavior of sodium-iodine batteries with three-dimensional Kelvin-cell-based foam electrodes. It examines how foam

properties influence the state of charge (SoC) and volumetric capacity, providing critical insights for optimizing the charging process to enhance battery performance.

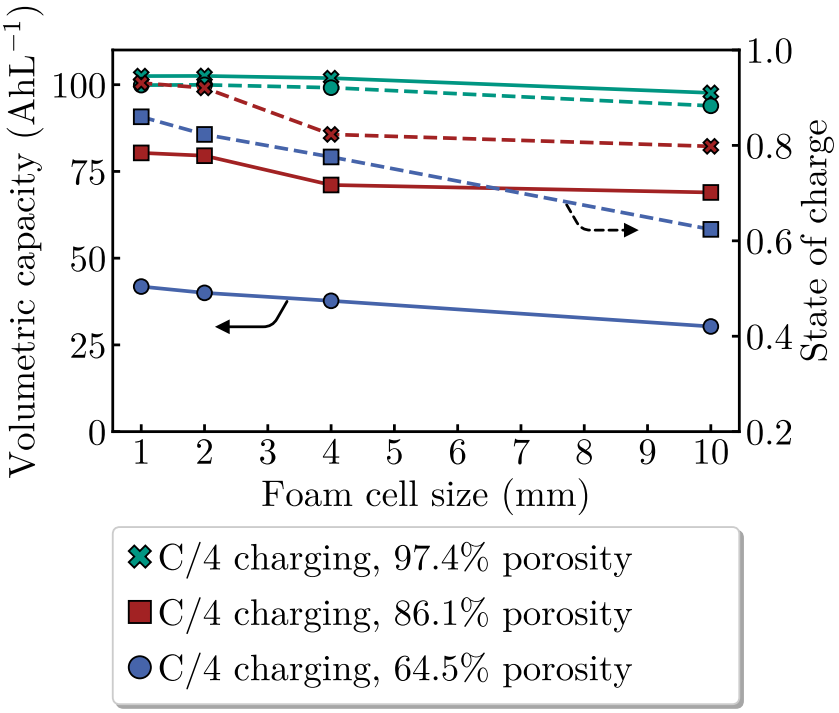

Figure 3.22: The solid lines illustrate the effective volumetric capacity of a sodium-iodine battery using glassy carbon foam structures as current collectors, while the dashed lines indicate the corresponding state of charge as a function of foam cell size. Under **C/4 charge** conditions, green lines represent a foam porosity of 97.4 %, red lines correspond to a porosity of 86.1 %, and blue lines denote a porosity of 64.6 %.

Figure 3.22 presents the charging process for the smoothed virtual foam structures previously analyzed. Charging is conducted under galvanostatic conditions at a C-rate of 0.25, and the results reveal a trend similar to the C/4 discharging process. There is a slight but consistent decrease in the achievable state of charge (SoC) across all foam structures.

For the most porous foam structure, the SoC at the end of the charging cycle decreases from 0.93 to 0.88. In contrast, the densest foam, with a porosity of 64.6 %, exhibits a later termination of the charging process compared to its discharging counterpart, reaching an SoC of 0.86 for a foam cell size of 1 mm. Similarly, the C/4 charging simulation for the same foam structure with the largest cell size of 10 mm yields nearly identical results to its discharging process, terminating at an SoC of 0.62.

The foam structure with 86.1 % porosity performs better during the C/4 charging process compared to the discharging process for foam cell sizes smaller than 2 mm, achieving SoCs greater than 0.9. However, similar to the densest foam structure, the achievable SoCs decline as the foam cell size increases. Consequently, the resulting volumetric capacities for the denser foam structures are

significantly lower than those of the more porous foams. The combination of lower achievable SoCs and reduced void volume available for electrolyte penetration results in volumetric capacities of less than 50 A h L^{-1} for the smoothed foam structures with 64.6 % porosity, whereas cathode half-cells utilizing foams with 97.4 % porosity exceed 100 A h L^{-1}.

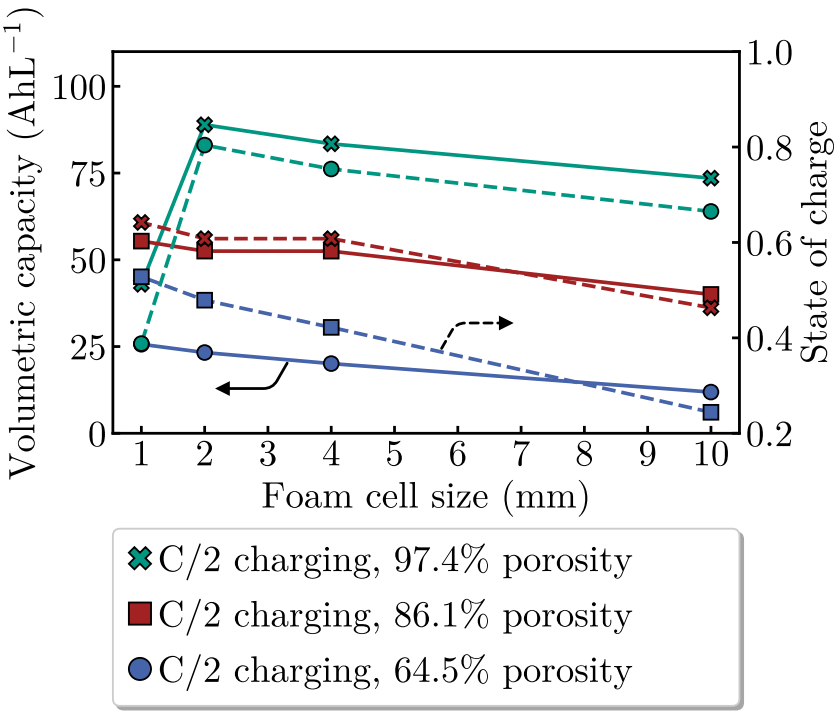

Figure 3.23: The solid lines illustrate the utilizable volumetric capacity of a sodium-iodine battery using glassy carbon foam structures as current collectors, while the dashed lines indicate the corresponding state of charge as a function of foam cell size. Under **C/2 charge** conditions, green lines represent a foam porosity of 97.4 %, red lines correspond to a porosity of 86.1 %, and blue lines denote a porosity of 64.6 %.

Figure 3.23 shows the charging process at a higher C-rate of 0.5. Here, a notable drop in achievable SoC is observed for the most porous foam structure with a 1 mm cell size, which previously performed the best, down to 0.39. The terminal SoC is significantly higher for larger foam cell sizes, ranging between 0.8 and 0.67.

The densest foam with 64.6 % porosity follows a similar trend in the C/2 charging process as observed in the C/4 charging process. The achievable SoC for the charging process with small cell sizes is higher than during discharging at the same C-rate. Batteries with larger cell sizes (> 4 mm) exhibit similar behavior during both the charging and discharging processes. Unlike the densest foam structure, batteries utilizing a foam structure with 86.1 % porosity achieve SoCs that are 0.1 to 0.05 higher during charging compared to discharging at C/2, with a slightly steeper decline for larger foam cell sizes.

For the charging process, fig. 3.21b illustrates the electrolyte species concentrations averaged along the axis perpendicular to the separator and the cathode current collector. The figure captures the concentration distribution at the same SoC for all porosities, equivalent to the terminal SoC of 0.47 achievable for the densest foam structure (fig. 3.23). The spatial distribution of mobile species indicates that the elemental iodine-to-sodium-ion ratio locally drops below $[I_{tot}]/[Na^+] < 0.475$ near the separator. This imbalance leads to the precipitation of iodine and potential dendrite formation, posing a risk of damaging the NaSICON ceramic separator, which serves as the barrier between the molten sodium and the aqueous electrolyte.

The three-dimensional simulations reveal that, contrary to initial expectations, species transport to and from the electrode surface within the foam cell does not present a significant limiting factor for battery performance. Both discharging and charging analyses highlight that the critical challenge lies in the efficient transport of sodium ions from the NaSICON separator throughout the cathode half-cell.

3.6 Revisiting assumptions in iodine/iodide aqueous solutions: a model-experiment comparison

This section evaluates key model assumptions related to solubility limits and reaction mechanisms within the iodine/iodide aqueous solution to enhance the accurate modeling of sodium-iodine batteries as a critical tool in advancing this battery technology. To achieve this, the strategy involves comparing experimentally obtained polarization curves with the predictions made by the developed model. The experimental data were collected during initial investigations using a prototype with a defined electrode surface, conducted by Frank Schäfer at Fraunhofer ICT. However, obtaining more comprehensive data was challenging due to several factors inherent to the system under investigation. Specifically, the high vapor pressure of the catholyte, the need to operate at elevated temperatures, and the corrosive nature of the iodine-based solution made it difficult to maintain the integrity of the prototype and minimize mass loss during lab-scale testing. These challenges limited the amount of experimental data, which is why the present comparison serves as a preliminary validation rather than a thorough, in-depth verification of the simulations. More extensive testing and optimization at the lab scale will be necessary in future work to fully validate the physical model.

Experimentally, a specific capacity of approximately $200\,\mathrm{A\,h\,L^{-1}}$ was observed, which surpasses the maximum theoretical capacity traditionally assumed when adhering to the solubility limits reported by Goldstein for sodium iodide solutions [124]. To reconcile the experimental data with the model predictions, one approach involves modifying the solubility constraints. By reducing the initial sodium-ion concentration $[Na^+]_0$ at the fully charged state, the theoretical capacity can

be increased, as it is directly proportional to the difference between the sodium-ion concentration in the fully charged and fully discharged states.

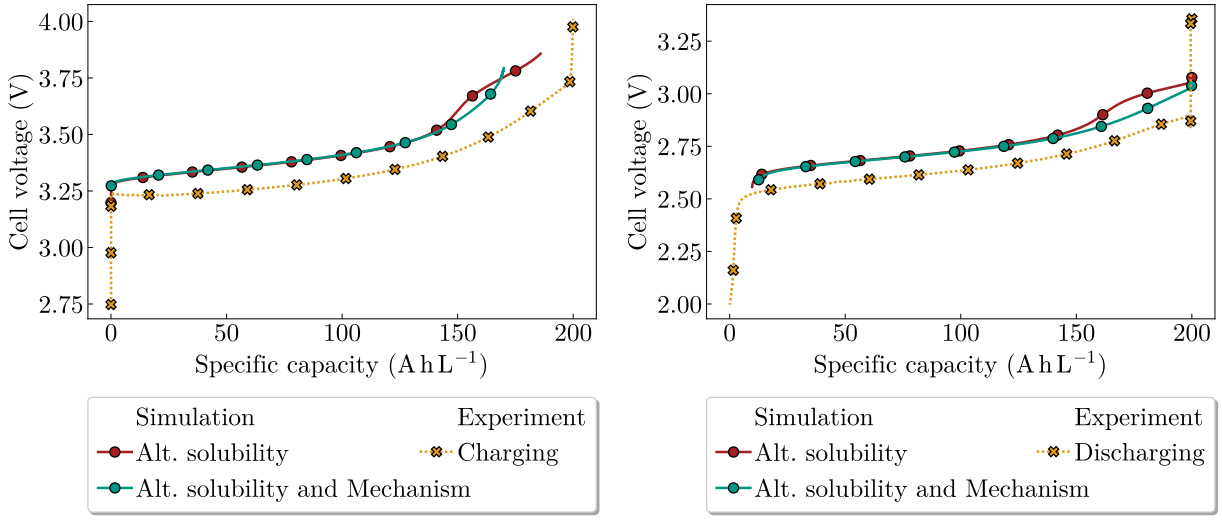

(a) Charging **(b)** Discharging

Figure 3.24: Comparison of experimentally obtained and simulated cell voltage curves for the charging and discharging processes in a sodium-iodine battery system. The experimental data (orange dashed line) is contrasted with the model predictions (green and red solid lines) under different assumptions of solubility limits and reaction mechanisms. The green line represents the simulation incorporating the revised solubility relation, while the red line includes the additional consideration of pentaiodide (I_5^-) formation. The comparison highlights the influence of solubility constraints and reaction dynamics on the overall electrochemical behavior and specific capacity of the battery.

Adjusting the model to fit the experimentally observed capacity resulted in the following expression for the minimum sodium-ion concentration in the catholyte:

$$[\mathrm{Na^+}]_{\mathrm{min}} \geq 0.137\ [\mathrm{I}] \tag{3.46}$$

The results of the experiment and the simulation during both the charging and discharging processes are depicted in fig. 3.24. The corresponding cell voltage curve, incorporating this revised solubility relation, is represented by the solid green line in the graph. Overall, a qualitative comparison indicates that the experimental and simulated curves are generally in good agreement. However, the simulated curve exhibits a higher cell potential near the fully charged state, a feature not observed in the experimental data. Specifically, in the specific capacity range of 150–200 A h L^{-1}, the slope of the simulated voltage curve exceeds that of the experimentally measured cell voltage, resulting in a noticeable inflection point in the curve.

This discrepancy is attributed to a significantly higher concentration of I_2 in this specific capacity range. During the charging process, the charge transfer reaction generates iodine, which typically recombines with iodide to form triiodide, keeping the iodine concentration relatively low. However, at a certain point, the equilibrium constant of the triiodide recombination reaction ($K_{I_3^-}$) necessitates

a substantial increase in iodine concentration, normally in the range of 1×10^{-2} M. This dramatic increase in concentration, spanning several orders of magnitude, alters the equilibrium potential governed by the Nernst equation (eq. (3.17)), leading to the observed deviation in the voltage curve.

To address the observed discrepancy in the voltage curve, one might consider revising the assumption that polyiodide formation is primarily limited to triiodide (I_3^-). The detailed reaction mechanisms within iodine/iodide aqueous solutions remain a subject of ongoing debate across various applications. A comprehensive review of this topic was recently published by Pesek and Silaghi-Dumitrescu [156]. It is plausible that higher polyiodides, such as pentaiodide (I_5^-), heptaiodide (I_7^-), and nonaiodide (I_9^-), could play a significant role in the catholyte solution of the sodium-iodine battery system under investigation.

As a first step, the potential formation of pentaiodide (I_5^-) is examined, governed by the equilibrium:

$$K_{I_5^-} = \frac{[I_5^-]}{[I_3^-][I_2]} \tag{3.47}$$

Adjusting the equilibrium constant of the pentaiodide recombination reaction ($K_{I_5^-}$) reported by Haddock et al. to the operating temperature of the sodium iodine battery yields a value of $K_{I_5^-} = 2.78\,\mathrm{mol\,m^{-3}}$ [157]. Maintaining equilibrium is achieved by assigning a sufficiently high value to the reaction rate constant (k_{f,I_5^-}), while ensuring numerical stability throughout the simulations. Therefore, incorporating I_5^- as an additional species alters the source terms in the electrolyte transport equation (eq. (3.4)) as follows:

$$r_{I_2} = -k_f\,[I_2]\,[I^-] + \frac{k_f}{K_{I_3^-}}\,[I_3^-] - k_{f,I_5^-}\,[I_2]\,[I_3^-] + \frac{k_{f,I_5^-}}{K_{I_5^-}}\,[I_5^-] \tag{3.48a}$$

$$r_{I^-} = -k_f\,[I_2]\,[I^-] + \frac{k_f}{K_{I_3^-}}\,[I_3^-] \tag{3.48b}$$

$$r_{I_3^-} = k_f\,[I_2]\,[I^-] - \frac{k_f}{K_{I_3^-}}\,[I_3^-] - k_{f,I_5^-}\,[I_2]\,[I_3^-] + \frac{k_{f,I_5^-}}{K_{I_5^-}}\,[I_5^-] \tag{3.48c}$$

$$r_{I_5^-} = k_{f,I_5^-}\,[I_2]\,[I_3^-] - \frac{k_{f,I_5^-}}{K_{I_5^-}}\,[I_5^-] \tag{3.48d}$$

Simulating the model with this revised mechanism and the alternative solubility relation produces the cell voltage curve indicated by the solid red line in the graph. Notably, within the specific capacity range of 0–150 A h L^{-1}, the inclusion of pentaiodide (I_5^-) in the model yields results consistent with the previous simulation. This is likely due to the dominance of triiodide (I_3^-) formation over pentaiodide formation, as indicated by the ratio $K_{I_3^-}/K_{I_5^-} \approx 44$. Therefore, pentaiodide formation becomes significant only at higher iodine concentrations, which occur closer to the fully charged state, corresponding to specific capacities above 150 A h L^{-1}.

In this high-capacity region, the revised simulation with pentaiodide formation shows a less pronounced increase in iodine concentration compared to the previous model. This behavior can be explained by the introduction of a secondary iodine storage mechanism through pentaiodide formation, which activates when the triiodide formation mechanism is saturated. Consequently, the previously observed inflection point in the voltage curve is less pronounced and occurs later in the charging process.

However, it is important to note that even with the adjusted reaction mechanism, the iodine concentration (I_2) near the fully charged state remains significantly higher when using the alternative solubility relation compared to the solubility limits reported by Goldstein. This raises intriguing questions about the physical plausibility of such high iodine concentrations in an aqueous solution, particularly given iodine's well-known low solubility in water. Further experimental validation and investigation into the solubility behavior of iodine under these conditions are warranted to confirm the accuracy of the model predictions.

3.7 Conclusion

The application of the microscale simulation model for sodium-iodine batteries presented in this study has yielded several significant conclusions. The model's validity is first established through a comparison with results derived from a one-dimensional model approximation, demonstrating a strong correlation that reinforces the model's reliability and accuracy.

In examining the **two-dimensional electrodes** , represented by a centrally placed titanium plate, the study reveals substantial diffusion limitations that critically undermine the efficiency of batteries designed with such a cell architecture. Specifically, it is determined that a cell thickness exceeding 1 cm is not feasible, highlighting the impracticality of using bulky electrodes in this design framework.

Among the tested configurations, an elemental iodine concentration of 8 M emerged as the most effective, offering an optimal balance between theoretical capacity and practical utilization. Notably, charge transport within the solid phase does not pose a significant limitation, provided that materials with appropriate conductivity are selected, allowing these two factors to be dismissed as a potential bottleneck in future research efforts.

The investigation into the spatial distribution of species concentrations further identifies that the primary mechanism leading to the termination of the battery's operation in the two-dimensional electrode design is local precipitation or depletion of charge-carrying species. In this context, the transport processes from the anode to the reactive surfaces within the cathode compartment are identified as the critical bottleneck in this design.

Moreover, the overpotentials observed are relatively modest, attributed to the rapid charge-transfer kinetics associated with iodide oxidation. This finding suggests that the surface area of the electrode is not a limiting factor to a significant extent. However, the study identifies a key issue in the distribution of available surface area across the positive electrode in the two-dimensional design, which emerges as a major challenge to be addressed in future developments.

The subsequent analysis of **three-dimensional electrodes** for sodium-iodine batteries shifted focus to the use of glassy carbon foams as electrode materials. Preliminary comparative simulations between the traditional two-dimensional cathode electrode design and the novel foam electrode structures demonstrated a significant enhancement in the achievable depth of discharge with the latter.

The glassy carbon foam structure was mathematically modeled using the packing of Kelvin unit cells, with additional virtual smoothing algorithms applied to closely replicate imaging data from actual glassy carbon foams. This approach was validated, confirming the accuracy of these techniques for future applications in modeling complex electrode architectures.

From a mathematical perspective, the analysis of computational foam creation revealed that efforts to maximize specific surface area inherently lead to a reduction in porosity. However, performance simulations indicated that prioritizing surface area at the cost of porosity is ultimately counterproductive for battery performance.

Crucially, the study found that larger pores relative to the foam cell size, which correlate with higher porosity, are essential for facilitating smooth sodium-ion transit between foam cells, thereby significantly enhancing battery efficiency. Conversely, reducing the cell size, which increases the surface area, produced only a modest improvement in performance, except in cases where the foam porosity was extremely high (approximately 97.4 %) and the cell sizes were smaller than 2 mm. This trend was consistent across different C-rates, during both charging and discharging processes.

These findings align with the results from studies on two-dimensional electrodes, reinforcing the conclusion that effective charge and species transport across the cathode half-cell is critical for achieving high utilizable capacities in sodium-iodine batteries.

The comparison between the initial, limited experimental data and the numerical solver results, using the same prototype geometry, raises questions about the current assumptions regarding the iodine/iodide aqueous solution. Notably, the specific capacity observed experimentally exceeds theoretical predictions by an impressive 70 %. By adjusting the model's solubility limits for the involved species, it was possible to approximate the experimentally observed capacity more accurately.

However, the inclusion of pentaiodide (I_5^-) as a catholyte species, which plays a role in the recombination reactions in the bulk electrolyte, proved necessary to reproduce the shape of the

polarization curve computationally. The formation of pentaiodide serves as an additional storage mechanism for elemental iodine, particularly near the fully charged state. This suggests that limiting the model to only I_2, I^-, and I_3^-may oversimplify the complex interactions within a highly concentrated iodine/iodide solution.

Despite this improvement, the I_2 concentration remains exceptionally high, even when accounting for pentaiodide formation, at specific capacities as elevated as $200\,\mathrm{A\,h\,L^{-1}}$. This raises doubts about whether iodine can remain dissolved at such concentrations. One plausible explanation is that the reaction mechanisms in solution are even more complex, possibly involving the formation of higher polyiodides. However, this is unlikely, as the equilibrium constant (equilibrium constant of the pentaiodide recombination reaction ($K_{I_5^-}$)) for pentaiodide is already 44 times lower than that for triiodide (equilibrium constant of the triiodide recombination reaction ($K_{I_3^-}$)).

Another possibility is that iodine precipitates in significant quantities. While the model prohibits iodine precipitation due to concerns over potential damage to the battery, particularly the separator, it is conceivable that the materials may withstand some level of precipitation over multiple cycles, leading to the observed higher capacity. To test this hypothesis, long-term experiments will be required once the battery system progresses beyond the early laboratory prototype stage.

Such findings underscore the critical role of electrochemical models in predicting the catholyte composition and ensuring safe operating conditions for the overall battery system. Long-term performance and material resilience must be investigated to validate these assumptions and optimize the system for practical use.

4 All-Solid-State Polymer-Ceramic Sodium-Ion Batteries

In the quest for advancing next-generation sodium-ion batteries, all-solid-state sodium-ion batteries have emerged as leading contenders due to their inherent safety, long cycle life, and the potential to employ sodium metal anodes. Although an increasing number of studies are experimentally examining materials and designs for all-solid-state sodium-ion batteries (ASSSIBs) (refer to section 2.1.2), theoretical methods have predominantly aimed at investigating active materials and electrolytes at the nanoscale [158, 159].

In recent years, simulation studies on sodium-ion batteries (SIBs) have primarily focused on traditional systems that utilize liquid electrolytes. For example, Xiang et al. employed equivalent circuit models to estimate the state-of-charge (SOC) and state-of-health (SOH) in SIBs, providing valuable insights into battery diagnostics and performance management [160]. Similarly, Chayambuka et al. explored the use of pseudo-two-dimensional (P2D) models in SIBs, specifically utilizing fluorinated sodium vanadium phosphate as the positive electrode material and hard carbon as the negative electrode [161]. Building on these developments, Garapati et al. introduced a reduced-order single-particle model that offers quick computation times and low computational cost while maintaining the accuracy of the more complex P2D models [162]. Jagad et al. recently introduced a one-dimensional, physics-based model for SIBs, leveraging machine learning techniques for parameter fitting, and incorporating $Na_{2/3}[Ni_{1/3}Fe_{1/12}Mn_{7/12}]O_2$ (NNFMO) as the active material [163].

However, as the focus of SIB technology shifts from liquid electrolytes to solid or hybrid systems, a new frontier of research is emerging. Solid-state and hybrid electrolytes present a different set of challenges and opportunities, particularly in the context of modeling and simulation studies [61]. Unlike liquid electrolytes, solid-state electrolytes promise enhanced safety, stability, and potentially higher energy densities. However, these benefits come with complexities that require novel simulation approaches. Accurate modeling of solid-state electrolytes involves capturing the intricate electrochemical interactions at the interfaces between the electrolyte and the electrode materials, as well as understanding the transport phenomena within the solid electrolyte itself [164].

Despite extensive research efforts, as detailed in section 2.2.1, the discovery of a single-phase solid electrolyte that meets all the necessary criteria for the realization of ASSSIBs remains elusive. A promising alternative approach involves combining two types of solid electrolytes to create a composite material, as discussed in section 2.2.2. Consequently, this work centers on a composite electrolyte composed of a polyethylene oxide (PEO) polymer matrix integrated with NaSICON inorganic active fillers, chosen for their exceptional properties and potential to enhance the overall performance of ASSSIBs.

To address emerging challenges associated with the application of CSEs for sodium ion batteries, this chapter delves into the effects of cell composition on the overall performance of ASSSIBs at the particle level. For the first time, a physics-based microstructure model is employed to resolve phenomena at the particle scale, enabling a detailed investigation of how various material properties and design parameters influence the electrochemical behavior of ASSSIBs. This approach allows for the simulation of complex interactions and transport processes that occur within the battery, providing comprehensive insights into the factors that affect battery efficiency, durability, and overall performance.

Theoretically, the design possibilities for the morphology of a composite solid electrolyte (CSE) are virtually limitless. For instance, Wang et al. proposed a CSE configuration featuring a nanostructured three-dimensional NaSICON framework embedded within a PEO matrix [165]. While this approach offers the potential for enhanced ionic conductivity, it appears impractical for current battery manufacturing processes, which predominantly rely on mixing and drying techniques. In this study, both the active filler and the active material are designed as particle systems, aligning with the more feasible manufacturing practices of today.

The overall goal is to contribute to the advancement of more efficient and reliable ASSSIBs by guiding the development of materials and designs that optimize battery performance at the microscopic level.

4.1 Working principle

The working principle of the all-solid-state sodium-ion battery with a polymer-ceramic composite electrolyte, as illustrated in fig. 4.1, mirrors the operation of other intercalation-based battery technologies, such as lithium-ion batteries. This battery features a sodium metal anode, where the discharge process initiates at the anode–separator interface. During discharge, elemental sodium is consumed, leading to a decrease in sodium content within the anode compartment. Sodium ions are generated at the anode–separator interface in the molten sodium anode, then migrate through the separator, and finally enter the cathode domain.

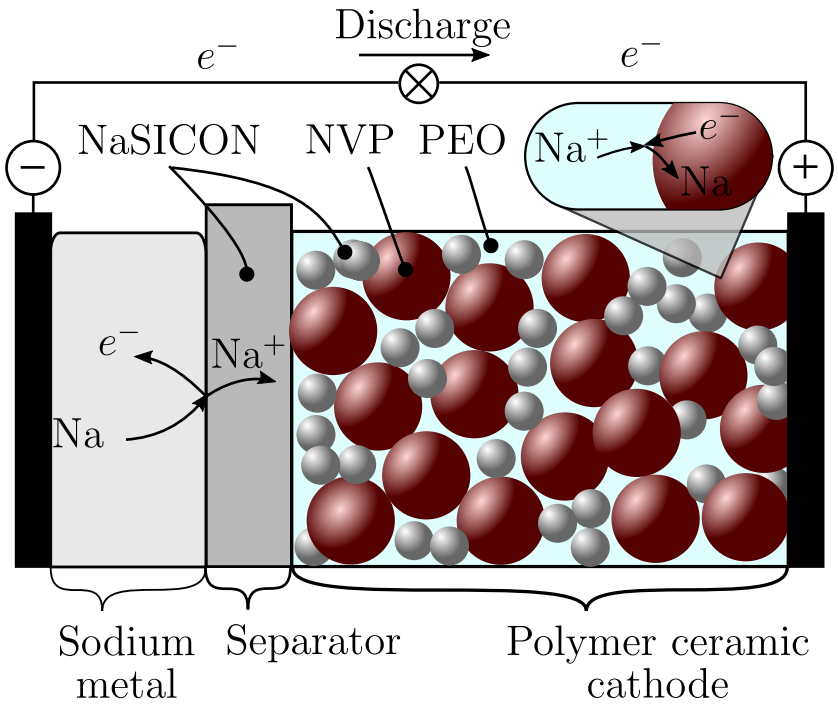

Figure 4.1: Working principle of an all-solid-state sodium-ion battery featuring a sodium metal anode and a hybrid polymer-ceramic electrolyte

In this study, the active cathode material is sodium vanadium phosphate (NVP), a polyanion-type material known for its stability, capacity, and cyclability, making it a prominent choice for SIBs [49, 50]. Notably, a recent study Park et al. reported a novel NVP material with a 15 % higher energy capacity than standard NVP, highlighting the ongoing potential for future improvements in this material [166]. The overall reaction within the sodium-ion battery is represented by:

$$Na_3V_2^{III}(PO)_4 \rightleftharpoons NaV_2^{IV}(PO)_4 + 2\,Na^+ + 2\,e^- \tag{4.1}$$

At the cathode, the insertion process involves the reaction where sodium ions intercalate into the NVP, as shown by:

$$Na\Theta_s \rightleftharpoons Na^+ + \Theta_s + e^- \tag{4.2}$$

Here, Θ_s symbolizes a site within the active material, with a typical potential of approximately 3.4 V versus Na^+/Na, involving the oxidation of vanadium from V^{3+} to V^{4+}.

The electrolyte in this battery is a composite system comprising a flexible polymer host embedded with brittle active-filler particles. The ceramic material NaSICON serves two purposes: as the active filler material within the composite electrolyte and as a separator. NaSICON is a well-known pure sodium ion conductor with high ionic conductivity, adding significant mechanical stability when used as a separator in the battery. While the solid composite electrolyte could potentially

function as a separator, the inclusion of a pure NaSICON separator is preferred to enhance the structural integrity of the battery system.

4.2 Three-dimensional model for all-solid-state sodium ion batteries

In this study, the three-dimensional simulations were conducted using the OpenFOAM software package, which operates on the finite-volume method. Although OpenFOAM was originally developed for computational fluid dynamics, its inherent versatility and open-source nature allowed for extensive customization. This customization was essential for implementing the governing equations and boundary conditions required by the electrochemical model central to our research.

The numerical solver employed in these simulations was developed by integrating elements from two distinct solvers: one designed for the sodium-iodine battery, as discussed in chapter 3, and another designed for lithium-ion batteries as described by Kespe and Nirschl [167]. This hybrid approach was carefully adapted to accurately model sodium-ion batteries with hybrid electrolytes, ensuring that the unique characteristics of these systems were effectively captured.

A key difference between the sodium-iodine battery solver and the ASSSIB model developed for this research lies in the incorporation of intercalation processes. Specifically, the ASSSIB model includes sodium (Na) transport within the active material, a critical aspect of battery operation. Additionally, the model employs concentrated solution theory to describe the potential and species distribution within a binary electrolyte system [23]. This theoretical framework allows for a more nuanced and accurate representation of the electrochemical processes occurring within the battery.

Furthermore, the model's implementation is designed with flexibility in mind, enabling it to accommodate a wide range of active materials and electrolytes. By adjusting the physical parameters, the model can be tailored to simulate different battery chemistries, making it a robust tool for studying various configurations of sodium-ion batteries.

4.2.1 Governing equations

In comparison to the all-liquid battery model outlined in section 3.2, the mathematical framework for this study introduces an additional equation that accounts for species transport within the active material. As a result, the model comprises a system of five coupled equations that collectively describe mass and charge conservation within both the insertion electrode and the electrolyte.

Similar to the equation presented in eq. (3.13), the transport of charge within the active material is governed by Ohm's law. This law defines the current density within a homogeneous, crystalline solid, where electrons are the primary charge carriers. The relationship is mathematically expressed in terms of the electrical active material conductivity (σ) and its corresponding active material potential (Φ_s):

$$\boldsymbol{i}_s = -\sigma \nabla \Phi_s \tag{4.3}$$

Although all materials in this battery setup are solid, the properties of the active materials are indicated by the subscript "s" and referred to as the solid phase to align with the nomenclature used in existing battery modeling literature. For the active material, sodium vanadium phosphate (NVP), the intrinsic electrical conductivity is quite low, approximately $3 \times 10^{-8}\,\mathrm{S\,cm^{-1}}$ as reported by [168]. To account for the enhanced conductivity typically achieved through carbon coating, the model incorporates this effect by assuming a constant, effective electrical conductivity throughout the material.

Given the assumption that electron transport occurs significantly faster than other processes within the electrode, the charge density can be considered constant over time, i.e., $\frac{\partial \rho_V}{\partial t} = 0$. This leads to a simplified equation of continuity for the solid-phase potential, which is a fundamental component of the model's charge conservation equations.

$$\nabla \cdot \boldsymbol{i}_s = 0 \tag{4.4}$$

In the solid phase, sodium ion transport is governed by Fick's first law, which states that the molar flux density of sodium is proportional to the concentration gradient. This relationship is captured by the continuity equation, which, in the context of solid diffusion, is represented by Fick's second law:

$$\frac{\partial c_s}{\partial t} = \nabla \cdot D_s \nabla c_s \tag{4.5}$$

This equation accounts for the time-dependent change in active material sodium ion concentration (c_s) depending on active material sodium diffusion coefficient (D_s), influenced by spatial concentration gradients.

The transport of sodium ions (Na^+) within the electrolyte is modeled using the concentrated solution theory, which provides a more accurate representation compared to the dilute solution theory, especially for high-concentration scenarios. The sodium ion flux in a binary electrolyte, considering both diffusion and migration, and depending on the electrolyte sodium ion diffusion coefficient (D_{el}), the transference number of sodium ions in the electrolyte (t_+^0), the electrolyte sodium ion concentration (c_{el}), the F and the $\boldsymbol{i}_{el}$ is expressed as:

$$\boldsymbol{J}_{c_{el}} = -D_{el}\left(1 - \frac{\mathrm{d}\ln c_{el,0}}{\mathrm{d}\ln c_{el}}\right)\nabla c_{el} + \frac{\boldsymbol{i}_{el} t_+^0}{F} \tag{4.6}$$

The term $1 - \frac{\mathrm{d}\ln c_{\mathrm{el},0}}{\mathrm{d}\ln c_{\mathrm{el}}}$ is known as the thermodynamic factor, which accounts for deviations from ideality in the concentration dependence of the chemical potential.

Given that the solvent velocity in solid electrolytes is typically negligible, the convection contribution is disregarded in this analysis. A more detailed derivation of this equation based on the Maxwell-Stefan relationship can be found in Plett [93]. In this study, the thermodynamic factor is set to 1, simplifying the mass-balance equation for the electrolyte to:

$$\frac{\partial c_{\mathrm{el}}}{\partial t} = \nabla \cdot D_{\mathrm{el}} \nabla c_{\mathrm{el}} - \frac{\nabla \cdot \left(\boldsymbol{i}_{\mathrm{el}} t_+^0\right)}{F} \tag{4.7}$$

Charge conservation in the electrolyte is enforced by the condition $\nabla \cdot \boldsymbol{i}_{\mathbf{el}} = 0$, indicating that the electric current density field is divergence-free. This condition is consistent with the assumption that the macroscopic model does not resolve double layer formation, expressed as $\frac{\partial \Phi_{\mathrm{el}}}{\partial t} = 0$. In a binary electrolyte, the electrolyte current density is given by

$$\boldsymbol{i}_{\mathrm{el}} = -\kappa \nabla \Phi_{\mathrm{el}} - \frac{\nu \kappa RT}{F} \left(\frac{s_+}{n\nu_+} + \frac{t_+^0}{z_+ \nu_+} - \frac{s_0 c_{\mathrm{el}}}{n c_0} \right) \nabla \ln c_{\mathrm{el}} \tag{4.8}$$

with signed stoichiometric coefficient (s_i), moles of ion i produced when a mole of its salt dissociates (ν_i), number of moles of ions into which a mole of electrolyte dissociates (ν) and the number of electrons produced by the reaction (n) [112]. This equation includes an additional diffusion term on the right-hand side, representing ion movement due to concentration gradients, which is not present in simpler formulations like Ohm's law [93]. The concentration dependence of the κ of a polymer is is modeled using a semi-empirical equation inspired by the work of Mongcopa et al. [169]:

$$\kappa\left(c_{\mathrm{el}}\right) = \kappa K_{\mathrm{NaTFSI}}(T) c_{\mathrm{el}} \left[\exp\left(-\frac{c_{\mathrm{el}}}{c_{\mathrm{el},\kappa_{\max}}(T)} \right) \right] \tag{4.9}$$

The derivation of the equation used in this work, along with the evaluation of the ionic conductivity prefactor for the PEO-NaTFSI system (K_{NaTFSI}) from experimental data reported in [170], is thoroughly explained in appendix A.1.

There are no negatively charged species involved in the reaction ($s_- = 0$), NaTFSI completely dissociates in PEO, and the solvent does not take part in the reaction ($s_0 = 0$). Also, the coefficient for Na^+ is -1 ($s_+ = -1$), and one electron is generated in the reaction ($n = 1$). Furthermore, $\nu_+ = \nu_- = z_+ = 1$ for most salts. With these assumptions and defining the electrolyte diffusional conductivity (κ_{d}) as:

$$\kappa_{\mathrm{d}} = \frac{2RT\kappa}{F}\left(1 - t_+^0\right) \tag{4.10}$$

eq. (4.8) simplifies to

$$\boldsymbol{i}_{\mathrm{el}} = -\kappa \nabla \Phi_{\mathrm{el}} + \frac{\kappa_{\mathrm{d}}}{c_{\mathrm{el}}} \nabla c_{\mathrm{el}} \tag{4.11}$$

This final equation highlights the dual influence of electric potential and concentration gradients on ion transport in the electrolyte, reflecting the complex interplay of these factors in all-solid-state sodium-ion batteries.

4.2.2 Electrochemical reaction kinetics

To accurately model the behavior of an all-solid-state sodium-ion battery, it is essential to couple the four previously introduced partial differential equations (PDEs)—namely, those governing charge conservation in the cathode eq. (4.4), sodium transport in the active material eq. (4.5), sodium transport in the electrolyte eq. (4.7), and the charge conservation in the electrolyte ($\nabla \cdot \boldsymbol{i}_{\mathbf{el}} = 0$). This coupling is achieved by introducing a fifth equation that captures the kinetics of the electrochemical reaction at the electrolyte-electrode interface.

This additional equation calculates the rate at which sodium ions are generated or consumed by the electrochemical surface reaction, a process fundamentally governed by charge transfer kinetics. These kinetics, which occur at the interface between the active material and the electrolyte, are typically described by the well-established Butler–Volmer equation [23, 171]. It takes the identical form as eq. (3.15) and is explained in detail in section 3.2:

$$i_{\mathrm{BV}} = i_0 \left[\exp\left(\frac{\alpha_a F}{RT} \left(\Phi_{\mathrm{s}} - \Phi_{\mathrm{el}} - U_{\mathrm{eq}}(c_{\mathrm{s}}) \right) \right) - \exp\left(-\frac{\alpha_c F}{RT} \left(\Phi_{\mathrm{s}} - \Phi_{\mathrm{el}} - U_{\mathrm{eq}}(c_{\mathrm{s}}) \right) \right) \right] \tag{4.12}$$

In the absence of detailed information about the specific reaction mechanisms, it is common practice to assume that the charge transfer reaction is symmetric. This assumption simplifies the model by setting the anodic and cathodic transfer coefficients α_a, α_c to 0.5. With this assumption, i_0 can be expressed as follows [112]:

$$i_0 = F k \sqrt{c_{\mathrm{s,max}} - c_{\mathrm{s}}} \sqrt{c_{\mathrm{s}}} \sqrt{c_{\mathrm{el}}} \tag{4.13}$$

In this equation, k is the Butler-Volmer reaction constant, $c_{\mathrm{s,max}}$ is the maximum concentration of sodium in the solid phase. The i_0 reflects the dynamic equilibrium of the charge transfer reaction and quantifies the rate at which electrons are exchanged at the interface when the electrode is in equilibrium. Determining the Butler-Volmer reaction constant (k) and the equilibrium potential (U_{eq}) requires experimental data, as these parameters are highly dependent on the specific materials and conditions of the battery system. The accuracy of the reaction kinetics model is crucial for predicting battery performance, especially under varying operational conditions.

4.2.3 Boundary conditions

Selecting appropriate boundary conditions is critical for solving the electrochemical model of an all-solid-state sodium-ion battery. These conditions define how the different variables—such as potentials and concentrations—behave at the interfaces and boundaries of the computational domain. The correct implementation of these conditions ensures that the model accurately represents the physical processes occurring within the battery.

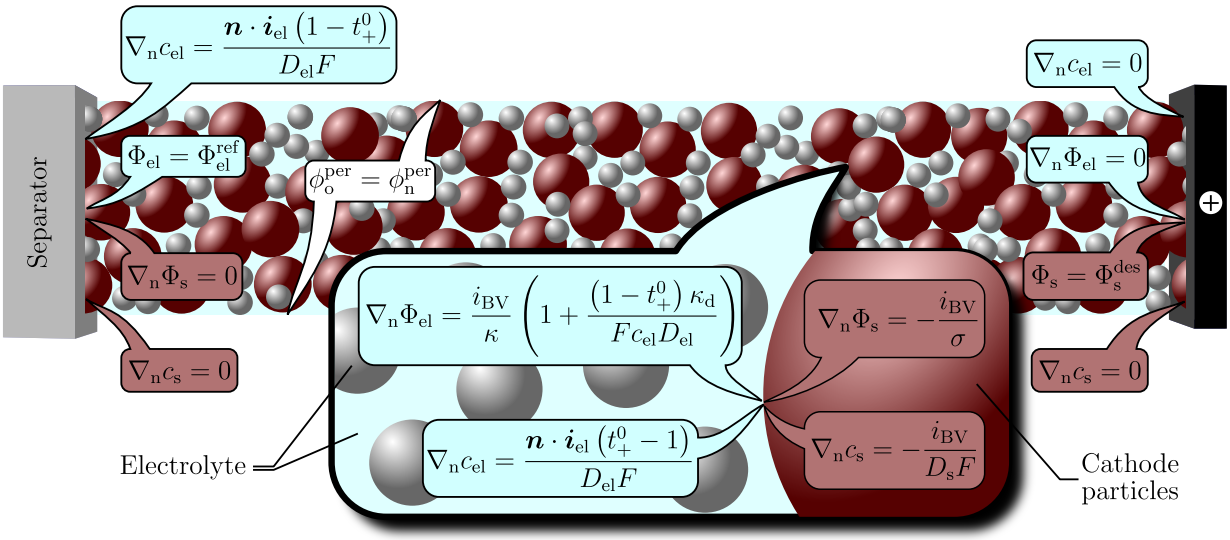

Figure 4.2: Depiction of the boundary and interface conditions used in the computational model for the cathode half-cell of a solid-state sodium-ion battery. The notation $\nabla_n \phi$ indicates the surface normal gradient, representing the dot product $\boldsymbol{n} \cdot \nabla \phi$.

Figure 4.2 provides an illustration of the boundary and interface conditions implemented in the model. The normal gradient of a scalar quantity ϕ at a surface is denoted by $\nabla_n \phi$, which represents the dot product of the surface unit normal vector pointing outside the computational domain ($\boldsymbol{n}$) with the gradient of ϕ, i.e., $\nabla_n \phi = \boldsymbol{n} \cdot \nabla \phi$.

At the cathode-to-electrolyte (cte) interface, the Neumann boundary condition is applied to the active material potential, which can be mathematically expressed as:

$$\boldsymbol{n} \cdot \nabla \Phi_s \Big|_{cte} = -\frac{i_{BV}}{\sigma} \tag{4.14}$$

The active material sodium ion concentration boundary gradient at the cte is calculated similarly, while the gradient at the separator equals zero:

$$\boldsymbol{n} \cdot \nabla c_s \Big|_{sep} = 0, \qquad \boldsymbol{n} \cdot \nabla c_s \Big|_{cte} = -\frac{i_{BV}}{D_s F} \tag{4.15}$$

Here, the zero gradient condition at the separator interface ensures no flux of sodium ions across this boundary, reflecting a physical barrier. In the electrolyte, the flux of anions is balanced by migration and diffusion, which leads to the following boundary conditions for the electrolyte concentration electrolyte sodium ion concentration:

$$\boldsymbol{n} \cdot \nabla c_{\mathrm{el}}\Big|_{\mathrm{sep}} = -\frac{\boldsymbol{n} \cdot \boldsymbol{i}_{\mathrm{el}} \left(1 - t_+^0\right)}{D_{\mathrm{el}} F}, \qquad \boldsymbol{n} \cdot \nabla c_{\mathrm{el}}\Big|_{\mathrm{etc}} = \frac{i_{\mathrm{BV}} \left(1 - t_+^0\right)}{D_{\mathrm{el}} F} \tag{4.16}$$

Substituting eq. (4.16) into the flux-density equation enables the derivation of the boundary condition for the electrolyte potential:

$$\boldsymbol{n} \cdot \nabla \Phi_{\mathrm{el}}\Big|_{\mathrm{etc}} = \frac{i_{\mathrm{BV}}}{\kappa} \left(1 + \frac{\left(1 - t_+^0\right) \kappa_{\mathrm{d}}}{F c_{\mathrm{el}} D_{\mathrm{el}}}\right) \tag{4.17}$$

This boundary condition ensures that the potential gradient in the electrolyte is consistent with both the ionic and electronic currents at the cte interface.

Additionally, the periodic setup of the computational domain demands specific boundary conditions to maintain consistency across the boundaries. The periodic patches refer to those perpendicular to the separator and the cathode current collector. These periodic conditions ensure that the flux densities, potential, and concentration values are continuous across the periodic boundaries. Standard Neumann or Dirichlet boundary conditions do not suffice for these requirements; hence, Robin-type boundary conditions are employed. In the OpenFOAM environment, such a boundary condition is calculated using the following equation:

$$\phi_{\mathrm{f}} = w \phi_{\mathrm{ref}} + (1 - w)(\phi_{\mathrm{c}} + \Delta \nabla \phi_{\mathrm{ref}}) \tag{4.18}$$

In this context, (ϕ_{c}) denotes the value at the center of the boundary cell, while the reference values (ϕ_{ref}), reference gradients ($\nabla \phi_{\mathrm{ref}}$), and value fractions ($w$) calculated to ensure charge conservation ($\boldsymbol{i}_{\mathrm{o}} = \boldsymbol{i}_{\mathrm{n}}$) and mass conservation ($\boldsymbol{J}_{\mathrm{o}} = \boldsymbol{J}_{\mathrm{n}}$) across the periodic boundaries.

Table 4.1: Boundary conditions applied in the OpenFOAM simulation environment for a periodic setup, ensuring uniform flux densities, potentials, and concentrations across the computational domain's periodic boundaries.

Quantity	Reference value (ϕ_{ref})	Reference gradient ($\nabla \phi_{\mathrm{ref}}$)	Value fraction (w)
Φ_{el}	$\Phi_{\mathrm{el,n}}$	$\frac{2RT}{F c_{\mathrm{el,o}}} \left(t_+^0 - 1\right) \nabla c_{\mathrm{el,o}} - \frac{\kappa_{\mathrm{d,n}}}{c_{\mathrm{el,n}} \kappa} \nabla c_{\mathrm{el,n}}$	$\frac{\kappa_{\mathrm{n}} \Delta_{\mathrm{n}}}{\kappa_{\mathrm{n}} \Delta_{\mathrm{n}} + \kappa_{\mathrm{o}} \Delta_{\mathrm{n}}}$
c_{el}	$c_{\mathrm{el,n}}$	0	$\frac{D_{\mathrm{el,n}} \Delta_{\mathrm{n}}}{D_{\mathrm{el,n}} \Delta_{\mathrm{n}} + D_{\mathrm{el,o}} \Delta_{\mathrm{o}}}$
Φ_{s}	$\Phi_{\mathrm{s,n}}$	0	0.5
c_{s}	$c_{\mathrm{s,n}}$	0	0.5

Proceeding from the conservation equations and comparing the coefficients with those in equation eq. (4.18) leads directly to the expressions for the periodic boundary conditions as outlined in table 4.1. The subscripts n and o refer to the neighboring and own cells, respectively, while f indicates the value at the shared face. The term Δ accounts for the distance between the face and the cell center, with a correction for non-orthogonal cells.

4.2.4 Model parameterization

The physics-based model requires a comprehensive set of parameters, ideally obtained from direct measurements or derived from measured quantities. The parameters with constant values used in the model are detailed in table 4.2.

Table 4.2: Modeling parameters for the hybrid sodium-ion battery cathode half-cell, featuring a polymer-ceramic hybrid electrolyte, evaluated at room temperature.

Parameter	Value	Reference
Symmetry factors (α_a, α_c)	0.5	†
NVP particle diameter (d_{NVP})	8 µm	†
NaSICON particle diameter (d_{NAS})	4 µm	†
Separator thickness (L_{sep})	20 µm	†
Sodium max concentration ($c_{\mathrm{s,max}}$)	$14.2\,\mathrm{mol\,L^{-1}}$	‡
Sodium min concentration ($c_{\mathrm{s,min}}$)	$0\,\mathrm{mol\,L^{-1}}$	‡
Butler-Volmer reaction constant (k)	$3 \times 10^{-12}\,\mathrm{m^{2.5}mol^{0.5}s^{-1}}$	[172]
NVP/C conductivity (σ)	$7.14\,\mathrm{S\,cm^{-1}}$	[173]
NaSICON conductivity (κ_{NAS})	$1.5 \times 10^{-3}\,\mathrm{S\,cm^{-1}}$	[174]
Polymer conductivity (κ_{pol})	$6 \times 10^{-5}\,\mathrm{S\,cm^{-1}}$	[175]
PEO-NaTFSI conductivity prefactor (K_{NaTFSI})	M^{-1}	[170]
Peak polymer conductivity concentration ($c_{\mathrm{el},\kappa_{\max}}$)	$1.085 \times 10^{-3}\,\mathrm{S\,cm^{-1}}$	[170]
NaSICON diffusion coefficient ($D_{\mathrm{el,NAS}}$)	$4 \times 10^{-12}\,\mathrm{m^2\,s^{-1}}$	[176]
Polymer diffusion coefficient ($D_{\mathrm{el,pol}}$)	$4.7 \times 10^{-14}\,\mathrm{m^2\,s^{-1}}$	[177]
Sodium ion transference number (t_+^0)	0.39	[175]

† geometric parameters used for simulation
‡ calculated based on gravimetric capacity reported in [178]

One critical parameter is the equilibrium potential, which significantly influences the shape of the polarization curves and reflects the characteristics of the active material used. However, a robust theoretical framework for the sodium ion intercalation process remains elusive. The equilibrium potential of sodium ion intercalation electrodes often deviates from predictions based on the

Nernst equation due to complex solid-state redox reactions. This deviation results in distinctive and anomalous voltage behavior, a subject that has been extensively explored and debated in the literature [49].

Given the current limitations in understanding solid-state redox reactions, researchers typically match experimental equilibrium potential profiles to empirical models for subsequent predictions [179]. Karthikeyan et al. proposed a method for modeling the equilibrium potential of insertion electrodes using excess functions derived from the thermodynamics of non-ideal solutions [180]. This method expresses the equilibrium potential (U_{eq}) as a function of the mole fraction (χ), the interaction parameters of the intercalating species, and other thermodynamic contributions.

$$\text{1P M} \quad FU_{\mathrm{eq}} = FU_{\mathrm{eq}}{}^{0} + RT \ln\left(\frac{1-\chi}{\chi}\right) + RT\left[-A\,(2\chi - 1)\right] \tag{4.19}$$

$$\text{2P M} \quad FU_{\mathrm{eq}} = FU_{\mathrm{eq}}{}^{0} + RT \ln\left(\frac{1-\chi}{\chi}\right) + RT\left[-A + 2A\chi - B + 3B\chi - \frac{3}{2}B\chi^{2}\right] \tag{4.20}$$

$$\text{v. L} \quad FU_{\mathrm{eq}} = FU_{\mathrm{eq}}{}^{0} + RT \ln\left(\frac{1-\chi}{\chi}\right) + RT\left[\frac{A\left(B\chi^{2} - 1 + 2\chi - \chi^{2}\right)}{(1 - \chi + B\chi)^{2}}\right] \tag{4.21}$$

$$\text{R-K} \quad FU_{\mathrm{eq}} = FU_{\mathrm{eq}}{}^{0} + RT \ln\left(\frac{1-\chi}{\chi}\right) + \sum_{k=0}^{N} A_k\left[(2\chi - 1)^{k+1} - \frac{2k\chi\,(1-\chi)}{(2\chi - 1)^{1-k}}\right] \tag{4.22}$$

To identify the most suitable thermodynamic model for this study, we compared several thermodynamic equations: the one-parameter Margules (1P M), two-parameter Margules (2P M), van Laar (v. L.), and Redlich-Kister (R-K) equations [181, 182]. The model equations are given in eqs. (4.19) to (4.22). Additionally, fig. 4.3 illustrates cell voltage measurements for carbon-coated NVP samples at low C-rates, extracted from Si et al. [183], along with the corresponding fits to the thermodynamic equations.

Table 4.3: Fit parameters and quality metrics for thermodynamic models applied to NVP.

Parameter	$U_{\mathrm{eq}}{}^{0}$	A	B	R^2
1P Mar	0.3781	2.1698	0	0.9616
2P Mar	3.3782	1.5837	0.2306	0.9509
Van Laar	3.3785	1.81	1.0424	0.9507
Redlich-Kister	3.3787	†	0	0.9860

† coefficients are listed in appendix A.2.

A non-linear least squares algorithm was employed to fit the data to the various thermodynamic equations. The quality of these fits was assessed for monotonicity and overall accuracy. Table 4.3 presents the fitting parameters used for evaluating the fit quality.

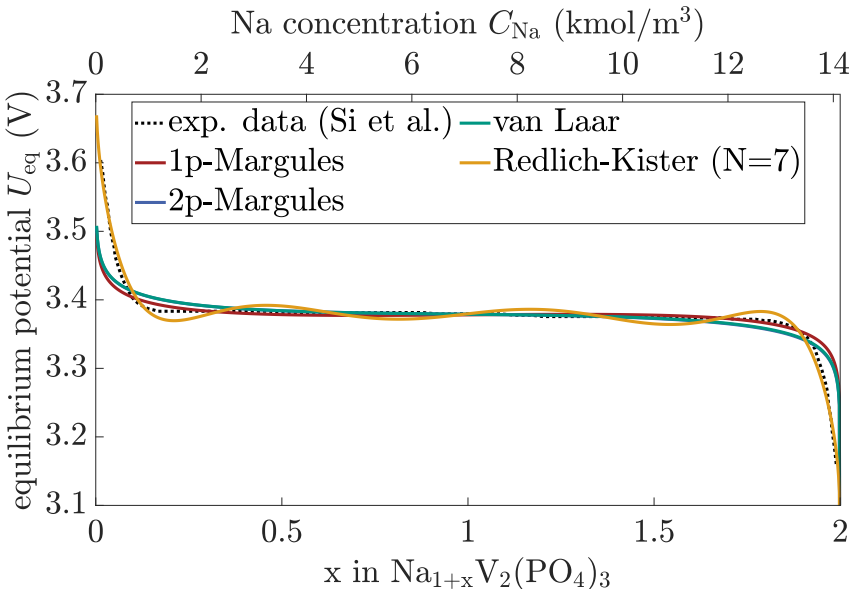

Figure 4.3: Cell voltage measurements of carbon-coated NVP samples at low C-rates, as reported by Si et al. [183], with corresponding fits to thermodynamic equations. The fits were derived using a nonlinear least squares algorithm.

The Redlich-Kister and one-parameter Margules models demonstrated high fit quality; however, they did not adequately capture the elongated flat plateau and exhibited non-monotonic behavior, which is physically unrealistic. Conversely, while the two-parameter Margules model showed slightly lower fit quality, it was preferred for its ability to maintain monotonicity and its simpler formulation, which facilitates easier interpretation and application in subsequent analyses.

4.3 Solver implementation and computational solution

The implementation of the electrochemical model for the all-solid-state sodium-ion battery shares several similarities with the solver designed for the sodium-iodine battery discussed in section 3.3. However, there are key differences that necessitate a specialized approach for the sodium-ion system.

A key distinction is that in the current model, the electrolyte concentration is represented by a single scalar, whereas in the sodium-iodine battery model, the electrolyte contained multiple species, each described by its own scalar and corresponding equation. Additionally, the solver for the sodium-ion battery is developed to accommodate periodic boundary conditions due to the use of periodic, non-symmetrical meshes (table 4.1). This feature introduces complexity in ensuring the convergence of all scalar fields within each time step.

During discharge, the movement of sodium ions (Na) from the anode, through the electrolyte as Na^+, and their subsequent intercalation into the cathode active material is governed by the transport equations (eq. (4.5) through eq. (4.7)). Simultaneously, the solver addresses charge

conservation in the cathode and ionic conservation in the electrolyte through their respective electric and ionic potentials. In this three-dimensional model, sodium mass is represented by a single scalar: Na^+ in the electrolyte and Na in the electrode. Similarly, a second scalar represents the potentials in both the electrolyte and cathode phases.

The numerical solution of these equations involves discretizing the two scalar fields using unstructured tetrahedral cells, employing a second-order finite-volume spatial scheme and an implicit first-order temporal scheme. The equations are solved in a segregated manner, with a conjugate gradient linear solver and a geometric-algebraic multigrid solver used for matrix preconditioning. Each scalar is implicitly solved across the entire cathode and electrolyte domain.

While solving uncoupled linear diffusion equations, such as eq. (4.5), is relatively straightforward and computationally efficient, even on large and complex three-dimensional mesh networks, the situation becomes significantly more challenging when non-linearities introduced by electrochemical reactions (eqs. (4.12) and (4.13)) and ion transport mechanisms (e.g., migration terms in eq. (4.8)) are considered.

The segregated solver tackles the partial differential equations for each computational domain separately, as illustrated in fig. 4.4. Within the cathode domain, multiple inner and outer iterations are conducted to ensure the consistency of the external current (I_s^{ex}), the current at the cathode–electrolyte interface (I_s^{cte}), and the current at the cathode current collector (I_s^{cc}) during galvanostatic cycling.

The iterative coupling between the electrolyte and cathode domains is facilitated by the Butler–Volmer charge transfer equation. To ensure computational stability, under-relaxation techniques are applied during the coupling process. Convergence is monitored by calculating the normalized root mean square deviation (NRMSD) of the currents at the coupled patches, $\boldsymbol{i}_{el}^{etc}$ and $\boldsymbol{i}_s^{cte}$. These values must fall below a predefined convergence criterion to guarantee current consistency across the interface.

Moreover, the concentration changes between successive iterations must be minimal to ensure solution stability. In most simulation scenarios, a convergence criterion δ_i of 1×10^{-3} was found to be sufficient for achieving reliable results.

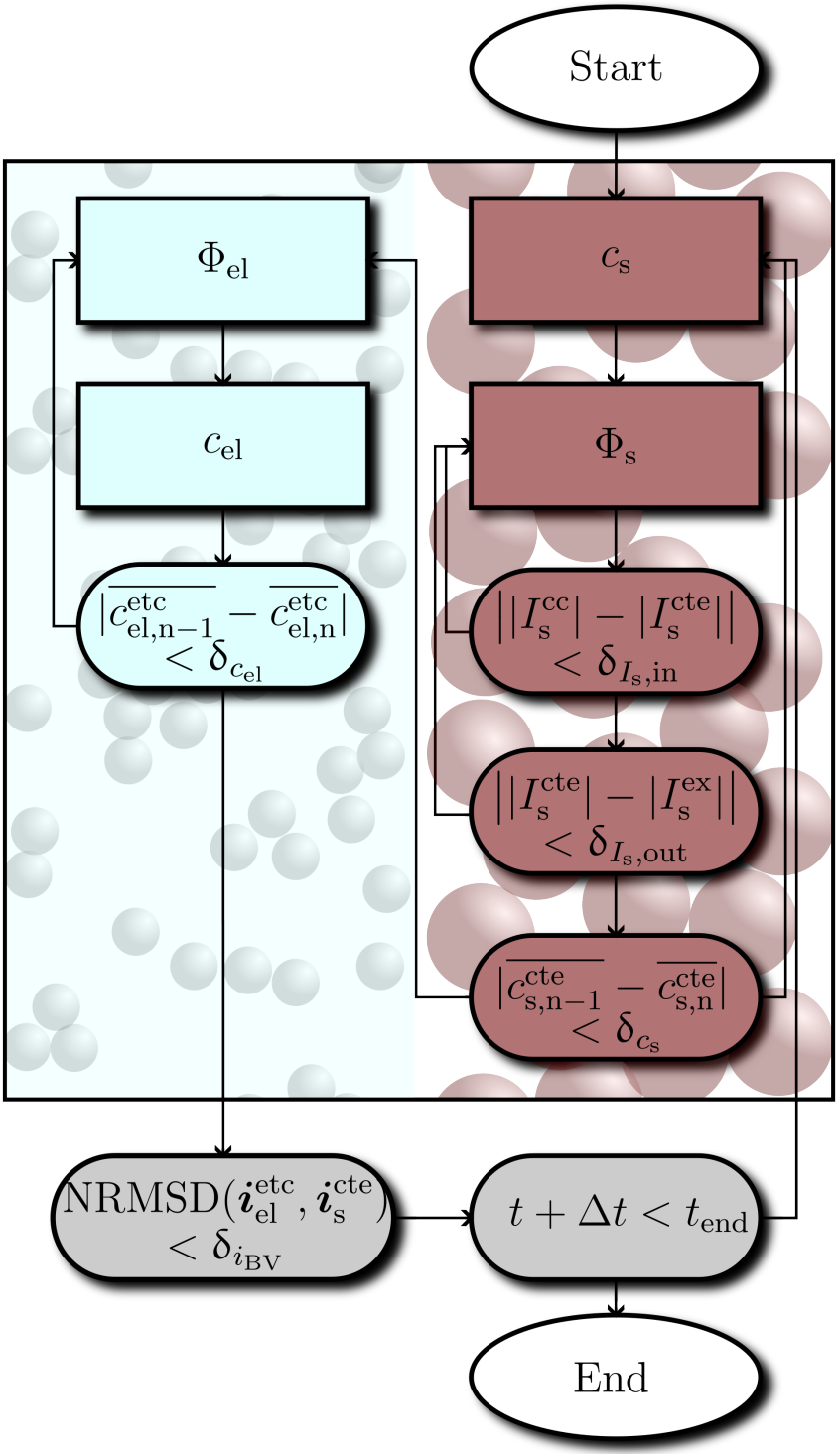

Figure 4.4: Schematic flowchart illustrating the iterative solution algorithm used in the segregated solver. The algorithm is designed to maintain current consistency during galvanostatic cycling. To ensure stability, under-relaxation techniques are applied. Convergence between the electrode and electrolyte currents at the coupled interfaces is evaluated using the normalized root mean square deviation (NRMSD).

4.4 3D Simulation: Impact of Cathode Electrode Properties on Battery Performance[4]

This section presents the effects of polymer-ceramic cathode electrode characteristics on the performance of the all-solid-state sodium-ion battery, as predicted by our computational model. A series of simulations systematically investigates how variations in key properties of the cathode electrode—such as the electrolyte active filler volume fraction, cathode thickness, and active material content—impact overall battery performance. This parametric study explores the effect of each parameter individually while holding the others constant. Examining these model predictions provides insights into the fundamental mechanisms that dictate battery behavior. Ultimately, these findings offer valuable guidance for the optimization and design of next-generation battery systems aimed at achieving superior performance.

4.4.1 Cathode microstructure generation and computational mesh

The cathode microstructures analyzed in this study consist of a randomly arranged stack of dense, smooth, spherical particles. These microstructures were generated using the discrete element method (DEM) through the open-source LIGGGHTS® software. This approach is adapted from a lithium-ion battery (LIB) microstructure generation algorithm described by Chauhan et al. [185]. Originally, this technique was employed to create computational meshes for investigating the influence of the carbon-binder domain on battery performance using a two-phase computational cathode domain (NMC and CBD) and a single-phase computational electrolyte domain.

In the present work, this microstructure generation workflow has been modified to produce a single-phase computational cathode domain (NVP) and a two-phase computational electrolyte domain, consisting of NaSICON particles embedded within a polymer host matrix. The simulations aimed to replicate the spatial distribution of the cathode half-cell components, with a focus on the geometric arrangement rather than detailed particle interactions.

The particle stack, representing the active material and NaSICON fillers, was generated within a simulation box. During this procedure, particles were allowed to settle and roll under periodic boundary conditions, with collisions modeled using the Hertz-Mindlin contact model. The dimensions of the simulation box were selected based on structural property studies [127], and uniaxial compression was applied to fix the cathode dimension, thereby adjusting the volume fractions.

[4] This section includes results and findings that were previously reported in Gerbig, F., Chauhan, A., Gietl, S., and Nirschl, H.: Performance Investigations on All-Solid-State Polymer-Ceramic Sodium-Ion Batteries through a Spatially Resolved Electrochemical Model. *Journal of The Electrochemical Society*, **2024**, 171(9), 090515. DOI: 10.1149/1945-7111/ad7763

In this work, electrodes were modeled at specific thicknesses for various studies, and the particle stacks were extended and trimmed along the simulation box dimensions to ensure the formation of periodic cathode geometries and half-cells. The electrolyte domain was formed by including the pore volume within the cathode and adding a separator thickness. To regulate the initial particle insertion, pseudo-random number generation was employed, and multiple microstructures with different seeds were generated for each study to maintain constant volume fractions and porosity, which ensures comparability of the results.

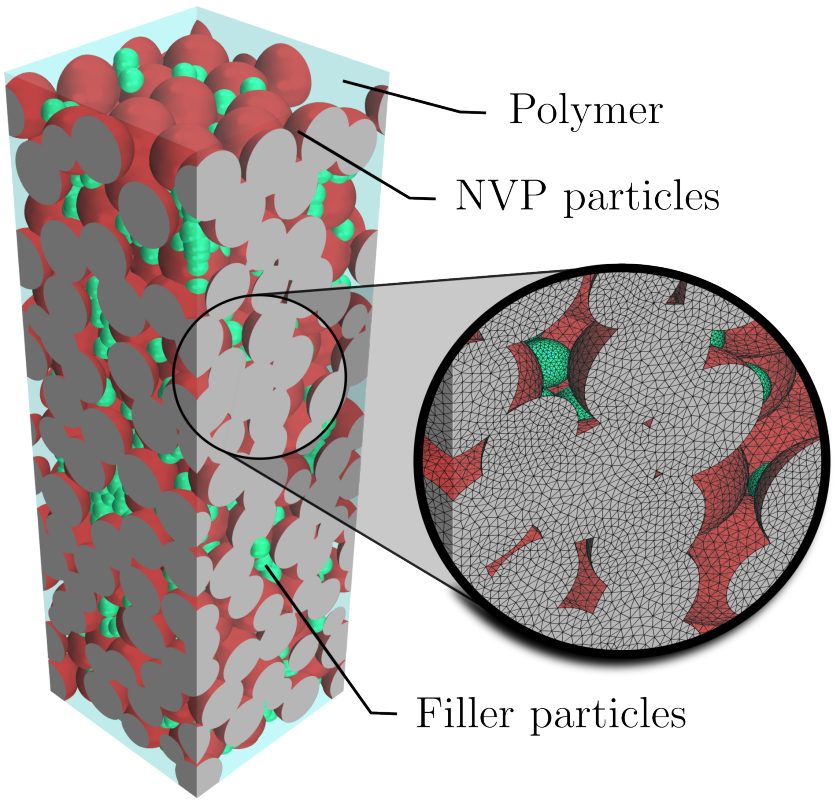

Figure 4.5: Visualization of the computational mesh and cathode microstructure created with LIGGGHTS software using the discrete element method (DEM). The image depicts a randomly packed arrangement of dense, smooth spherical particles, capturing the spatial distribution of the cathode components under periodic boundary conditions.

Figure 4.5 illustrates a virtual cathode structure resulting from the described microstructure generation workflow. Following this, the meshing of computational regions was carried out using Simcenter. An example of the resulting unstructured tetrahedral mesh is also shown in fig. 4.5. The mesh generated by Simcenter maintains a nonorthogonality within 65°. To ensure accurate flux approximation and address any potential issues arising from non-orthogonality, a non-orthogonal correction was applied to the surface normal gradient schemes and the Laplacian schemes within OpenFOAM. These adjustments help preserve the accuracy of the spatial discretization used in the second-order finite volume method.

4.4.2 Effect of filler content on battery performance

Figure 4.6 depicts the influence of varying active filler content on the discharge performance of a sodium-ion battery equipped with a hybrid composite solid electrolyte during C/5 discharging. The simulation examines how different levels of active filler content in the electrolyte affect the battery's discharge characteristics. The cathode, with a fixed length of 100 µm and an NVP content of 54 %, is analyzed. This configuration yields a theoretical specific capacity of 204 A h L^{-1}.

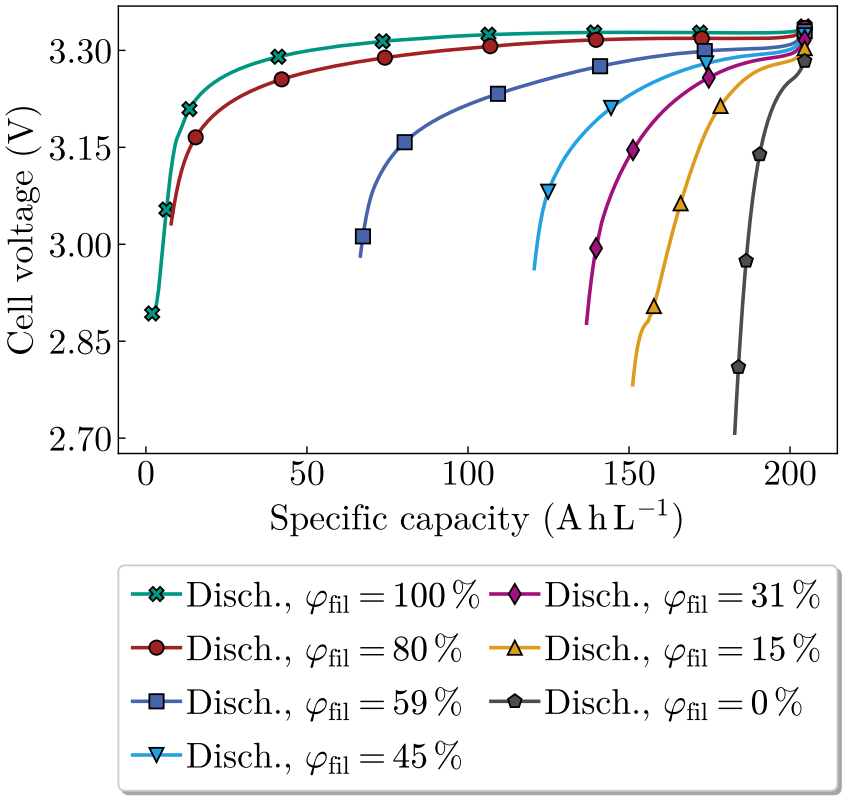

Figure 4.6: The figure shows the polarization curves of a sodium-ion battery during C/5 discharging, using a hybrid composite solid electrolyte with varying electrolyte active filler volume fractions ($\varphi_{el,fil}$) values. The solid lines illustrate these curves at a cathode length of 100 µm, with different colors and markers indicating distinct electrolyte active filler volume fractions levels as functions of the specific capacity.

During these simulations, the the electrolyte active filler volume fraction ($\varphi_{el,fil}$) was systematically varied from 0–100 %. The results reveal a substantial range in capacity utilization, from 21 A h L^{-1} for an electrolyte composed entirely of PEO to 202 A h L^{-1} for an electrolyte composed entirely of NaSICON. This variation highlights the critical role of filler content in determining battery performance.

In this situation, the observed reduction in capacity for electrolytes with a lower NaSICON content is primarily due to slower sodium ion transport within these electrolytes. Under galvanostatic cycling, the external current creates a significant potential gradient across the electrolyte to drive

ion transport and satisfy the charge transfer reaction demands. Consequently, electrolytes with insufficient NaSICON content fail to support adequate sodium ion movement, leading to premature termination of discharge in these configurations.

Specifically, an electrode with $\varphi_{\mathrm{el,fil}}$ of 80 % demonstrated lower capacity utilization compared to an electrode with pure NaSICON electrolyte, reflecting the limitations imposed by high filler content. Achieving such high $\varphi_{\mathrm{el,fil}}$ values in practice necessitates non-spherical filler particles to effectively occupy void spaces and enhance packing density. For instance, an electrode with $\varphi_{\mathrm{el,fil}}$ of 59 %, achievable with near-spherical filler particles and minimal compression, provided a capacity utilization of 138 A h L^{-1}, or approximately 67 % of the theoretical capacity.

Figure 4.7 illustrates the charging behavior of a sodium-ion battery with a hybrid composite solid electrolyte, varying in $\varphi_{\mathrm{el,fil}}$ during a C/5 charging process.

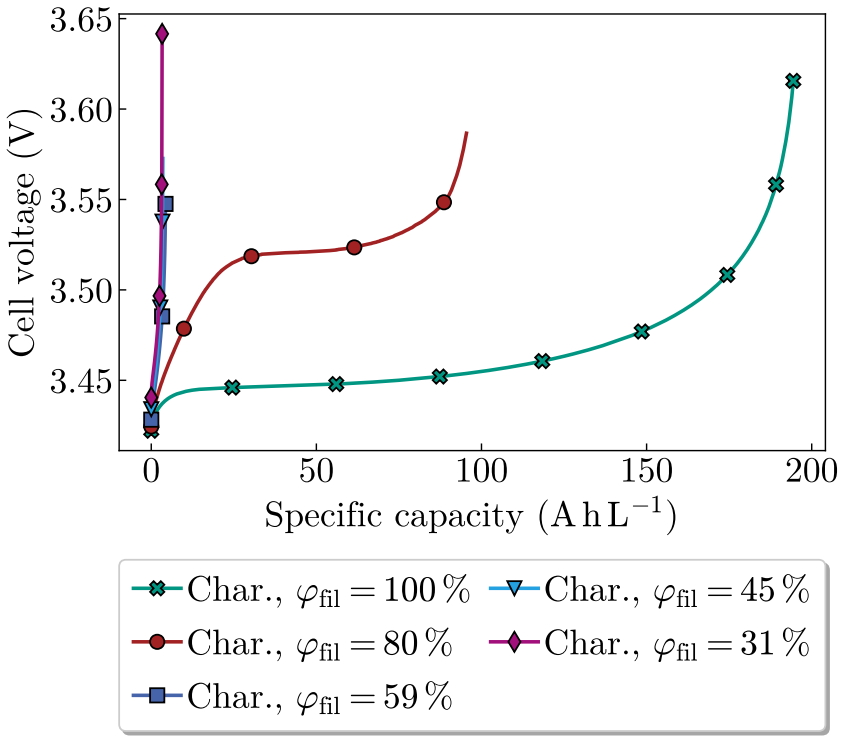

Figure 4.7: The figure shows the polarization curves of a sodium-ion battery during C/5 charging, using a hybrid composite solid electrolyte with varying electrolyte active filler volume fractions ($\varphi_{\mathrm{el,fil}}$) values. The solid lines illustrate these curves at a cathode length of 100 µm, with different colors and markers indicating distinct electrolyte active filler volume fractions levels as functions of the specific capacity.

The charging analysis reveals a pattern similar to the discharging process: a pure NaSICON electrolyte enables nearly complete utilization of the theoretical capacity, while the capacity utilization decreases with decreasing NaSICON content. This trend is particularly pronounced during the charging phase. For example, an electrode with an $\varphi_{\mathrm{el,fil}}$ of 80 % only achieves less than 50 % of the theoretical capacity, while electrodes with lower NaSICON content exhibit almost

negligible capacity utilization. Furthermore, simulations for configurations with $\varphi_{\mathrm{el,fil}}$ less than 31 % did not converge, indicating computational limitations at these filler levels.

To understand the observed performance disparities, we examined the electrolyte's sodium ion concentration distribution. Figure 4.8 shows c_{el} averaged along the axis from the separator to the cathode current collector throughout the charging process, from the start ($t = 0$) to near the end of the charging period ($t = \frac{9}{10}\mathrm{T_{end}}$).

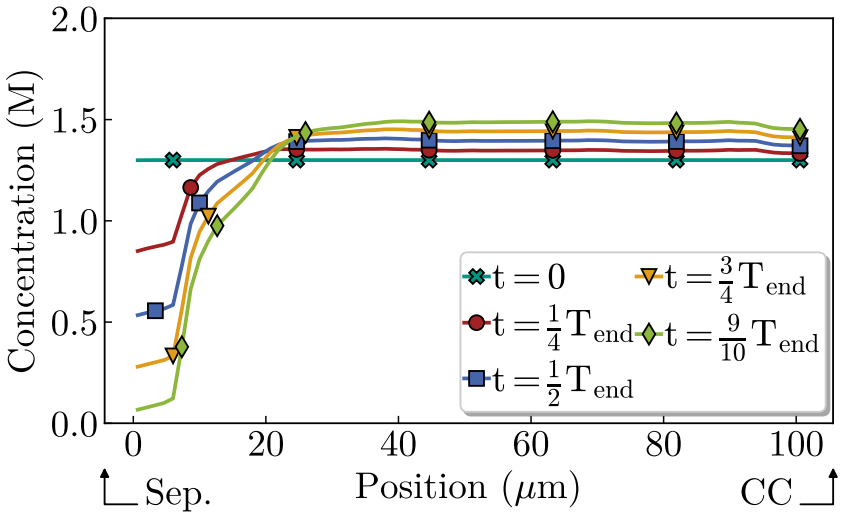

Figure 4.8: The solid lines depict the sodium ion concentration (electrolyte sodium ion concentration) during C/5 charging. The concentration values are averaged along the axis from the separator (Sep.) to the cathode current collector (CC).

During charging, the sodium ion concentration near the separator declines sharply from 1.3 M to nearly 0 M. This decrease results from sodium ions migrating from the cathode half-cell at the separator and entering the anode. Similar to the discharging process, most of the charge transfer reaction occurs near the separator. However, during charging, the reaction produces sodium ions in the electrolyte, which then exit the half-cell at the separator. The Butler–Volmer reaction alone cannot compensate for the loss of sodium ions near the separator, as ions must travel from the current collector to the separator. This transport is impeded by slow sodium ion movement across the electrolyte. Additionally, as the electrolyte concentration drops below a certain threshold, the polymer's conductivity significantly declines, reinforcing the problem and further hindering ion transport.

4.4.3 Impact of the cathode thickness

Increasing the cathode thickness offers several advantages, especially in bipolar configurations of sodium-ion batteries. Thicker cathodes reduce the need for multiple separators and current collectors, leading to a decrease in inactive material and a reduction in overall system costs.

Figure 4.9 illustrates the simulated cell voltage as a function of the capacity for cathode half-cells with thicknesses ranging from 70–250 µm. To facilitate a more effective comparison of performance, capacity is provided per unit area of the current collector, since the electrode volume varies with changes in the thickness of the half-cell.

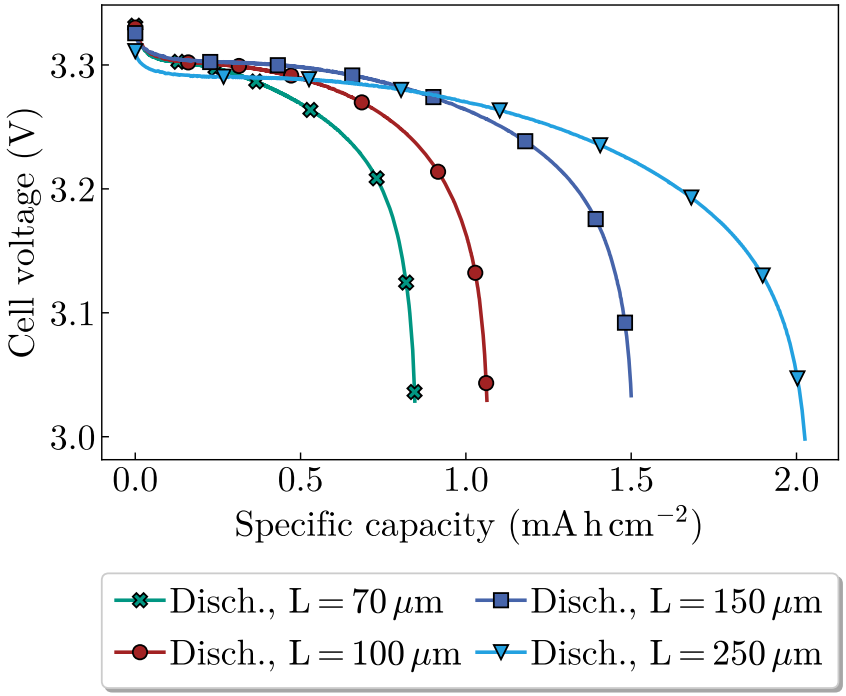

Figure 4.9: The solid lines display the polarization curves of a sodium-ion battery featuring a hybrid composite solid electrolyte, with an active material content of 55 ± 3 % and an electrolyte active filler volume fraction of 56 ± 3 %. The curves illustrate the impact of varying cathode thicknesses on cell performance.

In these simulations, both the active material content and the electrolyte active filler volume fraction were consistently maintained at 55 ± 3 % and 56 ± 3 %, respectively, taking into account the uncertainties inherent in the microstructure generation and meshing processes. The cells were initially discharged at a rate of 0.2 C.

As expected, increasing the cathode thickness results in higher capacity values. For instance, the thickest cathode (250 µm) achieved a capacity of approximately 2 mA h cm^{-2}, while the thinnest cathode (70 µm) reached only 0.8 mA h cm^{-2}. However, it is important to note that as the cathode thickness increases, the depth of discharge (DoD) decreases—from 60 % for the thinnest cathode to 40 % for the thickest. This trend suggests that a significant portion of the theoretical capacity remains unutilized in thicker cathodes, potentially due to limitations in ion transport and increased polarization within the electrode.

4.4.4 Analysis of active material content variations

Figure 4.10 illustrates the relationship between cell voltage and specific capacity for cathode electrodes with varying NVP content. In these simulations, the electrolyte active filler volume fraction is maintained at 50 %, and the cathode thickness is fixed at 100 µm. The charging process is conducted under galvanostatic conditions at a C-rate of 0.2.

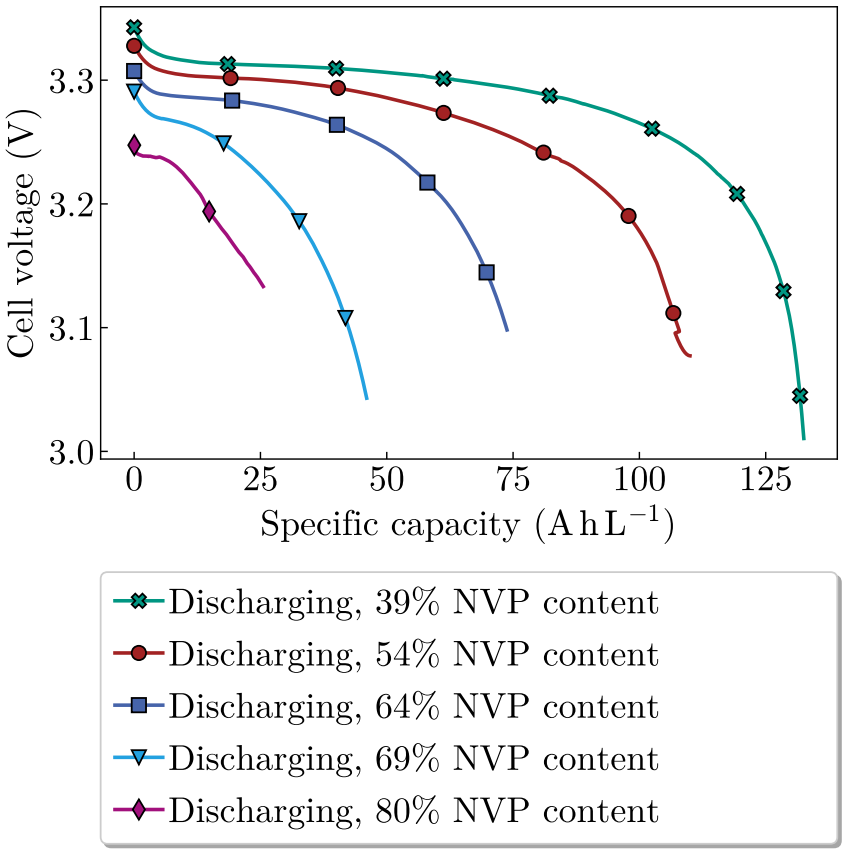

Figure 4.10: Cell polarization curves for a sodium-ion battery utilizing a hybrid composite solid electrolyte with a cathode length of 100 µm and an electrolyte active filler volume fraction of 50 % under C/5 discharge conditions. The curves depict the cell voltage as a function of state of charge, with different colors and markers indicating various active material contents.

Discharge termination occurs significantly earlier for cathodes with lower NVP content. For example, the electrode with 80 % NVP content achieves a state of charge (SOC) of 0.9, while the electrode with only 39 % NVP content ceases discharge at an SOC below 0.1. This discrepancy is primarily due to the limitations in Na^+ transport within the electrolyte.

Figure 4.11a shows a cross-sectional view of the cathode electrode, extending from the separator to the current collector, with two distinct color maps representing electrolyte sodium ion concentration (c_{el}) and active material sodium ion concentration (c_s). The ionic conductivity of the electrolyte is lower than the electronic conductivity of the cathode. As a result, current tends

to minimize its path through the electrolyte, causing the charge transfer reaction to predominantly occur near the separator.

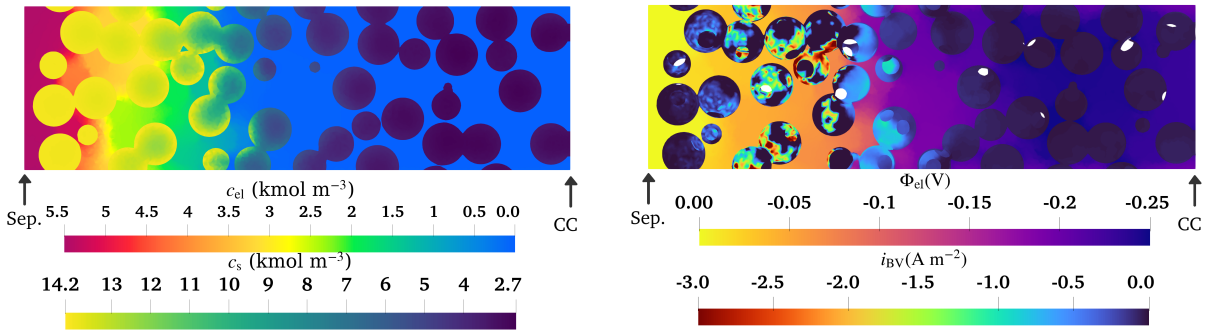

(a) Cross-sectional view of a sodium-ion battery cathode featuring a hybrid composite solid electrolyte, extending from the separator (left) to the current collector (right). The color maps depict the electrolyte sodium ion concentration (c_{el}) and the active material sodium ion concentration (c_s).

(b) Cross-sectional view of a sodium-ion battery cathode with a hybrid composite solid electrolyte, spanning from the separator (left) to the current collector (right). The color maps represent the electrolyte potential (Φ_{el}) and the Butler-Volmer current density (i_{BV}) at the cathode–electrolyte interface.

Figure 4.11: ASSSIB electrochemical potential and species distribution

During discharge, as the active material particles adjacent to the separator reach their maximum sodium ion concentration, the charge transfer reaction progressively shifts toward the current collector. To facilitate this shift, the electrolyte potential must increase, allowing ionic current to penetrate deeper into the cathode. This process is non-linear, leading to a substantial drop in electrolyte potential, which in turn reduces the overall cell potential.

Figure 4.11b provides detailed insights into the electrolyte potential (Φ_{el}) and the Butler-Volmer current density (i_{BV}) at the cathode-electrolyte interface toward the end of the discharge process. According to standard convention, Butler-Volmer current density is negative during discharging. Notably, regions with a high magnitude of Butler-Volmer current density migrate away from the separator, where the exchange current density decreases as the sodium ion concentration in the active material approaches its maximum of 14.2 M. To drive ionic current deeper into the electrode, the electrolyte potential must drop by more than 250 mV.

4.5 Pseudo two-dimensional model

4.5.1 Introduction to P2D models

This section aims to extend the analysis of all-solid-state sodium-ion batteries (ASSSIBs) with hybrid polymer-ceramic electrolytes by addressing the limitations inherent in the microstructure model discussed in sections 4.2 and 4.4. Although the microstructure model offers detailed

insight into the behavior of the battery, it is restricted by its high computational demand and time-consuming simulations, which significantly limits the range of parameters that can be feasibly investigated.

Optimizing multiple parameters often requires hundreds to thousands of simulations, a task that remains impractical even with access to high-performance computing resources. In this context, homogenized models, as introduced in section 2.3, offer a promising alternative due to their ability to significantly reduce computation times and simplify both pre- and post-processing.

To balance computational efficiency with the need for accurate simulation of complex battery behaviors, this study employs a pseudo-two-dimensional (P2D) model. The P2D model retains the ability to replicate key effects captured by the microstructure model while allowing for faster computation on standard workstation computers. Thus, this model represents an optimal compromise between computational effort and accuracy, making it a suitable choice for further investigations.

The following sections details the physical principles underlying the P2D model, describe the computational approach used to solve the model, and presents the simulation results obtained from this method.

The simulations conducted in this study utilized the Python Battery Mathematical Modelling (PyBaMM) software package, which implements the finite volume method as described by [186]. PyBaMM is an open-source Python framework designed for solving differential equations, with a comprehensive library of battery models and parameters. It also provides specialized tools for conducting and visualizing battery-specific experiments, facilitating efficient exploration of different battery designs and operational scenarios.

The numerical solver employed is adapted from the PyBAMM base solver implementation of the Doyle-Fuller-Newman (DFN) model [152], originally developed for lithium-ion batteries, and modified to simulate sodium-ion batteries with hybrid electrolytes. The model employs concentrated solution theory to describe the potential and species distribution within the binary electrolyte [112].

In the P2D model, the battery's electrode and separator are represented using a one-dimensional planar geometry, simplifying the governing equations to a one-dimensional form. The model also incorporates sodium ion (Na) diffusion within the active material particles, modeled along the radial dimension r under the assumption of spherical electrode particles. The full coupling of these two dimensions—one for the planar geometry and one for the radial diffusion—gives the model its designation as a pseudo-two-dimensional (P2D) model.

Figure 4.12 visually demonstrates the working principle and idealized geometry of the P2D model. This figure contrasts the intricate 3D structure of the battery system (as seen in fig. 4.1) with

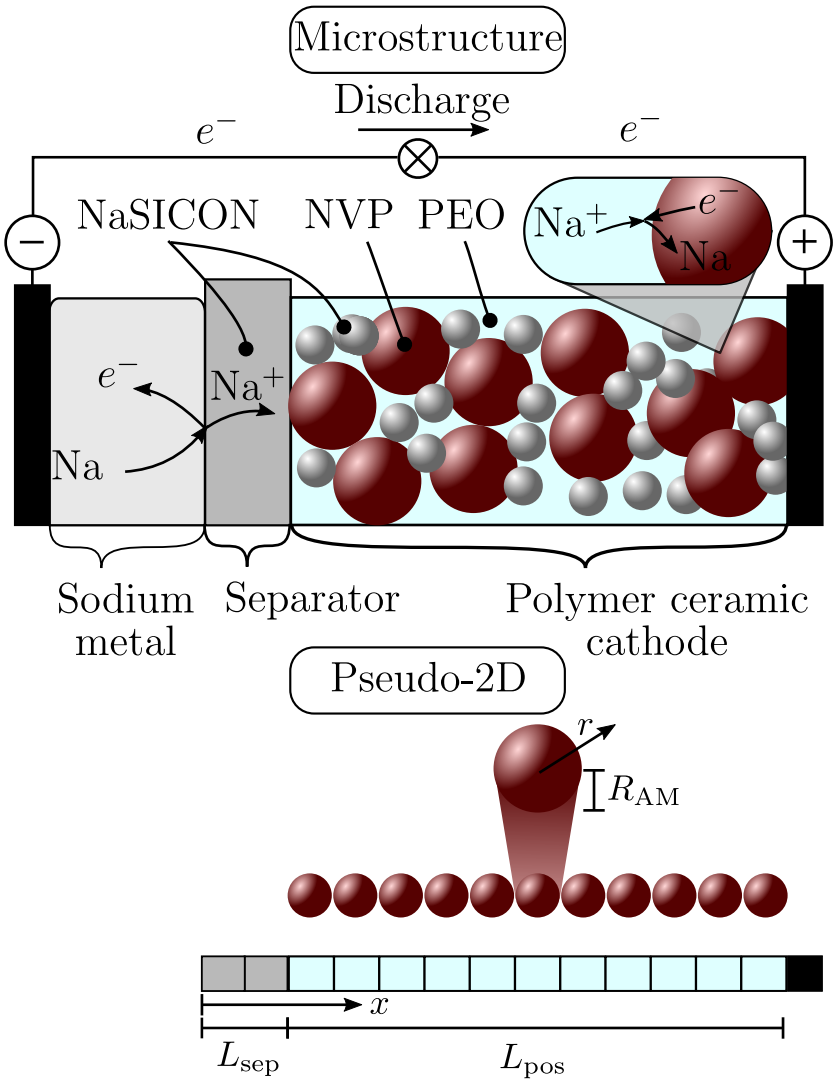

Figure 4.12: Illustration of the P2D model's working principle and idealized geometry for the battery system. The figure juxtaposes the detailed 3D representation of the battery system with its simplified 2D planar approximation as used in the P2D model. This comparison demonstrates the model's capability to encapsulate the multi-scale aspects of physics-based battery simulations, showing how the P2D model simplifies intricate 3D interactions into a more practical 2D framework while retaining key details.

its simplified 2D planar approximation, showcasing how the P2D model effectively captures the multi-scale physics of battery operation while significantly reducing computational complexity.

4.5.2 Governing equations

The mathematical framework of this study is anchored in five coupled equations that govern mass and charge conservation within both the solid insertion electrode and the electrolyte. This framework is derived from the microstructure model detailed in section 4.2 and extends to a

continuum-scale cell model. The derivation process involves applying volume averaging theorems to the microscale equations, as outlined by [187].

In these equations, the overline operator, denoted a $\overline{q_\alpha}$ represents the *intrinsic phase average* of q for phase α. This intrinsic phase average differs from the general phase average by focusing exclusively on the property of phase α averaged over the volume it occupies. This distinction ensures that the averaged property accurately reflects the phase-specific characteristics within the context of the broader continuum model.

The equation for active material current density ($\boldsymbol{i}_\mathrm{s}$) is expressed as:

$$\boldsymbol{i}_\mathrm{s} = -\sigma_\mathrm{eff} \nabla \overline{\Phi_\mathrm{s}} \tag{4.23}$$

To derive the continuity equation for the active material potential, we apply volume-averaging theorems to the respective microscale equation (eq. (4.4)). This approach involves evaluating the surface integral across the boundary between active material particles and the electrolyte phase. Substituting this term with the expression derived from the Butler-Volmer equation, which serves as a boundary condition in the microstructure model (see eq. (4.14)), yields:

$$\nabla \cdot \left(-\sigma_\mathrm{eff} \nabla \overline{\Phi_\mathrm{s}} \right) = -a_\mathrm{s} j_\mathrm{BV} \tag{4.24}$$

In this formulation, the Butler-Volmer flux density (j_BV) appears as a source term on the right-hand side of the equation, with specific interfacial surface area (a_s) acting as a scaling factor. This approach contrasts with microstructure models, where j_BV is typically incorporated into the boundary conditions at the electrolyte-electrode interface. The term a_s quantifies the interface area between the cathode and the electrolyte per unit volume.

In the continuum-scale model, sodium transport across the half-cell is neglected, while local diffusion within the active material particles is considered. According to Fick's first law, the molar flux density of sodium is proportional to the concentration gradient. The continuity equation, accounting for the sodium diffusion within a symmetrical spherical particle along the radial coordinate r, is governed by Fick's second law:

$$\frac{\partial c_\mathrm{s}}{\partial t} = \frac{1}{r^2} \nabla \left(r^2 D_\mathrm{s} \frac{\partial c_\mathrm{s}}{\partial r} \right) \tag{4.25}$$

This equation describes the time-dependent change in sodium concentration within the particle, considering the active material sodium diffusion coefficient and the radial symmetry of the problem.

As outlined in eq. (4.6), sodium transport within the electrolyte is modeled using concentrated solution theory for a binary electrolyte. In its volume-averaged form along the direction perpendicular to the current collector (x), the surface flux density ($\boldsymbol{J}$) is represented as:

$$\boldsymbol{J}_{c_{\mathrm{el}}} = -D_{\mathrm{el}} \left(1 - \frac{\mathrm{d} \ln c_{\mathrm{el},0}}{\mathrm{d} \ln \overline{c_{\mathrm{el}}}}\right) \frac{\partial \overline{c_{\mathrm{el}}}}{\partial x} + \frac{\boldsymbol{i}_{\mathrm{el}} t_+^0}{F} \tag{4.26}$$

By applying the same approach used for the charge transport equation in the active material (eq. (4.24)), the volume-averaged approximation for charge conservation in the electrolyte is derived. This involves using volume-averaging theorems, assuming uniform flux across the electrolyte-cathode interface, and substituting the relevant boundary condition for c_{el} (eq. (4.16)):

$$\frac{\partial \left(\varepsilon_{\mathrm{s}} \overline{c_{\mathrm{el}}}\right)}{\partial t} = \frac{\partial}{\partial x} \left(D_{\mathrm{el,eff}} \frac{\partial \overline{c_{\mathrm{el}}}}{\partial x}\right) + a_{\mathrm{s}} \left(1 - t_+^0\right) j_{\mathrm{BV}} \tag{4.27}$$

In this equation, the j_{BV} term appears as a source on the right-hand side, with a sign opposite to that in eq. (4.25).

By similar means, the volume-averaged approximation for charge transport in the electrolyte is obtained:

$$a_{\mathrm{s}} F j_{\mathrm{BV}} = -\frac{\partial}{\partial x} \left[\kappa_{\mathrm{eff}} \frac{\partial \overline{\Phi_{\mathrm{el}}}}{\partial x}\right] + \frac{\partial}{\partial x} \left[\kappa_{\mathrm{d,eff}} \frac{\partial \ln \overline{c_{\mathrm{el}}}}{\partial x}\right] \tag{4.28}$$

In transitioning from a microscale model to a more simplified continuum-scale model, such as the P2D model, it is essential to account for the effects of tortuosity and porosity on the effective properties of the electrolyte. These factors alter the diffusivity and conductivity of the ionic species within the electrolyte, necessitating a modification of these parameters to reflect the reduced transport efficiency in the practical electrode configuration. The presence of porous structures and the tortuous pathways for ion transport lead to effective diffusivity and conductivity values that are lower than their intrinsic counterparts. The effective values of electrolyte sodium ion diffusion coefficient and electrolyte ionic conductivity are adjusted by porosity and tortuosity as follows:

$$D_{\mathrm{el,eff}} = D_{\mathrm{el}} \frac{\varepsilon_{\mathrm{s}}}{\tau} \tag{4.29a}$$

$$\kappa_{\mathrm{eff}} = \kappa \frac{\varepsilon_{\mathrm{s}}}{\tau} \tag{4.29b}$$

The effective electrolyte diffusional conductivity is defined as

$$\kappa_{\mathrm{d,eff}} = \frac{2RT\kappa_{\mathrm{eff}}}{F} \left(1 - t_+^0\right) \tag{4.30}$$

As previously discussed, the variable j_{BV} is integral to linking the partial differential equations (PDEs) with the ordinary differential equations (ODEs) in the model. This term represents the rate of sodium ion production or consumption due to the electrochemical surface reaction. It encapsulates the critical kinetics of charge transfer occurring at the interface between the active material and the electrolyte. To provide a comprehensive overview, the Butler-Volmer equation [23, 171] is revisited here in its volume-averaged form:

$$\overline{j_{\mathrm{BV}}} = \frac{\overline{i_0}}{F} \sinh\left(\frac{F}{2RT}\left(\overline{\Phi_{\mathrm{s}}} - \overline{\Phi_{\mathrm{el}}} - U_{\mathrm{eq}}\left(\overline{c_{\mathrm{s}}}\right)\right)\right) \tag{4.31}$$

The exchange current density (i_0) yields the following expression:

$$\overline{i_0} = Fk\sqrt{c_{\mathrm{s,max}} - \overline{c_{\mathrm{s}}}}\sqrt{\overline{c_{\mathrm{s}}}}\sqrt{\overline{c_{\mathrm{el}}}} \tag{4.32}$$

4.5.3 Boundary conditions

Choosing suitable boundary conditions is essential for accurately solving the model. At the boundary between the current collector and the electrode, located at ($x = L_{\mathrm{sep}} + L_{\mathrm{pos}}$) , electronic current is transferred. However, no charge transfer occurs between the current collector and the electrolyte. To ensure charge conservation, the current flowing through the current collector must be equal to the total current in the system.

Similarly, at the boundary between the electrode and the separator, situated ($x = L_{\mathrm{sep}}$) , the electronic current is zero. This is because, at this boundary, charge transport occurs exclusively through ionic movement within the electrolyte, not through electronic conduction.

The boundary conditions for the active material potential are specified as follows:

$$\left.\frac{\partial\overline{\Phi_{\mathrm{s}}}}{\partial x}\right|_{x=L_{\mathrm{sep}}} = 0, \qquad \text{and} \qquad \left.\frac{\partial\overline{\Phi_{\mathrm{s}}}}{\partial x}\right|_{x=L_{\mathrm{sep}}+L_{\mathrm{pos}}} = \frac{-i_{\mathrm{cell}}}{\sigma_{\mathrm{eff}}} \tag{4.33}$$

In this context, the i_{cell} can be represented through the utilization of the current collector plate area (A_{cc}) as follows:

$$i_{\mathrm{cell}} = \frac{I_{\mathrm{ap}}}{A_{\mathrm{cc}}} = CL_{\mathrm{pos}}\varepsilon_{\mathrm{s}}F\left(c_{\mathrm{s,max}} - c_{\mathrm{s,min}}\right) \tag{4.34}$$

At the boundary between the current collector and the electrolyte, the ionic current density must be zero. Additionally, a reference potential is established at the separator-electrolyte interface. This reference potential is typically set to zero and is defined as follows:

$$\left.\overline{\Phi_{\mathrm{el}}}\right|_{x=0} = \Phi_{\mathrm{el,ref}}, \qquad \text{and} \qquad \left.\frac{\partial\overline{\Phi_{\mathrm{el}}}}{\partial x}\right|_{x=L_{\mathrm{sep}}+L_{\mathrm{pos}}} = 0 \tag{4.35}$$

The c_s gradient at the particle surface ($r = R_{AM}$) is directly proportional to the flux density, as described by the Butler-Volmer equation. In the context of radially symmetrical particles, the assumption of no net flux at the particle center implies that the total flux through the center of the particles must be zero.

$$\left.\frac{\partial c_s}{\partial r}\right|_{r=0} = 0, \qquad \text{and} \qquad \left.\frac{\partial c_s}{\partial r}\right|_{r=R_p} = -\frac{\overline{j_{BV}}}{D_s} \tag{4.36}$$

The flux of anions into both the separator and the active material is zero. Instead, their diffusion is balanced by migration processes, which determine the boundary conditions for electrolyte sodium ion concentration. Additionally, there must be no mass flux of ions from the electrolyte into the current collector, ensuring that the system's mass conservation principles are upheld.

$$\left.\frac{\overline{c_{el}}}{\partial x}\right|_{x=0} = -\frac{\left(1 - t_+^0\right) i_{cell}}{D_{el,eff} F}, \qquad \text{and} \qquad \left.\frac{\overline{c_{el}}}{\partial x}\right|_{x=0} = 0 \tag{4.37}$$

4.5.4 Effective transport properties in the P2D model

In the P2D model, the electrolyte is treated as a continuum, meaning that physical parameters such as the electric potential (Φ_{el}) and diffusivity (D_{el}) are assumed to be uniform within each control volume. This assumption simplifies the modeling of ion transport and potential distribution across the electrolyte by neglecting any spatial variations within the control volume. Although this approach enhances computational efficiency, it requires the derivation of effective parameters that accurately represent the behavior of heterogeneous materials.

In the context of a composite polymer-ceramic electrolyte, the heterogeneity arises from the distinct properties of the polymer and ceramic components. To faithfully model the electrolyte within the P2D framework, these distinct properties must be integrated into effective parameters that capture the combined behavior of the composite. Effective medium theories are typically employed to calculate these parameters, offering a means to estimate the macroscopic properties of a composite material based on the individual properties and volume fractions of its constituents.

For example, the effective ionic conductivity of a composite electrolyte is determined by considering the conductivities of both the polymer and ceramic phases, alongside their respective volume fractions. Similarly, the effective diffusivity can be calculated using these theories, ensuring that the continuum model accurately reflects the composite's heterogeneous nature. This approach enables the P2D model to represent complex, multi-phase materials within a simplified computational framework while maintaining essential details of their physical behavior.

The Maxwell-Garnett (MG) model is a commonly used theoretical approach for estimating the effective properties of composite materials made up of two distinct phases. This model has been effectively applied to the study of composite polymeric electrolytes by Jamnik et al. [188] and Przyluski et al. [189]. The MG model assumes that the composite material comprises spherical inclusion particles that are evenly dispersed within a continuous host matrix. A key assumption of the MG model is that the structural characteristics of each phase remain uniform up to the phase boundary, with minimal interfacial resistance—meaning that the interface between the phases does not significantly hinder the transfer of properties such as electrical or thermal conductivity.

The MG model predicts an effective physical quantity (q) from the properties of the host matrix q_{pol} and the inclusion phase q_{Nas}, along with the electrolyte polymer volume fraction ($\varphi_{\mathrm{el,pol}}$) and the space dimension (d):

$$q_{\mathrm{eff}} = q_{\mathrm{Pol}} \left[1 + \frac{d(q_{\mathrm{Nas}} - q_{\mathrm{pol}})\varphi_{\mathrm{el,pol}}}{q_{\mathrm{Nas}} + (d-1)q_{\mathrm{pol}} - (q_{\mathrm{Nas}} - q_{\mathrm{pol}})\varphi_{\mathrm{el,pol}}} \right] \tag{4.38}$$

In this equation, q_{eff} represents the effective property (such as conductivity or diffusivity) of the composite material, derived by considering the individual properties of the polymer and ceramic phases. The model is based on the assumption that the ceramic particles act as the inclusion phase, with a spherical shape and uniform distribution within the polymer host matrix, without overlapping. This approach is particularly well-suited for modeling composite polymer-ceramic electrolytes, as it accounts for the combined influence of the distinct properties of each phase on the overall behavior of the electrolyte.

An alternative model that has gained traction for analyzing granular materials and packed beds is the Zehner-Bauer-Schlünder (ZBS) model [190, 191]. This model is particularly applicable to systems made up of closely packed spherical particles, which are common in various engineering fields, including battery technology. The ZBS model adopts a unit cell approach, integrating the properties of individual phases with their microstructural arrangement [192].

The model relies on several crucial parameters: the properties of the individual phases, the porosity of the electrolyte (which corresponds to $\varphi_{\mathrm{el,pol}}$), a shape factor ($C_{\mathrm{f}}$), and a flattening coefficient (γ), which quantifies the relative contact area between particles. The shape factor C_{f}, set to 1.25 for spherical particles, accounts for the geometric characteristics of particle packing. Meanwhile, the γ parameter influences the charge and mass transfer at particle contact points by

representing the degree of flattening at these interfaces. The ZBS model's governing equations are detailed in eqs. (4.39a) to (4.39f):

$$\frac{\kappa}{\kappa_{\mathrm{pol}}} = \left(1 - \sqrt{1 - \varphi_{\mathrm{el,pol}}}\right) + \sqrt{1 - \varphi_{\mathrm{el,pol}}}\left[\gamma k_{\mathrm{P}} + (1 - \gamma) k_{\mathrm{c}}\right] \tag{4.39a}$$

$$\gamma = \frac{A_{\mathrm{c}}}{A_{\mathrm{f}} N_{\mathrm{P}}} \tag{4.39b}$$

$$k_{\mathrm{P}} = \frac{\kappa_{\mathrm{fil}}}{\kappa_{\mathrm{pol}}} \tag{4.39c}$$

$$k_{\mathrm{c}} = \frac{2}{N}\left(\frac{B}{N^2}\frac{k_{\mathrm{P}} - 1}{k_{\mathrm{P}}} \ln\frac{k_{\mathrm{P}}}{B} - \frac{B+1}{2} - \frac{B-1}{N}\right) \tag{4.39d}$$

$$N = 1 - \frac{B}{k_{\mathrm{P}}} \tag{4.39e}$$

$$B = C_{\mathrm{f}}\left(\frac{1 - \varphi_{\mathrm{el,pol}}}{\varphi_{\mathrm{el,pol}}}\right)^{10/9} \tag{4.39f}$$

The flattening coefficient (γ) can be determined experimentally or approximated using the total contact area of the domain (A_{c}), contact area between two particles (A_{f}), and the number of particles (N_{P}). The equations introduce two dimensionless parameters: the ratio of ionic conductivities of dispersed and continuous phase in the ZBS model (k_{P}) and reduced core ionic conductivity in the ZBS model (k_{c}). Here, k_{P} reflects the ratio between the active filler ionic conductivity (κ_{fil}) and the polymer ionic conductivity (κ_{pol}), representing the relative transport properties of the active filler and the polymer matrix, respectively. These parameters balance the contributions of the particles themselves and their contact points, further modulated by the shape factor and porosity.

Interestingly, both the ZBS and Maxwell-Garnett models do not depend on particle size. Instead, they emphasize the volumetric properties and spatial distribution of particles. This characteristic makes these models versatile, simplifying their application to a wide range of granular and composite materials.

4.5.5 Model parameterization

The P2D model, being a physics-based approach, requires a comprehensive set of physical parameters to accurately simulate the battery system. Since the same battery system is studied here as in the microstructure model, the parameters used for the P2D model are consistent with those previously established. Detailed values for these parameters remain unchanged and are provided in section 4.2.4.

4.5.6 Computational solution

During the discharge process, the transport of sodium ions (Na) is governed by a set of coupled equations eqs. (4.25) to (4.27). These equations describe the migration of sodium ions from the anode, through the electrolyte as Na^+, and their subsequent intercalation into the cathode's active material. Concurrently, charge conservation in the cathode and ionic conservation in the electrolyte are controlled by their respective electric and ionic potentials.

In the pseudo-2D (P2D) model, the sodium mass is abstracted into a single scalar representation, with Na^+ denoting the sodium ions in the electrolyte and Na representing them within the electrode. This abstraction reduces the complexity of the model while preserving its ability to capture the critical dynamics of the system. The equations are then discretized into a set of differential-algebraic equations (DAEs) using the PyBaMM software package [186] and solved with the CasADi solver [193]. This computational approach allows for an efficient and accurate simulation of the sodium transport and electrochemical processes occurring within the battery during discharge.

4.6 Pseudo-two-dimensional simulation results[5]

This section examines the influence of polymer-ceramic cathode electrode characteristics on the performance of all-solid-state sodium-ion batteries using the P2D model. Initially, a comparison is made between the predictions from the P2D model with those obtained from detailed microstructure simulations (see section 4.4) to validate the model's accuracy and reliability.

Subsequently, a series of computational simulations investigates how key properties of the cathode electrode namely—specifically the electrolyte active filler volume fraction, the active material porosity, the active material particle radius, and the spatial active filler content variation—affect the battery's performance metrics, including energy density, capacity retention, and rate capability. By delving into these results, the objective is to uncover the fundamental mechanisms that dictate battery behavior, providing valuable insights for optimizing electrode design and enhancing overall battery performance. This analysis serves as a foundation for the development of advanced cell design strategies that shall lead to the next generation of high-performance solid-state sodium-ion batteries.

[5] This section includes results and findings that were previously reported in Gerbig, F., Kühn, J., and Nirschl, H.: Optimizing all-solid-state sodium-ion batteries: Insights from a P2D Model on NaSICON-based polymer–ceramic electrolyte. *Energy Reports*, **2025**, 13, 105–116. DOI: https://doi.org/10.1016/j.egyr.2024.11.077.

4.6.1 Evaluation of P2D model parameters

Tortuosity estimation

Equation (4.29) introduces tortuosity factors to the P2D model, which are crucial for accurately modeling ion transport in porous materials. A common approach for estimating tortuosity involves directly associating it with the material's porosity. The Bruggeman equation is widely used for this purpose, where the electrode tortuosity (τ), is expressed as:

$$\tau = \varepsilon_s^{b_{\text{Brug}}} \tag{4.40}$$

For materials composed of spherical particles, a Bruggeman exponent (b_{Brug}) of -0.5 is typically assumed, a standard practice in modeling insertion batteries. To verify the validity of this assumption for the battery in question, a comparison of the tortuosity values derived from our microstructure simulations with those predicted by well-established tortuosity-porosity relationships for porous media is employed. Specifically, the tortuosity from the 3D microstructure model ($\tau_{\text{sim,3D}}$) was calculated using the methodology described in eq. (4.29b).

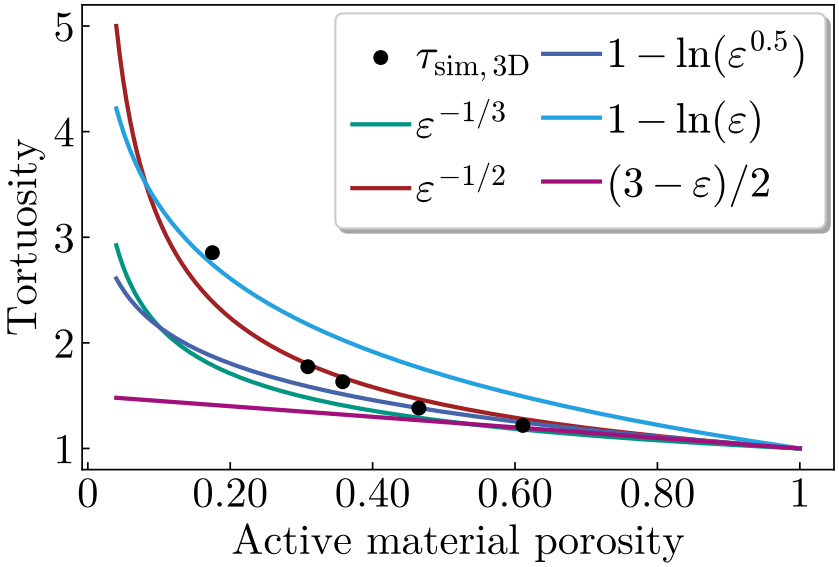

Figure 4.13: Comparison of various models describing the relationship between tortuosity and porosity for porous materials. The graph includes analytical relationships based on the Bruggeman equation and effective medium theory, alongside discrete values obtained from simulations of virtual electrodes using the microstructure model.

Figure 4.13 illustrates a comparison between several theoretical tortuosity-porosity relationships, including those derived from effective medium theory [195], and the tortuosity values obtained from the microstructure simulations. The data clearly show that the Bruggeman relation,

specifically the expression $\varepsilon^{-1/2}$ with an exponent of -0.5, provides the most accurate fit. Therefore, the study incorporates this relationship into the P2D model.

Flattening coefficient estimation

As highlighted in equations eqs. (4.39a) to (4.39f), accurately determining the flattening coefficient (γ) is crucial for fully parameterizing the Zehner-Bauer-Schlünder (ZBS) model. To achieve this, a comparative analysis is performed between the results of a particle-resolved model and the predictions of the proposed P2D model, with the intention of determining the optimal value for γ.

Polarization curves from the particle-resolved microstructure model, as detailed in section 4.4.4 [184], serve as the benchmark for this comparison. The intent is to align the continuum-scale P2D model as closely as possible with the more detailed microstructure model, thereby retaining the latter's accuracy while leveraging the computational efficiency of the P2D approach.

To find the best fit value for γ, this parameter is systematically varied from 0 to 1 in 1 % increments. The least squares algorithm is then applied to evaluate the quality of the fit for each γ value, ensuring the most accurate representation of microstructural effects in the continuum model.

Figure 4.14 shows the voltage curves obtained from the microstructure simulations and the P2D simulations with the optimal flattening coefficient for different active material porosity values. By tuning the flattening coefficients within the P2D model, the 3D simulation results are effectively reproduced for active material porosity (ε_s) values ranging from 0.39–0.64, However, when ε_s falls within the range of 0.69–0.83, the P2D simulations struggle to match the 3D simulations, as the simulated cell voltage remains elevated even when $\gamma = 0$. In particular, as ε_s decreases from 0.64–0.39, the γ values reduce from 0.16–0.03, an outcome that challenges expectations.

The flattening coefficient is generally understood to denote the proportion of the contact area to the entire surface area of the particles. Thus, reducing the void volume of a cathode—either virtual or real—and consequently its porosity, generally necessitates increased compression. For porosities below the close-packing threshold of equal spheres, significant deviations from the ideal spherical shape and even overlapping of particles become necessary. Theoretically, this should result in a higher flattening coefficient; however, the data show an opposite trend.

One possible explanation lies in the fact that the ZBS model was originally formulated for heat conduction in fixed beds, considering two phases: a heterogeneous phase and a homogeneous conducting phase. In contrast, the proposed battery model introduces a third phase, with the active material acting as an inert component from the perspective of the electrolyte. Although the ZBS model accounts for the lengthened transport paths and the reduced conductive volume via electrode tortuosity and active material porosity, additional effects may arise at lower ε_s. For instance, the distribution of the electrolyte filler particles could become increasingly uneven,

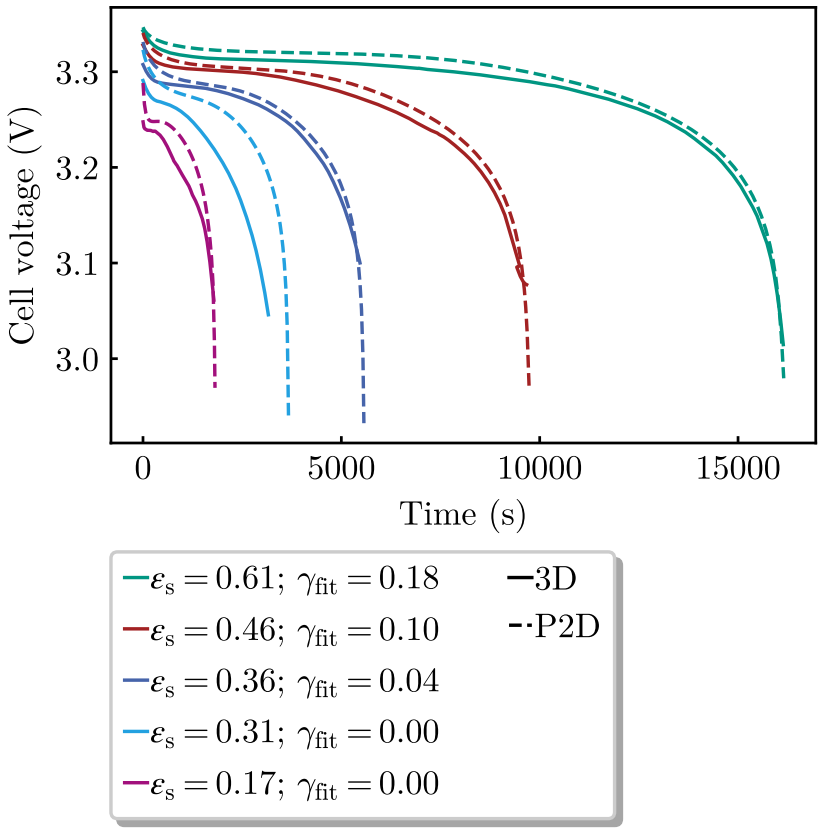

Figure 4.14: Estimation of the flattening coefficient (γ) for ZBS model calibration. This figure presents a comparison between voltage curves derived from particle-resolved microstructure simulations and those from the P2D model, across a range of γ values. The plot highlights voltage curves for varying active material porosities, illustrating the influence of γ on model fidelity and the P2D model's effectiveness in replicating the microstructure simulation outcomes.

leading to interruptions in the conductive pathways because of inadequate particle contact. Under high compression, the gaps between the active material particles may become too narrow to be effectively filled with the active material particles. In extreme cases, this could result in isolated, highly conductive islands of filler particles connected by a low-conductivity polymer, a scenario that is not adequately captured by the assumptions underlying the ZBS model.

Within the ε_s range of 0.31–0.61, the γ parameter obtained from fitting the cell voltage curves demonstrates a nearly linear relationship with active material porosity, with a high correlation coefficient of $R^2 = 0.9988$:

$$\gamma = -0.5579\varepsilon_s - 0.1593 \tag{4.41}$$

Finally, table 4.4 compares the effective electrolyte ionic conductivity values derived from the microstructure simulations ($\kappa_{eff,3D}$) with those calculated using both the ZBS and MG models across various ε_s values. In the ZBS model, γ is adjusted to achieve the best fit for the cell voltage curves. The difference in κ between the P2D and 3D simulations remains under 15.2 % for the

ZBS model within the ε_s interval of 0.36–0.61, but exceeds 23.9 % for the MG model. For lower active material porosity values, the ZBS model predicts an electrolyte ionic conductivity deviation greater than 27.8 % from $\kappa_{eff,3D}$, whereas the MG model offers a more accurate prediction, with deviations below 9.1 %.

Table 4.4: Fit parameters and quality metrics for the flattening coefficient estimation.

ε_s	$\kappa_{eff,3D}$ (mS m^{-1})	γ	κ_{ZBS} (mS m^{-1})	dev (%)	κ_{MG} (mS m^{-1})	dev (%)
0.61	15.9	0.18	13.8	15.2	9.75	63.1
0.46	8.7	0.10	9.2	−4.5	6.45	34.9
0.36	5.4	0.04	5.7	−5.3	4.36	23.9
0.31	3.7	0	4.5	−27.8	3.5	5.7
0.17	1.1	0	1.5	−36.7	1.21	−9.1

These findings align with the cell voltage curve fits (fig. 4.14) and suggest that the ZBS model, with γ as determined by equation eq. (4.41), is most suitable for medium to high active material porosities. For batteries with low ε_s values, however, the MG model provides a more accurate representation of the effective electrolyte ionic conductivity. This indicates that such an electrode operates in a regime where the electrolyte filler particles are not densely packed. For subsequent simulations, the appropriate model for calculating κ is selected based on ε_s, with a sigmoid function employed to ensure a smooth transition between the MG and ZBS models at $\varepsilon_s = 0.31$.

4.6.2 Impact of active filler content in the electrolyte

The ratio of host to inclusion material in a composite electrolyte is a critical factor influencing battery performance. In particular, the $\varphi_{el,fil}$ parameter represents the proportion of polymer within the electrolyte, which consists of both active filler particles and the encompassing polymer.

Figure 4.15 illustrates the effects of varying the NaSICON-type active filler content in the electrolyte on the battery's discharge performance. In this study, the NVP content is consistently maintained at 50 %, with a cathode length of 100 µm, yielding a theoretical specific capacity of 204 A h L^{-1}. The simulations were conducted by varying the $\varphi_{el,fil}$ from 0–100 % across different C-rates, ranging from 0.05 C to 10 C. The resulting Depth of Discharge (DoD) was then analyzed.

For low C-rates, such as 0.05 C, electrodes with a $\varphi_{el,fil}$ exceeding 0.3 achieve full utilization, reaching 100 % DoD. However, at C-rates of 0.5 C and higher, full capacity utilization is not achieved, even with a pure NaSICON electrolyte. Overall, the capacity utilization increases with higher $\varphi_{el,fil}$, particularly at lower C-rates. However, at C-rates of 1.0 C and higher, the addition

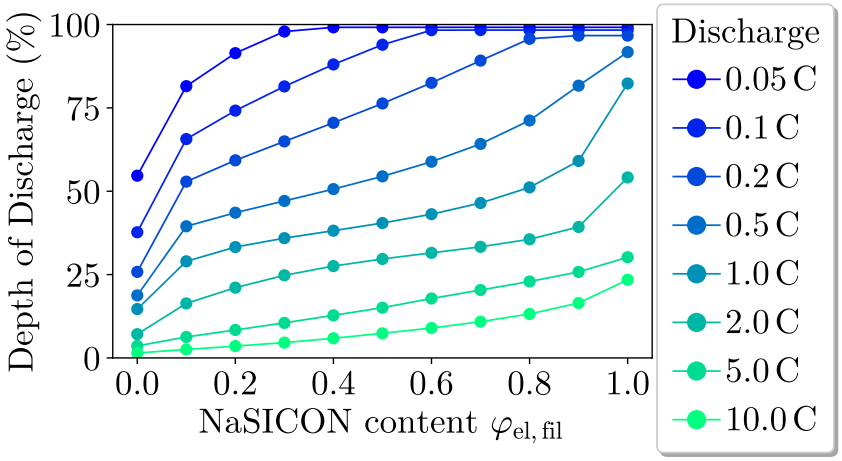

Figure 4.15: Influence of electrolyte electrolyte active filler volume fraction ($\varphi_{\mathrm{el,fil}}$) on battery **discharge** performance. This figure illustrates how varying the NaSICON-type active filler content within the composite electrolyte affects battery behavior, with a constant NVP content of 50 % and a cathode thickness of 100 µm. The simulations, conducted across C-rates from 0.05–10 C, demonstrate the resulting Depth of Discharge (DoD) relative to a theoretical specific capacity of 204 A h L^{-1}.

of NaSICON fillers does not result in satisfactory utilization, as the DoD remains below 50 % in all scenarios.

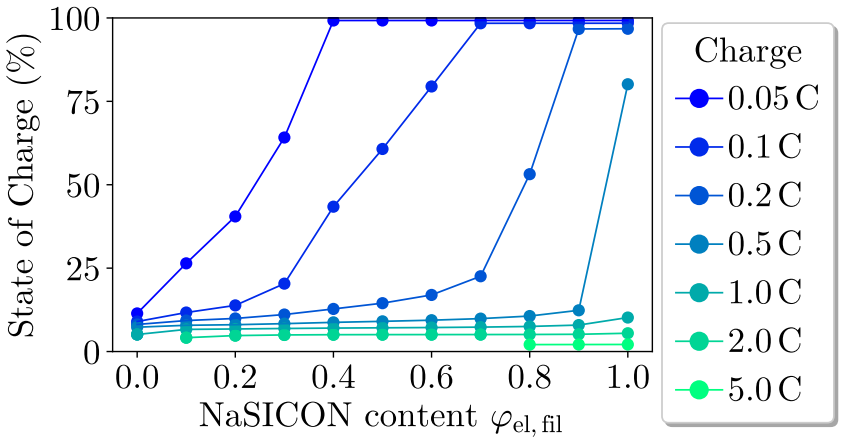

Figure 4.16: Influence of electrolyte electrolyte active filler volume fraction ($\varphi_{\mathrm{el,fil}}$) on battery **charge** performance. This figure illustrates how varying the NaSICON-type active filler content within the composite electrolyte affects battery behavior, with a constant NVP content of 50 % and a cathode thickness of 100 µm. The simulations, conducted across C-rates from 0.05–5 C, demonstrate the resulting State of Charge (SOC) relative to a theoretical specific capacity of 204 A h L^{-1}.

Figure 4.16 displays the influence of electrolyte active filler content on the charging performance of the battery system. In contrast to the discharge process, the charging efficiency significantly diminishes as C-rates increase. For example, when charging at 0.5 C, the electrode utilizes only 10 % of its capacity across most $\varphi_{\mathrm{el,fil}}$ values, compared to approximately 50 % during discharging. This distinct behavior is due to transport limitations within the electrolyte. At the initial stages

of charging or discharging, the majority of charge transfer reactions occur near the separator. As charging progresses, the consumption of Na^+ depletes the charge-carrying species in the electrolyte, potentially leading to an abrupt halt in the charging process if ionic transport is inadequate.

4.6.3 Influence of electrode porosity

The volume fraction of active material within the electrode is a pivotal factor in the design and optimization of battery systems. Increasing active material content (φ_{AM}) is generally beneficial, as it boosts the theoretical capacity of the battery, thereby enhancing its energy storage potential. However, surpassing a certain φ_{AM} threshold can lead to diminishing returns in resource utilization efficiency due to transport limitations within the electrode and electrolyte. These limitations arise from hindered ion and electron transport, which negatively impact the battery's overall performance and longevity. The degree to which these limitations affect the system is highly dependent on the specific materials employed. The following section delves into how these transport constraints influence the performance of the battery system under study.

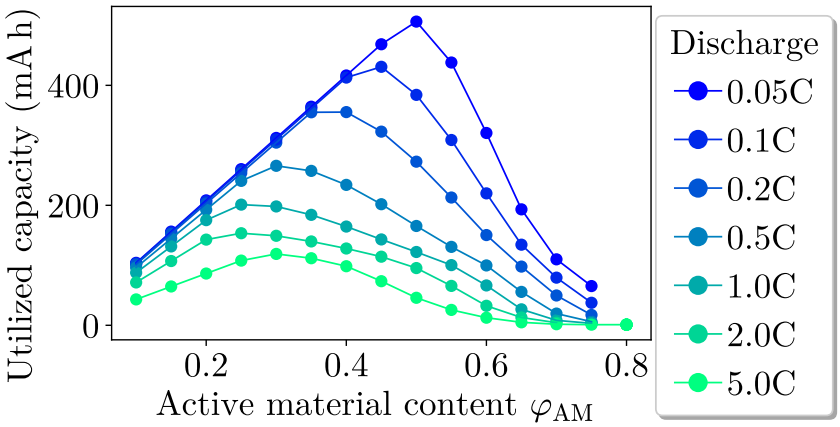

Figure 4.17: Utilized capacity in relation to active material content (φ_{AM}) throughout the discharge process at varying C-rates from 0.05–5 C, maintaining a consistent electrolyte active filler volume fraction of 50 %.

Figure 4.17 shows how the utilized capacity varies with φ_{AM} across different C-rates during the discharge process. The simulations are based on a cathode electrode with a cross-sectional area of 0.028 m^2 and a fixed electrolyte active filler volume fraction of 50 %. For all tested C-rates, capacity utilization exhibits a characteristic trend: it remains low at minimal φ_{AM} values, gradually increases as φ_{AM} rises, and subsequently declines at higher φ_{AM} levels. At low φ_{AM}, the capacity is constrained by the theoretical limit, whereas at elevated φ_{AM}, transport limitations within the electrolyte—resulting from reduced electrolyte volume, increased tortuosity, and higher current demands—become the dominant restricting factors. The optimal φ_{AM} is strongly dependent on

the C-rate: a φ_{AM} of 0.5 proves ideal for a 0.05 C discharge, while a φ_{AM} of 0.30 is more effective for a 5 C discharge.

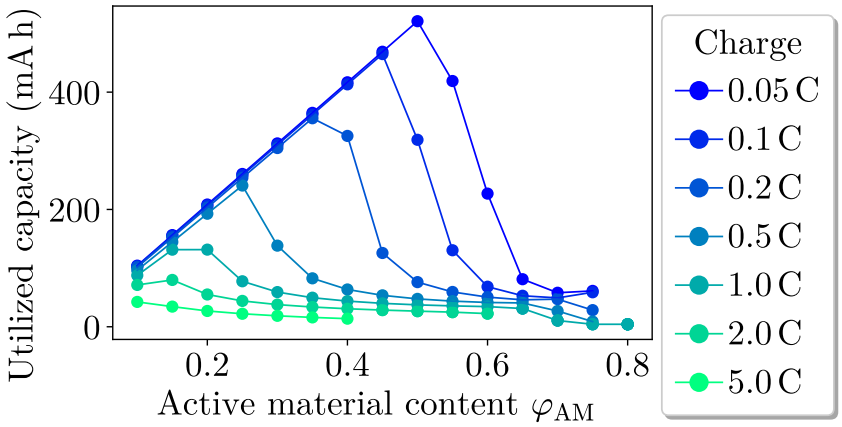

Figure 4.18: Utilized capacity in relation to active material content (φ_{AM}) throughout the charge process at varying C-rates from 0.05–5 C, maintaining a consistent electrolyte active filler volume fraction of 50 %.

Figure 4.18 illustrates the relationship between φ_{AM}, C-rate, and capacity utilization during the charge process. When φ_{AM} exceeds its optimal value, the decline in utilized capacity is more pronounced during charging than during discharging. Additionally, for C-rates above 0.2 C, the utilized capacity remains subpar, a trend consistent with findings from the investigation of $\varphi_{el,fil}$ variation in section 4.6.2.

4.6.4 Effect of active material particle size

The size of the active material particles is a critical morphological parameter in battery design and optimization, notable for its relative ease of control and measurement compared to more complex characteristics such as surface roughness, particle shape, and internal porosity. Consequently, particle size has garnered significant attention in the field of battery research and development. In practical battery applications, active material particles typically exhibit a distribution of sizes; however, this study focuses on monodisperse particles to isolate and precisely evaluate the effects of particle size on battery performance.

Figure 4.19 depicts the depth of discharge achieved at the end of the discharge process for electrodes with φ_{AM} = 50 % and a cathode length of 100 µm, across various particle sizes (R_{AM}) ranging from 0.25–100 µm. For particle sizes smaller than 2 µm, the depth of discharge remains almost constant. However, it declines sharply for particle sizes larger than 10 µm. This trend is consistent across all C-rates, with the depth of discharge values plateauing at low C-rates, a phenomenon attributed to transport limitations in the electrolyte that remain unaffected by changes in R_{AM}.

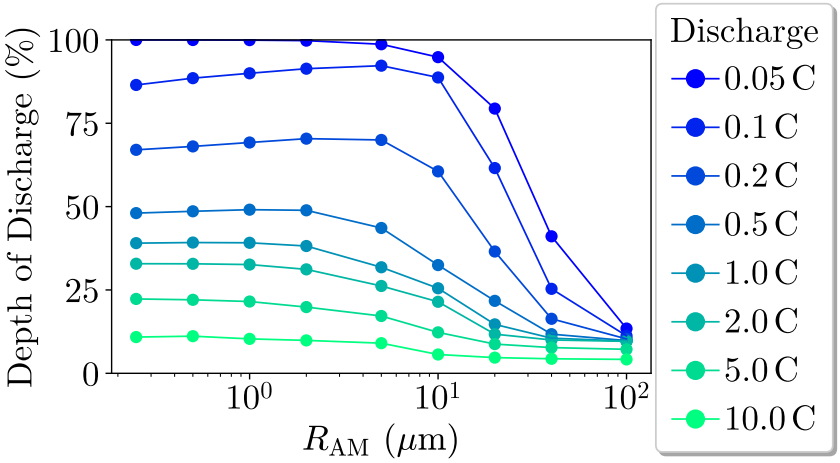

Figure 4.19: Variation in depth of discharge (DoD) with respect to (active material particle radius (R_{AM})) during the discharge process. This graph highlights the influence of particle size on battery performance, using an electrode with 50 % active material content and a cathode length of 100 µm. The data reveal how particle size impacts discharge efficiency across different scales.

Figure 4.20 shows the state of charge (SoC) for different R_{AM} values during the charging process. Similar to the discharge process, the capacity utilization during charging is reduced for C-rates exceeding 0.2 C. The SoC remains almost constant for particle sizes less than 2 µm contrasting a significant decrease in SoC for particle sizes greater than 10 µm.

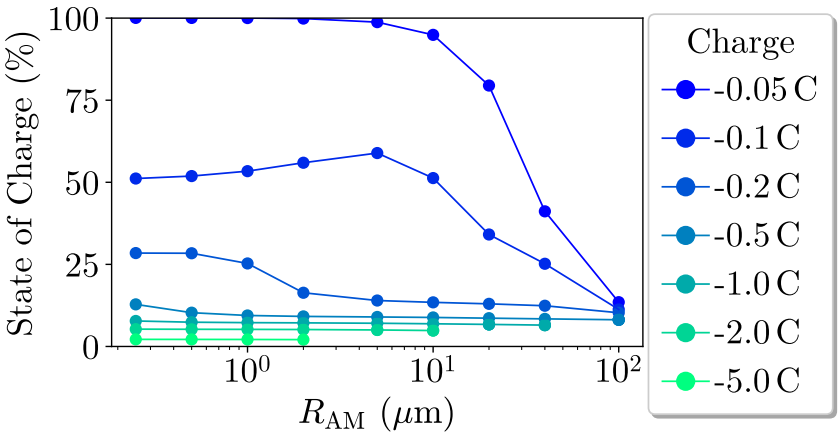

Figure 4.20: Variation in state of charge (SoC) with respect to (active material particle radius (R_{AM})) during the charging process. This graph highlights the influence of particle size on battery performance, using an electrode with 50 % active material content and a cathode length of 100 µm. The data reveal how particle size impacts discharge efficiency across different scales.

The findings suggest that a particle size of 4 µm is optimal for achieving the best performance. Reducing the particle size further does not provide a substantial improvement and may introduce practical challenges in manufacturing and handling. Moreover, smaller particles can lead to

decreased electrical conductivity within the electrode due to an increased number of particle-to-particle contacts.

4.6.5 Variation of spatial active filler content

In previous sections, the distribution of active material and active filler within the positive electrode was considered uniform. However, results from the present work suggest that battery processes, such as charge transfer reactions, are not evenly distributed and tend to concentrate in specific regions of the electrode. This suggests the potential for a non-uniform distribution of materials to enhance battery performance.

To explore this, the ratios of active material and active filler were systematically varied, while maintaining their average values constant at $\overline{\varphi_{\mathrm{AM}}} = 0.5$ and $\overline{\varphi_{\mathrm{fil}}} = 0.25$. The polymer volume fraction (φ_{pol}) remained fixed at 0.25 throughout the entire half-cell. Consequently, the sole variable was the distribution ratio between active material and active filler across the cathode. Three distribution functions were employed to model the spatial variation of the active material content: hyperbolic tangent (tanh), linear, and hyperbolic sine (sinh) functions, each with distinct slope characteristics.

The tanh distribution function, described by eq. (4.42), is defined by a parameter a, which modulates the slope:

$$\varphi_{\mathrm{AM}} = \begin{cases} \overline{\varphi_{\mathrm{AM}}} & \text{for} \quad a = 0 \\ \dfrac{\min\left(\overline{\varphi_{\mathrm{fil}}}, \overline{\varphi_{\mathrm{AM}}}\right)}{\tanh \frac{|a^*|}{2}} \tanh\left(a \dfrac{\frac{L_p}{2} - x_p}{L_p}\right) + \overline{\varphi_{\mathrm{AM}}} & \text{for} \quad a \neq 0 \end{cases} \tag{4.42}$$

Here, a determines whether the distribution approximates a step function for large values or a linear function for small values.

The linear distribution function, specified in Equation eq. (4.43), maintains physical validity with a ranging from -1 to 1:

$$\varphi_{\mathrm{AM}} = -2a \min\left(\overline{\varphi_{\mathrm{fil}}}, \overline{\varphi_{\mathrm{AM}}}\right) \frac{x_p}{L_p} + \overline{\varphi_{\mathrm{AM}}} + a\overline{\varphi_{\mathrm{fil}}} \qquad -1 \leq a \leq 1 \tag{4.43}$$

The sinh distribution function employed in this work is described by eq. (4.44). For large a values, the function approximates a nearly constant distribution with steep gradients at the separator and current collector. When a approaches zero, the function closely resembles a linear distribution:

$$\varphi_{\mathrm{AM}} = \frac{\min\left(\overline{\varphi_{\mathrm{fil}}}, \overline{\varphi_{\mathrm{AM}}}\right)}{\sinh \frac{|a^*|}{2}} \sinh\left(a^* \frac{\frac{L_p}{2} - x_p}{L_p}\right) + \overline{\varphi_{\mathrm{AM}}} \qquad \text{with} \qquad a^* = \mathrm{sgn}\,(a)\,(a_{\max} - \mid a \mid) \tag{4.44}$$

To compute the effective transport properties in the electrolyte, the solver additionally requires the distribution of $\varphi_{\text{el,pol}}$, which is calculated as:

$$\varphi_{\text{el,pol}} = \frac{\overline{\varphi_{\text{pol}}}}{1 - \varphi_{\text{AM}}} \tag{4.45}$$

The distributions of ε_{s} and $\varphi_{\text{el,pol}}$ are depicted in the middle column of fig. 4.21 (figs. 4.21b, 4.21e and 4.21h).

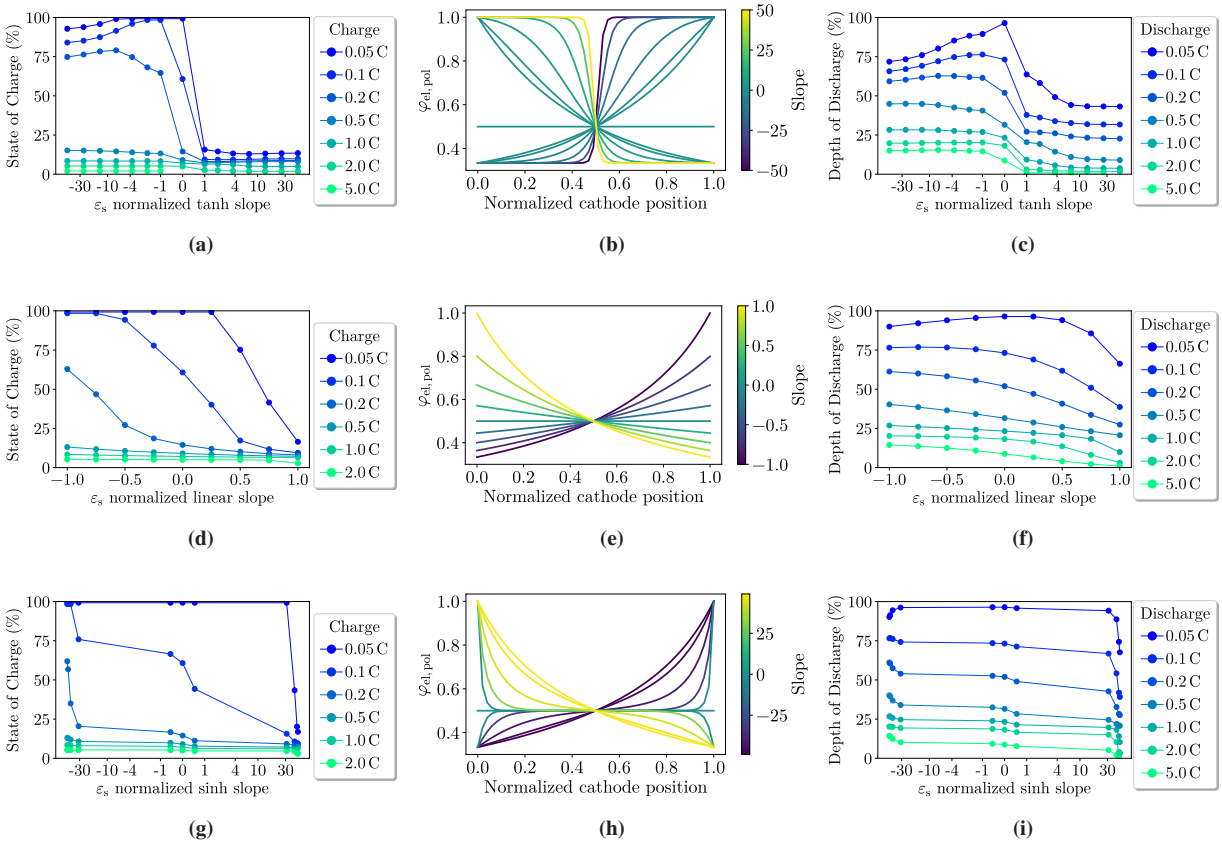

Figure 4.21: This multi-panel figure presents a comparative analysis of different distributions of active material porosity (ε_{s}) and active filler volume fraction (φ_{fil}) within the positive electrode, focusing on both charging and discharging performance. The figure is organized into three distinct columns and three rows as follows:

Left Column (figs. 4.21a, 4.21d and 4.21g) Displays the State of Charge (SOC) achieved at the end of the charging process for electrodes with tanh, linear, and sinh distributions of the active material. The SOC is plotted against the slope parameter of each distribution function, illustrating how different distribution profiles impact charging efficiency

Middle Column (figs. 4.21b, 4.21e and 4.21h) Illustrates the spatial distribution of the polymer volume fraction (φ_{pol}) within the half-cell for each distribution type (tanh, linear, and sinh). This column demonstrates the variations in φ_{pol} as influenced by different distribution slope parameters.

Right Column (figs. 4.21c, 4.21f and 4.21i) Shows the Depth of Discharge (DoD) at the end of the discharging process for electrodes with the same distributions of the active material. This column compares how different distribution profiles affect the discharge performance of the battery.

The left column (figs. 4.21a, 4.21d and 4.21g) illustrates the state of charge (SoC) at the end of the charging process for electrodes with tanh, linear, and sinh distributions of φ_{AM}. The SoC is plotted against the slope of the respective distribution, with the length of the positive half cell kept constant at 100 µm. Similarly, the right column (figs. 4.21c, 4.21f and 4.21i) shows the depth of discharge (DoD) upon completion of the discharge process. Different colors in the SoC and DoD plots represent charging and discharging at various C-rates.

In evaluating the spatial distribution of active filler content, it is observed that a negative slope in the active material distribution function (ε_{s}) consistently results in a higher achievable SoC at the end of the **charging** process compared to a positive slope. Specifically, a negative ε_{s} slope implies that the active material content is higher near the separator (normalized cathode position = 0), which provides additional space for active filler particles and thus reduces $\varphi_{\mathrm{el,pol}}$. Conversely, the ε_{s} value decreases towards the cathode current collector (normalized cathode position = 1), leading to an increase in $\varphi_{\mathrm{el,pol}}$ due to reduced space for active filler particles.

In greater detail, during the charging process at C-rates of 0.05 C and 0.1 C, every distribution evaluated achieves a depth of discharge (DoD) of 100 %, signifying complete capacity utilization. Among these, the sinh distribution with a large negative slope performs comparably to the linear distribution, suggesting that the sinh distribution does not offer a significant advantage over the linear distribution for charging purposes. In contrast, a battery with a tanh distribution reaches an SoC exceeding 75 % at the end of the charging process with moderately negative slopes and a 0.2 C charge rate, yielding a 15 % improvement over the linear ε_{s} distribution. For C-rates greater than 0.2 C, none of the distributions achieve satisfactory SoC levels.

At a 0.05 C **discharging** rate, batteries with tanh, linear, and sinh ε_{s} distributions (figs. 4.21c, 4.21f and 4.21i) achieve the highest DoD when a constant ε_{s} (i.e., $a = 0$) is employed, indicating that a uniform ε_{s} distribution is advantageous under these conditions. In contrast, for C-rates exceeding 0.05 C, a negative slope in the active material distribution function (ε_{s}) benefits the DoD across all distribution types. Nonetheless, the enhancement in DoD is less significant compared to charging, with improvements typically ranging from 0–10 %. The more complex sinh and tanh distributions do not offer advantages over the simpler linear distribution. Simulation results indicate that the most effective distribution has a normalized linear slope of -1, characterized by high porosity near the separator that decreases uniformly toward the current collector.

4.6.6 Global optimization of the cell-design

Preceding sections focused on varying individual parameters to improve battery performance. While this approach enhances understanding and enables predictions for parameter optimization, it is unlikely to yield a globally optimal battery design due to the complexity of the battery system.

A battery operates as a highly interconnected and non-linear system, where numerous input parameters interact with each other. Achieving an optimal design necessitates considering these interactions collectively rather than in isolation.

The P2D battery model, with its relatively low computational cost and short run time, serves as an ideal candidate for use in global optimization processes. For this purpose, a differential evolution algorithm was employed, as described by Storn and Price [196]. Differential evolution is particularly suitable for this type of optimization because it is capable of exploring extensive candidate spaces and circumvent local minima due to its stochastic nature, despite requiring more function evaluations compared to traditional gradient-based methods.

The Python package scipy, version 1.12.0, was used to implement the optimization. The P2D model of an all-solid-state sodium-ion battery featuring a hybrid electrolyte—developed in this work—serves as the objective function for the optimization routine. Specifically, the function evaluates the utilized gravimetric capacity of the battery.

The parameters subject to optimization include the active material content (φ_{AM}), the linear slope of the spatial active material distribution (a), and the length of the positive half cell (L_{pos}). In contrast, the particle size of the active material (R_{AM}) was excluded from the optimization process. As previously discussed in section 4.6.4, R_{AM} shows a monotonic relationship with capacity utilization, which would lead the optimizer to consistently favor the lower limit. Moreover, a very small R_{AM} is impractical due to challenges in manufacturing and processing, as well as the increased grain boundary surface area. Although R_{AM} could theoretically be included in the optimization as an additional objective, a simpler approach is to constrain R_{AM} to a user-defined value using the ε-constraint method [197]. This method is justified by the observation that values of R_{AM} smaller than 4 µm do not enhance battery performance.

Although advancements in technology may make it feasible to produce thinner NaSICON separators in the future, a thickness of 5×10^{-3} µm is currently used for length of the separator (L_{sep}) due to the fragility of thinner separators.

Table 4.5: Gravimetric properties of the all-solid-state sodium-ion battery.

Parameter	Value	Reference
ϱ_{PEO}	$1250\,\mathrm{kg\,m^{-3}}$	[198]
ϱ_{fil}	$3170\,\mathrm{kg\,m^{-3}}$	[199]
$\varrho_{\mathrm{NVP,C}}$	$3200\,\mathrm{kg\,m^{-3}}$	[200]
ϱ_{CC}	$0.012\,\mathrm{kg\,m^{-2}}$	[201]
N/P	1	[202]

Table 4.5 provides the densities of the battery materials, including the separator and current collector. These components, whose thicknesses are independent of L_{pos}, must be included in the optimization to prevent the algorithm from selecting excessively thin electrodes. The overall gravimetric capacity can be straightforwardly calculated using material densities, volume fractions, and utilized capacity. Ultimately,the optimization results for C-rates ranging from 0.05–0.5 C are summarized in table 4.6.

Table 4.6: Results of global optimization for the all-solid-state sodium-ion battery across different C-rates ranging from 0.05 C to 0.5 C. This table summarizes the optimal design parameters, including the volume fraction of active material (φ_{AM}), electrode thickness (L_{pos}), and the linear slope of the spatial active material distribution (a), for both charging and discharging processes. The table also highlights the achieved capacity utilization for each C-rate, illustrating the variations and trade-offs in battery performance. For each C-rate, the optimized design parameters are compared to those derived from separate optimizations for charging and discharging, providing insights into the performance limitations and the effectiveness of the global optimization approach.

C	φ_{AM}	a	L_{pos} (µm)	Used capacity ($A\,h\,kg^{-1}$)
		Discharging		
0.05	0.477	-0.00	97.2	37.8
0.1	0.448	-0.01	79.9	32.4
0.2	0.429	-0.22	66.2	27.3
0.5	0.370	-0.28	56.1	20.6
		Charging		
0.05	0.566	-0.62	117.3	47.8
0.1	0.543	-0.71	101.5	43.2
0.2	0.547	-0.72	79.6	38.5
0.5	0.525	-0.77	61.6	31.1
		Charging and Discharging		
0.05	0.478	-0.03	97.34	37.83
0.1	0.445	-0.20	85.6	32.3
0.2	0.401	-0.18	75.6	27.2
0.5	0.372	-0.30	56.5	20.5

Contrary to earlier predictions suggesting higher capacity utilization during discharge, the optimization reveals that charging processes achieve higher capacity than discharging for optimally selected cell design parameters. Specifically, the charging capacity is 10.5 $A\,h\,kg^{-1}$ (51 %) higher at 0.5 C and 10 $A\,h\,kg^{-1}$ (26.5 %) higher at 0.05 C compared to discharging. This improvement

is attributed to the increase in the thickness of the electrode during charging —by 5.4 µm at 0.5 C and 19.9 µm at 0.05 C—and a higher φ_{AM} during charging (0.155 for 0.5 C and 0.089 for 0.05 C).

For elevated C-rates, both L_{pos} and φ_{AM} decrease: L_{pos} ranges from 61.6–117.3 µm and φ_{AM} from 0.525–0.566 for charging, while for discharging, L_{pos} ranges from 56.1–97.2 µm and φ_{AM} from 0.370–0.477. The slope of the active material and filler particle distribution (a) increases with C-rate, ranging from −0.77–−0.62 for charging and −0.28–0 for discharging.

The final row of table 4.6 presents the combined optimization results for both charging and discharging processes. For each parameter set, simulations were performed for both charge and discharge cycles, with the lower utilized capacity being reported as the limiting factor. Simulations predict that the capacity utilization for the combined charging and discharging cycle is nearly equivalent to that for discharging alone. Although this finding may seem intuitive given the lower utilization observed during discharge in previous optimization studies, a more nuanced analysis reveals several insights.

Firstly, parameter studies indicate that the charging process is highly sensitive to input parameters, often terminating prematurely if parameters are suboptimal. Secondly, the optimization for combined charging and discharging yields different parameter sets for some C-rates compared to those electrodes optimized solely for discharging. For example, batteries optimized for both charging and discharging are thicker and have lower φ_{AM} values at C-rates of 0.1 and 0.2.

The global optimization of cell design offers the following key insights:

- The optimal cell design is highly dependent on the C-rate, with higher C-rates requiring lower φ_{AM}, reduced L_{pos}, and a more uneven particle distribution with increased porosity near the separator.
- Optimizing the design separately for charging and discharging results in distinct configurations.

4.7 Superionic interphases and their role in ionic transport[6]

As discussed in section 2.2.2, a variety of hypotheses have been proposed regarding the mechanisms governing ionic transport in polymer-ceramic composite electrolytes. Despite extensive research spanning decades, the exact nature of these transport processes remains a subject of ongoing debate

[6] This section includes results and findings that were previously reported in Gerbig, F., Röttgen, N., Holzapfel, M., Dück, G., Finsterbusch, M., and Nirschl, H.: Unraveling ionic transport in polymer-ceramic electrolytes: Insights into superionic interphases. *Electrochemistry Communications*, **2025**, 107960. DOI: 10.1016/j.elecom.2025.107960

within the scientific community. This section contributes to the broader effort by investigating the transport mechanisms within polymer-ceramic composite electrolytes, specifically focusing on the superionic interphase that is hypothesized to form between the two materials.

The primary goal of this study is to compare experimental measurements of ionic conductivity with those predicted by the numerical solver developed and employed throughout this work. By simulating the effective conductivities, this analysis seeks to provide insights into the role that interactions between polymers and ceramics play in enhancing ionic transport. To ensure the study focuses on the inherent properties of the composite electrolyte, all simulations and experiments were conducted using a pure electrolyte material, without any active electrode materials present, thereby isolating the composite effects.

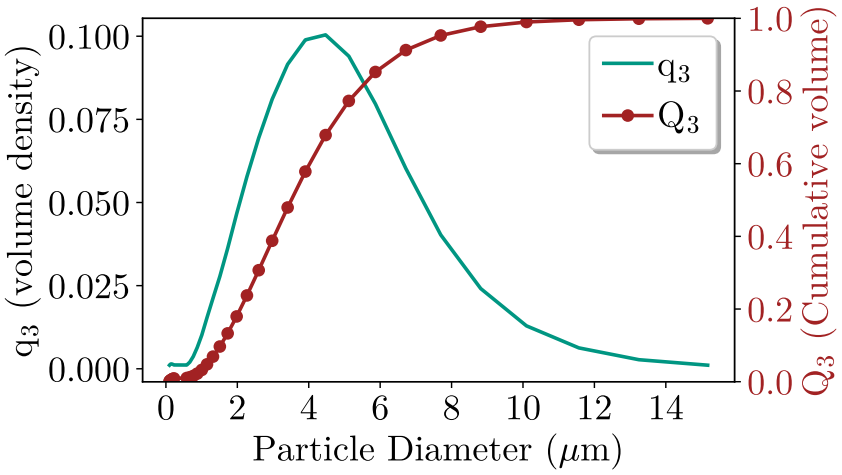

Figure 4.22: Measured particle size distribution of NaSICON particles used in the microstructure simulations, showing both the density distribution and the cumulative sum distribution of particle sizes, based on number. The distribution is monomodal with a median particle size (d_{50}) of 3.5 µm.

To accurately model the composite, it is essential to consider the individual conductivities of each phase: the polymer electrolyte (PEO) and the ceramic filler (NaSICON). For this study, conductivity measurements were available for two composite electrolyte samples, each consisting of a 50 % PEO matrix and 50 % of either $Na_{3.4}Zr_2Si_{2.4}P_{0.6}O_{12}$ or $Na_3Zr_2Si_{2.3}P_{0.7}O_{11.85}$. Determining these phase-specific conductivities along with the composite conductivity allows for a more precise understanding of how ionic transport occurs within the heterogeneous system.

Additionally, the particle size distribution of the ceramic phase plays a critical role in influencing transport properties and must be carefully incorporated into the model. For this purpose, experimental measurements of the particle size distribution were used to faithfully represent the microstructure of the composite in the simulations. The particle size distribution of the sample, depicted in fig. 4.22, was characterized by a monomodal distribution with a median particle size (d_{50}) of 3.5 µm. Particles smaller than 1 µm were excluded from the computational analysis to maintain consistency with the resolution of the computational mesh. The contribution of these

smaller particles to the total particle surface area was ensured to be less than 0.25 ‰, minimizing any impact on the overall simulation accuracy. The experimental data used for this analysis are shown in table 4.7 [203].

Table 4.7: Measured conductivity of solid electrolytes employed in this study [203].

	$\kappa(25\,^{\circ}\mathrm{C})$ (S m^{-1})	$\kappa(80\,^{\circ}\mathrm{C})$ (S m^{-1})
PEO	5.5×10^{-4}	8.9×10^{-2}
$Na_3Zr_2Si_{2.3}P_{0.7}O_{11.85}$	1.7×10^{-1}	7.9×10^{-1}
$Na_{3.4}Zr_2Si_{2.4}P_{0.6}O_{12}$	3.4×10^{-1}	1.7

These experimental results serve as the benchmark for validating the numerical predictions. To represent the system's geometry accurately, the methodology outlined in section 4.4.1 was adapted to incorporate the particle size distributions measured experimentally. This ensures that the simulated microstructure closely reflects the real composite material.

Simulations were subsequently performed using the ASSSIB microstructure solver, enabling a comprehensive analysis of ionic transport within the composite electrolyte. The solver was employed to numerically solve the charge conservation equation in the electrolyte phase. To determine the effective ionic conductivity (κ_{eff}), boundary conditions were imposed by setting fixed potentials at the opposing ends of the electrolyte domain ($\Phi_{\mathrm{el,x=L}}$ and $\Phi_{\mathrm{el,x=0}}$), commonly assigning a reference potential difference of 1 V. Utilizing the known length L and current collector area A, the ionic current at one boundary ($i_{\mathrm{el,x=L}}$) was used to compute the effective conductivity based on the following relation:

$$\kappa_{\mathrm{eff}} = \frac{L \left| i_{\mathrm{el,x=L}} \right|}{A \left(\Phi_{\mathrm{el,x=L}} - \Phi_{\mathrm{el,x=0}} \right)} \tag{4.46}$$

By comparing the simulated effective conductivities with experimental results, this study aims to shed light on the mechanisms responsible for the enhanced ionic transport observed in polymer-ceramic composite electrolytes.

In this study, conductivity measurements of $Na_{3.4}Zr_2Si_{2.4}P_{0.6}O_{12}$ revealed no noticeable improvement compared to the conductivity of pure PEO. At 80 °C, the conductivity of the composite solid electrolyte (CSE) dropped to 5.4×10^{-2} S m^{-1}, whereas the conductivity of PEO alone remained higher at 8.9×10^{-2} S m^{-1}. This indicates that the NaSICON phase does not significantly contribute to Na^+ transport, likely resulting in a reduced effective conductivity due to longer ion transport pathways and increased porosity. At room temperature (25 °C), below the melting point of the quasicrystalline phase, the CSE conductivity (6.4×10^{-4} S m^{-1}) is comparable to that of the solid polymer electrolyte (SPE) (5.5×10^{-4} S m^{-1}). This behavior could be attributed to

partial amorphization of the PEO, which offsets the negative impact of the filler particles at this lower temperature.

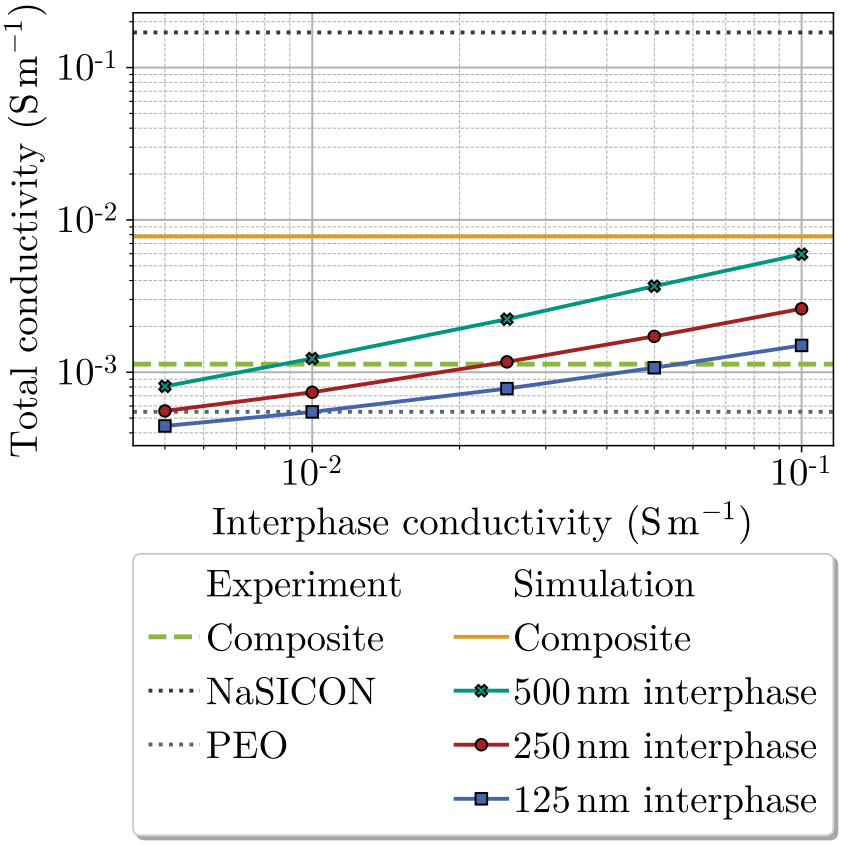

Figure 4.23: Comparison of total ionic conductivity as a function of interphase conductivity between experimental data and simulations for NaSICON-PEO composite electrolytes. Experimental data for NaSICON (gray dotted line), PEO (black dotted line), and the composite (green dashed line) are shown alongside simulation results for full ion transport (yellow solid line) and different interphase thicknesses: 500 nm (green crosses), 250 nm (red circles), and 125 nm (blue squares) at **25 °C**.

Figure 4.23 presents a comparison between the experimentally measured and simulated conductivities for this polymer-ceramic composite electrolyte at 25 °C. The green dashed line represents the experimental conductivity value for the composite, measured at 1.13×10^{-3} S m^{-1}, positioned between the conductivities of pure PEO and NaSICON, shown by the dotted lines. In contrast, the orange solid line represents the simulated conductivity (7.78×10^{-3} S m^{-1}), which assumes that full ionic transport occurs through both the polymer matrix (PEO) and the ceramic filler phase (NaSICON). The notable difference between these values suggests that the assumption of complete ionic transport through all phases may be an oversimplification.

To explore alternative mechanisms, a hypothesis was tested wherein ionic transport occurs primarily in a superionic interphase surrounding the ceramic filler particles, rather than through the ceramic phase itself. In this scenario, the conductivity of the ceramic particles was set to zero,

and enhanced ionic conductivity was introduced within the PEO matrix in close proximity to the ceramic particles. The simulations shown in fig. 4.23 were performed with varying thicknesses for this superionic interphase, representing regions with improved ionic transport properties.

Solid lines with markers in fig. 4.23 show the resulting simulated conductivities for interphase thicknesses of 125 nm, 250 nm, and 500 nm, with varying conductivities, as precise interphase properties remain uncertain. A linear relationship between total composite conductivity and the interphase conductivity is observed on a double logarithmic scale.

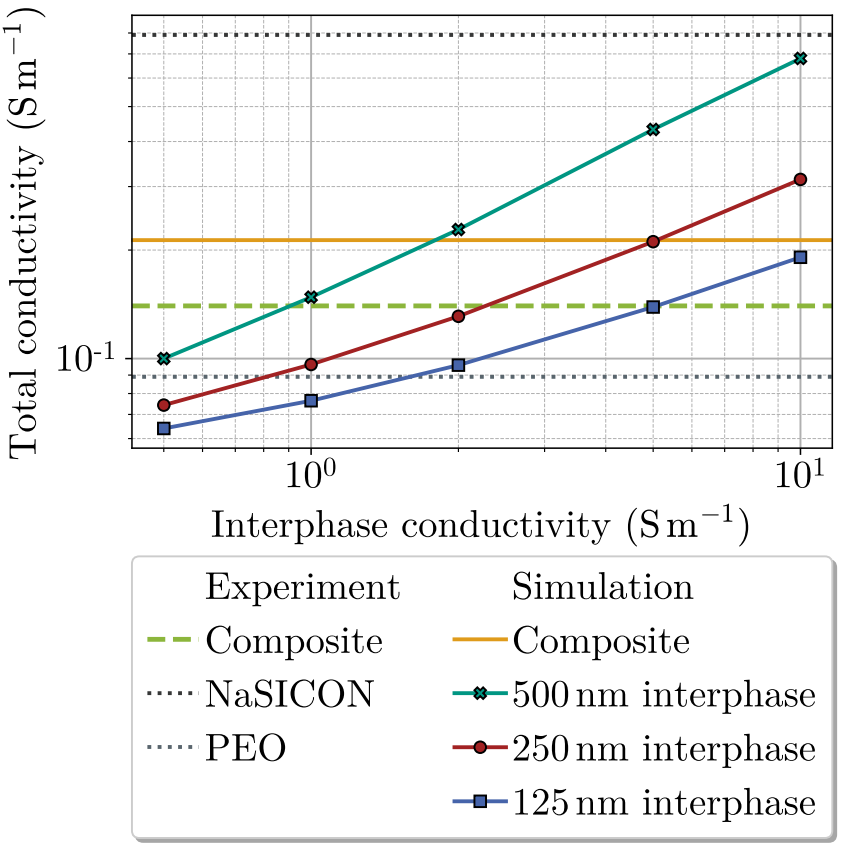

Figure 4.24: Comparison of total ionic conductivity as a function of interphase conductivity between experimental data and simulations for NaSICON-PEO composite electrolytes. Experimental data for NaSICON (gray dotted line), PEO (black dotted line), and the composite (green dashed line) are shown alongside simulation results for full ion transport (yellow solid line) and different interphase thicknesses: 500 nm (green crosses), 250 nm (red circles), and 125 nm (blue squares) at **80 °C**.

The intersection of these lines with the experimentally measured conductivity suggests that potential combinations of interphase thickness and conductivity, such as 125 nm with a conductivity of 5.5×10^{-2} S m^{-1}, 250 nm with a conductivity of 2.15×10^{-2} S m^{-1}, or 500 nm with a conductivity of 8.6×10^{-3} S m^{-1}, could help explain the measured performance. These results suggest that—in the investigated sample—ionic transport is confined to a superionic interphase, rather than occurring uniformly throughout the ceramic filler particles.

To explore the hypothesis that fillers improve conductivity by creating amorphous regions within the PEO matrix, which remain stable at ambient conditions, a comparable experiment was performed at 80 °C—a temperature above PEO's glass transition point, where the polymer exists primarily in an amorphous state. The outcomes of this comparative study at elevated temperature (80 °C) are presented in fig. 4.24. At this higher temperature, the conductivities of both the single phase electrolytes and the composite increase. Notably, the conductivity of the composite remains an order of magnitude higher than that of pure PEO. This observation challenges the theory that fillers enhance conductivity solely by inducing structural changes in the PEO bulk, as the polymer is already in an amorphous phase at 80 °C. Nevertheless, similar to observations at 25 °C, the simulation overestimates the effective conductivity of the composite electrolyte, though this overestimation is less pronounced at 80 °C. By neglecting the intrinsic conductivity of the filler particles and introducing superionic interphases, the measured conductivity at 80 °C can be explained with interphase thickness and conductivity combinations such as 125 nm with a conductivity of $4.84\,\mathrm{S\,m^{-1}}$, 250 nm with a conductivity of $2.06\,\mathrm{S\,m^{-1}}$, or 500 nm with a conductivity of $0.88\,\mathrm{S\,m^{-1}}$.

Notably, the interphase conductivity relative to the PEO conductivity is approximately halved at 80 °C compared to 25 °C. This reduction may be attributed to the relatively low conductivity of PEO at ambient temperature or could indicate an upper limit for the interphase conductivity. These findings emphasize the need for further investigation into the temperature dependence of ionic transport in polymer-ceramic composite electrolytes.

While these simulations offer a preliminary insight into possible transport mechanisms, it is important to emphasize that these results are exploratory and should be seen as an initial step toward understanding the complex behavior of polymer-ceramic composite electrolytes. Further research and more detailed experimental investigations will be required to validate these findings and refine the transport models.

4.8 Conclusion

The comprehensive application of the microscale simulation model and the pseudo-two-dimensional (P2D) simulation model for all-solid-state sodium-ion batteries (ASSIBs) featuring polymer-ceramic composite electrolytes has yielded several key conclusions.

The **microscale simulation model** proved to be highly effective in representing the particle structure within real cathode half-cells. The results of this model identified that slow sodium ion transport throughout the electrolyte is a major bottleneck affecting overall cell performance. This sluggish transport is mainly due to three critical factors: low porosity in the half-cell caused by a high active material content, the considerable distance between the separator and current collector

due to the thick half-cell, and the inherently low ionic conductivity of the electrolyte resulting from low active filler content. These factors collectively generate steep Na^+ concentration gradients, particularly near the separator, even at moderate C rates.

Given computational limitations, the study employed a one-factor-at-a-time approach to investigate the specific influence of crucial battery design parameters. The findings suggest that, at room temperature, cathodes with a electrolyte active filler volume fraction of approximately 80 % and electrode thicknesses of 100 µm or less are necessary to achieve adequate utilization of the theoretical battery capacity. These results underscore the critical need for the continued development of fast-ion-conducting solid electrolytes to enhance the performance of ASSSIBs. Furthermore, during the charging process, sodium ions are consumed primarily near the separator, significantly limiting utilization unless extremely high $\varphi_{\mathrm{el,fil}}$ values are achieved.

The pseudo-two-dimensional (P2D) model, which accounts for electrolyte transport throughout the half-cell while also considering diffusion within active material particles, allowed for the exploration of a broader parameter space. The microstructure simulation results were instrumental in informing the P2D model, thereby ensuring consistency and accuracy. A practical approach involved comparing the P2D model with results from the particle-resolved microstructure model to parameterize mixing rules for defining effective transport parameters in the electrolyte, reflecting the composition of a hybrid polymer-ceramic electrolyte in a tortuous active material matrix. The results suggest that the Zehner-Bauer-Schlünder model effectively represents low to medium active material content, while the Maxwell-Garnett model is more suitable for low active material porosity.

During discharging, cells with an electrolyte active filler volume fraction greater than 0.3 can achieve full utilization at low C-rates (around 0.05 C). However, at higher C-rates (0.5 C and above), even pure NaSICON electrolytes do not reach full utilization, suggesting that capacity utilization increases with $\varphi_{\mathrm{el,fil}}$ more significantly at lower C-rates. In contrast, the charging process exhibits drastically reduced utilization as C-rates increase. This disparity is due to transport limitations within the electrolyte, where the consumption of sodium ions near the separator during charging leads to the depletion of charge-carrying species and a premature end to the process if transport capabilities are inadequate.

Further analysis indicated that the depth of discharge remains consistent for active material particle radii below 2 µm and decreases sharply for values above 10 µm, regardless of the C-rate. This decline is attributed to transport limitations in the electrolyte. The simulations recommend R_{AM} of 4 µm, as smaller sizes do not significantly enhance performance and present manufacturing and handling challenges. Moreover, smaller particles can reduce electrical conductivity within the electrode due to increased particle-particle contacts.

A more sophisticated battery cell design, incorporating an uneven spatial distribution of active material and active filler particles, has the potential to enhance overall battery performance, as

suggested by the P2D simulation results. The study explored the impact of spatial variation in active material content by varying the ratios of active material particles and active filler particles while maintaining constant average values. The findings indicate that a negative slope in the ε_s distribution leads to higher achievable states of charge and depths of discharge. Specifically, electrodes with high porosity near the separator that gradually decreases towards the current collector exhibit superior performance. The more complex hyperbolic tangent and hyperbolic sine distributions did not show significant improvement over a linear spatial distribution. The linear distribution with a normalized slope of -1 was found to be optimal, describing a positive half-cell with high porosity at the separator that linearly decreases towards the current collector.

In contrast to previous studies, the optimization efforts highlight the inherent complexities in achieving a globally optimal battery design, given the highly interconnected and non-linear nature of battery systems. The P2D model demonstrated its capability to be integrated into a differential evolution global optimization algorithm, proving effective despite the high number of model solution evaluations required.

The optimization results, encompassing a range of C-rates from 0.05–0.5 C, bring to light several crucial findings. It becomes evident that the selection of optimal cell design parameters allows the charging process to exploit considerably more capacity than the discharge process, with this difference being notably pronounced at both high and low C-rates. This is primarily due to the design's capability to accommodate thicker electrodes and increased active material volume fractions during charging. Furthermore, the investigation highlights that for low to moderate C-rates, the optimal design parameters are intricately tied to the specific C-rate being employed. This often requires a reduction in active material volume fractions, thinner electrode layers, and a more uneven distribution of particles, which emphasizes higher porosity near the separator.

Additionally, the analysis indicates that distinct cell configurations are necessary to optimize the performance for charging and discharging separately. Interestingly, when a battery is optimized to perform adequately for both processes, its performance during discharge is comparable to that of a design optimized solely for discharging. This finding underscores the importance of the discharge process as the critical factor limiting the full utilization of the battery's capacity. Therefore, these insights provide essential guidance for fine-tuning the design parameters of all-solid-state sodium-ion batteries with hybrid electrolytes, with a specific focus on overcoming the challenges posed by the discharging phase.

The comparison between the initial, limited experimental data on transport phenomena in polymer-ceramic electrolytes raises important considerations about the role of active fillers in facilitating charge transport. Specifically, the addition of $Na_{3.4}Zr_2Si_{2.4}P_{0.6}O_{12}$ into a PEO matrix did not exhibit any significant improvement in conductivity compared to the single-phase polymer electrolyte. Conversely, a composite solid electrolyte incorporating $Na_3Zr_2Si_{2.3}P_{0.7}O_{11.85}$ active

fillers demonstrated enhanced conductivity, although the measured values remained below those predicted by the model, which assumes ideal charge transport through both phases.

These results suggest that the assumption of full charge transport through the ceramic fillers may be overly optimistic. Furthermore, our findings challenge the theory suggesting that enhanced conductivity in the PEO bulk is due to structural changes induced by active fillers, which stabilize amorphous regions at ambient temperatures. Notably, a significant increase in conductivity was observed at 80 °C, where PEO is already in an amorphous state. An alternative, plausible explanation for the discrepancy is the existence of a superionic interphase between the polymer and ceramic phases. Simulations attributing the observed conductivity enhancement solely to this interphase produced reasonable values for interphase thicknesses in the submicrometer range and interphase conductivities that could account for the experimental results.

However, in certain cases, such as at elevated temperatures (80 °C) with an interphase thickness of 125 nm, the required interphase conductivity would need to be as high as $4.84\,\mathrm{S\,m^{-1}}$. This raises questions about the feasibility of a polymer-based interphase achieving such high ionic conductivities. Furthermore, it remains unclear why such an interphase—if present in one composite—appears absent in the composite using $Na_{3.4}Zr_2Si_{2.4}P_{0.6}O_{12}$ fillers.

An alternative explanation is that charge transport does occur within the ceramic filler particles but is hindered by a charge transfer resistance at the particle surface. The magnitude of this resistance could vary across different compositions, potentially explaining the reduced or even inhibited charge transport observed in the NaSICON phases. These insights call for further experimental and theoretical investigation to fully understand the interfacial dynamics and the role of active fillers in composite electrolytes.

5 Summary and Outlook

5.1 Summary

The presented work is on the cell-design of novel sodium-based battery systems focusing on the positive half-cell. The main contributions lie in the development of detailed models and simulations that capture charge and mass transport, as well as electrochemical reactions, while accounting for the specific geometry of the electrodes.

Through physics-based electrochemical simulations, the study quantified how different cell design parameters influence the overall performance of next-generation sodium-ion batteries. These simulations were applied to investigate two promising battery systems, each representing a novel chemistry within the two main categories of sodium-based batteries: the **sodium-iodine battery** for molten sodium systems and the **all-solid-state sodium-ion battery with a polymer-ceramic composite electrolyte** for sodium-ion systems.

Sodium iodine batteries The sodium-iodine battery is a unique energy storage system that integrates a molten sodium anode with a multi-component aqueous catholyte. This study advances the modeling of such batteries by developing a spatially resolved, three-dimensional cathode half-cell model, which extends beyond the traditional one-dimensional homogenized approaches employed in previous research. This enhanced model accounts for the complex three-dimensional effects that are critical to accurately simulating the battery's behavior.

Computational modeling A key aspect of this modeling effort involved the precise formulation of boundary conditions at the electrolyte-cathode interface. A detailed analysis determined that a more accurate representation of these boundary conditions significantly influences the overall fidelity of the simulation results. Specifically, it is advantageous to approximate the iodine surface flux, derived from the heterogeneous charge-transfer reaction at the electrode, as being equivalent to the iodine surface flux resulting from the homogeneous triiodide recombination reaction occurring within the bulk of the catholyte. This approach provides a balance between computational stability and accuracy, ensuring that the derived

boundary conditions for species concentrations within the catholyte enabled robust and reliable simulations.

The numerical solver developed in this work, designed to tackle the resulting system of coupled partial differential equations, is implemented with a focus on reusability and accessibility, making it a valuable tool for ongoing and future research within the scientific community. The segregated nature of the solver requires the introduction of significant under-relaxation techniques to stabilize the coupling between the two distinct computational regions representing the cathode and the electrolyte. This stabilization is essential for achieving convergence in the simulations, which was meticulously monitored using the normalized root mean square deviation (NRSMD) of the related currents.

One of the critical challenges identified in this study is the determination of the correct electrode potential at the cathode current collector. The accuracy of this potential setting directly impacts the computation time and overall efficiency of the simulations. To enhance this aspect of the modeling process, the study suggests integrating the damped secant method, which optimizes the determination of the electrode potential and thereby reduce the computational burden associated with these simulations.

Two dimensional electrodes for sodium iodine batteries Following the validation of the spatially resolved sodium iodine battery model against established one-dimensional simulation results from the literature, an in-depth exploration of cell design parameters was undertaken. This study systematically investigated the influence of key design parameters on battery performance, particularly focusing on variations in C-rate during both charging and discharging cycles. The parameters under consideration included cathode length, catholyte concentration, and electrode conductivity. These were evaluated through a combination of macroscopic performance metrics, such as cell voltage, and microscopic insights, such as local concentration distributions, to comprehensively assess their impact on the overall efficiency and functionality of the battery.

The study highlights significant diffusion limitations of the electrolyte species as a primary constraint on the performance of sodium iodine batteries when employing a two-dimensional electrode architecture. These limitations critically impair the efficiency of the battery, particularly as the cell thickness approaches or exceeds 1 cm. This finding underscores the impracticality of incorporating bulky electrodes within this design framework, as the diffusion constraints severely restrict the attainable battery performance.

Among the various configurations examined, an elemental iodine concentration of $8\,\mathrm{mol\,L^{-1}}$ emerged as the most effective, offering an optimal compromise between theoretical capacity and practical utilization. This concentration level balances the demands of maintaining sufficient reactant availability while avoiding excessive transport limitations. Furthermore, charge transport within the solid phase of the electrode does not constitute a significant bottleneck, provided

that materials with suitable conductivity are employed. This insight allows researchers to focus on other limiting factors, as the solid-phase transport does not appear to impede the battery's performance under these conditions.

The study also provides critical insights into the spatial distribution of species concentrations within the cathode compartment. In this context, the local precipitation or depletion of charge-carrying species in the electrolyte emerges as the primary mechanism responsible for the cessation of battery operation in this two-dimensional electrode configuration. This phenomenon is closely linked to the transport processes that facilitate the movement of these species from the anode to the reactive surfaces within the cathode. The study reveals that these transport processes are a critical bottleneck, significantly influencing the overall battery performance and necessitating further optimization.

Moreover, the overpotentials associated with iodide oxidation are relatively modest, owing to the rapid kinetics of the charge-transfer reactions involved. This observation suggests that the surface area of the electrode, while important, is not a primary limiting factor within the studied design framework. However, according to the results of the study, a critical issue is related to the distribution of the available surface area in the positive electrode. In the context of the two-dimensional electrode design, the non-uniform distribution of surface area remains as a significant challenge.

Three-dimensional electrodes for sodium iodine batteries Building on the limitations identified in the two-dimensional electrode designs, this study strategically explored the use of glassy carbon foams as innovative three-dimensional electrode structures for sodium iodine batteries. The decision to investigate glassy carbon foams was driven by their distinctive properties, including chemical inertness, competitive electronic conductivity, and the flexibility to tailor their morphology. These characteristics makes them particularly attractive for enhancing battery performance.

Comparative simulations rigorously evaluated the performance of glassy carbon foam electrodes against traditional two-dimensional cathode designs. The results confirmed that the foam structures significantly improve the depth of discharge, overcoming the diffusion limitations that hinders the efficiency of two-dimensional designs. This outcome underscores the potential of three-dimensional electrodes to advance the overall performance and energy utilization of sodium iodine batteries.

To accurately model the complex structure of the glassy carbon foam, a mathematical approach was adopted that involved the packing of Kelvin unit cells—a geometric model frequently used to represent foam-like structures. The application of virtual smoothing algorithms refines the modeled geometry and better replicates the actual morphology of glassy carbon foams. This

methodological approach was validated against imaging data from real foams, verifying its accuracy and reliability for future use in modeling intricate electrode architectures.

From a mathematical perspective, the analysis reveals an inherent trade-off between maximizing the specific surface area of the foam and maintaining adequate porosity. While increasing the surface area is often desirable for enhancing reaction kinetics, doing so at the expense of porosity is often detrimental to battery performance. The reduced porosity restricts the effective migration of sodium ions across the electrolyte, a fundamental requirement for sustaining optimal performance during operation.

The study highlights the importance of larger pores relative to the foam cell size, as these larger pores correlate with higher overall porosity. Such a structure facilitates smoother sodium-ion transit between the cells of the foam, which in turn significantly boosts the efficiency and effectiveness of the battery. Conversely, while reducing the foam cell size to increase surface area did yield improved performance, this observed improvement is minor. In sharp contrast, foams with extremely high porosity (around 97.4 %) and small cell sizes (less than 2 mm), where the increase in surface area enhances performance without severely compromising ion transport, represent an exception to this trend.

These findings are consistent across a range of C-rates, suggesting that the relationship between pore size, surface area, and porosity is robust and critical for optimizing the design of three-dimensional electrodes. The insights gained from this study align with those derived from earlier investigations into two-dimensional electrodes, reinforcing the conclusion that efficient charge and species transport across the cathode half-cell is paramount for achieving high utilizable capacities in sodium iodine batteries. The results of this study provide a foundation for further exploration and optimization of three-dimensional electrode designs in advanced battery systems.

Comparison of NaI battery model predictions with preliminary experimental data

In this work, a comparison between early-stage experimental data and model predictions led to a reevaluation of several assumptions related to the behavior of iodine/iodide aqueous solutions in sodium iodine batteries. The initial experiments report a specific capacity 70 % higher than predicted by traditional solubility limits, suggesting that the theoretical framework needs adjustments. Refining the solubility limits in the model better approximates the experimentally observed capacity, yet it is evident that triiodide (I_3^-) by itself does not entirely account for the experimental observations. The inclusion of pentaiodide (I_5^-) as an additional catholyte species provesä necessary to accurately reproduce the shape of the polarization curve, indicating that more complex polyiodide formation plays a significant role in iodine storage near the fully charged state. Nevertheless, the modified model similarly anticipated notably elevated iodine concentration levels when fully charged, prompting questions about the solubility of such concentrations. These results imply that either supplementary polyiodides or iodine precipitation might play a role in

the long-term dynamics of the system, highlighting the necessity for further empirical evidence as the battery prototype progresses.

All-solid-state sodium-ion battery with polymer-ceramic composite electrolyte In the pursuit of developing next-generation sodium-ion batteries, all-solid-state sodium-ion batteries (ASSSIBs) have gained prominence due to their superior safety profile, extended cycle life, and the ability to incorporate sodium metal anodes. This study contributes to the growing body of research focused on utilizing composite polymer-ceramic electrolytes to advance this innovative battery technology.

For the first time, this work employs physics-based microscale models to conduct a comprehensive investigation into how various material properties and design parameters affect the electrochemical performance of ASSSIBs with composite electrolytes. These models provide a nuanced understanding of the interactions within the battery, offering valuable insights that can guide the optimization of future solid-state sodium-ion battery designs.

Computational modeling This study addressed the complex challenges of modeling ASSSIBs through a dual modeling approach, leveraging both a resolved microstructure model and a pseudo-two-dimensional (P2D) model. Each model offers unique insights into the electrochemical behavior and design optimization of ASSSIBs, contributing to a holistic understanding of battery performance.

The microstructure model builds upon the simulation framework initially developed for sodium-iodine batteries, with significant adaptations to account for diffusion processes within the active material particles. This model is finely tuned to represent the intricate details of ASSSIBs, incorporating a range of critical parameters. These include the equilibrium potential, which is accurately described using a Gibbs energy (GE) model, and the conductivity of the polymer electrolyte, which is expressed as a function of concentration. These additions enable the model to capture the nuanced effects of material properties and structural configurations on battery performance at the microscale.

In contrast, the P2D model, which lacks the resolved surface structures of the microstructure model, necessitates the use of effective transport properties to accurately represent the complex behavior of a two-phase electrolyte system. The results from the particle-resolved microstructure model help inform and refine the transport properties used in the P2D model. This approach enables the parameterization of mixing rules that define the effective transport parameters within the electrolyte, reflecting the composition of a hybrid polymer-ceramic electrolyte in a tortuous active material matrix.

Consequently, the optimality of different models varies in accordance with the degree of active material content and porosity. Specifically, the Zehner-Bauer-Schlünder (ZBS) effectively represents scenarios with low to medium active material content, providing a reliable estimate of transport properties under these conditions. Conversely, the Maxwell-Garnett model proved more suitable for situations involving low porosity within the active material, offering an alternative approach to capturing the effects of electrolyte composition and structure on overall battery performance.

Microstructure simulation results The microscale simulation model developed in this work is a useful tool for representing the complex particle structures found within actual cathode half-cells of all-solid-state sodium-ion batteries. The microstructure simulation results identify slow transport of sodium ions throughout the electrolyte as the primary obstacle to optimal cell performance. This limitation is largely attributed to three interrelated factors: the low porosity of the half-cell, driven by a high content of active material; the substantial thickness of the half-cell, which increases the distance between the separator and the current collector; and the inherently low ionic conductivity of the electrolyte, which results from a limited amount of active filler. These factors together create steep sodium ion concentration gradients within the electrolyte, particularly in regions close to the separator, even under moderate C-rate conditions.

A comprehensive parametric study using the microstructure model demonstrates that achieving sufficient utilization of the theoretical battery capacity at room temperature requires cathodes with an active filler volume fraction of approximately 80 % and electrode thicknesses of 100 µm or less. The model indicates that battery performance is particularly constrained during the charging process, where sodium ion consumption predominantly occurs near the separator. This localized depletion significantly limits capacity utilization unless the active filler volume fraction is exceptionally high.

Pseudo-two-dimensional model results The pseudo-two-dimensional (P2D) model developed in this study enabled the exploration of a broader range of parameters, complementing the insights gained from the microscale model. Exemplarily, the P2D model illustrates that electrodes with an active material volume fraction of 50 % can achieve full utilization during discharge at low C-rates, provided the active filler volume fraction exceeds 0.3. At higher C-rates, such as those above 0.5 C, full utilization becomes unattainable, even with pure ceramic electrolytes. During charging, the model emphasizes a more pronounced reduction in utilizable capacity as the C-rate increases. This behavior arises from transport limitations within the electrolyte, where sodium ions are rapidly depleted near the separator, leading to a localized shortage of charge carriers and a consequent decline in performance.

Further investigations focused on the optimal size of active material particles recommend an active material radius of 4 µm as reasonable, since further reductions in particle size do not result in significant performance gains and introduce additional challenges related to manufacturing and handling.

Additionally, the results of the P2D simulation suggest that a more sophisticated battery cell design, incorporating a non-uniform spatial distribution of active material and filler particles, significantly enhances overall battery performance. The findings indicate that a negative gradient in the distribution of particle volume fraction—with higher porosity near the separator that gradually decreases toward the current collector—yields superior states of charge and depths of discharge. More complex spatial distributions, such as those based on hyperbolic tangent or sine functions, did not show significant improvements compared to a linear gradient. As a result, the linear distribution with a normalized slope of -1 is the most effective, modeling a positive half-cell with high porosity near the separator that gradually decreases toward the current collector.

Furthermore, the P2D model demonstrated its effectiveness when integrated into a global optimization framework utilizing a differential evolution algorithm. This approach enables the optimization of key parameters, including cathode thickness, active material content, and the spatial distribution of both active material and filler volume fractions. The global optimization results emphasize the highly interconnected and non-linear nature of battery systems, showing that the optimized electrodes achieve superior performance during charging compared to discharging across all examined C-rates.

Finally, the study indicates that separate optimization for charging and discharging leads to distinct cell configurations. However, a design optimized for efficient operation during both processes delivers performance comparable to that of a design tailored exclusively for discharging. This outcome identifies discharging as the primary bottleneck for achieving high capacity utilization in all-solid-state sodium-ion batteries.

Reevaluation of ionic transport mechanisms in polymer-ceramic composite electrolytes This work compares early experimental data with microstructure-based model predictions of ionic conductivity in polymer-ceramic composite electrolytes, focusing on composites composed of NaSICON and PEO. The study challenges previously held assumptions about the mechanisms governing ionic transport in these materials.

To investigate the role of ceramic fillers, the hypothesis of superionic interphases—regions near the polymer-ceramic interface with enhanced ionic transport—was systematically tested. For NaSICONmaterial $Na_3Zr_2Si_{2.3}P_{0.7}O_{11.85}$, experimental results show no measurable increase in ionic conductivity beyond the baseline value of the bulk PEO polymer. This outcome suggests that the fillers do not enhance ionic transport as previously anticipated.

In contrast, the use of $Na_{3.4}Zr_2Si_{2.4}P_{0.6}O_{12}$ particles results in a moderate increase in ionic conductivity, though the observed values remain below those predicted by models assuming ideal ionic transport through the filler particles. Accounting for charge transport within superionic interphases at the polymer-ceramic boundary while neglecting charge transport within the ceramic particles aligns the model closely with experimental observations. The study identifies various combinations of interphase thickness and conductivity that are consistent with the experimental data. If future experimental work determines one of these parameters, the model provides valuable predictions for the other, aiding in the characterization of the superionic interphase.

5.2 Outlook

The research presented in this thesis has centered on microscale modeling and simulation for predicting performance and optimizing the cell design of sodium batteries, providing valuable insights into the fundamental mechanisms that influence battery efficiency and capacity. Future studies could expand on this work by applying these models to explore sodium batteries at different scales. One potential approach involves using the physics-based models developed here to investigate nanoscale processes. This could be achieved by extracting and refining macroscopic transport parameters through fitting the models to experimentally derived data sets.

A significant challenge in this endeavor is the current scarcity of high-quality experimental data that simultaneously report on electrochemical performance and provide well-characterized electrode material morphologies in sodium batteries. This paucity of data is largely due to the relatively low technology readiness level of sodium-based battery systems compared to more established technologies like lithium-ion batteries (LIBs). As sodium battery research is still in its formative stages, much of the focus remains on the chemical development of active materials and electrolytes, often at the expense of detailed studies on cell design and electrode architecture.

As sodium batteries continue to mature and move closer to commercialization, it is anticipated that research will increasingly shift towards understanding and optimizing electrode morphology and composition. In this context, future work could play a crucial role by integrating material science research with the models developed in this thesis. By refitting these models to new experimental data, it will be possible to evaluate and enhance transport properties within the battery, thus driving further advancements in cell design. Such efforts will not only contribute to the refinement of sodium-ion battery technology but also help bridge the gap between theoretical predictions and practical performance.

An alternative path forward could leverage the findings of this study by integrating them into battery or pack-level models, ultimately influencing techno-economic analyses. A significant challenge in this context is the disparity in length and time scales, which necessitates the careful

incorporation of the presented microscale models into such simulations. Achieving this requires maintaining a balance between model accuracy and computational efficiency.

A Appendix

A.1 Derivation and fitting of the electrolyte conductivity equation

Mongcopa et al. used quasi-elastic neutron scattering (QENS) to study the conductivity of PEO at different Li^+/EO ratios (r_s) and derived the following dependence of conductivity on LiTFSI salt concentration [169]:

$$\sigma = 0.043 r_s \left[\exp\left(-\frac{r_s}{0.085}\right)\right] \tag{A.1}$$

They attributed the constants 0.043 and 0.085 to the specific conductivity of the dilute electrolyte and the exponential slowing of segmental relaxation in the presence of salt, respectively.

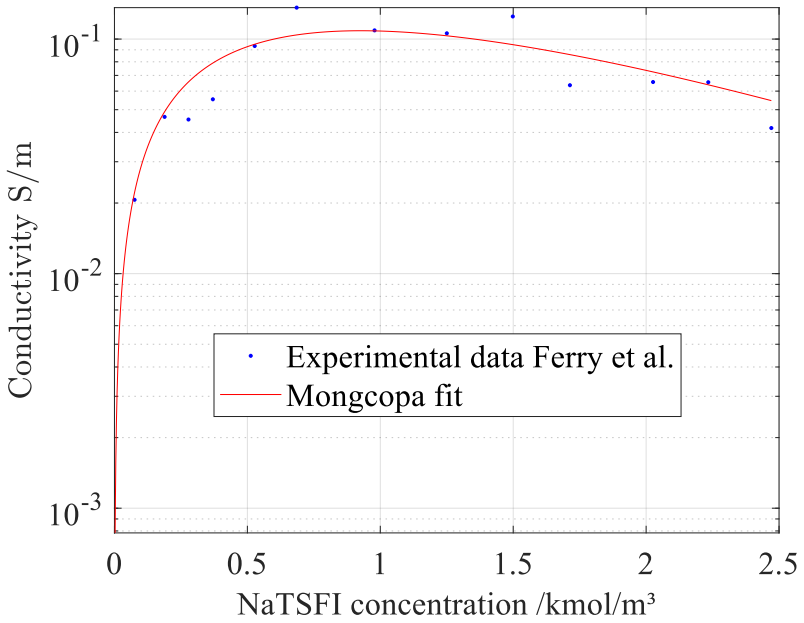

Figure A.1: Measured electrolyte conductivity data from Ferry et al. [170] compared with the conductivity function fitted in this research.

In this work the equation is expressed in terms of c_{el} rather than r_s to align with the formulation of the physics-based model. Mathematically, the numerator in the exponent represents the abscissa at the maximum turning point of the function which corresponds to the concentration at the peak

polymer conductivity ($c_{\mathrm{el},\kappa_{\max}}$). In our reformulated equation, a single empirical constant remains, specific to the materials used and denoted as K_{NaTFSI} in this study (see equation eq. (4.9)). The data fit to evaluate the value, based on data from Ferry et al., is shown in fig. A.1.

A.2 Fit parameters for the Redlich-Kistner thermodynamic model.

Table A.1: Fit parameters and quality assessments for the Redlich-Kistner thermodynamic model

Parameter	Value
U_0 (V)	3.3787
A_0	4242
A_1	-170.67
A_2	-6814.2
A_3	1406.3
A_4	302201
A_5	-3549.3
A_6	-37732
A_7	3876.5

List of Figures

List of Tables

Declaration about the use of generative AI

During the preparation of this work the author used OpenAI's ChatGPT (based on the GPT-4 architecture) to assist in the linguistic refinement ("copyediting") of the entire text of this manuscript. After using this tool/service, the author reviewed and edited the content as needed and takes full responsibility for the content of the published work.

List of Publications

Journal articles

Cernak, S., Gerbig, F., Kespe, M., and Nirschl, H.: Spatially resolved lithium–ion battery simulations of the influence of lithium–nickel–manganese–cobalt–oxide particle roughness on the electrochemical performance. *Energy Storage*, **2020**, 2(5). DOI: 10.1002/est2.156.

Gerbig, F., Cernak, S., and Nirschl, H.: 3D Simulation of Cell Design Influences on Sodium–Iodine Battery Performance. *Energy Technology*, **2021**, 2000857. DOI: 10.1002/ente.202000857.

Gerbig, F., Cernak, S., and Nirschl, H.: Towards a Novel Sodium-Iodine Battery with an Aqueous Catholyte: Numerical Investigations of Complex Cathode Structures. *ECS Transactions*, **2021**, 104(1), 123–130. DOI: 10.1149/10401.0123ecst.

Gerbig, F., Holzapfel, M., and Nirschl, H.: Simulating the Impact of Glassy Carbon Foam Electrodes on the Performance of Sodium Iodine Batteries. *Journal of The Electrochemical Society*, **2023**, 170(4), 040517. DOI: 10.1149/1945-7111/accab7.

Moradipour, F., Markert, A., Rudszuck, T., Röttgen, N., Dück, G., Finsterbusch, M., Gerbig, F., Nirschl, H., and Guthausen, G.: Na^+ Mobility in PEO-Based Composite Solid-State Electrolytes by NMR. *Journal of Energy and Power Technology*, **2023**, 05(04), 1–21. DOI: 10.21926/jept.2304032.

Gerbig, F., Chauhan, A., Gietl, S., and Nirschl, H.: Performance Investigations on All-Solid-State Polymer-Ceramic Sodium-Ion Batteries through a Spatially Resolved Electrochemical Model. *Journal of The Electrochemical Society*, **2024**, 171(9), 090515. DOI: 10.1149/1945-7111/ad7763.

Gerbig, F., Kühn, J., and Nirschl, H.: Optimizing all-solid-state sodium-ion batteries: Insights from a P2D Model on NaSICON-based polymer–ceramic electrolyte. *Energy Reports*, **2025**, 13, 105–116. DOI: https://doi.org/10.1016/j.egyr.2024.11.077.

Gerbig, F., Röttgen, N., Holzapfel, M., Dück, G., Finsterbusch, M., and Nirschl, H.: Unraveling ionic transport in polymer-ceramic electrolytes: Insights into superionic interphases. *Electrochemistry Communications*, **2025**, 107960. DOI: 10.1016/j.elecom.2025.107960.

Conference contributions

Gerbig, F., Cernak, S., and Nirschl, H.: Fully Resolved Simulation of Mid-Temperature Sodium-Iodine Secondary Batteries. *PRiME 2020* (online, Oct. 5–9, 2020). Poster presented. Honolulu, USA, 2020.

Gerbig, F., Cernak, S., and Nirschl, H.: Mid-Temperature Sodium-Iodine Secondary Battery – Numerical Investigations. *Batterieforum Deutschland* (online, Jan. 20, 2021). Poster presented. Berlin, Germany, 2021.

Gerbig, F., Cernak, S., and Nirschl, H.: Spatially resolved simulation of cathode structures for sodium-iodine secondary batteries. *MODVAL17 - 17th Symposium on Modeling and Experimental Validation of Electrochemical Energy Technologies* (online, Apr. 20–22, 2021). Talk presented. Sion, CH, 2021.

Gerbig, F., Cernak, S., and Nirschl, H.: 3D simulation of sodium iodine secondary batteries for stationary energy applications. *Advanced Battery Power Conference* (online, Apr. 27–29, 2021). Poster presented. Münster, Germany, 2021.

Gerbig, F. and Nirschl, H.: Investigating Molten Sodium Batteries with an Aqueous Catholyte [oral presentation]. *239th ECS Meeting and the 18th International Meeting on Chemical Sensors (IMCS)* (online, May 30–June 3, 2021). Talk presented. Chicago, USA, 2021.

Gerbig, F., Cernak, S., Vincent, T., Kee, R. J., and Nirschl, H.: Investigating Sodium-Iodine Battery Cathodes using EIS Simulations. *ModVal - 18th Symposium on Modeling and Experimental Validation* (Schloss Hohenkammer, Mar. 15–16, 2022). Poster presented. Hohenkammer, Germany, 2022.

Wolf, A., Kespe, S., Gerbig, F., and Nirschl, H.: Pore-scale resolved 3D simulation of aqueous organic flow batteries. *ModVal - 18th Symposium on Modeling and Experimental Validation* (Schloss Hohenkammer, Mar. 15–16, 2022). Talk presented. Hohenkammer, Germany, 2022.

Kee, R. J., Evans, T. A. P., Hoffman, R. M., Huayang, Z., Gerbig, F., and Vincent, T.: Extraction of Electrochemical Impedance Spectra from Physical Models. *241st ECS Meeting* (Vancouver Convention Center, May 29–June 2, 2022). Talk presented. Vancouver, Canada, 2022.

Gerbig, F., Wolf, A., and Nirschl, H.: Microstructure-resolved simulation of three-dimensional electrodes for sodium iodine batteries. *ModVal - 19th Symposium on Modeling and Experimental Validation* (Mercatorhalle, Mar. 21–23, 2023). Talk presented. Duisburg, Germany, 2023.

Gerbig, F. and Nirschl, H.: Multi-Scale Modeling and Simulation of All-Solid-State Sodium-Ion Batteries with Polymer-Ceramic Hybrid Electrolytes. *WCCE11 - 11th World Congress on Chemical Engineering* (UCA Convention Center, June 4–8, 2023). Talk presented. Buenos Aires, Argentina, 2023.

Gerbig, F., Chauhan, A., and Nirschl, H.: All-Solid-State Sodium-Ion Batteries: Simulating the Effects of Particle Properties on Polymer-Ceramic Hybrid Electrolytes. *PARTEC - International Congress on Particle Technology* (NürnbergConvention Center Ost, Exhibition Centre Nuremberg, Sept. 26–28, 2023). Lecture presented. Nürnberg, Germany, 2023.

Gerbig, F., Chauhan, A., and Nirschl, H.: Multi-Scale Modeling and Simulation of All-Solid-State Sodium-Ion Batteries with Polymer-Ceramic Hybrid Electrolytes. *ECS Meeting Abstracts*. 245th ECS Meeting (Marriott Marquis San Francisco, May 26–30, 2024). Vol. MA2024-01. 45. Talk presented. San Francisco, CA, 2024. DOI: 10.1149/MA2024-01452499mtgabs.

Gerbig, F., Schäfer, F., Holzapfel, M., and Nirschl, H.: Optimizing Mid-Temperature Sodium Iodine Batteries for Sustainable Large-Scale Energy Storage: A Comprehensive Modeling Approach and Experimental Validation. *ECS Meeting Abstracts*. 245th ECS Meeting (Marriott Marquis San Francisco, May 26–30, 2024). Vol. MA2024-01. 3. Talk presented. San Francisco, CA, 2024, 617. DOI: 10.1149/MA2024-013617mtgabs.

Bibliography

[1] U.S. Energy Information Administration: *International Energy Outlook 2023*. U.S. Department of Energy ed. Washington, 2023.

[2] Gür, T. M.: Review of electrical energy storage technologies, materials and systems: challenges and prospects for large-scale grid storage. *Energy & Environmental Science*, **2018**, 11(10), 2696–2767. DOI: 10.1039/C8EE01419A.

[3] Zhao, H., Wu, Q., Hu, S., Xu, H., and Rasmussen, C. N.: Review of energy storage system for wind power integration support. *Applied Energy*, **2015**, 137, 545–553. DOI: 10.1016/j.apenergy.2014.04.103.

[4] Larcher, D. and Tarascon, J.-M.: Towards greener and more sustainable batteries for electrical energy storage. *Nature chemistry*, **2015**, 7(1), 19–29. DOI: 10.1038/nchem.2085.

[5] Zubi, G., Dufo-López, R., Carvalho, M., and Pasaoglu, G.: The lithium-ion battery: State of the art and future perspectives. *Renewable and Sustainable Energy Reviews*, **2018**, 89, 292–308. DOI: 10.1016/j.rser.2018.03.002.

[6] Peters, J. F., Baumann, M., Zimmermann, B., Braun, J., and Weil, M.: The environmental impact of Li-Ion batteries and the role of key parameters – A review. *Renewable and Sustainable Energy Reviews*, **2017**, 67, 491–506. DOI: 10.1016/j.rser.2016.08.039.

[7] Degen, F., Winter, M., Bendig, D., and Tübke, J.: Energy consumption of current and future production of lithium-ion and post lithium-ion battery cells. *Nature Energy*, **2023**, 8(11), 1284–1295. DOI: 10.1038/s41560-023-01355-z.

[8] Yaroshevsky, A. A.: Abundances of chemical elements in the Earth's crust. *Geochemistry International*, **2006**, 44(1), 48–55. DOI: 10.1134/S001670290601006X.

[9] Yabuuchi, N., Kubota, K., Dahbi, M., and Komaba, S.: Research development on sodium-ion batteries. *Chemical reviews*, **2014**, 114(23), 11636–11682. DOI: 10.1021/cr500192f.

[10] Shannon, R. D.: Revised effective ionic radii and systematic studies of interatomic distances in halides and chalcogenides. *Acta Crystallographica Section A*, **1976**, 32(5), 751–767. DOI: 10.1107/S0567739476001551.

[11] Li, C., Xu, H., Ni, L., Qin, B., Ma, Y., Jiang, H., Xu, G., Zhao, J., and Cui, G.: Nonaqueous Liquid Electrolytes for Sodium–Ion Batteries: Fundamentals, Progress and Perspectives. *Advanced Energy Materials*, **2023**, 13(40), 2301758. DOI: 10.1002/aenm.202301758.

[12] Arblaster, J. W.: *Selected Values of the Crystallographic Properties of Elements*. Materials Park: ASM International, 2018. URL: https://ebookcentral.proquest.com/lib/kxp/detail.action?docID=5515132.

[13] Choi, J. W. and Aurbach, D.: Promise and reality of post-lithium-ion batteries with high energy densities. *Nature Reviews Materials*, **2016**, 1(4), 16013. DOI: 10.1038/natrevmats.2016.13.

[14] Kulova, T. L., Fateev, V. N., Seregina, E. A., and Grigoriev, A. S.: A Brief Review of Post-Lithium-Ion Batteries. *International Journal of Electrochemical Science*, **2020**, 15(8), 7242–7259. DOI: 10.20964/2020.08.22.

[15] Castillo, J., Qiao, L., Santiago, A., Judez, X., Buruaga, A. S. de, Jimenez, G., Armand, M., Zhang, H., and Li, C.: Perspective of polymer-based solid-state Li-S batteries. *Energy Materials*, **2022**, 2(1), 200003. DOI: 10.20517/energymater.2021.25.

[16] Liu, T., Vivek, J. P., Zhao, E. W., Lei, J., Garcia-Araez, N., and Grey, C. P.: Current Challenges and Routes Forward for Nonaqueous Lithium-Air Batteries. *Chemical reviews*, **2020**, 120(14), 6558–6625. DOI: 10.1021/acs.chemrev.9b00545.

[17] Lin, D., Liu, Y., and Cui, Y.: Reviving the lithium metal anode for high-energy batteries. *Nature nanotechnology*, **2017**, 12(3), 194–206. DOI: 10.1038/nnano.2017.16.

[18] Duffner, F., Kronemeyer, N., Tübke, J., Leker, J., Winter, M., and Schmuch, R.: Post-lithium-ion battery cell production and its compatibility with lithium-ion cell production infrastructure. *Nature Energy*, **2021**, 6(2), 123–134. DOI: 10.1038/s41560-020-00748-8.

[19] Liu, Y., Zhang, R., Wang, J., and Wang, Y.: Current and future lithium-ion battery manufacturing. *iScience*, **2021**, 24(4), 102332. DOI: 10.1016/j.isci.2021.102332.

[20] Ponrouch, A. and Palacín, M. R.: Post-Li batteries: promises and challenges. *Philosophical transactions. Series A, Mathematical, physical, and engineering sciences*, **2019**, 377(2152), 20180297. DOI: 10.1098/rsta.2018.0297.

[21] Job, R.: *Electrochemical Energy Storage*. De Gruyter, 2020. DOI: 10.1515/9783110484427.

[22] Jackowska, K. and Krysiński, P.: *Applied Electrochemistry*. De Gruyter, 2020. DOI: 10.1515/9783110600834.

[23] Newman, J. and Balsara, N. P.: *Electrochemical systems*. Fourth edition. The Electrochemical Society series. Hoboken, NJ: Wiley, 2021.

[24] Delmas, C.: Sodium and Sodium-Ion Batteries: 50 Years of Research // Sodium and Sodium–Ion Batteries: 50 Years of Research. *Advanced Energy Materials*, **2018**, 8(17), 1703137. DOI: 10.1002/aenm.201703137.

[25] Ellis, B. L. and Nazar, L. F.: Sodium and sodium-ion energy storage batteries. *Current Opinion in Solid State and Materials Science*, **2012**, 16(4), 168–177. DOI: 10.1016/j.cossms.2012.04.002.

[26] Hueso, K. B., Armand, M., and Rojo, T.: High temperature sodium batteries: status, challenges and future trends. *Energy & Environmental Science*, **2013**, 6(3), 734. DOI: 10.1039/c3ee24086j.

[27] Wang, Y., Zhou, D., Palomares, V., Shanmukaraj, D., Sun, B., Tang, X., Wang, C., Armand, M., Rojo, T., and Wang, G.: Revitalising sodium–sulfur batteries for non-high-temperature operation: a crucial review. *Energy & Environmental Science*, **2020**, 13(11), 3848–3879. DOI: 10.1039/D0EE02203A.

[28] Wei, S., Xu, S., Agrawral, A., Choudhury, S., Lu, Y., Tu, Z., Ma, L., and Archer, L. A.: A stable room-temperature sodium-sulfur battery. *Nature communications*, **2016**, 7(1), 11722. DOI: 10.1038/ncomms11722.

[29] Oshima, T., Kajita, M., and Okuno, A.: Development of Sodium-Sulfur Batteries. *International Journal of Applied Ceramic Technology*, **2004**, 1(3), 269–276. DOI: 10.1111/j.1744-7402.2004.tb00179.x.

[30] Nikiforidis, G., van de Sanden, M. C. M., and Tsampas, M. N.: High and intermediate temperature sodium-sulfur batteries for energy storage: development, challenges and perspectives. *RSC advances*, **2019**, 9(10), 5649–5673. DOI: 10.1039/c8ra08658c.

[31] Syali, M. S., Kumar, D., Mishra, K., and Kanchan, D. K.: Recent advances in electrolytes for room-temperature sodium-sulfur batteries: A review. *Energy Storage Materials*, **2020**, 31, 352–372. DOI: 10.1016/j.ensm.2020.06.023.

[32] Sudworth, J.: The sodium/nickel chloride (ZEBRA) battery. *Journal of Power Sources*, **2001**, 100(1-2), 149–163. DOI: 10.1016/S0378-7753(01)00891-6.

[33] Kreysa, G., Ota, K.-i., and Savinell, R. F.: *Encyclopedia of Applied Electrochemistry*. New York, NY: Springer New York, 2014. DOI: 10.1007/978-1-4419-6996-5.

[34] Wu, S., Zhang, X., Wang, R., and Li, T.: Progress and perspectives of liquid metal batteries. *Energy Storage Materials*, **2023**, 57, 205–227. DOI: 10.1016/j.ensm.2023.02.021.

[35] Hill, R. C., Gross, M. S., Percival, S. J., Peretti, A. S., Small, L. J., Spoerke, E. D., and Cheng, Y.-T.: Molten sodium batteries: advances in chemistries, electrolytes, and interfaces. *Frontiers in Batteries and Electrochemistry*, **2024**, 3, 1369305. DOI: 10.3389/fbael.2024.1369305.

[36] Small, L. J., Eccleston, A., Lamb, J., Read, A. C., Robins, M., Meaders, T., Ingersoll, D., Clem, P. G., Bhavaraju, S., and Spoerke, E. D.: Next generation molten NaI batteries for grid scale energy storage. *Journal of Power Sources*, **2017**, 360, 569–574. DOI: 10.1016/j.jpowsour.2017.06.038.

[37] Zhu, H., Bhavaraju, S., and Kee, R. J.: Computational model of a sodium–copper–iodide rechargeable battery. *Electrochimica Acta*, **2013**, 112, 629–639. DOI: 10.1016/j.electacta.2013.09.010.

[38] Zhu, H. and Kee, R. J.: Computational modeling of sodium-iodine secondary batteries. *Electrochimica Acta*, **2016**, 219, 70–81. DOI: 10.1016/j.electacta.2016.09.104.

[39] Holzapfel, M., Wilde, D., Hupbauer, C., Ahlbrecht, K., and Berger, T.: Medium-temperature molten sodium batteries with aqueous bromine and iodine cathodes. *Electrochimica Acta*, **2017**, 237, 12–21. DOI: 10.1016/j.electacta.2017.03.152.

[40] Hwang, J.-Y., Myung, S.-T., and Sun, Y.-K.: Sodium-ion batteries: present and future. *Chemical Society reviews*, **2017**, 46(12), 3529–3614. DOI: 10.1039/c6cs00776g.

[41] Ponrouch, A., Monti, D., Boschin, A., Steen, B., Johansson, P., and Palacín, M. R.: Non-aqueous electrolytes for sodium-ion batteries. *Journal of Materials Chemistry A*, **2015**, 3(1), 22–42. DOI: 10.1039/C4TA04428B.

[42] Tang, J., Dysart, A. D., and Pol, V. G.: Advancement in sodium-ion rechargeable batteries. *Current Opinion in Chemical Engineering*, **2015**, 9, 34–41. DOI: 10.1016/j.coche.2015.08.007.

[43] Eshetu, G. G., Elia, G. A., Armand, M., Forsyth, M., Komaba, S., Rojo, T., and Passerini, S.: Electrolytes and Interphases in Sodium–Based Rechargeable Batteries: Recent Advances and Perspectives. *Advanced Energy Materials*, **2020**, 10(20), 2000093. DOI: 10.1002/aenm.202000093.

[44] U.S. Department of Energy: *Critical Materials Assessement*. U.S. Department of Energy ed. Washington, D.C., 2023. URL: https://www.energy.gov/sites/default/files/2023-07/doe-critical-material-assessment_07312023.pdf.

[45] European Commission, Directorate-General for Internal Market, Industry, Entrepreneurship, SMEs, Grohol, M., and Veeh, C.: *Study on the critical raw materials for the EU 2023 – Final report*. Publications Office of the European Union, 2023. DOI: 10.2873/725585.

[46] Langdon, J. and Manthiram, A.: A perspective on single-crystal layered oxide cathodes for lithium-ion batteries. *Energy Storage Materials*, **2021**, 37, 143–160. DOI: 10.1016/j.ensm.2021.02.003.

[47] Armstrong, A., Linnell, S., Maughan, P., Silvan, B., and Tapia-Ruiz, N.: Sodium Layered Oxide Cathode Materials. In: *Sodium–Ion Batteries*. Titirici, M.-.-M., Adelhelm, P., and Hu, Y.-.-S. eds. Weinheim: Wiley, 2022, 93–127. DOI: 10.1002/9783527825769.ch4.

[48] Sapra, S. K., Pati, J., Dwivedi, P. K., Basu, S., Chang, J.-K., and Dhaka, R. S.: A comprehensive review on recent advances of polyanionic cathode materials in Na–ion batteries for cost effective energy storage applications. *WIREs Energy and Environment*, **2021**, 10(5), e400. DOI: 10.1002/wene.400.

[49] Chen, G., Huang, Q., Wu, T., and Lu, L.: Polyanion Sodium Vanadium Phosphate for Next Generation of Sodium–Ion Batteries—A Review. *Advanced Functional Materials*, **2020**, 30(34), 2001289. DOI: 10.1002/adfm.202001289.

[50] Liu, T., Zhang, Y., Chen, C., Lin, Z., Zhang, S., and Lu, J.: Sustainability-inspired cell design for a fully recyclable sodium ion battery. *Nature communications*, **2019**, 10(1), 1965. DOI: 10.1038/s41467-019-09933-0.

[51] Yu, H., Gao, Y., Jing, H., Wang, J., Liang, Q., Kang, J., Wang, X., Qi, W., and Du, C.-F.: Boron-Doping Induced Electron Delocalization in Fluorophosphate Cathode: Enhanced Na-Ion Diffusivity and Sodium-Ion Full Cell Performance. *Small (Weinheim an der Bergstrasse, Germany)*, **2023**, 19(39), e2302097. DOI: 10.1002/smll.202302097.

[52] Böckenfeld, N. and Balducci, A.: Determination of sodium ion diffusion coefficients in sodium vanadium phosphate. *Journal of Solid State Electrochemistry*, **2014**, 18(4), 959–964. DOI: 10.1007/s10008-013-2342-6.

[53] Zhu, W., Mao, Q., Jia, Y., Ni, J., and Gao, L.: Dual-Carbon-Decorated Na3V2(PO4)3 Material for Sodium-Ion Batteries. *Journal of Electronic Materials*, **2023**, 52(2), 836–846. DOI: 10.1007/s11664-022-10128-5.

[54] Kim, H., Kim, H., Ding, Z., Lee, M. H., Lim, K., Yoon, G., and Kang, K.: Recent Progress in Electrode Materials for Sodium-Ion Batteries // Recent Progress in Electrode Materials for Sodium–Ion Batteries. *Advanced Energy Materials*, **2016**, 6(19), 1600943. DOI: 10.1002/aenm.201600943.

[55] Sun, N., Liu, H., and Xu, B.: Facile synthesis of high performance hard carbon anode materials for sodium ion batteries. *Journal of Materials Chemistry A*, **2015**, 3(41), 20560–20566. DOI: 10.1039/C5TA05118E.

[56] Zhang, M., Li, Y., Wu, F., Bai, Y., and Wu, C.: Boost sodium-ion batteries to commercialization: Strategies to enhance initial Coulombic efficiency of hard carbon anode. *Nano Energy*, **2021**, 82, 105738. DOI: 10.1016/j.nanoen.2020.105738.

[57] Zou, Z., Li, Y., Lu, Z., Da Wang, Cui, Y., Guo, B., Li, Y., Liang, X., Feng, J., Li, H., Nan, C.-W., Armand, M., Chen, L., Xu, K., and Shi, S.: Mobile Ions in Composite Solids. *Chemical reviews*, **2020**, 120(9), 4169–4221. DOI: 10.1021/acs.chemrev.9b00760.

[58] Vignarooban, K., Kushagra, R., Elango, A., Badami, P., Mellander, B.-E., Xu, X., Tucker, T. G., Nam, C., and Kannan, A. M.: Current trends and future challenges of electrolytes for sodium-ion batteries. *International Journal of Hydrogen Energy*, **2016**, 41(4), 2829–2846. DOI: 10.1016/j.ijhydene.2015.12.090.

[59] Vasudevan, S., Dwivedi, S., and Balaya, P.: Overview and perspectives of solid electrolytes for sodium batteries. *International Journal of Applied Ceramic Technology*, **2023**, 20(2), 563–584. DOI: 10.1111/ijac.14267.

[60] Edelman, D. A., Brandt, T. G., Temeche, E., and Laine, R. M.: Sodium-based solid electrolytes and interfacial stability. Towards solid-state sodium batteries. *Materials Today Communications*, **2022**, 32, 104009. DOI: 10.1016/j.mtcomm.2022.104009.

[61] Darjazi, H., Falco, M., Colò, F., Balducci, L., Piana, G., Bella, F., Meligrana, G., Nobili, F., Elia, G. A., and Gerbaldi, C.: Electrolytes for Sodium Ion Batteries: The Current Transition from Liquid to Solid and Hybrid systems. *Advanced materials (Deerfield Beach, Fla.)*, **2024**, 36(35), e2313572. DOI: 10.1002/adma.202313572.

[62] Liu, Q., Zhao, X., Yang, Q., Hou, L., Mu, D., Tan, G., Li, L., Chen, R., and Wu, F.: The Progress in the Electrolytes for Solid State Sodium–Ion Battery. *Advanced Materials Technologies*, **2023**, 8(7), 2200822. DOI: 10.1002/admt.202200822.

[63] Bao, C., Wang, B., Liu, P., Wu, H., Zhou, Y., Wang, D., Liu, H., and Dou, S.: Solid Electrolyte Interphases on Sodium Metal Anodes. *Advanced Functional Materials*, **2020**, 30(52), 2004891. DOI: 10.1002/adfm.202004891.

[64] Gao, X., Xing, Z., Wang, M., Nie, C., Shang, Z., Bai, Z., Dou, S. X., and Wang, N.: Comprehensive insights into solid-state electrolytes and electrode-electrolyte interfaces in all-solid-state sodium-ion batteries. *Energy Storage Materials*, **2023**, 60, 102821. DOI: 10.1016/j.ensm.2023.102821.

[65] Schmickler, W. and Santos, E.: *Interfacial Electrochemistry*. Berlin, Heidelberg: Springer Berlin Heidelberg, 2010. DOI: 10.1007/978-3-642-04937-8.

[66] Dong, Y., Wen, P., Shi, H., Yu, Y., and Wu, Z.-S.: Solid–State Electrolytes for Sodium Metal Batteries: Recent Status and Future Opportunities. *Advanced Functional Materials*, **2024**, 34(5), 2213584. DOI: 10.1002/adfm.202213584.

[67] Gao, H., Xin, S., Xue, L., and Goodenough, J. B.: Stabilizing a High-Energy-Density Rechargeable Sodium Battery with a Solid Electrolyte. *Chem*, **2018**, 4(4), 833–844. DOI: 10.1016/j.chempr.2018.01.007.

[68] Chi, X., Zhang, Y., Hao, F., Kmiec, S., Dong, H., Xu, R., Zhao, K., Ai, Q., Terlier, T., Wang, L., Zhao, L., Guo, L., Lou, J., Xin, H. L., Martin, S. W., and Yao, Y.: An electrochemically stable homogeneous glassy electrolyte formed at room temperature for all-solid-state sodium batteries. *Nature communications*, **2022**, 13(1), 2854. DOI: 10.1038/s41467-022-30517-y.

[69] Lou, S., Zhang, F., Fu, C., Chen, M., Ma, Y., Yin, G., and Wang, J.: Interface Issues and Challenges in All-Solid-State Batteries: Lithium, Sodium, and Beyond. *Advanced materials (Deerfield Beach, Fla.)*, **2021**, 33(6), 2000721. DOI: 10.1002/adma.202000721.

[70] Gandi, S., Chidambara Swamy Vaddadi, V. S., Sripada Panda, S. S., Goona, N. K., Parne, S. R., Lakavat, M., and Bhaumik, A.: Recent progress in the development of glass and glass-ceramic cathode/solid electrolyte materials for next-generation high capacity all-solid-state sodium-ion batteries: A review. *Journal of Power Sources*, **2022**, 521, 230930. DOI: 10.1016/j.jpowsour.2021.230930.

[71] Kumar, S., Raghupathy, R., and Vittadello, M.: Sodium Polymer Electrolytes: A Review. *Batteries*, **2024**, 10(3), 73. DOI: 10.3390/batteries10030073.

[72] Agrawal, R. C. and Gupta, R. K.: Superionic solids: composite electrolyte phase – an overview. *Journal of Materials Science*, **1999**, 34(6), 1131–1162. DOI: 10.1023/A:1004598902146.

[73] Veelken, P. M., Wirtz, M., Schierholz, R., Tempel, H., Kungl, H., Eichel, R.-A., and Hausen, F.: Investigating the Interface between Ceramic Particles and Polymer Matrix in Hybrid Electrolytes by Electrochemical Strain Microscopy. *Nanomaterials (Basel, Switzerland)*, **2022**, 12(4), 654. DOI: 10.3390/nano12040654.

[74] Xu, X., Wang, Y., Yi, Q., Wang, X., Paredes Camacho, R. A., Kungl, H., Eichel, R. A., Lu, L., and Zhang, H.: Ion Conduction in Composite Polymer Electrolytes: Potential Electrolytes for Sodium-Ion Batteries. *ChemSusChem*, **2023**, 16(8), e202202152. DOI: 10.1002/cssc.202202152.

[75] Karmakar, A. and Ghosh, A.: Poly ethylene oxide (PEO)–LiI polymer electrolytes embedded with CdO nanoparticles. *Journal of Nanoparticle Research*, **2011**, 13(7), 2989–2996. DOI: 10.1007/s11051-010-0194-x.

[76] Bae, J., Li, Y., Zhang, J., Zhou, X., Zhao, F., Shi, Y., Goodenough, J. B., and Yu, G.: A 3D Nanostructured Hydrogel-Framework-Derived High-Performance Composite Polymer Lithium-Ion Electrolyte. *Angewandte Chemie (International ed. in English)*, **2018**, 57(8), 2096–2100. DOI: 10.1002/anie.201710841.

[77] Gong, Y., Fu, K., Xu, S., Dai, J., Hamann, T. R., Zhang, L., Hitz, G. T., Fu, Z., Ma, Z., McOwen, D. W., Han, X., Hu, L., and Wachsman, E. D.: Lithium-ion conductive ceramic textile: A new architecture for flexible solid-state lithium metal batteries. *Materials Today*, **2018**, 21(6), 594–601. DOI: 10.1016/j.mattod.2018.01.001.

[78] Tian, X. and Zhou, K.: 3D printing of cellular materials for advanced electrochemical energy storage and conversion. *Nanoscale*, **2020**, 12(14), 7416–7432. DOI: 10.1039/D0NR00291G.

[79] Zhang, X., Xie, J., Shi, F., Lin, D., Liu, Y., Liu, W., Pei, A., Gong, Y., Wang, H., Liu, K., Xiang, Y., and Cui, Y.: Vertically Aligned and Continuous Nanoscale Ceramic-Polymer Interfaces in Composite Solid Polymer Electrolytes for Enhanced Ionic Conductivity. *Nano letters*, **2018**, 18(6), 3829–3838. DOI: 10.1021/acs.nanolett.8b01111.

[80] Chauhan, A. K., Mishra, K., Kumar, D., and Singh, A.: Enhancing Sodium Ion Transport in a PEO-Based Solid Polymer Electrolyte System with NaAlO2 Active Fillers. *Journal of Electronic Materials*, **2021**, 50(9), 5122–5133. DOI: 10.1007/s11664-021-09051-y.

[81] Lei, D., He, Y.-B., Huang, H., Yuan, Y., Zhong, G., Zhao, Q., Hao, X., Zhang, D., Lai, C., Zhang, S., Ma, J., Wei, Y., Yu, Q., Lv, W., Yu, Y., Li, B., Yang, Q.-H., Yang, Y., Lu, J., and Kang, F.: Cross-linked beta alumina nanowires with compact gel polymer electrolyte coating for ultra-stable sodium metal battery. *Nature communications*, **2019**, 10(1), 4244. DOI: 10.1038/s41467-019-11960-w.

[82] Tamilselvi, S., Gunasundari, S., Karuppiah, N., Razak RK, A., Madhusudan, S., Nagarajan, V. M., Sathish, T., Shamim, M. Z. M., Saleel, C. A., and Afzal, A.: A Review on Battery Modelling Techniques. *Sustainability*, **2021**, 13(18), 10042. DOI: 10.3390/su131810042.

[83] Shi, S., Gao, J., Liu, Y., Zhao, Y., Wu, Q., Ju, W., Ouyang, C., and Xiao, R.: Multi-scale computation methods: Their applications in lithium-ion battery research and development. *Chinese Physics B*, **2016**, 25(1), 018212. DOI: 10.1088/1674-1056/25/1/018212.

[84] Silva, P. de: Quantum Mechanical Modeling of Flow Battery Materials. In: *Flow Batteries*. Roth, C., Noack, J., and Skyllas–Kazacos, M. eds. Wiley, 2023, 333–354. DOI: 10.1002/9783527832767.ch15.

[85] Spotte-Smith, E. W. C., Blau, S. M., Xie, X., Patel, H. D., Wen, M., Wood, B., Dwaraknath, S., and Persson, K. A.: Quantum chemical calculations of lithium-ion battery electrolyte and interphase species. *Scientific data*, **2021**, 8(1), 203. DOI: 10.1038/s41597-021-00986-9.

[86] Zhao, S., Wang, B., Zhang, Z., Zhang, X., He, S., and Yu, H.: First-principles computational insights into lithium battery cathode materials. *Electrochemical Energy Reviews*, **2022**, 5(1), 1–31. DOI: 10.1007/s41918-021-00115-5.

[87] Sun, Y., Yang, T., Ji, H., Zhou, J., Wang, Z., Qian, T., and Yan, C.: Boosting the Optimization of Lithium Metal Batteries by Molecular Dynamics Simulations: A Perspective. *Advanced Energy Materials*, **2020**, 10(41), 2002373. DOI: 10.1002/aenm.202002373.

[88] Muralidharan, A., Chaudhari, M. I., Pratt, L. R., and Rempe, S. B.: Molecular Dynamics of Lithium Ion Transport in a Model Solid Electrolyte Interphase. *Scientific reports*, **2018**, 8(1), 10736. DOI: 10.1038/s41598-018-28869-x.

[89] He, Q., Yu, B., Li, Z., and Zhao, Y.: Density Functional Theory for Battery Materials. *ENERGY & ENVIRONMENTAL MATERIALS*, **2019**, 2(4), 264–279. DOI: 10.1002/eem2.12056.

[90] Gavilán-Arriazu, E. M., Mercer, M. P., Barraco, D. E., Hoster, H. E., and Leiva, E. P. M.: Kinetic Monte Carlo simulations applied to Li-ion and post Li-ion batteries: a key link in the multi-scale chain. *Progress in Energy*, **2021**, 3(4), 042001. DOI: 10.1088/2516-1083/ac1a65.

[91] Wang, Q., Zhang, G., Li, Y., Hong, Z., Da Wang, and Shi, S.: Application of phase-field method in rechargeable batteries. *npj Computational Materials*, **2020**, 6(1), 176. DOI: 10.1038/s41524-020-00445-w.

[92] Newman, J. S. and Tobias, C. W.: Theoretical Analysis of Current Distribution in Porous Electrodes. *Journal of The Electrochemical Society*, **1962**, 109(12), 1183. DOI: 10.1149/1.2425269.

[93] Plett, G. L.: *Battery management systems: Volume 1: battery modeling*. Vol. 1. Artech House power engineering and power electronics. Boston: Artech House, 2015.

[94] Richardson, G., Denuault, G., and Please, C. P.: Multiscale modelling and analysis of lithium-ion battery charge and discharge. *Journal of Engineering Mathematics*, **2012**, 72(1), 41–72. DOI: 10.1007/s10665-011-9461-9.

[95] Goldin, G. M., Colclasure, A. M., Wiedemann, A. H., and Kee, R. J.: Three-dimensional particle-resolved models of Li-ion batteries to assist the evaluation of empirical parameters in one-dimensional models. *Electrochimica Acta*, **2012**, 64, 118–129. DOI: 10.1016/j.electacta.2011.12.119.

[96] Less, G. B., Seo, J. H., Han, S., Sastry, A. M., Zausch, J., Latz, A., Schmidt, S., Wieser, C., Kehrwald, D., and Fell, S.: Micro-Scale Modeling of Li-Ion Batteries: Parameterization and Validation. *Journal of The Electrochemical Society*, **2012**, 159(6), A697–A704. DOI: 10.1149/2.096205jes.

[97] Kim, S., Wee, J., Peters, K., and Huang, H.-Y. S.: Multiphysics Coupling in Lithium-Ion Batteries with Reconstructed Porous Microstructures. *The Journal of Physical Chemistry C*, **2018**, 122(10), 5280–5290. DOI: 10.1021/acs.jpcc.7b12388.

[98] Fuller, T. F., Doyle, M., and Newman, J.: Simulation and Optimization of the Dual Lithium Ion Insertion Cell. *Journal of The Electrochemical Society*, **1994**, 141(1), 1–10. DOI: 10.1149/1.2054684.

[99] Richardson, G. W., Foster, J. M., Ranom, R., Please, C. P., and Ramos, A. M.: Charge transport modelling of Lithium-ion batteries. *European Journal of Applied Mathematics*, **2022**, 33(6), 983–1031. DOI: 10.1017/S0956792521000292.

[100] Atlung, S., West, K., and Jacobsen, T.: Dynamic Aspects of Solid Solution Cathodes for Electrochemical Power Sources. *Journal of The Electrochemical Society*, **1979**, 126(8), 1311–1321. DOI: 10.1149/1.2129269.

[101] Brosa Planella, F., Ai, W., Boyce, A. M., Ghosh, A., Korotkin, I., Sahu, S., Sulzer, V., Timms, R., Tranter, T. G., Zyskin, M., Cooper, S. J., Edge, J. S., Foster, J. M., Marinescu, M., Wu, B., and Richardson, G.: A continuum of physics-based lithium-ion battery models reviewed. *Progress in Energy*, **2022**, 4(4), 042003. DOI: 10.1088/2516-1083/ac7d31.

[102] Milazzo, G. and Caroli, S.: *Tables of standard electrode potentials: Project of the IUPAC Electrochemistry Commission*. Vol. 125. A Wiley-Interscience publication. Chichester: Wiley, 1978.

[103] Rumble, J. R., Bruno, T. J., and Doa, M. J., eds.: *CRC handbook of chemistry and physics: A ready-reference book of chemical and physical data*. 101st edition, 2020-2021. Boca Raton, London, and New York: CRC Press Taylor & Francis Group, 2020.

[104] Anantharamulu, N., Koteswara Rao, K., Rambabu, G., Vijaya Kumar, B., Radha, V., and Vithal, M.: A wide-ranging review on Nasicon type materials. *Journal of Materials Science*, **2011**, 46(9), 2821–2837. DOI: 10.1007/s10853-011-5302-5.

[105] Gross, M. M., Small, L. J., Peretti, A. S., Percival, S. J., Rodriguez, M. A., and Spoerke, E. D.: Tin-based ionic chaperone phases to improve low temperature molten sodium–NaSICON interfaces. *Journal of Materials Chemistry A*, **2020**, 8(33), 17012–17018. DOI: 10.1039/D0TA03571H.

[106] Vetter, K. J.: *Electrochemical Kinetics: Theoretical Aspects*. Burlington: Elsevier Science, 1967. DOI: 10.1016/C2013-0-12183-6.

[107] Wroblowa, H. S. and Saunders, A.: Flow-through electrodes. *Journal of Electroanalytical Chemistry and Interfacial Electrochemistry*, **1973**, 42(3), 329–346. DOI: 10.1016/S0022-0728(73)80323-7.

[108] Atkins, P. W., Paula, J. de, and Keeler, J.: *Atkins' physical chemistry*. Eleventh edition. Oxford and New York: Oxford University Press, 2018.

[109] Newman, J. S. and Thomas-Alyea, K. E.: *Electrochemical systems*. 3. ed. Electrochemical Society series. Hoboken, NJ: Wiley-Interscience, 2004.

[110] Vardner, J. T., Russell, S. T., Brady, N. W., Inaba, Y., Kumar, S. K., and West, A. C.: Application of Concentrated Solution Theory to the Measurement of Salt Transference Numbers in Ion-Selective Membranes. *Journal of The Electrochemical Society*, **2020**, 167(2), 020546. DOI: 10.1149/1945-7111/ab6c52.

[111] Dané, L. M., Janssen, L., and Hoogland, J. G.: The iodine/iodide redox couple at a platinum electrode. *Electrochimica Acta*, **1968**, 13(3), 507–518. DOI: 10.1016/0013-4686(68)87022-7.

[112] Thomas, K. E., Newman, J., and Darling, R. M.: Mathematical Modeling of Lithium Batteries. In: *Advances in lithium-ion batteries*. van Schalkwijk, W. A. and Scorsati, B. eds. New York: Kluwer Academic/Plenum Publ, 2002, 345–392. DOI: 10.1007/0-306-47508-1_13.

[113] Behl, W. K. and Chin, D.-T.: Electrochemical Overcharge Protection of Rechargeable Lithium Batteries: I . Kinetics of Iodide/Tri–Iodide/Iodine Redox Reactions on Platinum in Solutions. *Journal of The Electrochemical Society*, **1988**, 135(1), 16–21. DOI: 10.1149/1.2095545.

[114] Zhao, Y., Wang, L., and Byon, H. R.: High-performance rechargeable lithium-iodine batteries using triiodide/iodide redox couples in an aqueous cathode. *Nature communications*, **2013**, 4, 1896. DOI: 10.1038/ncomms2907.

[115] Macagno, V. A., Giordano, M. C., and Arvía, A. J.: Kinetics and mechanisms of electrochemical reactions on platinum with solutions of iodine-sodium iodide in acetonitrile. *Electrochimica Acta*, **1969**, 14(4), 335–357. DOI: 10.1016/0013-4686(69)85005-X.

[116] Palmer, D. A., Ramette, R. W., and Mesmer, R. E.: Triiodide ion formation equilibrium and activity coefficients in aqueous solution. *Journal of Solution Chemistry*, **1984**, 13(9), 673–683. DOI: 10.1007/BF00650374.

[117] Anderko, A. and Lencka, M. M.: Computation of Electrical Conductivity of Multicomponent Aqueous Systems in Wide Concentration and Temperature Ranges. *Industrial & Engineering Chemistry Research*, **1997**, 36(5), 1932–1943. DOI: 10.1021/ie9605903.

[118] Cantrel, L., Chaouche, R., and Chopin-Dumas, J.: Diffusion Coefficients of Molecular Iodine in Aqueous Solutions. *Journal of Chemical & Engineering Data*, **1997**, 42(1), 216–220. DOI: 10.1021/je960178u.

[119] Cantrel, L., Fulconis, J.-M., and Chopin-Dumas, J.: Voltammetric Analysis of Iodide and Diffusion Coefficients Between 25 and 85°C. *Journal of Solution Chemistry*, **1998**, 27(4), 373–393. DOI: 10.1023/A:1022679716395.

[120] Bazant, M. Z.: Theory of chemical kinetics and charge transfer based on nonequilibrium thermodynamics. *Accounts of chemical research*, **2013**, 46(5), 1144–1160. DOI: 10.1021/ar300145c.

[121] Bessler, W., Warnatz, J., and Goodwin, D.: The influence of equilibrium potential on the hydrogen oxidation kinetics of SOFC anodes. *Solid State Ionics*, **2007**, 177(39-40), 3371–3383. DOI: 10.1016/j.ssi.2006.10.020.

[122] Fu, H., Yin, Q., Huang, Y., Sun, H., Chen, Y., Zhang, R., Yu, Q., Gu, L., Duan, J., and Luo, W.: Reducing Interfacial Resistance by Na-SiO 2 Composite Anode for NASICON-Based Solid-State Sodium Battery. *ACS Materials Letters*, **2020**, 2(2), 127–132. DOI: 10.1021/acsmaterialslett.9b00442.

[123] Hayashi, A., Noi, K., Sakuda, A., and Tatsumisago, M.: Superionic glass-ceramic electrolytes for room-temperature rechargeable sodium batteries. *Nature communications*, **2012**, 3, 856. DOI: 10.1038/ncomms1843.

[124] Goldstein, S. W.: The iodide-iodine solubility relation. *Journal of the American Pharmaceutical Association. American Pharmaceutical Association*, **1952**, 41(6), 333–335. DOI: 10.1002/jps.3030410618.

[125] Weller, H. G., Tabor, G., Jasak, H., and Fureby, C.: A tensorial approach to computational continuum mechanics using object-oriented techniques. *Computers in Physics*, **1998**, 12(6), 620. DOI: 10.1063/1.168744.

[126] Moukalled, F., Mangani, L., and Darwish, M.: *The finite volume method in computational fluid dynamics: An advanced introduction with OpenFOAM and Matlab*. Vol. volume 113. Fluid mechanics and its applications. Cham et al.: Springer, 2016.

[127] Kespe, M. A.: *Simulation von Transportvorgängen in Lithium-Ionen Batterien auf der partikulären Ebene*. 2019. DOI: 10.5445/IR/1000097980.

[128] Armijo, L.: Minimization of functions having Lipschitz continuous first partial derivatives. *Pacific Journal of Mathematics*, **1966**, 16(1), 1–3. DOI: 10.2140/pjm.1966.16.1.

[129] Deuflhard, P.: *Newton Methods for Nonlinear Problems*. Vol. 35. Berlin, Heidelberg: Springer Berlin Heidelberg, 2011. DOI: 10.1007/978-3-642-23899-4.

[130] Gerbig, F., Cernak, S., and Nirschl, H.: 3D Simulation of Cell Design Influences on Sodium–Iodine Battery Performance. *Energy Technology*, **2021**, 9(6), 2000857. DOI: 10.1002/ente.202000857.

[131] Yamada, S. and Sato, H.: Some Physical Properties of Glassy Carbon. *Nature*, **1962**, 193(4812), 261–262. DOI: 10.1038/193261b0.

[132] Sweet, J. N., Roth, E. P., and Moss, M.: Thermal conductivity of Inconel 718 and 304 stainless steel. *International Journal of Thermophysics*, **1987**, 8(5), 593–606. DOI: 10.1007/BF00503645.

[133] Gerbig, F., Holzapfel, M., and Nirschl, H.: Simulating the Impact of Glassy Carbon Foam Electrodes on the Performance of Sodium Iodine Batteries. *Journal of The Electrochemical Society*, **2023**, 170(4), 040517. DOI: 10.1149/1945-7111/accab7.

[134] Walsh, F. C., Arenas, L. F., Ponce de León, C., Reade, G. W., Whyte, I., and Mellor, B. G.: The continued development of reticulated vitreous carbon as a versatile electrode material: Structure, properties and applications. *Electrochimica Acta*, **2016**, 215, 566–591. DOI: 10.1016/j.electacta.2016.08.103.

[135] Pletcher, D. and Walsh, F. C.: Three-Dimensional Electrodes. In: *Electrochemistry for a cleaner environment*. Genders, J. D. and Weinberg, N. L. eds. East Amherst, NY: Electrosynthesis Company, 1992, 51–100. DOI: 10.1007/SpringerReference_67825.

[136] Kurtis Chad Kelley, Washington, IL SS John J. Votoupal, Hudson, IL: Battery Including Carbon Foam Current Collectors. US6979513B2.

[137] Fraser, E. J., Le Houx, J. P., Arenas, L. F., Dinesh, K. R., and Wills, R.: The soluble lead flow battery: Image-based modelling of porous carbon electrodes. *Journal of Energy Storage*, **2022**, 52, 104791. DOI: 10.1016/j.est.2022.104791.

[138] Kim, S. and Lee, C.-W.: A Review on Manufacturing and Application of Open-cell Metal Foam. *Procedia Materials Science*, **2014**, 4, 305–309. DOI: 10.1016/j.mspro.2014.07.562.

[139] Dukhan, N.: *Proceedings of the 11th International Conference on Porous Metals and Metallic Foams (MetFoam 2019)*. Cham: Springer International Publishing, 2020. DOI: 10.1007/978-3-030-42798-6.

[140] Thomson, W.: LXIII. On the division of space with minimum partitional area. *The London, Edinburgh, and Dublin Philosophical Magazine and Journal of Science*, **1887**, 24(151), 503–514. DOI: 10.1080/14786448708628135.

[141] Weaire, D. and Phelan, R.: A counter-example to Kelvin's conjecture on minimal surfaces. *Philosophical Magazine Letters*, **1994**, 69(2), 107–110. DOI: 10.1080/09500839408241577.

[142] Shakibanezhad, R., Sadighi, M., and Hedayati, R.: Numerical and Experimental Study of Quasi-Static Loading of Aluminum Closed-Cell Foams Using Weaire–Phelan and Kelvin Tessellations. *Transport in Porous Media*, **2022**, 142(1-2), 229–248. DOI: 10.1007/s11242-021-01729-5.

[143] Cunsolo, S., Iasiello, M., Oliviero, M., Bianco, N., Chiu, W. K. S., and Naso, V.: Lord Kelvin and Weaire–Phelan Foam Models: Heat Transfer and Pressure Drop. *Journal of Heat Transfer*, **2016**, 138(2), 022601. DOI: 10.1115/1.4031700.

[144] Bai, M. and Chung, J. N.: Analytical and numerical prediction of heat transfer and pressure drop in open-cell metal foams. *International Journal of Thermal Sciences*, **2011**, 50(6), 869–880. DOI: 10.1016/j.ijthermalsci.2011.01.007.

[145] Tentorio, A. and Casolo-Ginelli, U.: Characterization of reticulate, three - dimensional electrodes. *Journal of Applied Electrochemistry*, **1978**, 8(3), 195–205. DOI: 10.1007/BF00616422.

[146] Czerwiński, A., Rogulski, Z., Obrębowski, S., Siwek, H., Paleska, I., Chotkowski, M., and Łukaszewski, M.: RVC as new carbon material for batteries. *Journal of Applied Electrochemistry*, **2009**, 39(5), 559–567. DOI: 10.1007/s10800-009-9791-8.

[147] Mastragostino, M. and Gramellini, C.: Kinetic study of the electrochemical processes of the bromine/bromine aqueous system on vitreous carbon electrodes. *Electrochimica Acta*, **1985**, 30(3), 373–380. DOI: 10.1016/0013-4686(85)80198-5.

[148] Steinhaus, H.: *Mathematical snapshots*. 3. American ed., rev. and enl. Mineola, NY: Dover Publ, 1999. URL: http://www.loc.gov/catdir/description/dover032/99033052.html.

[149] Cundy, H. M. and Rollett, A. P.: *Mathematical models*. 3. ed., repr. St. Albans: Tarquin Publications, 2007.

[150] Harris, J. and Stöcker, H.: *Handbook of mathematics and computational science*. New York, Berlin, and Heidelberg: Springer, 2006.

[151] Gerbig, F., Cernak, S., and Nirschl, H.: Towards a Novel Sodium-Iodine Battery with an Aqueous Catholyte: Numerical Investigations of Complex Cathode Structures. *ECS Transactions*, **2021**, 104(1), 123–130. DOI: 10.1149/10401.0123ecst.

[152] Doyle, M., Fuller, T. F., and Newman, J.: Modeling of Galvanostatic Charge and Discharge of the Lithium/Polymer/Insertion Cell. *Journal of The Electrochemical Society*, **1993**, 140(6), 1526–1533. DOI: 10.1149/1.2221597.

[153] Emereuwa, C. A.: Mathematical homogenization and stochastic modeling of energy storage systems. *Current Opinion in Electrochemistry*, **2020**, 21, 117–124. DOI: 10.1016/j.coelec.2020.01.009.

[154] Blender Developement Team: *Blender - a 3D modelling and rendering package*. Stichting Blender Foundation, Amsterdam, 2021. URL: http://www.blender.org.

[155] Catmull, E. and Clark, J.: Recursively generated B-spline surfaces on arbitrary topological meshes. *Computer-Aided Design*, **1978**, 10(6), 350–355. DOI: 10.1016/0010-4485(78)90110-0.

[156] Pesek, S. and Silaghi-Dumitrescu, R.: The Iodine/Iodide/Starch Supramolecular Complex. *Molecules (Basel, Switzerland)*, **2024**, 29(3), 641. DOI: 10.3390/molecules29030641.

[157] Haddock, A., Steidemann, M., and Readnour, M.: Polyiodide Equilibria in Aqueous Solutions of Iodine and Iodide. *Synthesis and Reactivity in Inorganic and Metal-Organic Chemistry*, **1979**, 9(1), 39–56. DOI: 10.1080/00945717908057450.

[158] Åvall, G., Mindemark, J., Brandell, D., and Johansson, P.: Sodium–Ion Battery Electrolytes: Modeling and Simulations. *Advanced Energy Materials*, **2018**, 8(17), 1703036. DOI: 10.1002/aenm.201703036.

[159] Kim, H.-K., Barai, P., Chavan, K., and Srinivasan, V.: Transport and mechanical behavior in PEO-LLZO composite electrolytes. *Journal of Solid State Electrochemistry*, **2022**, 26(9), 2059–2075. DOI: 10.1007/s10008-022-05231-w.

[160] Xiang, H., Wang, Y., Li, K., Zhang, X., and Chen, Z.: A comprehensive study on state-of-charge and state-of-health estimation of sodium-ion batteries. *Journal of Energy Storage*, **2023**, 72, 108314. DOI: 10.1016/j.est.2023.108314.

[161] Chayambuka, K., Mulder, G., Danilov, D. L., and Notten, P. H.: Physics-based modeling of sodium-ion batteries part II. Model and validation. *Electrochimica Acta*, **2022**, 404, 139764. DOI: 10.1016/j.electacta.2021.139764.

[162] Garapati, V. K., Dingari, N. N., Mynam, M., and Rai, B.: Physics-Based Reduced Order Model for Sodium-Ion Batteries. *Journal of The Electrochemical Society*, **2023**, 170(1), 010517. DOI: 10.1149/1945-7111/acb01b.

[163] Jagad, H. D., Fu, J., Fullerton, W. R., Li, C. Y., Detsi, E., and Qi, Y.: A Physics-based Model Assisted by Machine-Learning for Sodium-ion Batteries with both Liquid and Solid Electrolytes. *Journal of The Electrochemical Society*, **2024**, 171(6), 060516. DOI: 10.1149/1945-7111/ad4a11.

[164] Kim, E. J., Kumar, P. R., Gossage, Z. T., Kubota, K., Hosaka, T., Tatara, R., and Komaba, S.: Active material and interphase structures governing performance in sodium and potassium ion batteries. *Chemical science*, **2022**, 13(21), 6121–6158. DOI: 10.1039/d2sc00946c.

[165] Wang, Y., Wang, Z., Sun, J., Zheng, F., Kotobuki, M., Wu, T., Zeng, K., and Lu, L.: Flexible, stable, fast-ion-conducting composite electrolyte composed of nanostructured Na-super-ion-conductor framework and continuous Poly(ethylene oxide) for all-solid-state Na battery. *Journal of Power Sources*, **2020**, 454, 227949. DOI: 10.1016/j.jpowsour.2020.227949.

[166] Park, S., Wang, Z., Choudhary, K., Chotard, J.-N., Carlier, D., Fauth, F., Canepa, P., Croguennec, L., and Masquelier, C.: Obtaining $V_2(PO_4)_3$ by sodium extraction from single-phase $NaxV_2(PO_4)_3$ ($1 < x < 3$) positive electrode materials. *Nature materials*, **2024**. DOI: 10.1038/s41563-024-02023-7.

[167] Kespe, M. and Nirschl, H.: Numerical simulation of lithium-ion battery performance considering electrode microstructure. *International Journal of Energy Research*, **2015**, 39(15), 2062–2074. DOI: 10.1002/er.3459.

[168] Novikova, S. A., Larkovich, R. V., Chekannikov, A. A., Kulova, T. L., Skundin, A. M., and Yaroslavtsev, A. B.: Electrical Conductivity and Electrochemical Characteristics of $Na_3V_2(PO_4)_3$-Based NASICON-Type Materials. *Inorganic Materials*, **2018**, 54(8), 794–804. DOI: 10.1134/S0020168518080149.

[169] Mongcopa, K. I. S., Tyagi, M., Mailoa, J. P., Samsonidze, G., Kozinsky, B., Mullin, S. A., Gribble, D. A., Watanabe, H., and Balsara, N. P.: Relationship between Segmental Dynamics Measured by Quasi-Elastic Neutron Scattering and Conductivity in Polymer Electrolytes. *ACS macro letters*, **2018**, 7(4), 504–508. DOI: 10.1021/acsmacrolett.8b00159.

[170] Ferry, A., Doeff, M. M., and Jonghe, L. C. de: Transport Property and Raman Spectroscopic Studies of the Polymer Electrolyte System $P(EO)_n$–NaTFSI. *Journal of The Electrochemical Society*, **1998**, 145(5), 1586–1592. DOI: 10.1149/1.1838522.

[171] Bazant, M. Z.: Unified quantum theory of electrochemical kinetics by coupled ion-electron transfer. *Faraday discussions*, **2023**, 246(0), 60–124. DOI: 10.1039/d3fd00108c.

[172] Gao, H., Xue, L., Xin, S., Park, K., and Goodenough, J. B.: A Plastic-Crystal Electrolyte Interphase for All-Solid-State Sodium Batteries. *Angewandte Chemie (International ed. in English)*, **2017**, 56(20), 5541–5545. DOI: 10.1002/anie.201702003.

[173] Liu, X., Feng, G., Wang, E., Chen, H., Wu, Z., Xiang, W., Zhong, Y., Chen, Y., Guo, X., and Zhong, B.: Insight into Preparation of Fe-Doped $Na_3V_2(PO_4)_3$@C from Aspects of Particle Morphology Design, Crystal Structure Modulation, and Carbon Graphitization Regulation. *ACS applied materials & interfaces*, **2019**, 11(13), 12421–12430. DOI: 10.1021/acsami.8b21257.

[174] Kaus, M., Guin, M., Yavuz, M., Knapp, M., Tietz, F., Guillon, O., Ehrenberg, H., and Indris, S.: Fast Na^+ Ion Conduction in NASICON-Type $Na_{3.4}Sc_2(SiO_4)_{0.4}(PO_4)_{2.6}$ Observed by ^{23}Na NMR Relaxometry. *The Journal of Physical Chemistry C*, **2017**, 121(3), 1449–1454. DOI: 10.1021/acs.jpcc.6b10523.

[175] Serra Moreno, J., Armand, M., Berman, M. B., Greenbaum, S. G., Scrosati, B., and Panero, S.: Composite PEO_n:NaTFSI polymer electrolyte: Preparation, thermal and electrochemical characterization. *Journal of Power Sources*, **2014**, 248, 695–702. DOI: 10.1016/j.jpowsour.2013.09.137.

[176] Moradipour, F., Markert, A., Rudszuck, T., Röttgen, N., Dück, G., Finsterbusch, M., Gerbig, F., Nirschl, H., and Guthausen, G.: Na^+ Mobility in PEO-Based Composite Solid-State Electrolytes by NMR. *Journal of Energy and Power Technology*, **2023**, 05(04), 1–21. DOI: 10.21926/jept.2304032.

[177] Wróbel, P., Kubisiak, P., and Eilmes, A.: NaFSI and NaTFSI Solutions in Ether Solvents from Monoglyme to Poly(ethylene oxide)–A Molecular Dynamics Study. *The Journal of Physical Chemistry B*, **2021**, 125(36), 10293–10303. DOI: 10.1021/acs.jpcb.1c05793.

[178] Zheng, Q., Yi, H., Liu, W., Li, X., and Zhang, H.: Improving the electrochemical performance of $Na_3V_2(PO_4)_3$ cathode in sodium ion batteries through Ce/V substitution based on rational design and synthesis optimization. *Electrochimica Acta*, **2017**, 238, 288–297. DOI: 10.1016/j.electacta.2017.04.029.

[179] Sequeira, C. and Hooper, A.: The study of lithium electrode reversibility against $(PEO)_xLiF_3CSO_3$ polymeric electrolytes. *Solid State Ionics*, **1983**, 9-10, 1131–1138. DOI: 10.1016/0167-2738(83)90142-X.

[180] Karthikeyan, D. K., Sikha, G., and White, R. E.: Thermodynamic model development for lithium intercalation electrodes. *Journal of Power Sources*, **2008**, 185(2), 1398–1407. DOI: 10.1016/j.jpowsour.2008.07.077.

[181] Redlich, O. and Kister, A. T.: Thermodynamics of Nonelectrolyte Solutions - x-y-t relations in a Binary System. *Industrial & Engineering Chemistry*, **1948**, 40(2), 341–345. DOI: 10.1021/ie50458a035.

[182] Walas, S. M.: *Phase Equilibria in Chemical Engineering*. Stoneham, Massachusetts: Butterworth Publishers, 1985. DOI: 10.1016/C2013-0-04304-6.

[183] Si, L., Yuan, Z., Hu, L., Zhu, Y., and Qian, Y.: Uniform and continuous carbon coated sodium vanadium phosphate cathode materials for sodium-ion battery. *Journal of Power Sources*, **2014**, 272, 880–885. DOI: 10.1016/j.jpowsour.2014.09.046.

[184] Gerbig, F., Chauhan, A., Gietl, S., and Nirschl, H.: Performance Investigations on All-Solid-State Polymer-Ceramic Sodium-Ion Batteries through a Spatially Resolved Electrochemical Model. *Journal of The Electrochemical Society*, **2024**, 171(9), 090515. DOI: 10.1149/1945-7111/ad7763.

[185] Chauhan, A., Asylbekov, E., Kespe, S., and Nirschl, H.: Influence of carbon binder domain on the performance of lithium–ion batteries: Impact of size and fractal dimension. *Electrochemical Science Advances*, **2023**, 3(1), e2100151. DOI: 10.1002/elsa.202100151.

[186] Sulzer, V., Marquis, S. G., Timms, R., Robinson, M., and Chapman, S. J.: Python Battery Mathematical Modelling (PyBaMM). *Journal of Open Research Software*, **2021**, 9(1), 14. DOI: 10.5334/jors.309.

[187] Gray, W. G. and Lee, P.: On the theorems for local volume averaging of multiphase systems. *International Journal of Multiphase Flow*, **1977**, 3(4), 333–340. DOI: 10.1016/0301-9322(77)90013-1.

[188] Jamnik, J., Kalnin, J. R., Kotomin, E. A., and Maier, J.: Generalised Maxwell-Garnett equation: application to electrical and chemical transport. *Physical chemistry chemical physics : PCCP*, **2006**, 8(11), 1310–1314. DOI: 10.1039/b514448p.

[189] Przyluski, J., Siekierski, M., and Wieczorek, W.: Effective medium theory in studies of conductivity of composite polymeric electrolytes. *Electrochimica Acta*, **1995**, 40(13-14), 2101–2108. DOI: 10.1016/0013-4686(95)00147-7.

[190] Tsotsas, E. and Martin, H.: Thermal conductivity of packed beds: A review. *Chemical Engineering and Processing: Process Intensification*, **1987**, 22(1), 19–37. DOI: 10.1016/0255-2701(87)80025-9.

[191] Rodrigues, S. J., Vorhauer-Huget, N., and Tsotsas, E.: Prediction of effective thermal conductivity of packed beds of polyhedral particles. *Powder Technology*, **2023**, 430, 118997. DOI: 10.1016/j.powtec.2023.118997.

[192] Blumberg, W. and Schlünder, E.-U.: Thermal conductivity of packed beds consisting of porous particles wetted with binary mixtures. *Chemical Engineering and Processing: Process Intensification*, **1995**, 34(3), 339–346. DOI: 10.1016/0255-2701(95)00583-8.

[193] Andersson, J. A. E., Gillis, J., Horn, G., Rawlings, J. B., and Diehl, M.: CasADi: a software framework for nonlinear optimization and optimal control. *Mathematical Programming Computation*, **2019**, 11(1), 1–36. DOI: 10.1007/s12532-018-0139-4.

[194] Gerbig, F., Kühn, J., and Nirschl, H.: Optimizing all-solid-state sodium-ion batteries: Insights from a P2D Model on NaSICON-based polymer–ceramic electrolyte. *Energy Reports*, **2025**, 13, 105–116. DOI: https://doi.org/10.1016/j.egyr.2024.11.077.

[195] Shen, L. and Chen, Z.: Critical review of the impact of tortuosity on diffusion. *Chemical Engineering Science*, **2007**, 62(14), 3748–3755. DOI: 10.1016/j.ces.2007.03.041.

[196] Storn, R. and Price, K.: Differential Evolution – A Simple and Efficient Heuristic for global Optimization over Continuous Spaces. *Journal of Global Optimization*, **1997**, 11(4), 341–359. DOI: 10.1023/A:1008202821328.

[197] Haimes, Y. Y.: *Integrated System Identification and Optimization*. C.T. Leondes ed. Vol. 10. Control and Dynamic Systems. Academic Press, 1973, 435–518. DOI: 10.1016/B978-0-12-012710-8.50013-3.

[198] Teran, A. A. and Balsara, N. P.: Thermodynamics of block copolymers with and without salt. *The Journal of Physical Chemistry B*, **2014**, 118(1), 4–17. DOI: 10.1021/jp408079z.

[199] Fuentes, R. O., Marques, F. M. B., and Franco, J. I.: Síntesis y propiedades de Nasicon preparado a partir de diferentes precursores basados en circonia. *Boletín de la Sociedad Española de Cerámica y Vidrio*, **1999**, 38(6), 631–634. DOI: 10.3989/cyv.1999.v38.i6.908.

[200] Zeng, J., Yang, Y., Lai, S., Huang, J., Zhang, Y., Wang, J., and Zhao, J.: A Promising High-Voltage Cathode Material Based on Mesoporous $Na_3V_2(PO_4)_3$/C for Rechargeable Magnesium Batteries. *Chemistry (Weinheim an der Bergstrasse, Germany)*, **2017**, 23(66), 16898–16905. DOI: 10.1002/chem.201704303.

[201] Chun, J., Wang, X., Zhang, Y., Wei, C., Wang, Z., and Feng, J.: $Ti_3C_2T_x$ film current collectors for high-performance sodium-ion batteries. *Vacuum*, **2023**, 207, 111476. DOI: 10.1016/j.vacuum.2022.111476.

[202] Yim, C.-H., Houache, M. S., Baranova, E. A., and Abu-Lebdeh, Y.: Understanding key limiting factors for the development of all-solid-state-batteries. *Chemical Engineering Journal Advances*, **2023**, 13, 100436. DOI: 10.1016/j.ceja.2022.100436.

[203] Gerbig, F., Röttgen, N., Holzapfel, M., Dück, G., Finsterbusch, M., and Nirschl, H.: Unraveling ionic transport in polymer-ceramic electrolytes: Insights into superionic interphases. *Electrochemistry Communications*, **2025**, 107960. DOI: 10.1016/j.elecom.2025.107960.